UNIVERSITY OF OKLAHOMA

GRADUATE COLLEGE

PORE-SCALE MODELING AND MULTI-SCALE CHARACTERIZATION OF LIQUID TRANSPORT IN SHALES

A DISSERTATION

SUBMITTED TO THE GRADUATE FACULTY

in partial fulfillment of the requirements for the

Degree of

DOCTOR OF PHILOSOPHY

By

DA ZHENG
Norman, Oklahoma
2018

PORE-SCALE MODELING AND MULTI-SCALE CHARACTERIZATION OF LIQUID TRANSPORT IN SHALES

A DISSERTATION APPROVED FOR THE
MEWBOURNE SCHOOL OF PETROLEUM AND GEOLOGICAL ENGINEERING

BY

Dr. Zulfiquar Reza, Chair

Dr. Liangliang Huang

Dr. Benjamin Shiau

Dr. Xingru Wu

Dr. Hamidreza Karami

Dedicate to my dear mom and dad who gave me countless love and support.

谨以此文献给我敬爱的父母，感谢你们对我无私的爱与支持，

愿你们一生幸福快乐。

Acknowledgements

I would like to express my highest appreciation to Dr. Zulfiquar Reza for his support during my Ph.D. study. His in-depth analyses and thoughtful comments are incentives for me to think more critically. His rather earnest attitude towards scientific research stimulates me to overcome tough obstacles in chasing the aim of research work. Without his endless guidance and assistance, it is impossible for me to perform valuable investigations in petroleum engineering.

I also would like to acknowledge the advisory committee members, Dr. Liangliang Huang, Dr. Xingru Wu, Dr. Benjamin Shiau and Dr. Hamidreza Karami for their guidance and support of my research. Their comments and advisories are important for me to perform better research.

I would like to thank my parents, Mr. Xingbo Zheng and Mrs. Hongru Li. Even though we were staying in the opposite side of the world, your love is the solid support for me to chasing my dream. Studying abroad for six years, I feel deeply remorseful that I didn’t perform enough responsibility as a child. For the rest of my life, I will do my best to make our family happy and harmonious. Love you!

Finally, I would like to thank my country. Wherever I stay, I feel immensely proud of being a citizen of China. A great and united country is the most powerful support for me to step on the ground of any country in the world. Even though my ability is limited, I will dedicate myself for the whole life in the ideal of making it better.

Table of Contents

Acknowledgements v

Table of Contents vi

List of Tables x

List of Figures xi

Abstract xxii

Chapter 1 Introduction 1

- 1.1 Background 1
- 1.2 Motivations 3
- 1.3 Organization 6

Chapter 2 Literature Review 9

- 2.1 Theoretical Pore-network Models 9
  - 2.1.1 Bundle-of-Tube Model 9
  - 2.1.2 Lattice Model 10
  - 2.1.3 Sphere Packing Model 13
  - 2.1.4 Tree-like Model 16
- 2.2 Extracted Pore-network Modeling 21
  - 2.2.1 Multi-orientation Scanning Algorithm 21
  - 2.2.2 Medial axis-based algorithms 24
  - 2.2.2.1 Burning Algorithm 24
  - 2.2.2.2 Thinning Algorithm 27
  - 2.2.2.3 Hybrid Algorithm 28

2.2.2.4 Discussions 29
2.2.3 Maximal-Ball Algorithm 32
Chapter 3 Integrated Pore-Scale Characterization Using Dendroidal Theoretical Pore-network Model 37
3.1 Characterization of Pore Connectivity 37
3.2 Experimental Data 40
3.3 Dendroidal Model 41
3.3.1 Dendroidal Pore-network Model Description 41
3.3.2 Correction of Mercury Drainage Experimental Data 45
3.3.3 Pore-Throat Shapes 46
3.3.4 Isothermal Adsorption/Desorption Measurement 49
3.3.5 Mechanisms of Mercury Intrusion 50
3.3.6 Mechanisms of Mercury Retraction 53
3.3.6.1 Piston-Type Imbibition 54
3.3.6.2 Pore-Body Filling 55
3.3.6.3 Snap-off 57
3.3.7 Integrated Procedures of Dendroidal-Model Construction 60
3.4 Absolute Permeability 65
3.5 Apparent Permeability 67
3.6. Relative Permeability 72
3.7 Case Study 73

3.8 Discussions 87
Chapter 4 Extracted Pore-Network Model for Shales Characterizing Geometry of Void Space 91
4.1 Skeleton Characterization 91
4.2 Classification of Pore Bodies and Pore Throats 94
4.3 Pore Shape Characterization 100
4.4 Pore Size Determination 103
4.5 Case Study 106
4.6 Results and Analysis 108
Chapter 5 Multi-scale Characterization of Liquid Flow in Shale Porous Media.......... 117
5.1 Integrated Procedures of Multi-Scale Modeling of Liquid flow 117
5.2 Physical Mechanisms of Nanoconfined Fluid 118
5.3 Modified Navier-Stokes Equation for Single-phase Nanoconfined Liquid Flow 120
5.3.1 Nanotube with Circular Cross-section 122
5.3.2 Nanotube with Rectangular and Triangular Cross-section 125
5.4 Modified Navier-Stokes Equation for Liquid Flow in Nanoconfined Pores with Adsorption Film 130
5.4.1 Nanotubes with Circular Cross-section 131
5.4.2 Nanotubes with Triangular and Rectangular Cross-section....................... 134
5.5 Characterization of Alkane Flow in Nanotube 137
5.5.1 Density Distribution... 137

    - 5.5.2 Viscosity Distribution and Slip Length 139
- 5.6 Characterization of Water Flow in Nanotube 141
    - 5.6.1 Slip Length 141
    - 5.6.2 Viscosity Distribution 143
- 5.7 Characterization of Water Film 144
- 5.8 Construction of Multi-scale Liquid Flow Model 146
- 5.9 Case Study 148
    - 5.9.1 Apparent Permeability of Single Tube 149
    - 5.9.2 Sensitivity Analysis of Octane Flow within Single Tube 159
    - 5.9.2 Prediction of Apparent Permeability of Core Sample 169

Chapter 6 Limitations and Future Recommendations 173

- 6.1 Limitations 173
- 6.2 Future Recommendation 174

Chapter 7 Conclusion 176

Reference 179

List of Tables

Table 3.1 The measured data of rock core samples from Marcellus and Wolfcamp shales. 75

Table 3.2 Parameters of the dendroidal pore-network model of the shale core samples from Marcellus and Wolfcamp. 77

Table 4.1 Statistics of pore body and pore throat of the four subsections from the Marcellus shale core sample. 108

Table 5.1 Slip length estimated by non-equilibrium molecular dynamic simulation within octane-graphene system. (Wang et al. 2016a) 152

Table 5.2 Slip length estimated by non-equilibrium molecular dynamic simulation within octane-silica system. (Wang et al. 2016b) 153

Table 5.3 Geometry of the pore-throat cross section of each case. 156

Table 5.4 Flux in rectangular pore-throat calculated by the modified Navier-Stokes equation, where total octane flux is the flux of octane in the whole cross section. 157

Table 5.5 Flux in triangular pore throats calculated by the modified Navier-Stokes equation, where total octane flux is the flux of octane in the whole cross section. 158

List of Figures

Figure 2.1 Schematic of bundle-of-tube model, where the circular tubes represent the void space.. 9

Figure 2.2 Schematic of a two-dimensional regular-square lattice model. Black points represent pore bodies and red lines represent pore throats. The thickness of red lines represents the radius of pore throats. 11

Figure 2.3 Mercury drainage simulation using the lattice model, where black lines represent the pore throats not invaded by mercury, red lines represent pore throats invaded by mercury, and black points represent pore bodies. Wider lines represent pore throats with larger diameter, narrower lines represent pore throats with smaller diameter. 13

Figure 2.4 An example of sphere packing model. (Bryant et al. 1992)............................ 14

Figure 2.5 A 3D view of Delaunay cell. (Mousavi et al. 2010)....................................... 15

Figure 2.6 Mercury injection capillary pressure curve for a shale core sample, where the plateau-like shape does not exist... 17

Figure 2.7 Schematic of a tree-like model, where the black lines represent pore throats. The thickness of lines represents the radius of pore throats. 18

Figure 2.8 (a) Pressure distribution in a tree-like model at the start of the transient pulse decay measurement, where the pore pressure is uniform. (b) Pressure distribution of tree-like model when the core sample begins to be evacuated. ($\boldsymbol{pmax > p1 > p2 > p3 > poutlet}$) Arrows represent the flow direction. (Sakhaee-pour et al. 2012)................... 19

Figure 2.9 (a) and (b) are two types of semi-tree like model for the same mercury drainage experimental data. The thickness of lines represents the characteristic size of pore throats. The black lines represent pore throats without mercury invaded and red lines represent pore throats with mercury. (Sakhaee-pour et al. 2012) 20

Figure 2.10 Thirteen-orientation scanning algorithm of constructing extracted pore-network models. (Zhao et al. 1994) 23

Figure 2.11 An example of burning algorithm, where the medial axis is identified. (a) the number identification incorporating the void structure effects. (b) the number identification without incorporating the void structure effects caused by irregularities of grains. The medial axis is the voxels colored by blue and green, and grain voxels re colored by gray. (Doyen et al. 1988) 25

Figure 2.12 Medial axis determination scenarios. (a) (b) (c) and (d) represent the identification of medial-axis voxel from different burning directions. (Doyen et al. 1988) 26

Figure 2.13 Schematic of the medial axis achieved by the algorithm of Distance Ordered Homotopic Thinning method. (Jiang et al. 2007) 29

Figure 2.14 Skeleton of a two-dimensional object and the corresponding characterized medial axis. (Silin et al. 2006) 30

Figure 2.15 The illustration of the dependence of thinning process on the start pixel. (a) is the complementary of the medial axis of (b). (Silin et al. 2006) 32

Figure 2.16 Schematic of a rectangular pore with different maximal balls, where maximal ball B is the slave of A and the master of C. (Silin et al. 2006)....................................... 34

Figure 2.17 The definition of hierarchy in a maximal-ball algorithm. (Al-Kharusi et al. 2007) 35

Figure 3.1 Injected mercury saturation change with capillary pressure, expressed in terms of relative capillary pressure for the reason of comparison. Plateau-trend shape only exists in the curves for sandstones, while the injected mercury saturation in shales increase continuously with capillary pressure. 39

Figure 3.2 Streamlines and pressure distributions in a three-dimensional reconstruction of shale sample simulated by Lattice Boltzmann methods. (Chen et al. 2015). 39

Figure 3.3 Schematic diagram of dendroidal model, where solid lines represent main flow paths, dashed lines represent branching paths and circles represent pore bodies. The thickness of lines represents the radius of pore throats. 43

Figure 3.4 General procedures of constructing a dendroidal model. 44

Figure 3.5 Schematic of pore throats, pore bodies and the general connections implemented in the dendroidal model. 47

Figure 3.6 Relationship of the shape factor and the corner half-angle for a triangular pore throat. The admissible values for corner half-angle are within the range of the "dome". G= √ 3/36 is the shape factor for a equilateral triangle. 48

Figure 3.7 Feasible range of corner half-angles with respect to different shape factors. . 49

Figure 3.8 Fluid distribution within a pore throat, where the wetting phase fluid is distributed in the central region and the non-wetting phase is trapped in corners. 52

Figure 3.9 Schematic of snap-off in the pore throats with triangular and rectangular cross sections ($\boldsymbol{\theta a < \pi 2 - \beta i}$). 58

Figure 3.10 Schematic of snap-off in the pore throat whose cross section is triangular or rectangular ($\boldsymbol{\theta a > \pi/2 - \beta 1}$) 59

Figure 3.11 Schematic diagram of mercury drainage simulation using the dendroidal model. Lines represent pore throats and circles represent pore bodies. The gray pore throats and pore bodies are empty, while the red ones are invaded by mercury. 63

Figure 3.12 The schematic of mercury retraction process. Lines represent pore throats and circles represent pore bodies. The gray pore throats and pore bodies are empty, while the red ones are invaded by mercury. 65

Figure 3.13 The correlation factor between apparent permeability and intrinsic permeability within a pore throat predicted by (1) Dusty Gas Model, (2) Beskok-Karniadakis correlation, (3) Beskok-Karniadakis-Civan Correlation, and (4) Klinkenberg's slippage correlation. 71

Figure 3.14 Incremental volume of injected mercury with respect to capillary pressure plot from the mercury drainage/imbibition experiments for Marcellus and Wolfcamp shale samples. 74

Figure 3.15 The plot of cumulative injected-mercury volume with respect to capillary pressure from mercury drainage/imbibition experiments for Marcellus and Wolfcamp shale samples. 76

Figure 3.16 Original and corrected curves of mercury-intrusion capillary pressure vs. mercury saturation for Marcellus (top) and Wolfcamp (bottom) shale samples. 78

Figure 3.17 Nitrogen adsorption/desorption isotherm for shale samples from Marcellus and Wolfcamp formations 78

Figure 3.18 Simulated and measured adsorption/desorption isotherm for Marcellus (top) and Wolfcamp shales (bottom). 79

Figure 3.19 Pore-body size distributions of the shale samples from Marcellus and Wolfcamp formations characterized by isothermal adsorption/desorption measurement. 80

Figure 3.20 Measured and simulated mercury drainage and imbibition data for shale samples from (a) Marcellus and (b)Wolfcamp. 81

Figure 3.21 Frequency of the triangular pore-throat shape factor. 82

Figure 3.22 Frequency of the pore-throat lengths. 82

Figure 3.23 Frequency of the rectangular pore throat aspect ratio (a/b). 83

Figure 3.24 Frequency of the coordination number 83

Figure 3.25 Frequency of the imbibition-events occurring during the simulation of mercury imbibition 84

Figure 3.26 Intrinsic permeabilities of the Marcellus shale core sample calculated by the dendroidal model constructed with various spatial distribution of pores. 84

Figure 3.27 Correction factor and apparent permeability for Marcellus sample at various pressures predicted by the dendroidal model. 86

Figure 3.28 Relative permeability curve of the Marcellus shale sample predicted based on the dendroidal model 87

Figure 4.1 Schematic of the MIS seeking procedure which starts from a voxel itself. 93

Figure 4.2 Radius definition of an MIS composed of a single voxel. 93

Figure 4.3 The largest MIS is located and assigned an as an ancestor. (a) Ancestor 1 has overlapping MIS with smaller radius, including the MIS with second-largest radius. (b) Ancestor 1 has an overlapping MIS with the same radius. 96

Figure 4.4 Schematic of locating the second-largest MIS. (a) The second-largest MIS without overlapping any ancestors is assigned as a new ancestor (“Ancestor 23”). (b) the second-largest MIS overlaps an ancestor (“Ancestor 1”), and it is regarded as the first generation of the ancestor. Another second-largest MIS overlapping the first generation is regarded as the second generation. 97

Figure 4.5 Schematic of two series of MIS belonging to two different ancestors, where red and blue balls represent ancestor or generations inheriting two different ancestors. The gray ball represents the common offspring. 97

Figure 4.6 Schematic of two groups of MIS with different ancestor, where black dashed lines of the contour represent the real void space in porous media. The gray circle is the common offspring of the two MIS groups. The red and yellow circles represent the one-MIS-path between the common offspring and each ancestor. The black circles are the overlapping MIS of each group, and they also carry information about morphology of void space. The blue dashed line connecting one-MIS-path represent the true throat length, and Lt represents the Euclidean distant between the two ancestors. 98

Figure 4.7 The schematic of pore body size definition, where the solid line represents the geometry of real void space. The thick-dashed-line circles represent the ancestor MIS, and the narrow-dashed-line circles represent the overlapping MIS containing morphological information about void space. 99

Figure 4.8 A Scanning Electron Microscope image with the resolution of 4 nm. A pore composed by 5 pixels is indicated in the image. 99

Figure 4.9 (a) A pore body represented by 5 voxels in the 3D reconstructed model. (b) The MIS cannot be determined in this manner because the voxels cannot form a full sphere. (c) The pore body can be captured with this new algorithm in this manner. 100

Figure 4.10 Schematic of pore-throat morphology characterization. Trans-section 1 and trans-section 2 are two cross sections of the pore throat, and their directions are indicated by the black arrows. 101

Figure 4.11 Comparison of the possible schemes of pore-throat volume and area estimation with its surrounded matrix voxels. These schemes are described in 2D, since their mechanism is same as 3D. 102

Figure 4.12 Comparison of the possible schemes of pore-body volume and area estimation with its surrounded matrix voxels. These schemes are described in 2D, since their mechanism is same as 3D. 102

Figure 4.13 Schematic of the cross sections across each MIS center within one-MIS-path. The cross sections are used for pore-throat size determination. 105

Figure 4.14 Schematic of two ancestors connected by two common offspring, where the red and yellow circles represent the one-MIS-path and the black circles are the overlapping MIS belongs to these two ancestors. 105

Figure 4.15 Schematic of two ancestors connected by one common offspring, but there are two paths connecting to this offspring from one ancestor. The red and yellow circles represent the one-MIS-path and the black circles are the overlapping MIS. 106

Figure 4.16 Top-surface SEM images of the four subsections of reconstructed pore-scale model....... 107

Figure 4.17 The three-dimensional pore-scale model reconstructed using SEM images with the resolution of 4 nm, where gray part represents organic matter and yellow part represents inorganic matter....... 107

Figure 4.18 The pore-network models extracted by the novel algorithm from the four subsections $(\boldsymbol{900 \times 600 \times 300})$ $(\boldsymbol{nm})$ of the Marcellus shale core sample....... 110

Figure 4.19 The extracted pore-network model of a part of the subsection in an amplified view....... 111

Figure 4.20 Coordination-number distributions of the four subsections of the Marcellus shale core sample....... 112

Figure 4.21 Size distributions of pore bodies and throats for the four subsections of the Marcellus shale core sample....... 113

Figure 4.22 The shape-factor distribution of the pore bodies in the extracted pore-network model of the Marcellus shale core sample....... 114

Figure 4.23 The shape-factor distribution of the pore throats in the extracted pore-network model of the Marcellus shale core sample....... 114

Figure 4.24 Pore-throat length distributions of the extracted pore-network model of the four subsections of the Marcellus shale core sample....... 116

Figure 5.1 The flowchart of the construction of multi-scale liquid flow model and its applications....... 118

Figure 5.2 Schematic of modified Navier-Stokes model of single-phase fluid flow in a circular tube. $\boldsymbol{I}$ represents the central region (bulk fluid) and $\boldsymbol{II}$ represents the liquid film. $\boldsymbol{Ls}$ is the slip length and $\boldsymbol{vs}$ is the slip velocity on wall. The velocity distribution outside the walls are fictious to represent the trend of velocity to $\boldsymbol{vz = 0}$. 121

Figure 5.3 (a) Density distribution and (b) viscosity distribution of liquid computed by non-equilibrium molecular dynamics simulation in a 5.24 nm organic slit channel, where the temperature is 353K and the pressure is 30 MPa. (Wang et al. 2016a) 122

Figure 5.4 The schematic of 1/4 of a pore throat with rectangular cross section. The corresponding boundary condition is shown on each side. Region $\boldsymbol{I}$ is the bulk fluid and region $\boldsymbol{II}$ is the film fluid. The thickness of adsorbed liquid film is represented by $\boldsymbol{\delta}$, in the unit of nm. 127

Figure 5.5 The schematic of the pore throat with triangular cross section. The corresponding equation of each side in the Cartesian coordination system are shown. Region $\boldsymbol{I}$ is the bulk fluid and region $\boldsymbol{II}$ is the film fluid. The thickness of adsorbed liquid film is represented by $\boldsymbol{\delta}$, in the unit of nm. 127

Figure 5.6 Schematic of a pore throat with complicated and irregular shape. Region $\boldsymbol{I}$ and $\boldsymbol{II}$ represent the bulk fluid and film liquid separately. $\boldsymbol{\Omega I}$ and $\boldsymbol{\Omega II}$ are the boundaries of different regions. 130

Figure 5.7 The schematic of two-fluid flow system. Region $\boldsymbol{I}$ and $\boldsymbol{II}$ represent the bulk and film liquid separately. The discontinuity of velocity distribution in different regions is caused by the slippage effect between different types of fluid. $\boldsymbol{LsI}$ and $\boldsymbol{LsII}$ are the slip lengths of two contact surfaces separately. 131

Figure 5.8 Schematic of modified Navier-Stokes equation within a rectangular nanotube. The boundary conditions are shown on each corresponding side. Region $\boldsymbol{I}$ is the bulk fluid and region $\boldsymbol{II}$ is the film fluid. The thickness of the adsorbed liquid film is represented by $\boldsymbol{\delta}$, in the unit of nm. 135

Figure 5.9 The difference of real slip length measured by MD simulation and estimated by hydraulic diameter with respect to difference geometry factor. 151

Figure 5.10 Schematic of the velocity profile in inorganic pore throats with a triangular cross section. x axis and y axis represent the dimensionless length, which are defined as $\boldsymbol{x = l0x}$ and $\boldsymbol{y = l0y}$, where $\boldsymbol{l0}$ is 100 nm. 153

Figure 5.11 Schematic of the velocity profiles in organic pore throats with a rectangular cross-section. x axis and y axis represent dimensionless length, which are defined as $\boldsymbol{x = l0x}$ and $\boldsymbol{y = l0y}$, where $\boldsymbol{l0}$ is 100 nm. 154

Figure 5.12 Schematic of the velocity profile in a inorganic pore throat with rectangular cross section. x axis and y axis represent dimensionless length, which are defined as $\boldsymbol{x = l0x}$ and $\boldsymbol{y = l0y}$, where $\boldsymbol{l0}$ is 100 nm. 155

Figure 5.13 Change of flux of bulk liquid, film liquid and entire liquid with respect to the variation of pressure gradient in both inorganic pores and organic pores. The measurements are under the same operation conditions except for the pressure gradient. (a) Inorganic rectangle pore; (b) Inorganic triangle pore; (c) Organic rectangle pore; (d) Organic triangle pore. 161

Figure 5.14 Change of flux of bulk fluid, film fluid and entire fluid with respect to the variation of the hydraulic radius in both inorganic pores and organic pores. The measurements are under the same operation conditions except for the hydraulic radius. (a) Inorganic rectangle pore; (b) Inorganic triangle pore; (c) Organic rectangle pore; (d) Organic triangle pore. 163

Figure 5.15 Change of flux of bulk liquid, film liquid and entire fluid with respect to the variation of temperature in both inorganic pores and organic pores. The measurements are under the same operation environments except for the temperature. (a) Inorganic rectangle pore; (b) Inorganic triangle pore; (c) Organic rectangle pore; (d) Organic triangle pore. 165

Figure 5.16 In organic pores, the change of enhancement factor with respect to different parameters, including (a) driving force, (b) hydraulic diameter, and (c) temperature.... 167

Figure 5.17 In inorganic tubes, the enhancement factor change with respect to different parameters, including (a) driving force, (b) hydraulic diameter, and (c) temperature.... 169

Figure 5.18 Enhancement factor with respect to different hydraulic diameter in (a) organic pores and (b) inorganic pores.. 170

Abstract

Distinct from conventional reservoirs, shale formations have limited pore connectivity and unique pore spatial-distribution. Consequently, theoretical pore-network models developed for conventional formations are not representative of the porous media in unconventional rocks. This work presents a novel theoretical pore-network model, the dendroidal model, based on the analysis of pore-scale model reconstruction extracted from Scanning Electron Microscope images. The dendroidal model is a “semi-acyclic” model, which characterizes the limited connectivity of void space without sacrificing the interaction among main flow paths. The dendroidal model infers pore-body distribution based on the hysteresis effect of isothermal adsorption/desorption measurements and characterizes pore-throat distribution using mercury drainage capillary pressure experiments. The use of dual-compressibility model in the pore-network model construction eliminates the compressibility effect of void space, including connected pores and dead-end pores, in mercury drainage experiments. The total organic carbon (TOC) content and minerology are measured by experiments to determine the composition of pore bodies and pore throats in the dendroidal model. The difference in mercury intrusion and extraction caused by the trapping hysteresis and contact-angle hysteresis affects the stochastically distributed parameters, including pore-throat length, pore-throat cross-sectional geometry, coordination number and pore-body spatial distribution. I validate the dendroidal model by predicting the absolute permeability of the core samples from Marcellus and Wolfcamp shales. This newly developed pore-network model integrates the

aforementioned seven distinct types of experiments to capture the realistic pore structures of shales.

Extracted pore-network modeling is an efficient and reliable way to provide a platform for mathematical simulation of fluid flow in porous media and for predicting the transport properties. However, the existing algorithms for pore-network extraction have deficiencies in characterizing the porous media of shale core samples in as much as they cannot capture the unique features of unconventional reservoirs. In nano-scale pores, the accurate characterization of the porous geometry is important, since the relative error will be significant without considering trivial information. The newly developed approach, based on the maximal-ball method, proposes a novel and enhanced algorithm for the classification of pore throats and pore bodies. It also has a better performance in characterizing the corresponding properties that include pore-throat length, pore size and geometric factors. The Marcellus shale core samples are scanned using scanning electron microscope imaging with the resolution of 4 nm. The pore-network models based on the tomographic images are constructed, and the aforementioned parameters are compared and analyzed.

The quantification of liquid transport in liquid-rich shales is crucial for an economical exploitation of hydrocarbon. The laboratory measurement of permeability is challenging as it is time-consuming and includes large uncertainties. Direct pore-scale modeling and extracted pore-network modeling are alternatives for the prediction of transport properties. But due to its prohibitively high computational cost, its applications are limited to micro-scale. The emphasis of this work is to understand the mechanisms of

nano-confined liquid transportation (nano-scale) and to quantify the liquid transport capacity in the scales of core samples (centi-scale). A modified Navier-Stokes equation is developed to integrate the variation of fluid properties with respect to the strength of liquid-wall interaction. To predict the apparent permeability in large scale, the dendroidal theoretical pore-network model is constructed by integrating mercury drainage/imbibition and isothermal adsorption/desorption experiments. The dendroidal model also integrates the data of Fourier Transform infra-red spectroscopy experiments to characterize the mineralogy distribution and total organic carbon to distinguish organic pores and inorganic pores. Results from molecular dynamics simulation indicate that the flow capacity of nano-confined liquid can be 1-3 orders different from that calculated by Navier-Stokes equation without considering the boundary-slippage effect. The geometry and composition also have considerable effect on the surface friction factor and viscosity in the near-wall fluid film, which in turn significantly influence the flow capacity in nano-pores. This work investigates the mechanisms of liquid flow in nano-confined pores with various composition and geometries. Accurate characterizations of liquid transport in shales will provide significant advantage in the field development planning of unconventional resources.

Chapter 1 Introduction

1.1 Background

Over the past decade, the combination of hydraulic fracturing and horizontal drilling has provided access to large volumes of fossil fuel resources in shale formations. The pore structure of shale formations and the corresponding physical and chemical processes are not fully understood yet. Many questions concerning hydrocarbon production from these unconventional resources keep shale gas from becoming a bridge to clean energy. For instance, more than 40% of explored oil and gas are trapped in subsurface shale formations. These trapped oil and gas cannot be extracted because of the complex physical and chemical influences of shale rocks. The production rate often drops off quickly after the onset of operation (Ye et al. 2016; Yuan et al. 2017; Zheng et al. 2017). To propose effective solutions for these critical problems, I need to gain deeper understanding of the structures and attributes of shale rocks.

Pore-scale models are convenient representations of porous media to investigate single-phase or multi-phase fluid flow. In pore-scale models, the void space is divided into two parts: pore throat and pore body (Ye et al. 2017). Pore bodies are the relatively larger void space, while pore throats are the narrower void space connecting pore bodies with parameterized geometry. There are three types of pore-scale model: theoretical pore-network model, extracted pore-network model, and direct pore-network model.

Theoretical pore-network model is a simplified pore-scale model possessing the representativeness of the porous structure of formations. The construction of theoretical pore-network models requires experiments to characterize the spatial distribution and connectivity of pores, and it also needs to make enough assumptions about the topological features of porous media. The advantages of theoretical pore-network model are simple and its fast prediction of transport properties, while the deficiency is inaccuracy.

Making reasonable assumptions and capturing the topological features of core samples via some characterizing experiments, theoretical pore-network modeling is an efficient approach to construct a pore-scale model and to predict transport properties. The first pore-network model was proposed by Purcell et al. (1949) named bundle-of-tube model. The later proposed lattice model improves the representativeness of the pore-network model by considering interactions between pores. Bryant et al. (1992) proposed the sphere packing model to characterize unpacked sandstones with good connectivity of pores. To capture the distinct features of shale formations, Sakhaee-pour et al. (2012) proposed cyclic models namely tree-like model and semi tree-like model. Even though the tree-like model can predict transport properties of shale core samples, the model has been simplified too much to represent the porous media correctly and reasonably.

Extracted pore-network modeling is the representative model of porous media extracted from three-dimensional pore-space scanning images. In these pore-network models, researchers use spheres to represent pore bodies and circular tubes to represent pore throats. The simplified topology of pore bodies and pore throats can significantly reduce the computational cost. However, the identification of pore bodies and pore throats from three-dimensional reconstructions of porous media would take considerable time due to the enormous number of pores even in a small rock core sample. The algorithms for constructing extracted pore-network model can be divided into three categories: multi-orientation scanning algorithm, medial-axis algorithm, and maximal-ball algorithm. Since the algorithm of multi-orientation and medial axis have technical problems in accurately identifying pore bodies and pore throats, the maximal-ball method is currently the most widely used one (Dong et al. 2009).

Investigators generally implement the no-slip boundary condition to characterize liquid flow in conventional rock core samples. However, recent investigations indicate that the properties of nanoconfined liquid differs significantly with those of bulk fluid (Heuberger et al. 2001; Scatena et al. 2001). For water/oil flowing through shale porous media, high apparent permeability was observed in the experiments (Werder et al. 2001; Levinger et al. 2002). This discovery implies that liquid slippage occurs in nano-scaled pores. So, understanding the flow of liquid within nano-scale pores is critical in predicting the apparent permeabilities and resolving many challenging problems in science and engineering, such as water purification (Shannon et al. 2008), geophysical process (Warner et al. 2012) and energy storage (Siria et al. 2013).

1.2 Motivations

Accurate and fast prediction of transport properties of rock core samples is important in not only petroleum engineering, but also in environmental engineering and hydrology (Shannon et al. 2008). Laboratory experiments is a reliable method to measure the transport properties of a rock core sample for conventional reservoirs. But for shale formations, since the permeability of core samples could be as small as tens of nanodarcy, experimental methods are extremely time-consuming and also inaccurate due to large relative errors. Measuring the relative permeability with laboratory experiments is more challenging. Conducting two-phase flow in low-permeability core samples takes more time, and the predicted properties can have dramatic relative errors (Blunt et al. 2012). Consequently, simulating fluid flow in pore-scale models becomes an effective method to investigate the flow capacities of shale porous media.

The existing theoretical pore-network models cannot accurately characterize the porous structure of shale formations. The lattice model and sphere packing model were developed for conventional reservoirs with good connectivity of pores, while bundle-of-tube model is too simplified to represent any realistic porous medium. Even though the tree-like model and semi-tree like model developed for shale formations can capture the limited connectivity of porous media and predict the intrinsic permeability of core sample, it has several discrepancies in characterizing pore structures in shales (Zheng et al. 2018a; Zheng et al. 2018b).

Extracted pore-network modeling is an efficient and reliable approach to provide a mathematical simulation platform for fluid flow in porous media and to predict the transport properties. However, the existing pore-network extraction algorithms have deficiencies in characterizing the shale porous media because they cannot capture the unique features of unconventional reservoirs including extremely small pores and limited connectivity. For the extracted pore-network modeling, the multi-orientation algorithm and medial-axis algorithm have been proven to have technical problems in accurately identifying pore bodies and pore throats (Silin et al. 2006; Jiang et al. 2007). The maximal ball-algorithm is the most widely used method recently. However, the existing maximal-ball algorithms were developed for conventional reservoirs, and they cannot capture the extremely small-size pores in shale formations (Silin et al. 2006; Dong et al. 2009; Al-Kharusi et al. 2006; Ye et al. 2018). Moreover, the maximal-ball method cannot characterize the geometry of pores, which has significant effects on fluid flow capacities and trapping behavior. Therefore, a new pore-network model extraction algorithm for shale formations needs to be proposed.

The fluid flow simulation in shale porous media is challenging due to the complex physics and the multi-scale porous structure. The interactions between fluid molecules and matrix become more intense in shale formations than those in conventional formations due to the difference in pore sizes. Experiments show that the liquid flow capacity in nano-scale pores could be orders of magnitude higher than that in larger pores (Barrat et al. 1999; Holt et al. 2006; Majumder et al. 2005). Therefore, the traditional Navier-Stokes equation with no-slip boundary condition cannot be directly implemented to compute the liquid flow capacity in a single pore.

The apparent permeability of liquid flowing through porous media of shale formations has not been well predicted yet, because the nanoconfinement effect and boundary-slippage effect are not correctly coupled in the multi-scale porous media. In shale formations, neglecting interactions between wall and liquid molecules could bring significant discrepancies in permeability prediction. Meanwhile, some factors, including temperature, driving force, the geometry and composition of the pore matrix, can influence the intensity of boundary-slippage effect. These factors need to be accounted for to accurately predict the apparent permeability of a single nanopore. Consequently, accurate prediction of apparent permeability of rock core samples needs to consider the nanoconfinement effect and boundary-slippage effect.

1.3 Organization

Chapter 2 reviews the existing literatures of theoretical pore-network models and extracted pore-network models. The theoretical pore-network models reviewed in this chapter include bundle-of-tube model, lattice model, sphere packing model, semi-tree like model and tree-like model. Extracted pore-network models include multi-orientation scanning algorithm, medial-axis algorithm and maximal-ball algorithm. The advantages and disadvantages of each model have been reviewed with respect to the applications in shales. Thereafter, I discuss the inaccuracy problem of applying existing algorithms in shale formations.

In Chapter 3, I construct a novel theoretical pore-network model, the dendroidal model, based on the analysis of streamlines computed using Lattice Boltzmann Method within the three-dimensional reconstructions of shale core samples. It describes the procedures of constructing a dendroidal model using some characterization experiments. The dendroidal model infers the pore-body size distribution based on the hysteresis effect of isothermal adsorption/desorption measurements and characterizes pore-throat size distribution using mercury drainage experiments. I implement dual-compressibility model to eliminate the compressibility effect of both void space and matrix during the mercury drainage/imbibition experiments. Total organic carbon (TOC) content and minerology determine the composition of pore bodies and pore throats. Afterwards, I predict absolute permeability, apparent permeability and relative permeability based on the dendroidal model. Shale core samples from Marcellus formations and Wolfcamp formations are used in case studies.

In Chapter 4, I develop a new method to extract pore-network models for shale formations. The newly developed approach, based on maximal-ball method, proposes a novel and enhanced algorithm for classification of pore throats and pore bodies. Moreover, the novel algorithm can capture the geometry of pore throats and pore bodies, and it employs an equivalent pore throat to represent the complex connection between two adjacent pore bodies. The new approach can also capture the extremely small pores that cannot be characterized by previous methods. The corresponding case study employs Marcellus shale core samples to perform the pore-network extraction. The core samples are scanned using Scanning Electron Microscope (SEM) with the resolution of 4 nm, and I use the scanning images to build three-dimensional reconstructions. I implement the novel algorithm to extract the pore-network model based on the three-dimensional reconstruction and analyze the statistics. These statistics include parameters from the distributions of pore-throat size, pore-body size, coordination number and pore-throat length.

In Chapter 5, I develop a multi-scale characterization model to predict the apparent permeability of liquid in centimeter core samples. The multi-scale characterization model couples the apparent permeability of each single pore into the dendroidal model of the shale core sample. I use molecular dynamics (MD) simulation to investigate the complex physics happening in nanoconfined fluid flowing through a single pore. Then I derive a modified Navier-Stokes equation coupling the nanoconfinement and boundary-slippage effect in a single pore with various cross-sectional geometries. The new model also considers the extent of boundary-slippage effect caused by various pore compositions. The flow capacities in angular pores considering the boundary-slippage effect and nanoconfinement effect significantly deviate from those characterized by the traditional Navier-Stokes equation. For the case study, I characterize the apparent permeability of octane in both organic pores (graphene) and inorganic pores (silica), and investigate the effects of different parameters (temperature, driving force, and hydraulic diameter) on the apparent permeability. Finally, I implement the dendroidal model to predict the apparent permeability of the shale core sample in centimeter-scale.

Chapter 6 states the limitations of the pore-network modeling methods and the multi-scale characterization approach proposed in this work. Meanwhile, it provides some recommendations for future work, with which the prediction of liquid transport properties in shales can be more accurate.

Chapter 7 concludes this dissertation. It summarizes the advancements and applications of the dendroidal theoretical pore-network model and the new extracted pore-network model. For the multi-scale characterization of liquid transport, this last chapter also concludes the effects of different parameters on the flow capacity of liquid in shale formations.

Chapter 2 Literature Review

2.1 Theoretical Pore-network Models

2.1.1 Bundle-of-Tube Model

Purcell (1949) proposed the first theoretical pore-network model, the bundle-of-tube model, to represent the porous media of sandstone formations. The model is constructed based on mercury drainage experiments, which correlates the porosity of the porous media with mercury injection capillary pressure (MICP) curve.

The bundle-of-tube model is composed of a series of parallel circular tubes with different radii. The length of the tubes is the same as the length of core sample (Figure 2.1). With the MICP curve, the pore-throat radius is evaluated with Young-Laplace equation,

$$R = \frac{2\gamma \cos\theta_r}{p_c} \tag{2.1}$$

where R is the radius of pore throats, γ is the surface tension, θ_r is the receding contact angle and p_c is the capillary pressure.

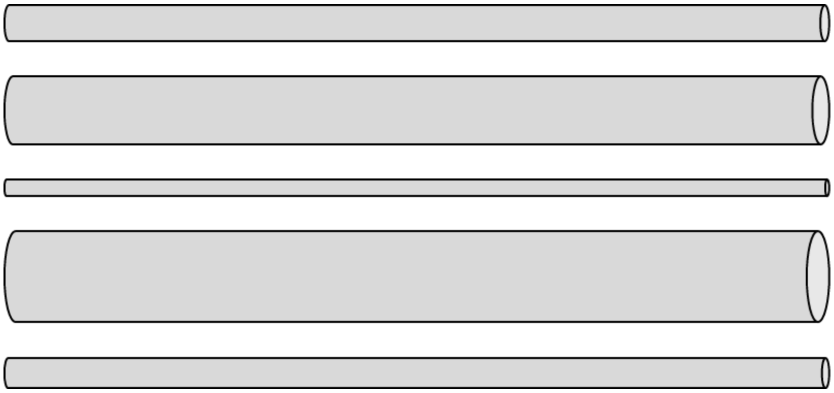

Figure 2.1 Schematic of bundle-of-tube model, where the circular tubes represent the void space.

The permeabilities predicted by the bundle-of-tube model is influenced by the total cross-sectional area of all the tubes. Purcell (1949) predicted the intrinsic permeability using the data of mercury drainage experiments:

$$k = F\frac{\gamma^2}{2}\int_{S=0}^{S=1}\frac{dS}{P_c^2} \tag{2.2}$$

where S is the mercury saturation injected into the porous media, γ is the surface tension, F is the lithology factor and p_c is the capillary pressure. Here, the lithology factor is a fitting parameter estimated by fitting many rock core samples.

The advantage of the bundle-of-tube model is that it is simple to be constructed and it can perform fast prediction of intrinsic permeability, but it does not honor the connectivity of porous media and the real spatial distribution of the pores. Especially for the conventional reservoirs having good connectivity of pores, the bundle-of-tube model fails to provide a realistic representative model of porous media.

2.1.2 Lattice Model

Fatt (1956) proposed another theoretical pore-network model, the lattice model, which honors the good connectivity of porous media. Inspired by the random resistor network, Fatt (1956) assumed that the pore-throat distribution in the lattice model is similar as the lattice pattern and the bonds connecting different sites have various diameters. The schematic of a lattice model is shown in Figure 2.2.

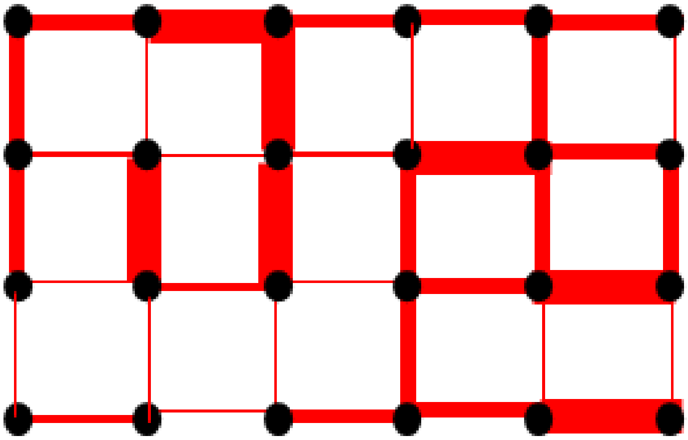

Figure 2.2 Schematic of a two-dimensional regular-square lattice model. Black points represent pore bodies and red lines represent pore throats. The thickness of red lines represents the radius of pore throats.

To characterize the pore-size distribution, the lattice model implements percolation theory, which was developed by Flory (1941) and Stock-Mayer (1943) to describe the process that small branching molecules react and form large macromolecules. Broadbent and Hammersley (1957) first introduced the mathematic application of percolation theory. They originally solved the problem of the spread of fluid particles within a random medium. The terms fluid and medium are general concepts: the fluid can be liquid, electric current, infection, heat flux and others; the media can be porous media, trees and others.

Kirkpatrick et al. (1973) employed the lattice model with percolation theory to describe the mercury injection capillary pressure (MICP) curve, which is the first time that the mercury drainage experiment is simulated by a theoretical pore-network model. In a mercury drainage experiment, investigators raise the capillary pressure gradually and record the corresponding injected non-wetting phase (mercury) saturation (S_{nw}). When the capillary pressure becomes high enough, some of the pore throats have the potential to be invaded by mercury. However, the pore throats could be inaccessible for the mercury because they are connected only by narrower throats from the surfaces of the core sample, which means those narrower pore throats restrict the non-wetting phase from invading into the wider ones.

In Figure 2.3, black points represent pore bodies and black lines represent pore throats. The radii of all the pore throats are stochastically distributed by either normal distribution or Weibull distribution. At the beginning of the mercury drainage experiment, the saturation of mercury (non-wetting phase) increases slowly with capillary pressure increase due to the restriction of the narrower pore throats (Figure 2.3 (a) (b) and (c)). At some specific capillary pressure, the threshold capillary pressure, a self-spanning cluster would form (Figure 2.3 (d)). Approaching the threshold capillary pressure, mercury would invade into a large amount of pore throats with a slightly increase of capillary pressure. This phenomenon results in the plateau-like trend in MICP curves, which can be captured by the theoretical pore-network model with random spatial distribution of pore throats and good connectivity of pore bodies.

Schmidt and McDonald (1979) employed the lattice model to investigate the process of diagenesis, considering chemical effects and geometrical effects. Schmidt and McDonald (1979) characterized the pore-size distribution using the mercury drainage experiment and isothermal adsorption-desorption experiment. Meanwhile, the pore-space topology was also characterized by the isothermal adsorption-desorption experiment. The percolation theory based on the lattice model provides a tool to investigate the displacement process and to characterize the porous media. The previously proposed theoretical pore-network models are not adequate to be implemented to interpret the mercury drainage experiment and nitrogen isothermal adsorption/desorption measurement. Therefore, the lattice model leads the way of constructing representative theoretical pore-network models to characterize the porous media of rock core samples.

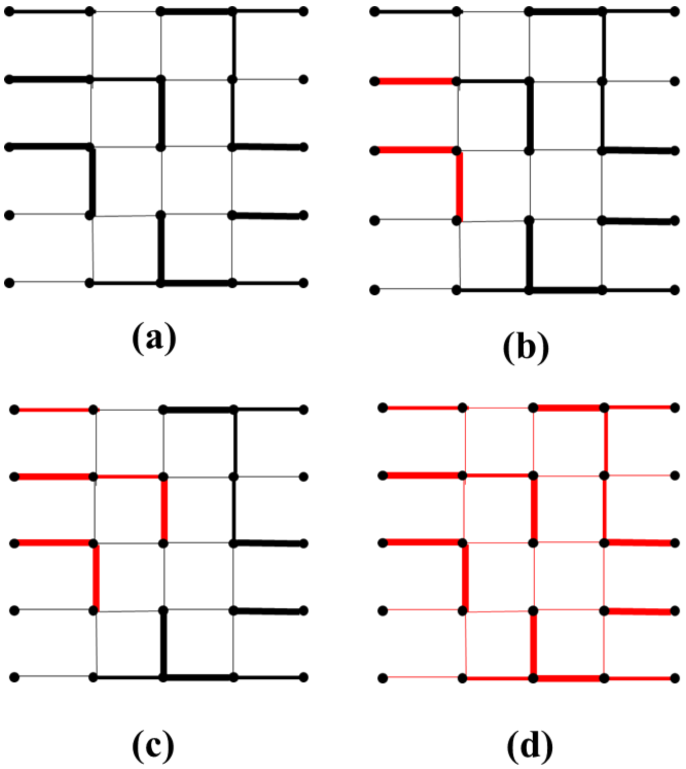

Figure 2.3 Mercury drainage simulation using the lattice model, where black lines represent the pore throats not invaded by mercury, red lines represent pore throats invaded by mercury, and black points represent pore bodies. Wider lines represent pore throats with larger diameter, narrower lines represent pore throats with smaller diameter.

2.1.3 Sphere Packing Model

Sphere packing model is another widely-used theoretical pore-network model, which uses spheres to represent the matrix and the void among spheres to represent the pore space. Finney (1970) used the measured spatial coordination of 8000 bearing balls to evaluate the void spatial coordination. Bryant et al. (1993) constructed a physical model to characterize the pore-size distribution and permeabilities based on the void spatial coordination. Bryant et al. (1993) used the sphere packing model to study the effects of grain sedimentation and diagenesis. Thane et al. (2006) used the cooperative rearrangement algorithm (Cargill, 1984) to construct a sphere packing model with a random distribution of spheres, and they used Delaunay triangulation technique to evaluate the flow capacities of the pore space extracted from the sphere packing model. Figure 2.4 shows an example of the random sphere packing model. The sphere packing method has also been used to evaluate the transport properties of unconsolidated sandstones with good connectivity (Oren et al., 1998). However, the sphere packing model cannot be used to represent the porous media of shale formations due to its good pore connectivity.

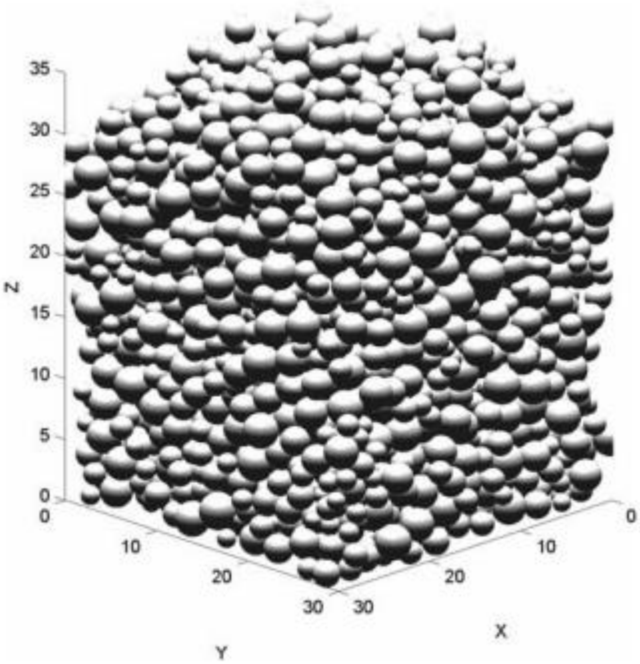

Figure 2.4 An example of sphere packing model. (Bryant et al. 1992)

Thane et al. (2006) used computer programs to construct a sphere packing model, where the exact positions of the spheres are known, and then extracted the void-space geometry of the porous media. Thane predict the flow resistance of core samples based on this theoretical pore-network model. Gladkikh and Bryant (2006) introduced an algorithm to calculate the flow resistance of the porous media extracted from sphere packing models. The tessellation is a computational geometric structure splitting the void space into polygonal regions. The slitting process is performed by grouping every four adjacent spheres. An example of a group of four adjacent spheres is shown in Figure 2.5. The pore throat in this figure is at the surface of a tetrahedron, and the flow resistance the pore throat can be calculated based on the opening area available at surface.

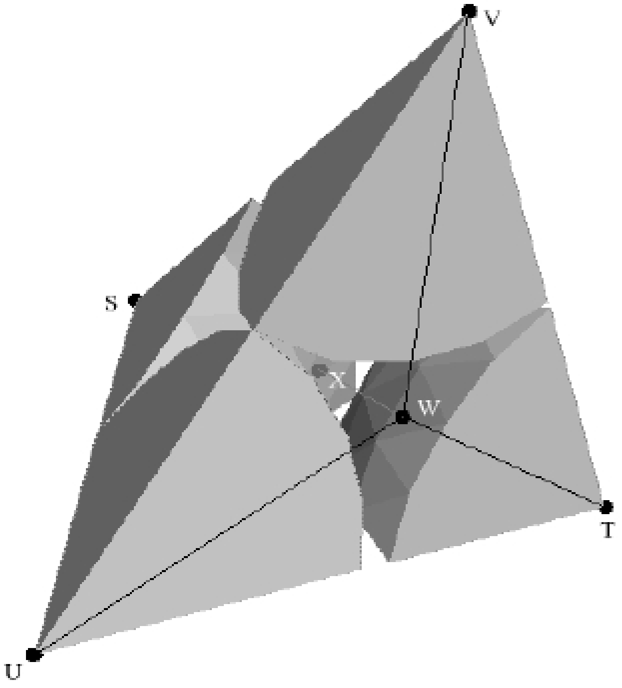

Figure 2.5 A 3D view of Delaunay cell. (Mousavi et al. 2010)

The sphere packing model (Oren et al. 1998; Bryant et al. 1993) can be implemented to predict the permeabilities of unconsolidated sandstones, because it has good representativeness of the intergranular pores constructing the void space of unconsolidated sandstones. Mousavi et al. (2007) implemented the sphere packing model to investigate the process of cementation and compaction of the intergranular pores in unconsolidated sandstones. Mousavi et al. (2007) studied the compaction by considering the hard and soft grains penetrating each other, and they studied the process of cementation by increasing the grain size.

The sphere packing model is appropriate to represent the porous media of unconsolidated sandstones. But, the sphere packing model is not applicable for tight gas sandstones and shales since a significant fraction of the pores are intragranular. Mousavi (2007) investigated the applicability of implementing the sphere packing model to simulate the mercury drainage experiments, and it has been proved that the intergranular model alone is not applicable to analyze two-phase displacements.

2.1.4 Tree-like Model

Sakhaee-Pour et al. (2015) developed tree-like model and semi-tree like model. The tree-like model uses straight tubes to represent pore throats. The cross-sectional geometries of the pore throats are circle or slit. Sakhaee-Pour et al. (2015) first-time introduced the definition of "acyclic" model to characterize the limited connectivity of porous media in shales and tight gas sandstones. In the acyclic pore-network model, there is only one flow path between every two pore bodies. While, there are more than one flow path between every two pore bodies in cyclic model, like the lattice model.

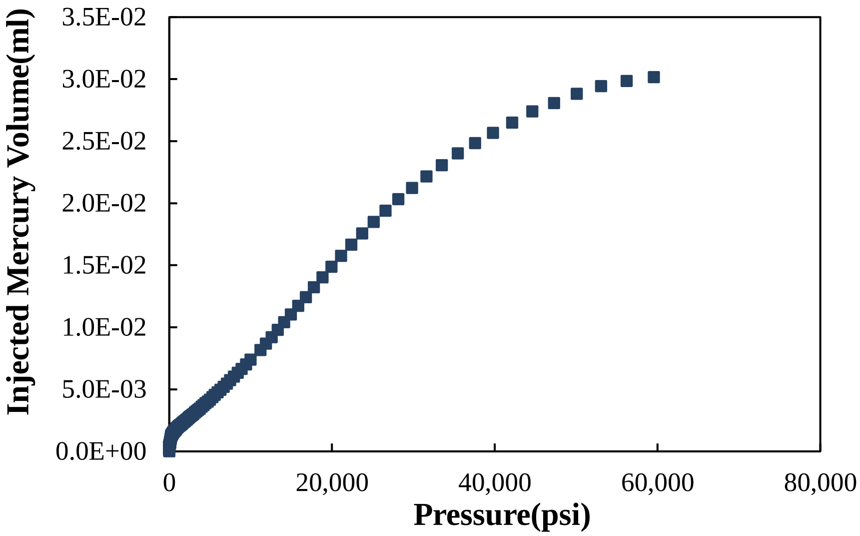

Figure 2.6 Mercury injection capillary pressure curve for a shale core sample, where the plateau-like shape does not exist.

The scanning electron microscope (SEM) is an imaging technique to produce high-resolution images of a rock core sample. SEM scans the surface of rock core samples with focused ion beams (FIB). The rock core samples scanned by the FIB-SEM are limited in micrometer scale. Therefore, the pore connectivity of a general shale core sample (centimeter scale) cannot be directly characterized by FIB-SEM images. Experiment measurements, like isothermal adsorption/desorption experiment (Adesida et al. 2011) and mercury drainage/imbibition experiment (Heath et al. 2011), could be implemented to characterize the structure of porous media in centimeter-scale. The tree-like model and the semi tree-like model are constructed by implementing the results of mercury drainage experiment.

Sakhaee-pour (2012) implemented the “acyclic” model to capture the unique characteristic of the porous media of shale formations, where no wider pore throats are accessible from the rock surface by narrower pore throats. There is only one flow path connecting every two pore bodies, unlike the traditional lattice model and sphere packing model. Even though the bundle-of-tube model do not have good connectivity among pores, its pores, which do not have any connections, cannot represent the real porous media. The tree-like model, shown in Figure 2.7, arranges the pore throats with the diameters from large to small.

The tree-like model cannot be used to simulate steady-state flow due to its dead-end pore throats. However, it can be used to simulate the transient pulse decay method. To predict the permeability, the pressure distribution needs to be calculated first (Figure 2.8).

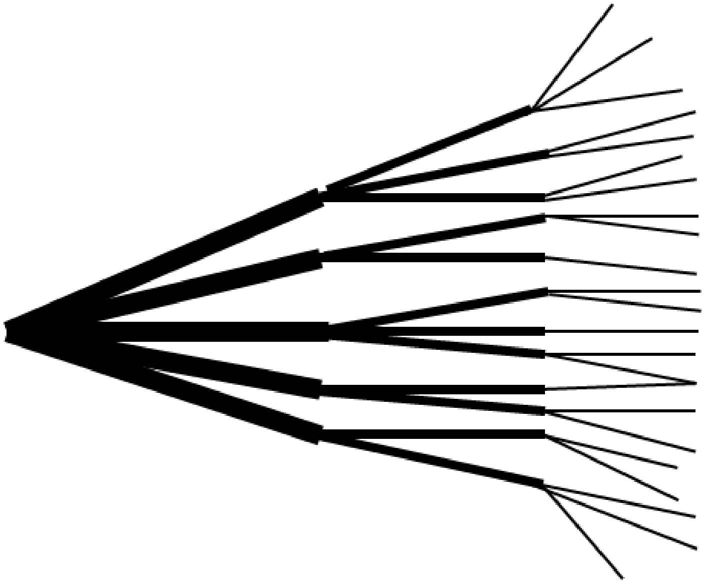

Figure 2.7 Schematic of a tree-like model, where the black lines represent pore throats. The thickness of lines represents the radius of pore throats.

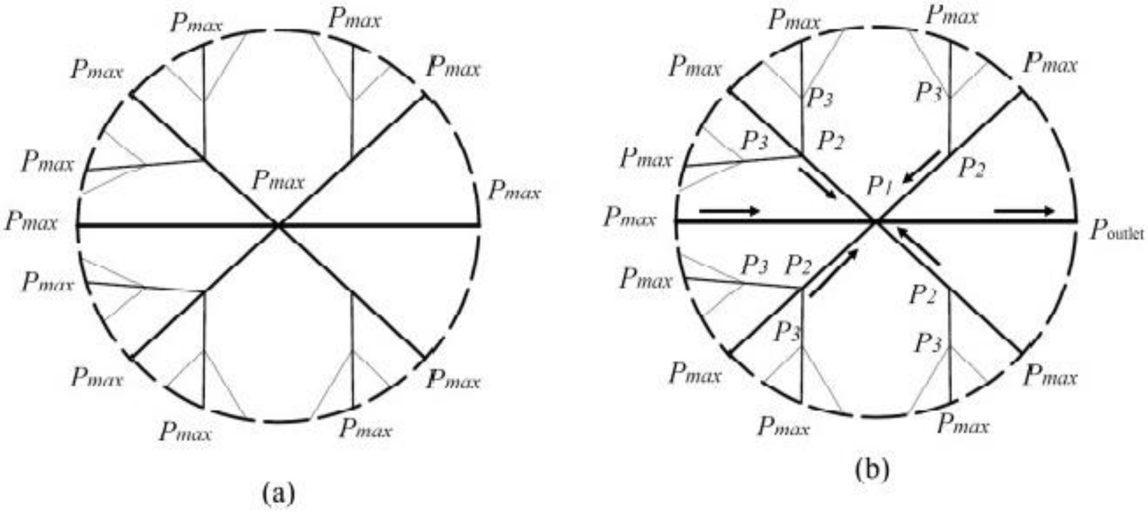

Figure 2.8 (a) Pressure distribution in a tree-like model at the start of the transient pulse decay measurement, where the pore pressure is uniform. (b) Pressure distribution of tree-like model when the core sample begins to be evacuated. $(\boldsymbol{p_{max}} > \boldsymbol{p_1} > \boldsymbol{p_2} > \boldsymbol{p_3} > \boldsymbol{p_{outlet}})$ **Arrows represent the flow direction. (Sakhaee-pour et al. 2012)**

The length of the tree-like model is same as that of the core sample, and it also equals to the length of the pore throat with the largest diameter. The threshold capillary pressure of the tree-like model is the pressure at which mercury start to invade into the rock core sample. A fitting parameter, branching ratio, is introduced to describe the length ratio of the pore throats with different diameters. Sakhaee-Pour et al. (2012) calculated the total cross-sectional area of the pore throats with a specific diameter using the length of the pore throats and the volume of mercury injected at the specific capillary pressure:

$$A_{throat}L_{throat} = V_p\Delta S_w \qquad (2.3)$$

where A_{throat} is the pore-throat area and L_{throat} is the pore-throat. V_p is the total pore volume of the core sample, and ΔS_w is the increased mercury saturation at an incremental capillary-pressure step.

The other acyclic model proposed by Sakhaee-Pour (2012) is the semi-tree like model, which does not have a unique representation for a given mercury drainage experimental data. Figure 2.9 shows two cases of semi-tree like model for the same mercury drainage experimental data. Figure 2.9(a) indicates one type of the semi-tree like model, whose narrow pore throats are connected to the wider pore throats; while Figure 2.9(b) indicates another type of model, which have some narrow pore throats directly connected to the widest pore throats. Figure 2.9 also show the process of mercury invasion in the porous media.

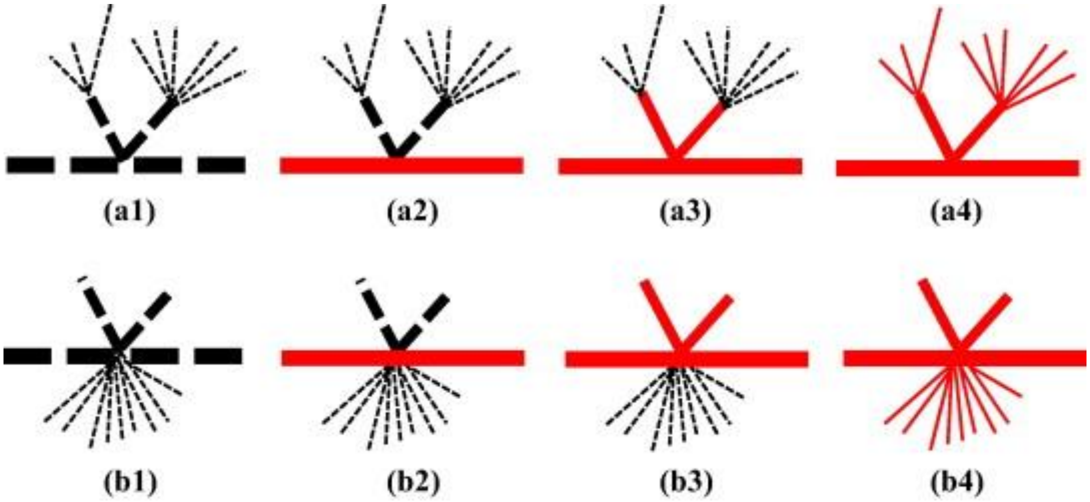

Figure 2.9 (a) and (b) are two types of semi-tree like model for the same mercury drainage experimental data. The thickness of lines represents the characteristic size of pore throats. The black lines represent pore throats without mercury invaded and red lines represent pore throats with mercury. (Sakhaee-pour et al. 2012)

Nevertheless, the tree-like model has its deficiencies in characterizing the unconventional reservoirs, which include: (1) it only has one flow path connecting from the upstream to the downstream of the core sample, where other paths are branches connecting to this main flow path; (2) the cross-sectional area of the only flow conduit across the entire pore-network is constant; moreover, the size of pores in the pore-network model are much larger than the real pore size; (3) all the flow paths of the tree-like model are straight, namely, it does not consider the tortuosity of the porous media. Even though the tree-like model can predict the intrinsic permeability of the core sample, these discrepancies make the tree-like model proposed by Sakhaee-pour (2015) inadequate to capture the realistic shale porous media.

2.2 Extracted Pore-network Modeling

The pore-structure characterization in petroleum formations in terms of topological and geological properties is important, by which the flow regimes can be determined. It is not practical to simulate fluid flow directly on the voxels of the scanning images of rock core samples due to its large computational cost. Extracted pore-network modeling provides an efficient way to investigate the displacement process and to predict the transport properties.

Attempts to extract reasonable pore networks from generic and arbitrary 3D images have been tried for decades. The algorithms can be categorized into groups, which are multi-orientation scanning algorithm, medial-axis based algorithm, and maximal-ball algorithm.

2.2.1 Multi-orientation Scanning Algorithm

The multi-orientation algorithm proposed by Zhao (1994) was first-time used to identify the pore-size distribution based on 3D reconstructions. The definition of pore throat is the void space with relatively small characterized size separating the pore bodies with relatively large volume of void space. Therefore, reasonable identification of pore throats is the criterion to determine the pore-body distributions and coordination numbers. Meanwhile, pore throats need to be identified from the normal direction of the cross-sections of a pathway. Consequently, Zhao (1994) argued that a sequence of normal scanning of the core sample is essential to locate the pore throats, instead of scanning from only one direction. Zhao (1994) proposed the algorithm of measuring two-dimensional features from a sequence of sections identified from the same pathway. Since a sequence of scanning sections can be normal to a portion of the pathways, several sequences of scanning section from multi-orientation can identify all the pathways.

The multi-orientation scanning algorithm does not require physically scan for several times from different orientations; instead, it physically scans the sample from only one orientation, and the other orientational scanning is performed on the digital three-dimensional array stored in the computer memory. Once the core sample is scanned, the scan from other directions can be performed automatically by the algorithm.

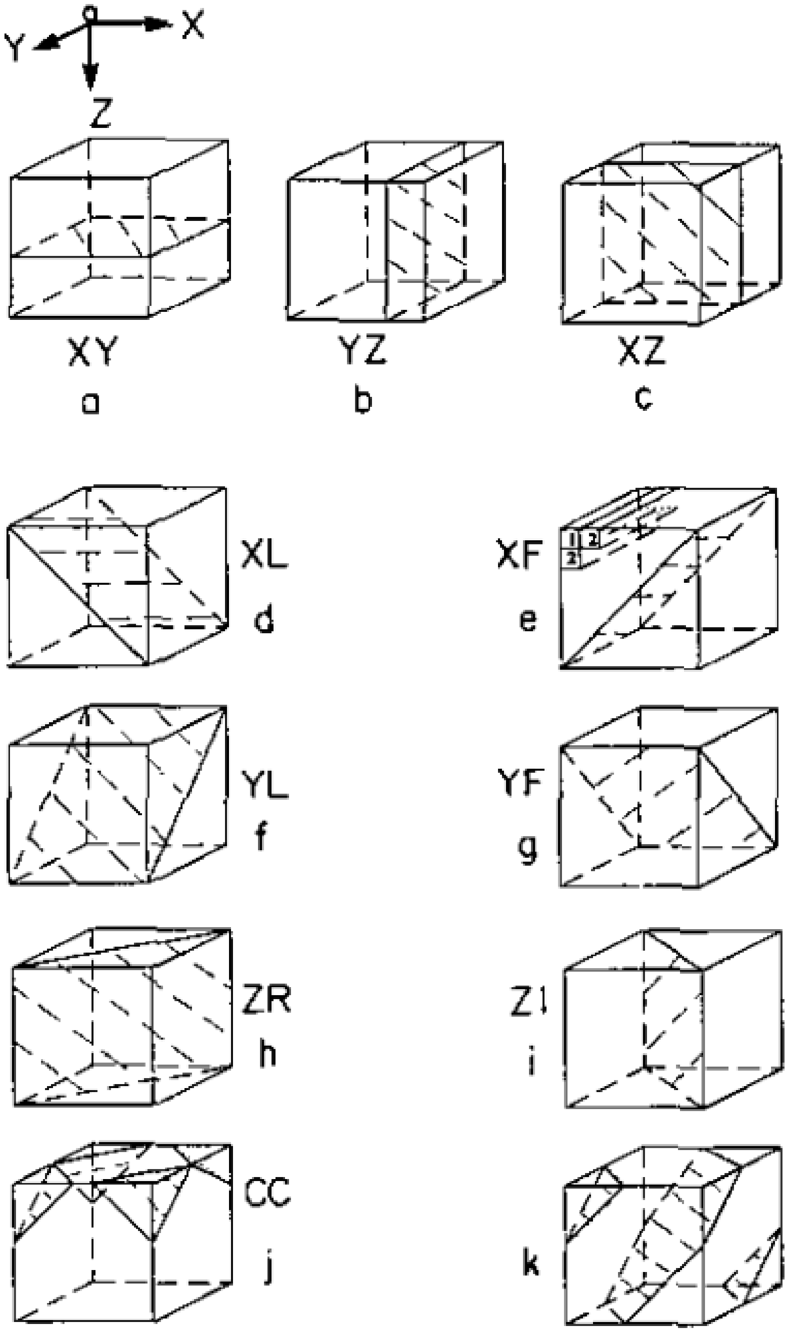

Figure 2.10 Thirteen-orientation scanning algorithm of constructing extracted pore-network models. (Zhao et al. 1994)

Kwiecien et. al (1990) developed an algorithm to scan samples from seven orientations, but they did not provide adequate reasons of choosing seven orientation. Zhao

(1994) indicated 13-orientation scanning would provide a more accurate pore-network model (Figure 2.10). Meanwhile, Silin et al. (2003) indicated that the resolution of the two-dimensional serial scanning sections has effects on the extracted pore network model. High-resolution digital data is required to ensure an accurate pore-network model extracted by the multi-orientation scanning algorithm. The critical departure angle of the scanning algorithm with different orientations (7, 9 or 13) can be calculated using the Euclidean geometry. But it has been proved that the thirteen-orientation scanning method can provide a more accurate pore-network model (Kwiecien et al. 1990). The main problem of the multi-orientation scanning algorithm is time-consuming.

2.2.2 Medial axis-based algorithms

Since Calabi and Harnett (1968) propose the concept of grassfire, many different pore-network extraction algorithms were developed based on the medial axis algorithm (Malandain et al. 1998; Doyen et al. 1988). The existing pore-network extraction algorithms based on medial axis theory can be classified into three categories (Jiang et al. 2007): medial axis transformation, thinning methods and hybrid methods.

2.2.2.1 Burning Algorithm

The medial axis transformations use the distance map algorithm (Malandain and Fernandez, 1998; Calabi and Harnett, 1968). The main idea of this algorithm is to calculate the distance map of the porous media at first and then to connect the maxima. Based on the medial axis theory, Lindquist et al. (1996) developed burning algorithm to define the pore bodies and pore throats. Delerue et al. (1999) introduced the ball-growing algorithm to extract the pore-network model.

The first step of burning algorithm is to construct a discrete medial axis. The three-dimensional tomographic image is composed of discrete voxels, where each of the voxels is defined as matrix or void space using number 1 or 0. It isolates a sub-region (u) of the void space and then performs "burn" algorithm. It labels all the voxels in the exterior region with integer -1, and all the grain voxels in u with integer 0. Define all the unlabeled voxels adjacent to the labeled voxels (k) as $k-1$. This iterative procedure "burns" all the voxels in the void space. The burning rate from burned layer to unburned layer is one layer per iteration. A simple illustration is shown in Figure 2.11.

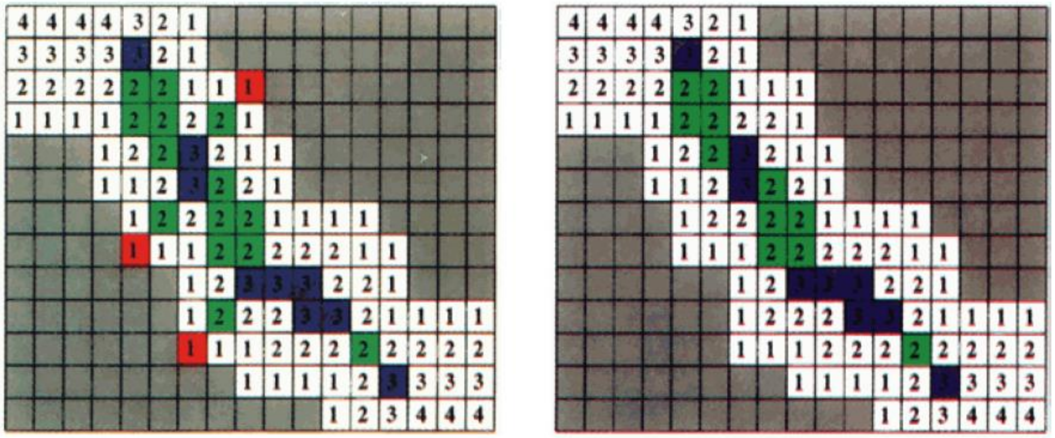

4	4	4	4	3	2	1										
3	3	3	3	3	2	1										
2	2	2	2	2	2	1	1	1								
1	1	1	1	2	2	2	2	1								
			1	2	2	3	2	1	1							
			1	1	2	3	2	2	1							
				1	2	2	2	2	1	1	1	1				
				1	1	1	2	2	2	2	2	1	1			
						1	2	3	3	3	2	2	1			
						1	2	2	2	3	3	2	1	1	1	1
						1	1	1	2	2	2	2	2	2	2	2
								1	1	1	1	2	3	3	3	3
											1	2	3	4	4	4

(a)

4	4	4	4	3	2	1										
3	3	3	3	3	2	1										
2	2	2	2	2	2	1	1	1								
1	1	1	1	2	2	2	2	1								
			1	2	2	3	2	1	1							
			1	1	2	3	2	2	1							
				1	2	2	2	2	1	1	1	1				
				1	1	1	2	2	2	2	2	1	1			
						1	2	3	3	3	2	2	1			
						1	2	2	2	3	3	2	1	1	1	1
						1	1	1	2	2	2	2	2	2	2	2
								1	1	1	1	2	3	3	3	3
											1	2	3	4	4	4

(b)

Figure 2.11 An example of burning algorithm, where the medial axis is identified. (a) the number identification incorporating the void structure effects. (b) the number identification without incorporating the void structure effects caused by irregularities of grains. The medial axis is the voxels colored by blue and green, and grain voxels re colored by gray. (Doyen et al. 1988)

If the burning process achieves a voxel from more than one direction simultaneously, the voxel is defined as a medial axis voxel. The discrete medial-axis voxels will be used to define the continuum medial axis afterwards. The burning process can enter the voxel from different directions, which is shown in Figure 2.12, and the medial axis will be defined correspondingly. Doyen et al. (1988) proposed an iterative three-dimensional erosion algorithm based on the burning algorithm.

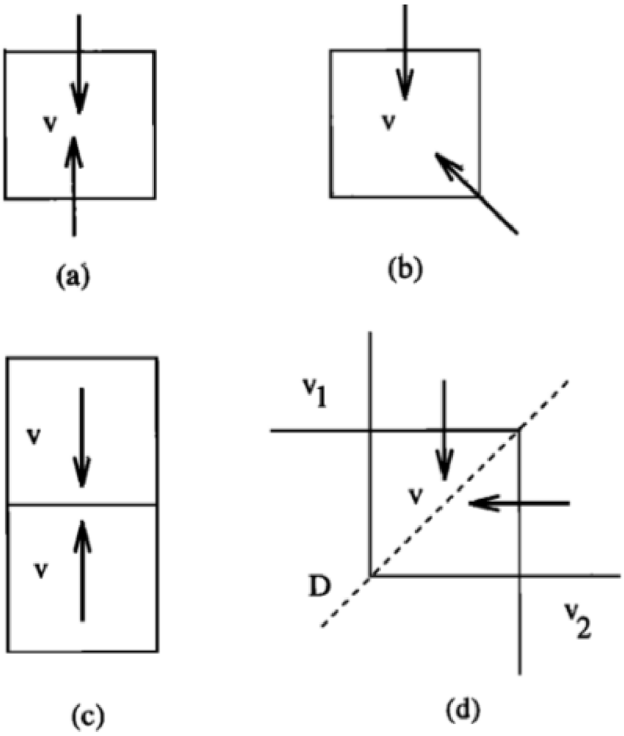

Figure 2.12 Medial axis determination scenarios. (a) (b) (c) and (d) represent the identification of medial-axis voxel from different burning directions. (Doyen et al. 1988)

The burn numbers can be categorized into different one-parameter families, and then these one-parameter families can be used to characterize the void structure of core samples. The pore connectivity in a rock core sample characterized by the burning algorithm indicates that the distribution of medial axis volume satisfies the power-law distribution for the formations of sandstone, chalk and carbonate.

2.2.2.2 Thinning Algorithm

Thinning algorithm is defined as the process of deleting voxels from a three-dimensional reconstruction iteratively until all the redundant voxels are deleted (Kong et al. 1989). This algorithm can be described as peeling off the boundary voxels of the void space in a layer-by-layer manner. The purpose of this approach is to remove the redundant voxels in an efficient way without influencing the geometry of pore space. Morgenthaler (1981) improved the thinning algorithm by introducing the notion of “simple point”. Simple points represent the redundant voxels that can be deleted from the void space efficiently. Afterwards, various methods were proposed to characterize the simple point (Bertrand et al. 1994; Bertrand et al. 1996; Lohou et al. 2005). There are three ways to perform the simple-point algorithm: sequential detection, parallel detection and morphological operation. The advantage of the thinning algorithm is that the porous-media topology can be preserved.

Jiang et al. (2007) proposed another medial-axis method combining an efficient thinning algorithm with the Euclidean distance transformation to get the medial axis from the void space of three-dimensional reconstructions. This algorithm detects and delete the redundant voxels based on medial axis, instead of the simple point. Meanwhile, this thinning algorithm uses distance transformation method to convert a digital binary image into a gray scale image. The isolated pore bodies and pore throats, which have no contributions in transporting fluid, are removed during the construction of pore-network model. Only the topological information of the void space is preserved. The medial axis is generated based on the topological information. Consequently, it would lose much geometry information, such as dead-end pores and boundary voxels. For the investigation of fluid flow in porous media, it is important to identify the inlet and outlet of the pore-network model. However, the thinning algorithm tends to remove most of the voxels of boundary.

2.2.2.3 Hybrid Algorithm

The hybrid method combines the thinning algorithm with the burning algorithm to characterize the media axis and then extract the pore-network model (Pudney et al. 1996; Saito et al. 1995; Pudney et al. 1998). Morgenthaler et al. (1981) proposed a new method, the Distance Ordered Homotopic Thinning method, which delete the simple points iteratively with the burning method and thinning method in an increasing distance map order. This method could cause the problems that the medial axis is not defined in the center of the void space, which is shown in Figure 2.13.

To get rid of the effects of spurious throats in the thinning process, Sheppard et al. (2005) proposed a method to merge the pores based on the quality of the potential pore throats to be deleted. Sheppard et al. (2005) introduced a non-linear function of length-width ratio and constriction ratio to evaluate the quality of each pore throat. Constriction ratio is defined as the smaller aspect ratio of a pore throat, which is the ratio of the smaller inscribed radius of the two adjacent pore bodies connecting this pore throat. The definition of length-width ratio is the ratio between the distance of the two adjacent pore centers and the width of the pore throat linking these two pores. Sheppard et al. (2005) defined that the short pore throats are of inferior quality, while the constrictive pore throats are of decent quality. The low-quality pore throats would be deleted based on the threshold value proposed by Sheppard et al. (2005). Because the high noise level of digital images can cause many spurious branches, Sheppard et al. (2005) used the Gaussian smoothing kernel to get rid of the noise before the pore skeleton extraction. Since the complexity of the clean-up procedures is reduced, the characterized medial axis would contain less furious branches.

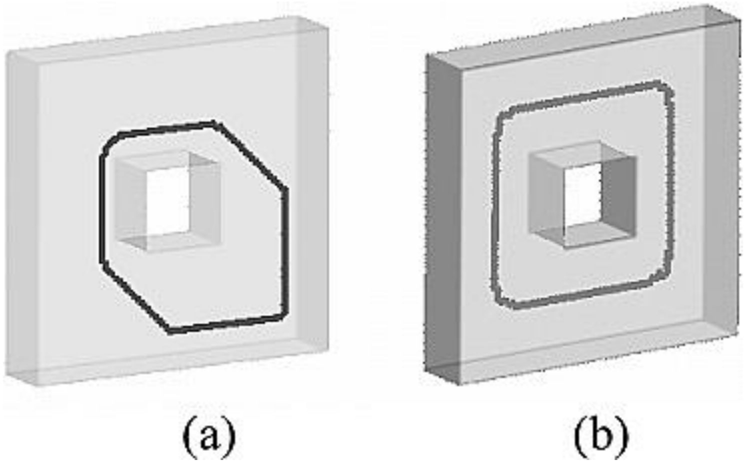

Figure 2.13 Schematic of the medial axis achieved by the algorithm of Distance Ordered Homotopic Thinning method. (Jiang et al. 2007)

2.2.2.4 Discussions

The medial axis algorithm mathematically preserves the topology and geometry of void space, but the pore-throat identifications could be ambiguous for some conditions. It is essential to implement the clean-up procedure to remove the trifling details of rock matrix, which is caused by the high sensitivity of the thinning algorithm to the noises occurring in three-dimensional reconstructions (Venkatarangan et al. 2000). This method always has more than one junction of the medial axis, so an efficient merging algorithm needs to be developed to trim the extracted skeleton reasonably. The junctions are required to be fused together to avoid unrealistic high coordination numbers (Shin et al. 2005; Sheppard et al. 2005).

The effects of the clean-up process indicate that the medial-axis algorithm is highly sensitive to the connection between void-matrix surface and the disconnected clusters caused by the inappropriate segmentations. It also has trimming effect, where all the dead-end pores without fluid will be trimmed.

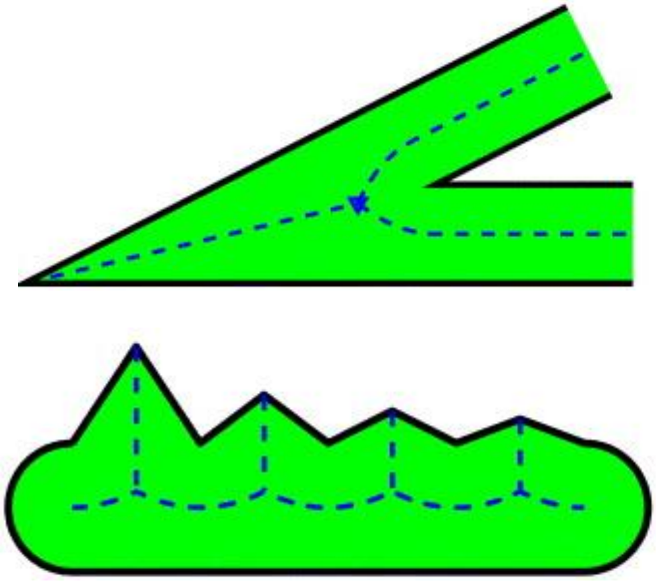

Figure 2.14 Skeleton of a two-dimensional object and the corresponding characterized medial axis. (Silin et al. 2006)

It has been proved that the medial-axis method could have some problems in identification of pore throats and pore bodies (Silin et al. 2006). Since the thinning algorithm cannot eliminate the side-effects of skeleton extraction, it could lead to some unexpected medial axis in angular pores (Figure 2.14). The skeleton of void space is dimension-independent, so it will be straightforward to express the mechanisms in a two-dimensional space. The extracted porous skeleton could be bizarre for the pores having complex shapes. For a three-dimensional object, even a pore space with simple geometry can have complex skeletons extracted by this method.

The reproducibility of the pore-network model extracted by thinning algorithm is another problem. There are two factors influencing the pore-network extraction significantly: the orientation of the images, and the order the voxels to be eliminated. Figure 2.15 is an illustrative example, which is a two-dimensional set of voxels. It assumes that every two pixels are regarded as connected if they have a common vertex and the connectivity need to be preserved during the thinning process. The inlet and outlet of the core sample need to be connected during the process of pixel-removal, where the inlet and outlet are the pixels with number 1 and 5 in Figure 2.15. Supposing I start with deleting the pixel labeled as number 3, the pixels labeled as number 2 and 4 cannot be deleted without breaking the connectivity of the remaining set. Alternatively, it will cause the set of pixels forming the chain 1-3-5 if I sequentially remove pixels labeled as number 2 and 4. Therefore, it can extract two mutually exclusive porous skeletons following the same procedures and assumptions. It indicates that different selection of the starting pixel will cause different results.

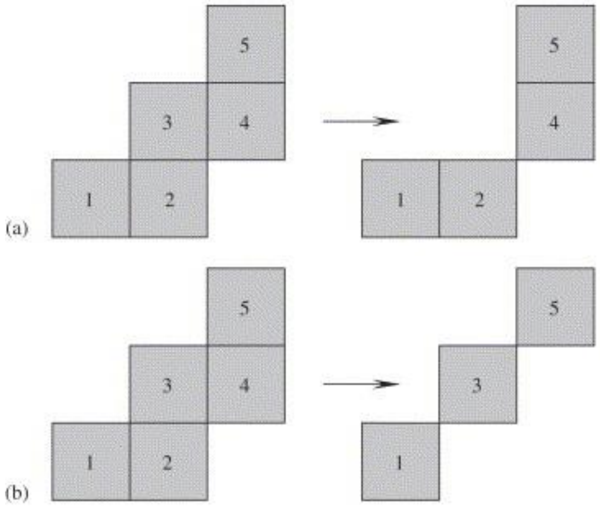

Figure 2.15 The illustration of the dependence of thinning process on the start pixel. (a) is the complementary of the medial axis of (b). (Silin et al. 2006)

2.2.3 Maximal-Ball Algorithm

Silin et al. (2003) proposed maximal-ball method to perform the pore-network extraction. Dong et al. (2009) improved the maximal-ball method by enhancing the algorithm of identification of pore bodies and pore throats; meanwhile, he use the extracted pore-network model to predict the intrinsic permeability and apparent permeability.

In Dong's method (2009), the first step of the maximal-ball algorithm is to define the maximum inscribed balls associating with each void space voxel. The searching process starts from the voxel itself, where the radius is recorded as zero, and it increases the radius of the maximal ball by one-unit-voxel layer for each step until it reaches the matrix voxels. It can be roughly estimated that the computation times should be the total number of the one-unit-voxel layers of every ball. Therefore, the computational burden will be intense if the image is large and the porous media have high porosity. If the image resolution increases, the computational burden will be more intensive. The second step is to remove the redundant maximal balls whose voxels are repetitive. After defining all the inscribed balls associated to each voxel, it can be identified that some of the maximal balls are the subset of others. Consequently, a removing process is required to delete all the redundant maximal balls.

Next step is to distinguish the masters and slaves among all the maximal balls. To characterize the configuration, the hierarchy of the all the maximal balls need to be defined. If are two maximal balls overlap each other, the larger one is announced as master and the smaller one is labeled as the slave. But many voxels are defined as both masters and slaves at the same time. Figure 2.16 shows an example of the maximal ball classification in a rectangular pore space. In Figure 2.16, Voxel A, B and C are the center voxels of the maximal balls. The maximal ball B is the slave of A and the master of C at the same time. Here, the maximal ball B characterizes the topology of corner and the maximal ball A characterizes the opening. An improved algorithm is introduced to define the hierarchy of all the maximal balls. At first, the master maximal ball, which is not a slave of any other balls, is selected and defined as super-master. The super-master can represent the local maxima of the maximal balls. The super-master is Figure 2.16 is the maximal ball A. Then, all the slaves associated with this super-master need to be rearranged using the depth-first type searching algorithm. In Figure 2.16, the master A finds its intermediate slave B and the corresponding slaves C. Consequently, both B and C are the slaves belongs to A.

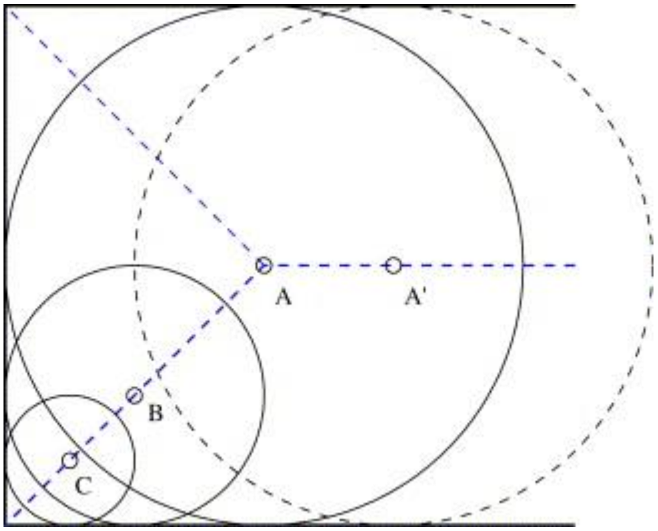

Figure 2.16 Schematic of a rectangular pore with different maximal balls, where maximal ball B is the slave of A and the master of C. (Silin et al. 2006)

Al-Kharusi et al. (2007) improved this method by introducing a new algorithm to determine the maximal ball hierarchy. Al-Kharusi et al. (2007) also extended the new algorithm to study the porous media of carbonates and sandstones. Instead of just defining two types of relationship, the master and slave, Al-kharusi et al. (2007) introduced a new relationship, the cluster, to better describe the porous skeleton. The cluster was used to describe the maximal balls adjacent to each other (Figure 2.17). The new hierarchy-definition resolves the problem of ambiguity, where some master maximal balls have the same size with the adjacent slave balls. They used the pore-network model extracted from two-dimensional images to characterize the one-phase and multi-phase fluid flow. The absolute permeability and relative permeability are successfully predicted. But, the computational cost of this algorithm limits the size the rock core sample can be characterize in micrometer-scale. Since the new algorithm requires tremendous memory of computer, only the porous media with thousands of pores can be skeletonized (Ye et al. 2018a).

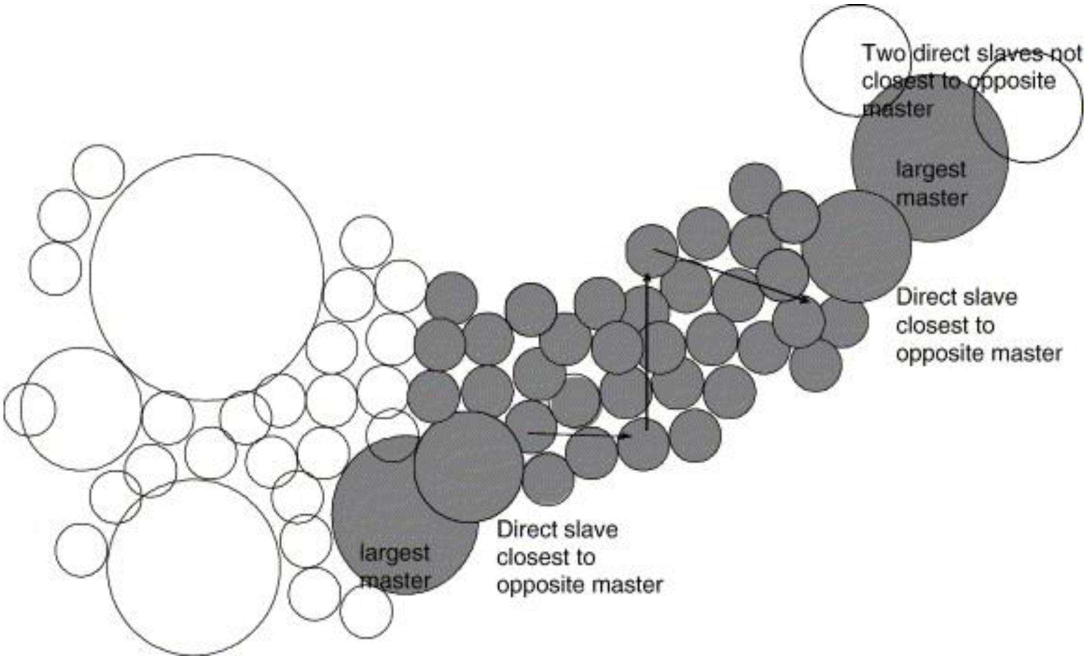

Figure 2.17 The definition of hierarchy in a maximal-ball algorithm. (Al-Kharusi et al. 2007)

Based on Al-Kharusi's method, Dong et al. (2009) developed a new algorithm, which is more efficient to extract pore network models from sandstones and carbonates. The major novelty of the method is the algorithm of maximal-ball searching and hierarchy definition. Instead to inflating the inscribed ball by a one-unit-voxel layer for each step, he introduced a new two-step algorithm. Dong et al. (2009) used an inflating algorithm to identify the potential searching range of the maximal balls and used a deflating algorithm to locate the genuine nearest solid voxels to identify the maximal-ball radius. 26 directions have been searched in the inflating process (6 lateral, 8 diametrical and 12 diagonal). The "stop point" defines the range of deflating algorithm, where all the voxels included in the range are analyzed to define the genuine nearest matrix voxel.

The other improvement of Dong's method is the hierarchical arrangement of the maximal balls. The new algorithm did not define the master, cluster and slave as precious methods, and it introduced a clustering process to classify the pore bodies and pore throats. The clustering process arrange the all the maximal balls by families based on their size and rank. The new algorithm sorts the maximal balls from big to small and divide them into subsections according to their size. Each subsection contains all the maximal balls with the same size. Then it ranks the largest maximal balls first and regard them as the ancestor. All the maximal balls with smaller radius overlapping on the ancestors are regarded as its offspring. Each ancestor and its offspring are defined as a family, based on which the pore bodies and pore throats are classified. However, Dong's method developed for conventional reservoirs has some deficiencies in extracting the pore-network models for shale formations, because the algorithm cannot capture the extremely small pores. Moreover, the geometry information of each pore cannot be captured by Dong's method.

Chapter 3 Integrated Pore-Scale Characterization Using Dendroidal Theoretical Pore-network Model

3.1 Characterization of Pore Connectivity

During a mercury drainage experiment, the capillary pressure increases continuously in discrete pressure steps and the corresponding increment of mercury-saturation is recorded. Once the capillary pressure approaches the threshold capillary pressure of a pore throat, mercury can be injected into the specific pore throat. However, some of the pore throats cannot be invaded as they are connected only through narrower pore throats from the sample interface; those narrow pore throats that have high invasion capillary-pressure requirement restrict the nonwetting phase from invading into the wide pore throats. Fatt (1956) introduced the percolation theory based on the lattice pore-network model to characterize this phenomenon. At the initial phase of mercury drainage experiment, the nonwetting-phase saturation increases slowly due to the restriction of narrow pore throats. As the capillary pressure approaching the threshold pressure, the mercury saturation suddenly increases to a considerable extent with a slight increase of capillary pressure due to the formation of a self-spanning cluster. The self-spanning cluster connects large amount of wide pore throats restricted by narrow pore throats before, and it provides an accessible flow path across the entire sample. This phenomenon causes a plateau-like trend in the mercury injection capillary pressure (MICP) curve. The lattice model can capture this phenomenon because of its spatially random distribution of pore throats and good pore connectivity.

The MICP curve of unconventional formations does not have the plateau-like trend due to its limited connectivity. In the mercury drainage experiment of a shale core sample, the saturation of non-wetting phase increases gradually with capillary pressure increase (Figure 3.1). Chen et al. (2015) used Lattice Boltzmann Method to simulate fluid flow in a three-dimensional reconstruction of a shale core sample located in Sichuan, China. Figure 3.2 shows the pressure distribution and streamline of the direct simulation, and it also indicates that the connectivity of the porous media is limited. In Figure 3.2, the major flow contributions are from several main flow paths, which indicates that there are only several flow conduits traveling across the entire core sample. Other flow channels connecting to the main flow paths are the branching paths, that have relatively small effects to the flow capacity of the core sample. Besides, the main flow paths seldom connect to each other. Integrating the unique features of MICP curves from mercury drainage experiments and the extracted pore networks from scanning electron microscope (SEM) images, I propose a novel theoretical pore-network model, the dendroidal model, to characterize the porous structure of shales.

Since there is no plateau-like trend existing in the MICP curve of shale core samples, the mercury intrusion happening in wide pores are merely restricted by narrower ones. Sakhaee-Pour et al. (2015) proposed a theoretical pore-network model named “acyclic-model”, considering the limited pore connectivity in shales. In the acyclic model, there is only one unique flow path linking every two pore bodies and the spatial distribution of pore throats with different sizes are in a tapering manner. But the acyclic pore-network model cannot represent the realisms and the stochastic nature of the spatial distributions of pore throats and pore bodies. To ensure both non-plateau trend of MICP curve and realistic pore spatial distributions, I introduced the 'semi-acyclic' model to accommodate the scenario of multi-path connecting pores.

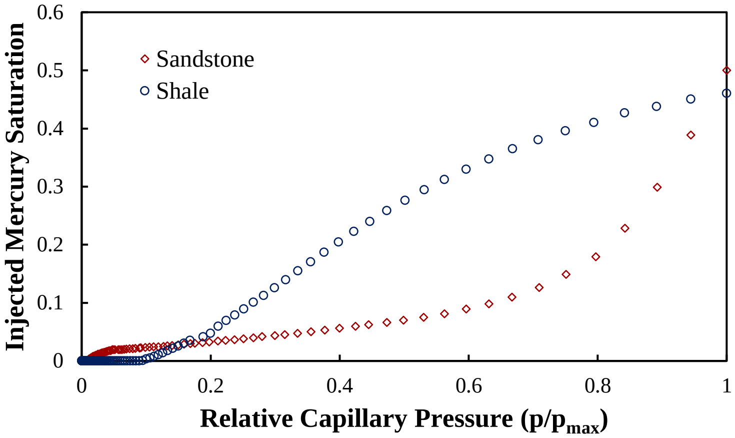

Figure 3.1 Injected mercury saturation change with capillary pressure, expressed in terms of relative capillary pressure for the reason of comparison. Plateau-trend shape only exists in the curves for sandstones, while the injected mercury saturation in shales increase continuously with capillary pressure.

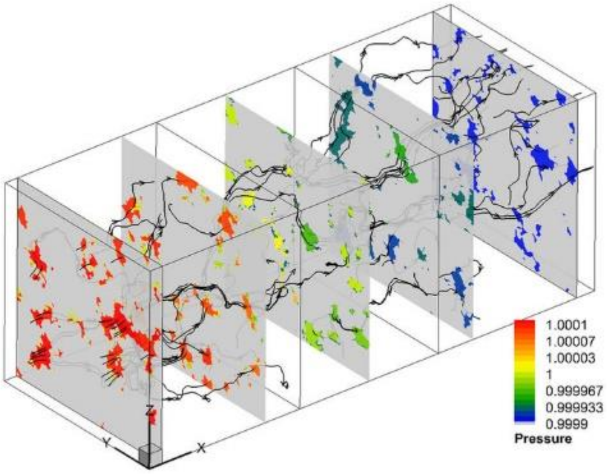

Figure 3.2 Streamlines and pressure distributions in a three-dimensional reconstruction of shale sample simulated by Lattice Boltzmann methods. (Chen et al. 2015).

3.2 Experimental Data

This section briefly discusses the experimental data used in constructing a pore-network model. For each shale core sample, experiments are performed to get the static properties, including total organic carbon (TOC), mineralogy, porosity and contact angle. I obtained TOC using a LECO^{TM} analyzer; minerology using transmission Fourier Transform Infrared (FTIR) Spectroscopy; total porosity from Low Pressure Helium Pycnometry (LPP); contact angle by Sessile Drop Method after optically determining the wetting properties of a localized region on a solid surface. The traditional mercury drainage and imbibition experiments provide the size and spatial distribution of pores. The isothermal adsorption-desorption measurement (IADM) characterizes the pore-body size distribution using Micromeritics Tristar 3020 gas adsorption analyzer. After adsorption-desorption isotherm measurements, shale core samples are burned by exposing to oxygen plasma to remove the organic matters. This process gets rid of any remaining hydrocarbon that has not been removed during the process of oven-drying along with kerogen and bitumen in the samples.

For the IADM, I crush the original shale core samples and sieve them into 35 mesh-size cubes. To eliminate the effect of moisture and hydrocarbons, I dry the samples at 100℃ for 24 hours with experimental ovens. The temperature of drying process needs to ensure not to alter the kerogen and bitumen. I inject nitrogen with continuously increasing capillary pressure from 1.1 psi to 14.7 psi at a constant temperature and record the corresponding adsorbed gas volume. Once the capillary pressure achieves 14.7 psi, I decrease the pressure continuously to obtain the gas desorption volume for each pressure step. Since the pressure range for the IADM in this research is low, the size and compressibility of pores will not be changed.

To eliminate the effect of temperature change and mercury compressibility during the experimental process, I analyze the blank cores before collecting any data. Additionally, I prepare all the core samples through multiple processes, including polishing, drying and vacuuming. These processes ensure the fluid to be evacuated from the porous media, and the pore pressure is approximately zero at the start of the experiment. Integrated Core Characterization Center at The University of Oklahoma conducted all the aforementioned experiments.

3.3 Dendroidal Model

3.3.1 Dendroidal Pore-network Model Description

The dendroidal model (Figure 3.3), a three-dimensional theoretical pore-network model, distinguishes pores into main flow paths and branching flow paths by the critical capillary pressure. Main flow paths are the flow channels across the entire core sample along flow direction and branching flow paths are the conduits initiated from individual pore bodies located in main flow paths. Both main flow paths and branching flow paths are composed of pore bodies and pore throats with various sizes. Figure 3.3 schematically shows one main flow path of the dendroidal model and the associated branching paths. The other main flow paths have similar spatial distributions of pores. The adjacent main flow paths are connected to each other by the branching paths at the end pores of each branching. In another word, the end pores of each branching path stemmed from the main flow paths enable the limited connectivity amongst multiple main flow paths. Thence, this semi-acyclic model improves the connections among main flow paths without sacrificing the limited connectivity.

The dendroidal model use spheres to represent pore bodies, whose size distribution is characterized with IADM experiments. The pore throats are represented by tubes with various cross-section shapes: triangles, circles and rectangles. Randomly generated corner angles determine the triangles, while randomly generated aspect ratios (ratio of two adjacent sides) describe the rectangles. The lengths of pore throats and the coordination numbers of the pore bodies are also stochastically assigned by normal distribution. The dendroidal model is used as a platform to simulate the mercury drainage/imbibition experiments considering contact-angle hysteresis and trapping hysteresis. The results of simulation are fitted with the experimental data by adjusting the stochastically distributed parameters aforementioned.

An additional feature of the dendroidal model is compensating for compressibility. The experimental results of mercury drainage/imbibition experiments are corrected by dual-compressibility model to eliminate the compressibility effect of void space (isolated pores and connected pores). The compressibility compensation is elaborated in the ensuing section.

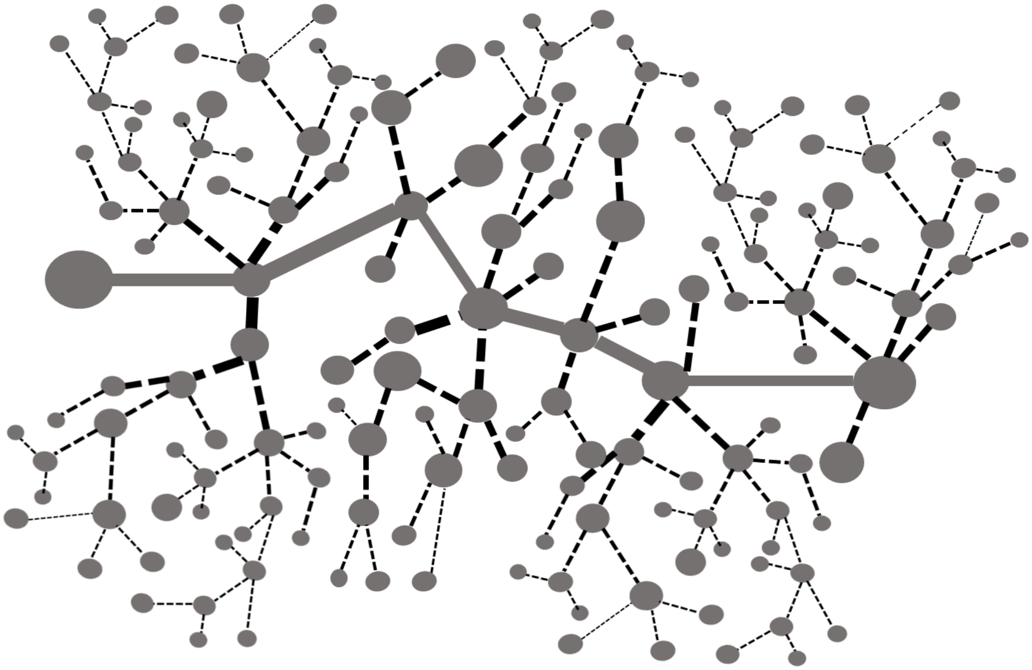

Figure 3.3 Schematic diagram of dendroidal model, where solid lines represent main flow paths, dashed lines represent branching paths and circles represent pore bodies. The thickness of lines represents the radius of pore throats.

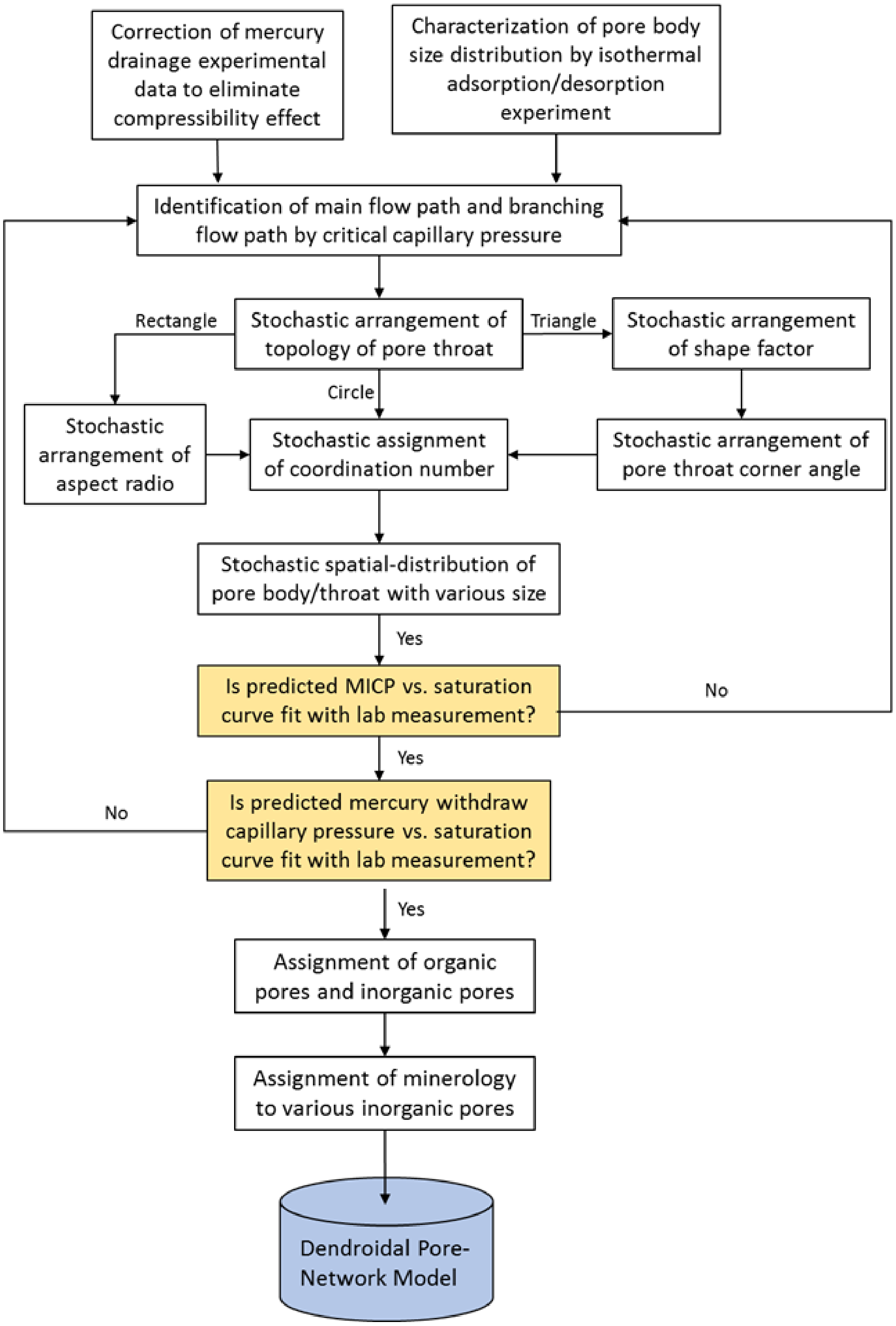

Figure 3.4 General procedures of constructing a dendroidal model.

Since the composition of pore walls has influence on transport properties and the capacities of gas adsorption/desorption, the dendroidal model differentiates organic pores and inorganic pores by analyzing the total organic carbon (TOC). For inorganic pores, further minerology classification is performed using the Fourier's Transform Infrared Spectroscopy (FTIR) measurements. Figure 3.4 illustrates the general procedures of constructing the dendroidal model by integrating the seven distinct experiments aforementioned.

3.3.2 Correction of Mercury Drainage Experimental Data

The previous theoretical pore-network models, including bundle-of-tube model, percolation model, sphere model and tree-like model, do not account for the compressibility effect while implementing mercury drainage experimental data in constructing pore-network models. Consequently, the pore-network model developed through those previous algorithms could deviate from the real pore structure significantly. Many studies addressed the compressibility effect on MICP curve by experiments or theoretical considerations (Zimmerman, et al. 1986; Laurent et al. 1993; Comisky et al. 2011). The dendroidal model use the dual-compressibility model (Lan et al. 2017) to correct the mercury drainage experimental results by eliminating the compressibility effect. The compressibility of mercury is low enough to be neglected, and its chemical effects can be neglected as well due to its high chemical stability. The compressibility correction of MICP curve can be treated as a dynamic problem, in which the compressibility changes as an exponential function of effective stress. The mercury drainage experiment is delineated into three phases: conformance, compression and intrusion. The volume of mercury increased in the conformance phase helps envelop the external shape of the core sample instead of invading porous media. Thus, the conformance phase cannot be used to identify the pore volume.

Within the range of conformance and critical intrusion pressure, the capillary pressure is not high enough for the mercury to invade into the porous media. The recorded mercury volume increase is the volume change caused by the compression of both accessible and inaccessible pores.

Mercury starts to invade into the accessible pores with the pressure approaching critical intrusion pressure, at which the capillary pressure is high enough for mercury to be injected into porous media. In constructing the dendroidal model, I implement dual-compressibility model to compensate the compressibility effect during mercury drainage experiments. This ensures the mercury volume recorded are corresponds to the increase of accessible pore volume.

3.3.3 Pore-Throat Shapes

The cross-sectional geometry of pore throats and pore bodies are complex in real porous structure. Here, I represent pore bodies using spheres and pore throats using triangular, rectangular and circular tubes (Figure 3.5).

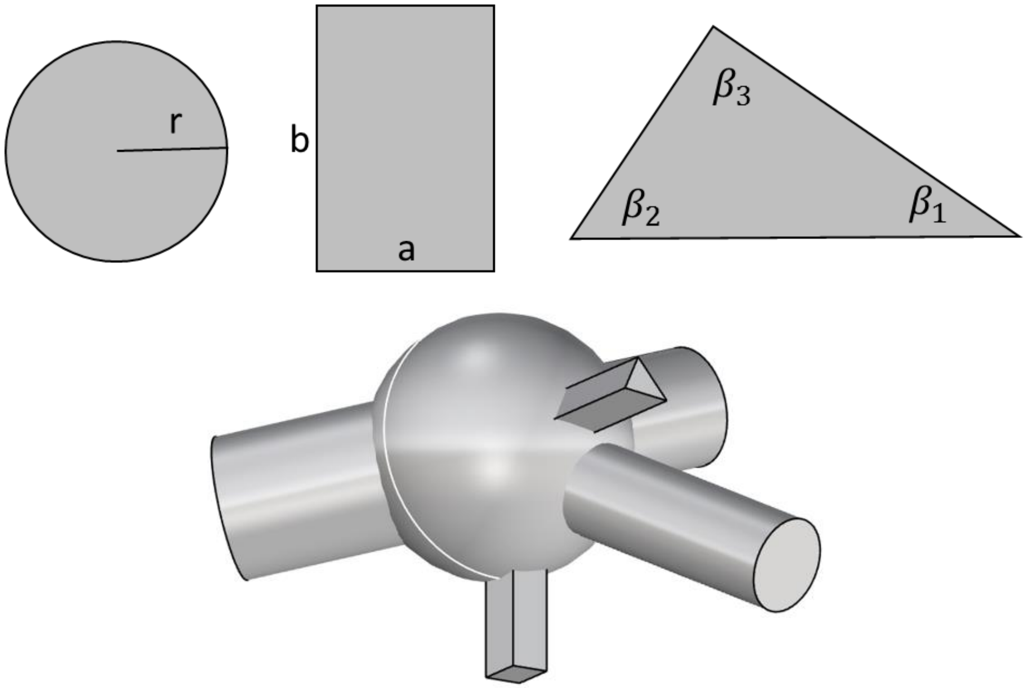

Figure 3.5 Schematic of pore throats, pore bodies and the general connections implemented in the dendroidal model.

To define a rectangle, the lengths of two adjacent sides (a and b) are required, and the radius (r) is required to determine a circle. Three parameters are required to define a triangle: shape factor (G), inscribed radius (r), and half-angle of one corner (β_2). The half-angle of three corners have the relationship, $0 < \beta_1 < \beta_2 < \beta_3 < \frac{\pi}{2}$, which is satisfied with the convention that β_3 is the largest angle in opposite of the longest side of the triangle. The dimensionless shape factor (G) described by Mason and Morrow (1991) is,

$$G = \frac{A}{P^2} = 0.25 \tan \beta_1 \tan \beta_2 \cot(\beta_1 + \beta_2) \qquad (3.1)$$

where A is the cross-sectional area of the pore throat and P is the perimeter. This shape factor ranges from the maximum, $\sqrt{3}/36$, for an equilateral triangle, to the minimum by approaching 0 for an extremely slit-like triangle. For a given shape factor of a triangular-tube, the admissible range for the corner half-angle (β_2) is limited, $\beta_{2,min} < \beta_2 < \beta_{2,max}$. The standard trigonometry reveals that Eq. 3.1 has three real roots for $0 < G < \sqrt{3}/36$,

$$\beta_{2,max} = \tan^{-1}\left\{\frac{2}{\sqrt{3}}\cos\left[\frac{\cos^{-1}(-12\sqrt{3}G)}{3}\right]\right\} \tag{3.2}$$

$$\beta_{2,min} = \tan^{-1}\left\{\frac{2}{\sqrt{3}}\cos\left[\frac{\cos^{-1}(-12\sqrt{3}G)}{3} + \frac{4\pi}{3}\right]\right\} \tag{3.3}$$

$$\beta_1 = -0.5\beta_2 + 0.5\sin^{-1}\left[\sin(\beta_2)\frac{\tan\beta_2+4G}{\tan\beta_2-4G}\right] \tag{3.4}$$

Figure 3.6 shows the relationship between the shape factor and the second-large half-corner angle, while Figure 3.7 illuminates the relationship among different half-corner angles.

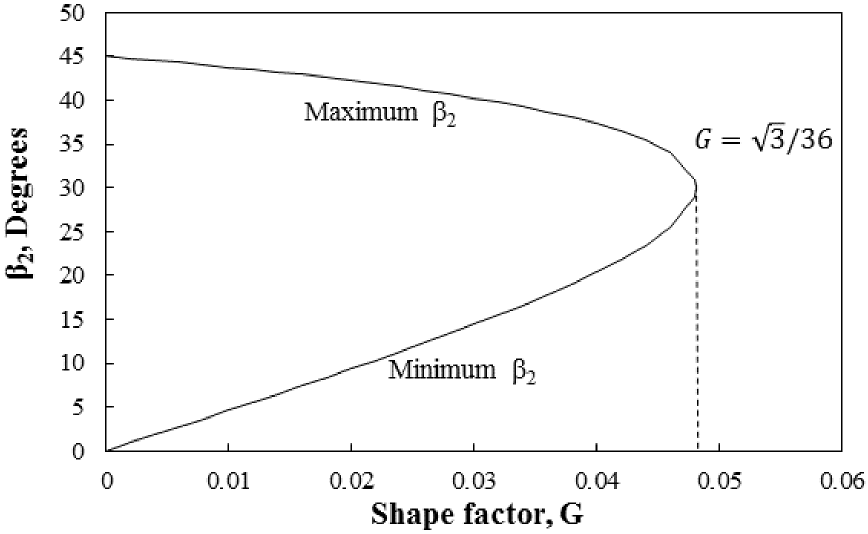

Figure 3.6 Relationship of the shape factor and the corner half-angle for a triangular pore throat. The admissible values for corner half-angle are within the range of the "dome". G= √ 3/36 is the shape factor for a equilateral triangle.

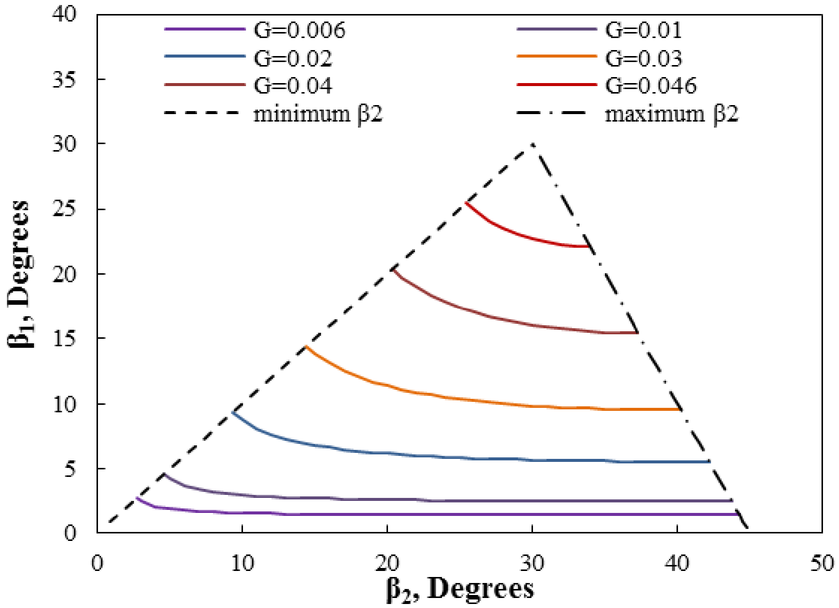

Figure 3.7 Feasible range of corner half-angles with respect to different shape factors.

3.3.4 Isothermal Adsorption/Desorption Measurement

Since the first-time use of isothermal adsorption/desorption experiments (IADM) in the estimation of pore-size distribution by Barrett (1951) and pore connectivity by Seaton (1991), various methods were developed to characterize the porous structure. Zapata et al. (2017) proposed a method to evaluate pore-body size distribution for shales based on an acyclic model. This approach is implemented in the dendroidal model to characterize the pore-body size distribution. Zapata assumed that the incremental adsorption volume is only corresponding to the adsorbed gas volume in pore bodies, neglecting the effects of pore throats. Since pore bodies construct most volume of the void space, the feasibility of neglecting the effect of pore throats has been proven to be reasonable (Zapata et al. 2017).

Halsey’s model determines the thickness of an adsorbed layer stick on the pore wall as follows,

$$t = 3.54\left[-\frac{5}{\ln(p/p_0)}\right]^{1/3} \tag{3.5}$$

where p/p_0 is the relative pressure. However, Halsey’s model is not accurate at high pressure because it neglects the effects of condensation and evaporation. To account for these effects in nano-pores, the threshold relative pressures corresponding to evaporation and condensation are calculated as follows,

$$\ln(p/p_0)_{condensation} = -\frac{\gamma V_{mol}\cos\theta}{RT(r_p - t)} \tag{3.6}$$

$$\ln(p/p_0)_{evaporation} = -\frac{\gamma V_{mol}\cos\theta}{RT(r_p - t)} \tag{3.7}$$

where R is the gas constant, V_{mol} is the molar volume of the gas, T is temperature, θ is the contact angle of the gas on the solid wall, r is the radius of pore body, γ is interfacial tension, $(p/p_0)_{condensation}$ and $(p/p_0)_{evaporation}$ are the relative pressure corresponding to condensation and evaporation. These equations indicate that the critical relative pressures of evaporation and condensation are dependent on the original pore-body radius. The IADM can be simulated using this algorithm based on acyclic models to characterize the pore-body size distribution.

3.3.5 Mechanisms of Mercury Intrusion

Mercury intrusion is a drainage process, where the non-wetting phase is injected into porous media in a quasi-static manner. At the equilibrium condition, the capillary pressure must overcome the threshold pressure for the mercury invasion. The capillary pressure required for invasion is determined by the shape and size of the pore throat. The non-wetting phase will invade into the pore bodies whenever it is injected into the connected pore throats due to the size difference between pore bodies and pore throats. Even though pore bodies cannot restrict the fluid from invading into the porous media, their storing capacity can influence the MICP curve. Consequently, the pore-body distribution considerably influences the characterization of mercury-intrusion experiments.

Young-Laplace equation as follows determines the threshold capillary pressure for a cylinder ($P^e_{c,d,cir}$):

$$P^e_{c,d,cir} = \frac{2\sigma \cos\theta_r}{r} \tag{3.8}$$

where r is pore-throat radius, σ is interfacial tension, and θ_r is receding contact angle.

To estimate the threshold capillary entry-pressure for the pore throats with triangular cross-sectional shape (Figure 3.8), I follow the generalization of Mason and Morrow's (1991) expression. The Mayer-Stowe-Princen (MSP) algorithm of calculating the entry capillary pressure relies on equating the curvature of invading interface to the corner arc meniscus (AM). The threshold capillary pressure of mercury drainage ($P^e_{c,d}$) in a triangular tube is calculated (Patzek et al. 2001) by

$$P^e_{c,d,t} = \frac{\sigma\left(1+2\sqrt{\pi G}\right)\cos\theta_r}{r_s} F_d(\theta_r, G) \tag{3.9}$$

where σ is interfacial tension, r_s is the radius of the inscribed circle of the cross-sectional triangle, θ_r is receding contact angle, and

$$F_d(\theta_r, G) = \frac{1+\sqrt{1+4GT/\cos\theta_r}}{1+2\sqrt{\pi G}} \tag{3.10}$$

is a function of corner half-angles:

$$T = \sum_{i=1}^{3}\left[\cos\theta_r \frac{\cos(\theta_r+\beta_i)}{\sin\beta_i} - \left(\frac{\pi}{2} - \theta_r - \beta_i\right)\right]. \tag{3.11}$$

T is not applicable for a given shape factor if any of the pore corners does not have an AM. If the receding contact angle is 0, $T = 1$ regardless of the number of the pore corners containing AM.

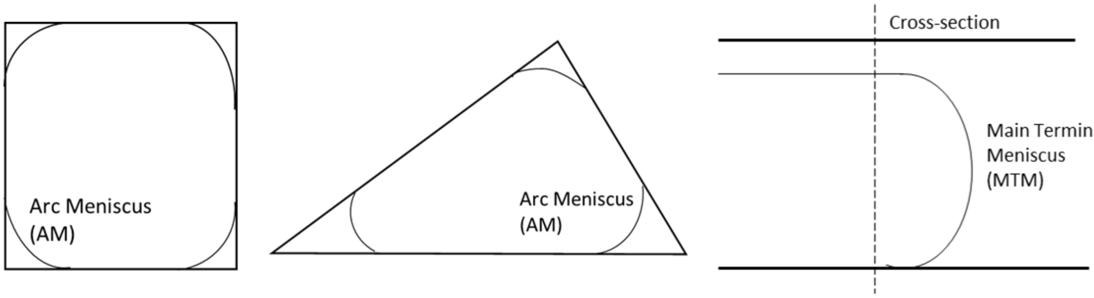

Figure 3.8 Fluid distribution within a pore throat, where the wetting phase fluid is distributed in the central region and the non-wetting phase is trapped in corners.

For a rectangular-cross-section pore throat (Figure 3.8), Mason et al. (1991) proposed a general relationship between the curvature of main terminal meniscus (MTM) and the properties including corner angle, contact angle and curvature:

$$\left(\frac{cos^2\theta_r}{\tan\beta_i} - \frac{\sin 2\theta_r}{2} - \frac{\pi}{2} - \beta_i - \theta_r\right)\frac{1}{C_n^2} - \frac{\cos\theta_r}{tan\beta_i}\frac{2}{C_n} + \frac{1}{\tan\beta_i} = 0. \tag{3.12}$$

The solution of Eq. 3.12 is

$$C_n = \cos\theta_r + \sqrt{\frac{\tan\beta_i}{2}\left[\sin 2\theta_r + \pi(1 - 2\beta_i - 2\theta_r)\right]}, \text{ for } \theta_r < \frac{\pi}{2} - \beta_i \tag{3.13}$$

$$C_n = 2\cos\theta_r, \text{ for } \theta_r > \frac{\pi}{2} - \beta_i. \tag{3.14}$$

Therefore, the drainage capillary pressure in a rectangular pore throat is

$$P_{c,d,r}^{e} = \frac{\sigma}{r_s}\left\{\cos\theta_r + \sqrt{\frac{1}{2}\left[\sin 2\theta_r + \pi(1 - \pi - 2\theta_r)\right]}\right\}, \text{ for } \theta_r < \frac{\pi}{2} - \beta_i \tag{3.15}$$

$$P_{c,r}^{e} = \frac{2\sigma\cos\theta_r}{r_s}, \text{ for } \theta_r > \frac{\pi}{2} - \beta_i \tag{3.16}$$

where r_s is the inscribed radius of rectangular pore throats.

3.3.6 Mechanisms of Mercury Retraction

As mentioned previously, I vacuumed the core samples at the preparation phase of the mercury drainage experiments. Thence, the porous media is almost fully saturated with mercury after the drainage process, except for the nooks and crannies on pore walls, where mercury-gas high curvatures reside. Mercury retraction is an imbibition process that gas (wetting phase) displaces mercury (non-wetting phase). The mercury retraction occurs continuously as the capillary pressure decrease.

The mechanism of mercury retraction is much more complicated than that of mercury drainage, which includes pore-throat piston-type imbibition, snap-off and pore-body filling. The imbibition progresses slowly in a quasi-static manner, and the gas spans the entire porous media through corner filaments. Consequently, some mercury gets trapped in the porous media since the wetting phase (air) cuts off the escape paths.

The mercury is withdrawn from the narrow pore throats at first, and then it is extracted from the wider pore throats with capillary pressure decrease. Since there is no MTM at the beginning, the wetting phase fill the pore throats by snap-off and then by piston-type imbibition. Correspondingly, the wetting phase fill the pore bodies attached to the invaded throats through I_n events, where I_n represents n connected pore throats.

3.3.6.1 Piston-Type Imbibition

Because of the contact-angle hysteresis ($\theta_r < \theta_a$), the corner arc meniscus (AM) in each corner of triangular and rectangular pore throats hinges at its contact line, which is pinned at a distance from the apex. As the hinging contact angle ($\theta_{h,i}$) approaching the advancing angle, the AM starts to slide with decreasing the curvature radius to accommodate the imbibition capillary pressure. Since the radius of the AM curvature within the sharpest corner is small, it slides first; while the AM slides last in the most obtuse corners. The decrease of pinned AM curvature is processed by corner-fluid swelling.

Patzek (2001) investigated the contact-angle effects on the imbibition threshold capillary pressure. For triangular pore throats, the following non-linear equation system determines the threshold capillary pressure of spontaneous imbibition coupling contact-angle hysteresis effect:

$$\theta_{h,i} = min\left\{\cos^{-1}\left[\frac{r_{pd}\cos(\theta_r+\beta_i)}{r_p}\right] - \beta_i, \theta_a\right\} \tag{3.17}$$

$$\alpha_i = \sin^{-1}\left(\frac{b_i \sin\beta_i}{r_p}\right), if\ \theta_{h,i} \le \theta_a \tag{3.18}$$

$$\alpha_i = \frac{\pi}{2} - \theta_a - \beta_i, if\ \theta_{h,i} > \theta_a \tag{3.19}$$

$$b_i = \frac{\cos(\theta_r+\beta_i) r_{pd}}{\sin\beta_i}, if\ \theta_{h,i} \le \theta_a \tag{3.20}$$

$$b_i = \frac{\cos(\theta_a+\beta_i) r_{pd}}{\sin\beta_i}, if\ \theta_{h,i} > \theta_a \tag{3.21}$$

$$r_p = \frac{\frac{r^2}{4G} - r_p \sum_{i=1}^{3} b_i \cos\theta_{h,i} + r_p^2 \sum_{i=1}^{3}\left(\frac{\pi}{2} - \theta_{h,i} - \beta_i\right)}{2r_p \sum_{i=1}^{3} \alpha_i + \left(\frac{r}{2G} - 2\sum_{i=1}^{3} b_i\right)\cos\theta_a} \tag{3.22}$$

where $i = 1, 2, 3$, and r_p is the radius of AM. Solving the equations, I can get the threshold capillary pressure for piston-type imbibition in a triangular pore throat is $P_{c,PT,t}^{e} = \frac{\sigma}{r_p}$.

For a circular-cross-section pore throat, the threshold capillary pressure of piston-type imbibition can be calculated by $P_{c,PT,cir}^{e} = 2\sigma\cos\theta_a / r$. For rectangular-cross-section pore throats, Eq. 3.15 and Eq. 3.16 can be used to evaluate the piston-type imbibition capillary pressure.

3.3.6.2 Pore-Body Filling

The largest radius of mercury/gas interface curvatures within a pore body and the mercury-filled pore throats connecting to it determines the capillary pressure required to fill the pore body. The threshold capillary pressure for pore-body filling is always lower than that required for piston-type imbibition in the connected pore throats, because the radius of pore throats is smaller than that of the connected pore bodies. Therefore, mercury withdrawn from a pore body is always accompanied by the mercury imbibition from the adjoining pore throats. Thence, the capillary pressure required for mercury retraction from a pore body depends on the its radii and the number and cross-sectional area of the connected pore throats. If there is only one pore throat filled with mercury connecting to the pore body, the pore-body filling mechanism is the same as the piston-type invasion. If there are m ($m > 1$) number of pore throats filled with mercury connecting to the pore body, the number of pore-body filling mechanism is $m - 1$, represented by I_1 to I_{m-1}.

I employ the algorithm proposed by Blunt (1997) to describe the parametric model for pore-body filling. If $\theta_a < \theta_{a,max}$, I calculate the mean radius of curvature ($\overline{R_n}$) for pore-body filling by I_n mechanism by

$$\overline{R_n} = \frac{r_0 + \sum_{i=1}^{n}(a_i r_i x_i)}{\cos\theta_a}, \tag{3.23}$$

where r_i is the radius of the pore throats filled with the wetting phase, r_0 is the radius of pore body, a_i is the geometrical constant and x_i is a random number between 0 and 1. Consequently, the capillary pressure for I_n pore-body filling mechanism is

$$P_{c,n}^{e} = \frac{2\sigma}{\overline{R_n}}. \tag{3.24}$$

Because it requires numerical simulation to calculate the geometrical constant, the following equation is proposed for simplicity (Blunt et al. 1997):

$$\overline{R_n} = \frac{\left[r_0 + \sum_{i=1}^{n}(m_i r_i)\right]}{\cos\theta_a}, \tag{3.25}$$

where r_0 is the radius of pore body, r_i is the radius of the pore throats filled by wetting phase connecting this pore body, and m_i is the weight of each pore throat for this I_n event.

Patzek (2001) simplified this equation by combining each single weight factor into an average weight factor ($\overline{m_l}$) and picking all the combinations of throat-radius pairs with random weight:

$$\overline{R_n}\cos\theta_a = r_0 + \overline{m_n}\frac{\sum_{n,pairs}\left[M_{n,pairs}\sum_{i=1}^{n}(r_i)\right]}{\sum_{n,pairs}M_{n,pairs}}. \tag{3.26}$$

For each combination of the n pore throats, $M_{n,pairs}$ is the random weight between zero and one, and the denominator is the normalizing factor. Numerical experiments are implemented to provide the consecutive weight. The weight evaluated by this model is similar to Blunt's model (1997) and the weight factor provided by Oren (1998).

3.3.6.3 Snap-off

Snap-off is an imbibition process, where the corner wetting-layer swelling so much that the interface between wetting phase and non-wetting phase becomes unstable and then it fills the pore throat. Without considering contact-angel hysteresis effect, the corner arc meniscus (AM) moves smoothly along the pore-throat wall as capillary pressure decrease. Until the critical point that all corner arc menisci (AM) within the pore throat fuse together and the interface becomes unstable, the wetting phase fills the entire pore throat and break the continuity of non-wetting phase within the pore. Snap-off can only take place in a pore throat if the non-wetting phase fills the center of all the connected pore throats. Meanwhile, snap-off can only happen when the piston-like imbibition is impossible to take place due to the topology or spatial distribution, because the threshold capillary pressure for snap-off is always smaller than that of piston-like imbibition.

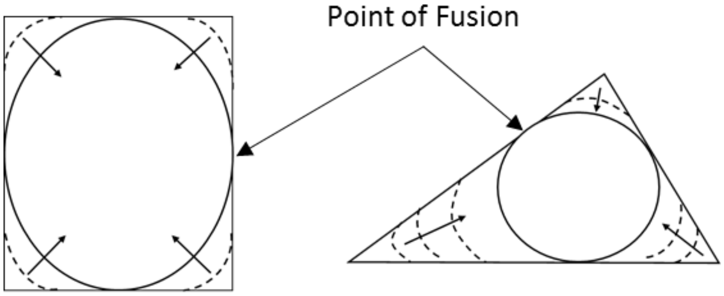

Figure 3.9 Schematic of snap-off in the pore throats with triangular and rectangular cross sections ($\boldsymbol{\theta_a < \frac{\pi}{2} - \beta_i}$).

Considering the contact-angle hysteresis effect, the maximum capillary pressure in mercury drainage experiment establishes the angle of AM. The AM will move when the hinging angle within the sharpest corner reaches θ_a. In triangular pore throats, the AM in the sharpest corner keeps advancing to the center with capillary pressure decrease. For rectangular pore throats, the AM in all the four corners start to move at the sample capillary pressure, since their angles are same. The snap-off takes place when at least two advancing AMs intersect (Figure 3.9). Hughes (2000) derived the threshold capillary pressure for rectangular tubes,

$$p_{c,s,r}^{e} = \frac{\sigma}{r_s}(\cos\theta_a - \sin\theta_a) \tag{3.27}$$

For triangular pore throats, snap-off occurs at the condition ($\theta_a < \frac{\pi}{2} - \beta_{min}$), and the corresponding capillary pressure is

$$p_{c,s,t}^{e} = \frac{\sigma}{r_s}\left(\cos\theta_a - \frac{2\sin\theta_a}{\cot\beta_1 - \cot\beta_2}\right) \tag{3.28}$$

If the advancing contact angle satisfies the condition ($\theta_a > \frac{\pi}{2} - \beta_{min}$), snap-off can occur when the AM in the sharpest corner meets the AM pinned at a wider corner, instead of two moving AM intersect. The corresponding threshold capillary pressure can be calculated by,

$$p^e_{c,s,t} = \frac{\sigma}{r_s}\left(\frac{\cos\theta_a\cot\beta_1 - \sin\theta_a + \cos\theta_{h3}\cot\beta_3 - \sin\theta_{h3}}{\cot\beta_1 + \cot\beta_2}\right) \tag{3.29}$$

If $\theta_a < \frac{\pi}{2} - \beta_i$, the capillary pressure of AM is negative while moving along the side. Once the hinging contact angle within the sharpest-angle corner increases to the advancing contact angle, the AM starts to advance towards the center with a negative capillary pressure and the absolute value of the contact angle decrease. Snap-off takes place once two AMs intersect (Figure 3.10), and the corresponding capillary pressure is,

$$\begin{cases} p^e_c = p_{c,max}\frac{\cos(\theta_a+\beta_1)}{\cos(\theta_r+\beta_1)}, at\ \theta_a \le \pi/2 - \beta_1 \\ p^e_c = p_{c,max}\frac{\cos(\theta_a+\beta_1)}{\cos(\theta_r+\beta_1)}, at\theta_a > \pi/2 - \beta_1 \end{cases}. \tag{3.30}$$

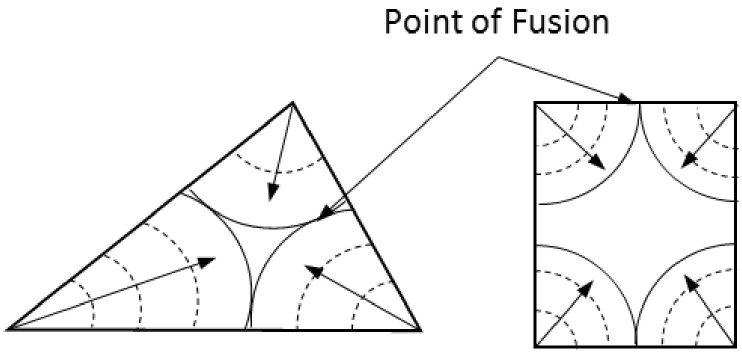

Figure 3.10 Schematic of snap-off in the pore throat whose cross section is triangular or rectangular ($\theta_a > \pi/2 - \beta_1$)

3.3.7 Integrated Procedures of Dendroidal-Model Construction

Eliminating the compressibility effect of pore space (connected pore and isolated pore), dendroidal model employs the dual-compressibility model to correct the drainage and imbibition experimental data. The isothermal adsorption-desorption measurement provides the pore-body size distribution considering the hysteresis effect.

The dendroidal model first identifies the main flow paths and the connected branching paths by guessing a value of critical pressure. The critical pressure determines the number of main flow paths and branching paths. The main flow paths are composed by those pores with the threshold invasion capillary pressure higher than the critical pressure, while the branching paths are composed of those pores with the threshold invasion capillary pressure lower than the critical pressure. The dendroidal model first constructs the main flow paths and then assigns the branching paths connected to them.

The dendroidal model employs tortuosity to keep the flow paths from being unrealistic straight tubes. Tortuosity is the ratio between the length of actual flow path and the sample length along the flow direction. A Large value of tortuosity represents a longer and more tortuous flow path, while a lower value represents a more straightly channel. Tortuosity is (Chen et al. 2015) defined as an exponential function in Bruggeman's equation,

$$\tau = \varepsilon^{-\alpha} \tag{3.31}$$

Here α is close to 0.5 for conventional reservoirs. This index is empirically determined from the sphere packing pore-network model. However, a value of 0.5 is not representative of the complex pore structure of shales. Chen (2014) proposed a value range for α, 1.33 to 1.65, based on the predictions of effective diffusivity using Lattice Boltzmann simulation. The range proposed by Chen is much larger than 0.5, which implies the porous media in shales are much more tortuous compared with conventional reservoirs.

To construct main flow paths, the dendroidal model randomly distributes the pore throats whose invasion pressure is larger than the critical capillary pressure. The length of the main flow path is determined by the core-sample length and the tortuosity. Then I randomly assign the cross-sectional shapes (triangular, rectangular and circular) of each pore throat. Young-Laplace equation (Eq. 3.8) determines the radius for circular pore throats. For rectangular pore throats, Eq. 3.15 is implemented to define the side length using a stochastically assigned aspect ratio, which is the ratio of two sides (a/b). For the pore throats with triangular cross section, I stochastically assign the value of dimensionless shape factor (G) by normal distribution, and randomly assign the value of half-corner (β_2) within the admissible range given by Eq. 3.2 and Eq.3.3. Eq. 3.4 determines the other corner half-angles (β_1 and β_3). Subsequently, the following equations can be used to determine the length of each side and the inscribed radius in a triangular pore throat,

$$r_s = \frac{2A}{P} = 2GP = 2G(a + b + c) \qquad (3.32)$$

$$\frac{a}{sin\beta_1} = \frac{b}{sin\beta_2} = \frac{c}{sin\beta_3} \qquad (3.33)$$

where r_s is the inscribed radius, and P is the perimeter, which is the summation of the length of three sides (a, b and c).

For each incremental pressure step in the mercury drainage experiment, the increased mercury volume is corresponding to the pore volume with the specific invasion threshold capillary pressure. However, the pore bodies do not restrict mercury to be injected into the porous media due to its large size. Since the pore throats are the main restriction of mercury invasion, the invasion threshold capillary pressure of these pore throats is corresponding to the capillary pressure recorded in the experiments. Neglecting the effect of pore bodies at the first instance, I temporally compose the pore-network model with pore throats only; while the pore bodies will be added to the model afterwards. Given the cross-sectional area and length of each pore throat, I calculate the volume of each pore-throat segment. The length and tortuosity of the rock core sample define the length of main flow paths, and then the number of main flow paths can be determined.

The dendroidal model composes the branching pore throats in the same manner of the main flow path construction. Each branching flow path initiates from the intersection of adjacent pore-throat segments in the main flow paths. A stochastically-assigned coordination number determines the number of branching paths connected to each intersection. The branching pore throats linked to the main flow paths are regarded as first generation, and the following pore throats are regarded as the second generation. The branching paths are denominated in the same way until all the pore throats are assigned. The coordination numbers of all the intersections are stochastically distributed by the normal distribution. The spatial distribution of pore throats in the branching paths is not fully stochastic, since it follows the rule that the later generation has a higher threshold invasion capillary pressure than that of its earlier generations. The IADM is used to characterize the pore-body size distribution. The dendroidal model randomly inserts the pore bodies at each intersection between two adjacent pore-throat segments within both the main flow paths and the branching paths. The volume of inserted pore bodies are subtracted from its adjacent pore throats to maintain the pore volume consistency.

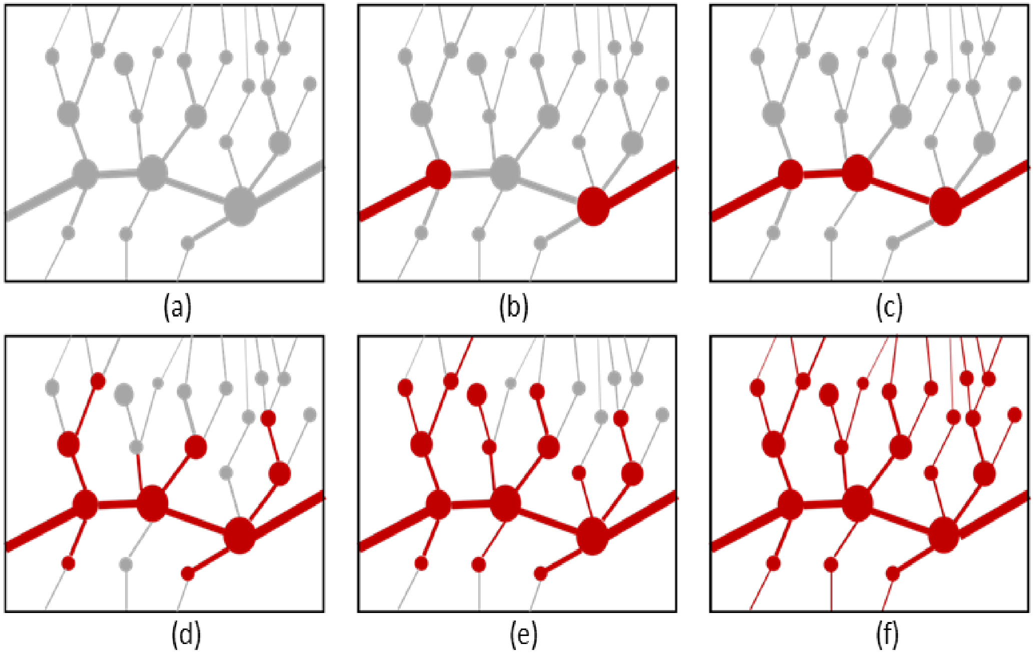

Figure 3.11 Schematic diagram of mercury drainage simulation using the dendroidal model. Lines represent pore throats and circles represent pore bodies. The gray pore throats and pore bodies are empty, while the red ones are invaded by mercury.

With the dendroidal model constructed, the mercury drainage simulation is performed to verify the correct value of the critical capillary pressure. During mercury drainage, the threshold capillary pressure of invasion into the pore throats is controlled by its size and shape. Comparing to the branching flow paths constructed by pore throats in a tapering manner, the main flow paths are constructed by randomly-distributed pore throats. Therefore, the value of critical capillary pressure is the key parameter determining the shape of MICP curve. The process of mercury drainage simulated in the dendroidal model is expressed in Figure 3.11.

The simulation of mercury retraction (Figure 3.12), considering the effect of contact-angle hysteresis and trapping hysteresis, testifies the parameters, including pore-throat length, pore-throat cross-sectional geometry, coordination number and spatial distribution. The dendroidal model reconstructs by adjusting these parameters iteratively to fit the experimental profiles. Snap-off is important in mercury retraction, because it is a pore-throat breaking mechanism and is responsible for large-scale mercury trapping in the porous media. The order of pore-body filling event and pore-throat snap-off event determines the value of residual saturation and then the profile of mercury retraction capillary pressure vs. non-wetting phase saturation. If the mercury retraction is dominated by pore-body filling events, the residual non-wetting saturation is low; if the displacement is dominated by snap-off, the saturation of mercury trapping is high. The competition of pore-throat snap-off and pore-body filling is central to fitting the mercury retraction experimental data. The balance of snap-off and pore-body filling can be expressed as

$$\frac{p_{c,s}}{p_{c,f}} = \frac{(1-\tan\beta_{min}\tan\theta_a)}{C_{I_n}} \tag{3.34}$$

where C_{I_n} is the input parameter provided by Hughes and Blunt (2000), where $C_{I_1} = 1.7, C_{I_2} = 1.15, C_{I_3} = 0.7, C_{I_{n\geq 4}} = 0.5$. C_{I_n} is used to account for the largest radius achieved for the pore-body filling event, which depends on the number of connected pore throats filled by the wetting phase. Eq. 3.34 indicates that the competition of snap-off and pore-body filling is controlled by the aspect ratio of the pore body and adjacent pore throats (size ratio between a pore body and a connected pore throat), contact angle, corner half-angle and coordination number.

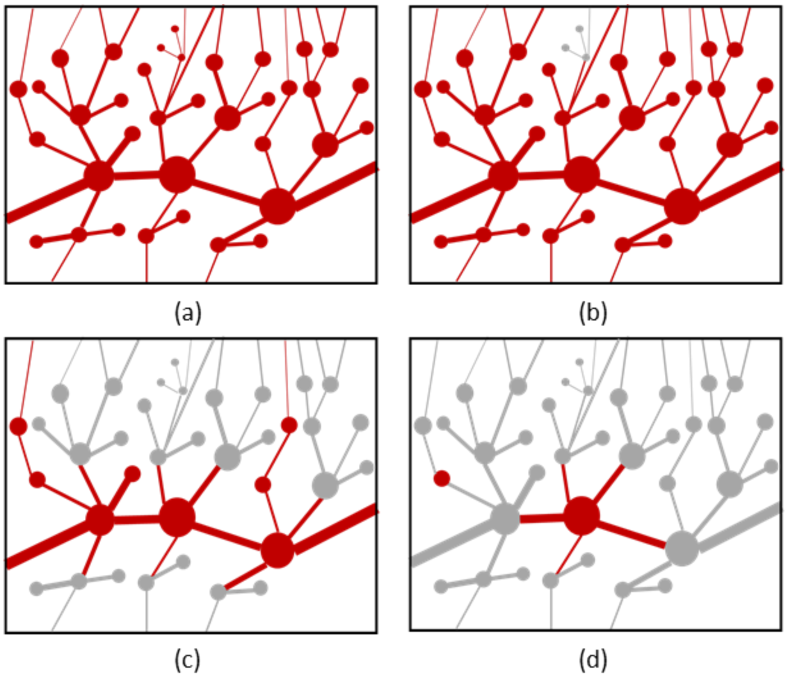

Figure 3.12 The schematic of mercury retraction process. Lines represent pore throats and circles represent pore bodies. The gray pore throats and pore bodies are empty, while the red ones are invaded by mercury.

Subsequently, I randomly classify the pores into organic and inorganic ones based on the TOC and assign mineral composition of inorganic pores using the measurement of transmission Fourier Transform Infrared (FTIR) Spectroscopy. Since the pores have different composition, dendroidal model can characterize different physical/chemical effects between fluid and matrix within different pores.

3.4 Absolute Permeability

The dendroidal model can be used to calculate the absolute permeability of a rock core sample, by which I can validate the theoretical pore-network model. Since the geometry and size of each pore throat and pore body are known, the absolute permeability can be determined by accounting for the pressure distribution. For a circular pore throat, the permeability can be estimated by

$$k_{throat,cir} = \frac{r^2}{8} \tag{3.35}$$

where r is the radius of the cross-sectional circle. The absolute permeability of triangular and rectangular pore throat can be calculated by (Patzek et al. 2001),

$$k_{throat,t} = \frac{3}{5}\mathrm{GA} \tag{3.36}$$

$$k_{throat,r} = 0.5623\mathrm{GA} \tag{3.37}$$

where G is the shape factor, A is the cross-sectional area, and k_{throat} is the permeability of a single pore throat. The pressure distribution can be calculated by

$$q = \frac{k_1 A_1}{\mu} \cdot \frac{\Delta p_1}{L_1} = \frac{k_2 A_2}{\mu} \cdot \frac{\Delta p_2}{L_2} = \frac{k_3 A_3}{\mu} \cdot \frac{\Delta p_3}{L_3} = \cdots = \frac{k_n A_n}{\mu} \cdot \frac{\Delta p_n}{L_n}. \tag{3.38}$$

Here, k_i is the intrinsic permeability of each single pore-throat segment, μ is the viscosity of the fluid, L is the pore-throat length, Δp is the pressure difference of each pore throat segment, and n is the number of segments in a main flow path. The total pressure difference implemented on the pore-network model is ΔP_{total}, which can be expressed by

$$\Delta p_{total} = \Delta p_1 + \Delta p_2 + \Delta p_3 + \cdots + \Delta p_n. \tag{3.39}$$

Combining Eq. 3.38 and Eq. 3.39, I can calculate the pressure difference of a specific pore-throat segment by

$$\Delta p_i = \Delta p_{total} \cdot \frac{L_i}{k_i A_i} \cdot \frac{1}{\left(\frac{L_1}{k_1 A_1} + \frac{L_2}{k_2 A_2} + \frac{L_3}{k_3 A_3} + \cdots + \frac{L_n}{k_n A_n}\right)}. \tag{3.40}$$

With the pressure difference of each individual pore-throat segment within the main flow path, flow rate can be calculated by substituting Eq. 3.40 into Eq. 3.38. Similarly, the flow rate of each main flow path is evaluated by Eq. 3.38 and Eq. 3.39. The permeability of the whole rock core sample is calculated by Darcy's Law,

$$k_{sample} = \frac{Q\mu}{A_{sample}} \cdot \frac{L_{sample}}{\Delta p_{total}} \tag{3.41}$$

where Q is the total flow rate of the model, L_{sample} is the length of the entire sample, A_{sample} is the cross-sectional area of the sample, and k_{sample} is the permeability of the shale core sample.

3.5 Apparent Permeability

The permeability of gas (apparent permeability) in shale is higher than the intrinsic permeability because the gas-slippage effect could be significant, which is mainly caused by the slippage of gas molecules on the rock surface with the absence of electro-kinetic and chemical reactions (Heid et. al 1950). Based on the study of Knudt and Warburg (1875), Klinkenberg (1941) first-time addressed the effect of gas-slippage effect in porous media and the corresponding influence on permeability. The first order linear correlation proposed by Klinkenberg to correct the measured permeability is given by

$$k_a = f_c \cdot k_d = \left(1 + \frac{b_k}{p}\right) k_d \tag{3.42}$$

where k_d is the intrinsic permeability, which is the permeability measured at a very large pressure when Klinkenberg's slippage factor can be neglected. b_k is the Klinkenberg slippage factor depending on the pore size, pressure and molecular mean-free path. f_c is the correction factor for apparent permeability with respect to intrinsic permeability.

Zhu (2007) stated that the Klinkenberg first-order correlation is not adequate for predicting the gas permeability in ultra-tight formations and proposed some higher-order correlations. Tang et al. (2005) proposed a second-order equation to correlate the apparent permeability with the intrinsic permeability,

$$k_a = k_d\left(1 + \frac{A}{\bar{p}} + \frac{B}{\bar{p}^2}\right) \tag{3.43}$$

Tang (2005) studied the two-dimensional Navier-Stokes equation considering boundary-slippage condition within microchannels, and derived the following equation:

$$k_a = k_d(1 + 8C_1 Kn + 16C_2 Kn^2) \tag{3.44}$$

which can capture the slip flow regime and the transition flow regime. Kn is the Knudsen number, while C_1 and C_2 are the coefficients describing the first-order term and second-order term respectively.

Beskok et. al (1999) derived a rigorous second-order equation to express the volumetric flow in a microtube. The equation is proved to be rigorous for the entire range of Knudsen numbers, which is validated by both theoretical methods and experiments. The equation is as follows:

$$f_c = (1 + \alpha(Kn)Kn)\left(\frac{1 - bKn + 4Kn}{1 - bKn}\right) \tag{3.45}$$

where b is the slip coefficient, and $\alpha(Kn)$ is the rarefaction coefficient, denoting the reduction effect of intermolecular collision with Knudsen number increase. In this equation,

$$\alpha(Kn) = \alpha_0 \frac{2}{\pi} tan^{-1}\left(\alpha_1 Kn^{\beta_1}\right) \tag{3.46}$$

where α_1 and β_1 have the value of 4.0 and 0.4 respectively, and the rarefaction coefficient (α_0) has the expression

$$\alpha_0 = \alpha_{Kn\to\infty} = \frac{64}{3\pi\left(1-\frac{4}{b}\right)} \tag{3.47}$$

$Kn \to \infty$ denotes free molecular flow regime, where gas molecules rarely collide with each other. b is the slip coefficient, which has the value of -1 for slip flow and transition flow regime.

Civan (2010) proposed another rarefaction coefficient applicable for all four flow regimes, including viscous, slip, transition and free molecular flow regime. The equation is as follows:

$$\alpha(Kn) = 1.358/(1 + 0.170Kn^{-0.4348}). \tag{3.48}$$

Dusty Gas Model (Veldsink et al. 1995) can also determine apparent permeability of gas in porous media. In this model, total flux of gas is divided into two parts: one is the viscous flow and the other is the Knudsen diffusion. The total flux is calculated by

$$J = J_d + J_k. \tag{3.49}$$

The total flux of gas can be expressed by apparent permeability

$$J = -\frac{\rho k_a}{\mu}\nabla p \tag{3.50}$$

where J is the mass flux, ρ is the gas density, ∇p is the pressure gradient, J_d is the flux of viscous flow and J_k is the flux of Knudsen diffusion. The fluxes of viscous flow and Knudsen diffusion are given by

$$J_d = -\frac{\rho k_d}{\mu}\nabla p \tag{3.51}$$

$$J_k = -MD_k\nabla C = -MD_k\nabla\left(\frac{p}{zRT}\right) = -\frac{\rho}{p}D_k\nabla p. \tag{3.52}$$

Here, z is the gas compressibility factor, R is the universal gas constant, M is the molar mass, and T is the absolute temperature. When the mean-free path of molecules is larger than the characteristic pore size, the collisions among the molecules is less frequent than the collisions between the molecules and solid walls. D_k is the Knudsen diffusivity and it has the following expression for a single pore,

$$D_k = \frac{d_p}{3}\sqrt{\frac{8RT}{\pi M}} \tag{3.53}$$

where d_p is the characteristic diameter of a pore. Correction factor f_c can be expressed as,

$$f_c = 1 + \frac{D_k \mu}{p k_d}. \tag{3.54}$$

Figure 3.13 shows the correction factor for apparent permeability within a cylinder predicted by different expressions, including Klinkenberg's slippage, Beskok-Karniadakis, Beskok-Karniadakis-Civan, and Dusty Gas Model (DGM) correlations. Figure 3.13 indicates that all the predictive equations have similar corrections for the Darcy flow regime, where the Knudsen diffusion effect can be neglected. But, the effect of Knudsen diffusion becomes stronger with the Knudsen number increase. Therefore, the discrepancies between the first-order correlation (Klinkenberg's slippage correlation) and the second-order correlations become large for slip flow regime, transition flow regime and free molecular flow regime. For all the four flow regimes, Beskok-Karniadakis and Beskok-Kariadakis-Civan equations have similar predictions of correction factor.

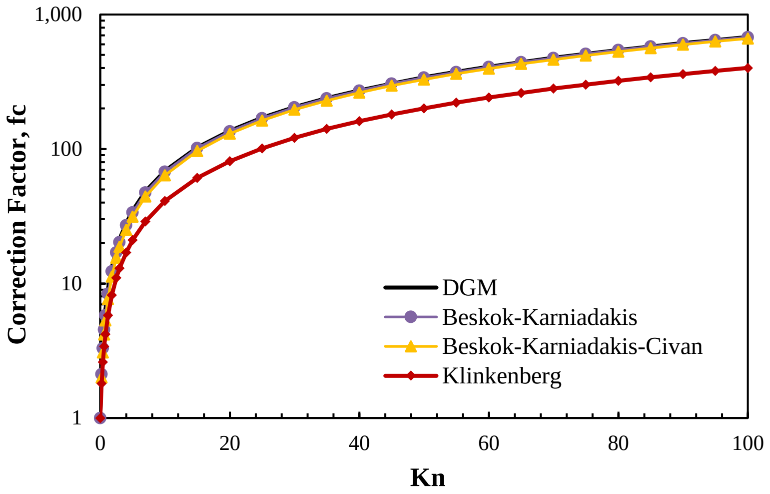

Figure 3.13 The correlation factor between apparent permeability and intrinsic permeability within a pore throat predicted by (1) Dusty Gas Model, (2) Beskok-Karniadakis correlation, (3) Beskok-Karniadakis-Civan Correlation, and (4) Klinkenberg's slippage correlation.

It is noted that the pores are characterized with different size across the entire porous media, so the local Knudsen number varies from one pore to another. The dendroidal model can capture the variation of pore size, thus the Knudsen number can be evaluated correspondingly for each single pore. With the intrinsic permeability of each pore evaluated, the apparent permeability of the pores can be calculated by different correlations aforementioned. The apparent permeability can be predicted then because the pressure difference is ultra-small between the inlet and outlet of the core sample due to the extremely small sample dimensions. Thus, the pressure of the entire system can be considered constant at an average of upstream and downstream pressures. Consequently, simulation is no longer essential to determine the pressure distribution and thus the apparent permeability. The Dusty Gas Model and the second-order correlations between apparent permeability and intrinsic permeability are implemented to calculate the apparent permeability for shales. It indicates that the gas flow within shales falls into slip and transition flow regimes.

3.6. Relative Permeability

The relative permeability is calculated by simulating the process of displacement of oil by water within the dendroidal model, where oil is the wetting phase and water is the non-wetting phase. Initially, the core sample is filled by oil. Water is injected from left with an increasing pressure. The capillary pressure required to invade a pore throat is calculated by the Yang-Laplace equation. For each incremental step of capillary pressure, the non-wetting phase invade into more pores, and the corresponding change of saturation is recorded. The relative permeability is calculated by

$$k_{rw} = \frac{q_{mw}}{q_{sw}} \tag{3.55}$$

$$k_{rnw} = \frac{q_{mnw}}{q_{snw}} \tag{3.56}$$

where q_{mw} is the flow rate of one wetting phase in multiphase flow condition, and q_{sw} is the flow rate of wetting phase in single-phase flow condition. q_{mnw} is the flow rate of one non-wetting phase in multiphase flow condition, and q_{snw} is the flow rate of non-wetting phase in single-phase flow condition. The total flow rate in multiphase flow is calculated by the mass conservation at every pore i,

$$\sum_j q_{i,j} = 0 \tag{3.57}$$

where j represents the pore throat connected to the specific pore body i. Implementing this method, I assume that the pressure drops caused by viscous effect can be neglected and the fluid is incompressible. Then, the flow rate between every two pores can be expressed as

$$q_{w,ij} = \frac{k_{rw,ij} A_{ij}}{\mu L_{ij}} \left(p_i - p_j \right) \tag{3.58}$$

where $k_{rw,ij}$ is the relative permeability of the wetting phase within the pore throat j, A_{ij} and L_{ij} are the cross-sectional area and length of the pore throat j connecting to the pore body i. A linear equation set can be defined by implementing Eq. 3.57 and Eq.3.58 into every pore throat, and then I can solve the pore pressure distribution. With the pore pressure of each pore body calculated, the relative permeability for each phase can be predicted correspondingly by Eq. 3.58.

3.7 Case Study

I construct dendroidal models for the shale core samples from Marcellus and Wolfcamp formations. The MICP raw data, shown in Figure 3.14 and Figure 3.15, is collected from the Integrated Core Characterization Center at The University of Oklahoma. The other measured data are shown in Table 3.1.

The dual-compressibility model is implemented to eliminate the compressibility effect of void space (Lan et al. 2017), and the corrected mercury drainage and imbibition data are shown in Figure 3.16. Figure 3.16 indicates that there is practically no plateau-like trend existing in the MICP curve, which implies the restricted connectivity of the porous media.

The IADM data for the Marcellus and Wolfcamp shales is shown in Figure 3.16. Considering the hysteresis effect, simulations of adsorption and desorption are performed on the dendroidal model, and the results are fitted with the experimental data of IADM by adjusting the pore-body size distribution (Figure 3.18). Figure 3.19 presents the final pore-body size distribution characterized by IADM.

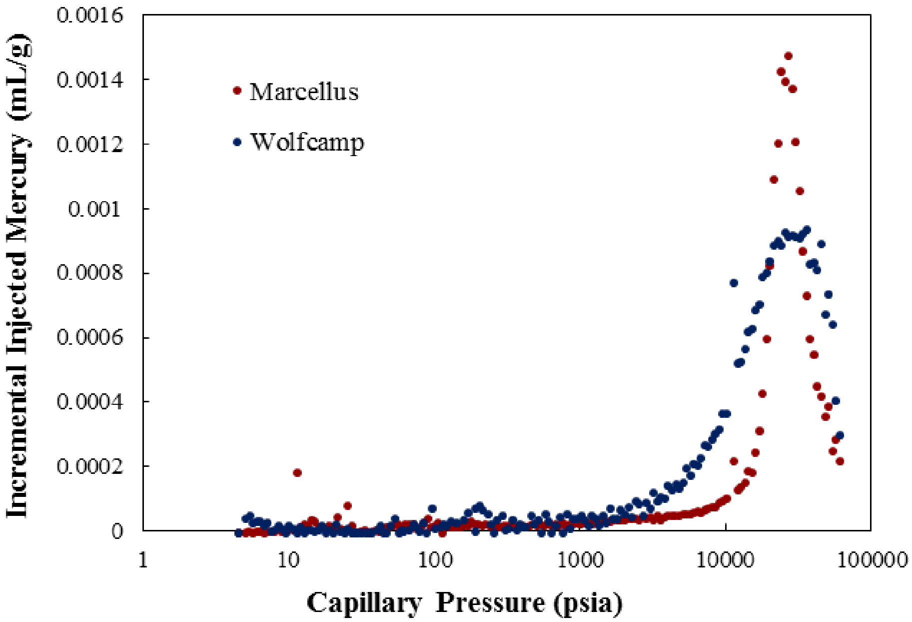

Figure 3.14 Incremental volume of injected mercury with respect to capillary pressure plot from the mercury drainage/imbibition experiments for Marcellus and Wolfcamp shale samples.

Table 3.1 The measured data of rock core samples from Marcellus and Wolfcamp shales.

	Marcellus	Wolfcamp
Bulk Density (g/cc)	2.30	2.47
Mass(g)	4.81	7.93
Porosity	9.96%	7.72%
TOC (wt%)	9.76	8.51
Contact Angle of Hg (degree)	130	130
Quartz (volume%)	13%	17%
Siderite (volume%)	0%	2%
Illite (volume%)	26%	51%
Orthoclase Feldspar (volume%)	2%	0%
Mixed Clays (volume%)	37%	18%
Oglioclase Feldspar (volume%)	0%	3%
Albite (volume%)	13%	7%
Siderite (volume%)	6%	0%
Apatite (volume%)	0%	0%
Aragonite (volume%)	3%	0%

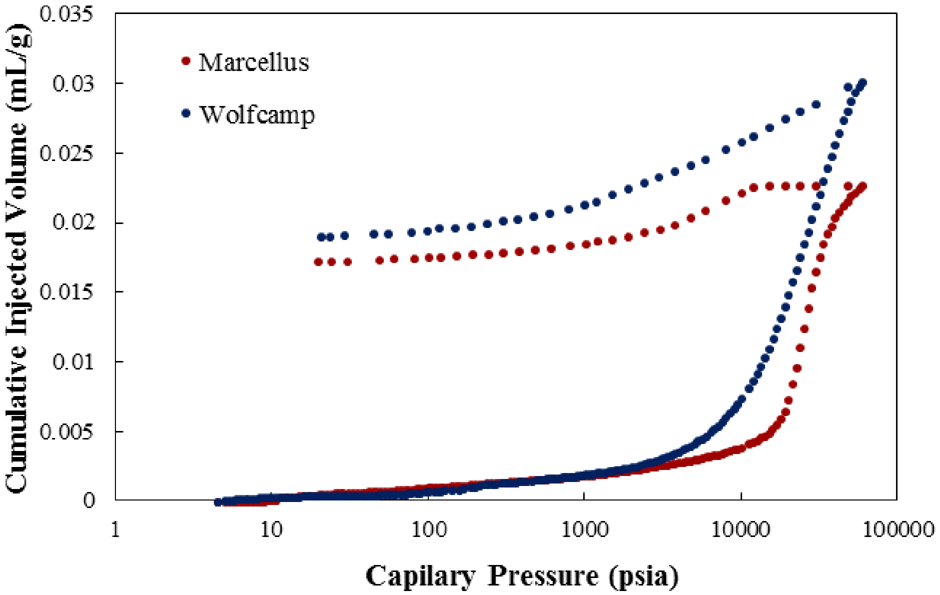

Figure 3.15 The plot of cumulative injected-mercury volume with respect to capillary pressure from mercury drainage/imbibition experiments for Marcellus and Wolfcamp shale samples.

In the dendroidal model for shale core samples from Marcellus and Wolfcamp, organic pores and inorganic pores are assigned based on the measurement of TOC. The relationships between TOC and organic porosity in Marcellus and Wolfcamp formation are proposed by several researchers (Milliken et al. 2013; Curtis et al. 2014). The mineral composition of inorganic pores is assigned based on the FTIR mineralogy measurement. The absolute permeability of Marcellus and Wolfcamp shale core samples are calculated to be 55.4 nd and 78.2 nd, which are within the reasonable range as reported in the literature (Curtis et al. 2014).

Table 3.2 Parameters of the dendroidal pore-network model of the shale core samples from Marcellus and Wolfcamp.

	Marcellus	**Wolfcamp**
Critical capillary pressure (psi)	8507	9200
Frequency of Triangular Pore Throat	65.45%	45.23%
Frequency of Rectangular Pore Throat	26.23%	42.34%
Frequency of Circular Pore Throat	8.32%	12.43%
Number of Pore Throats in Main Flow Path	11864	21548
Number of Pore Bodies in Main Flow Path	11864	21548
Number of Pore Throats in Branching Flow Path	2755905	3485967
Number of Pore Throats in Branching Flow Path	2755905	3485967
Scale	0.001	0.001

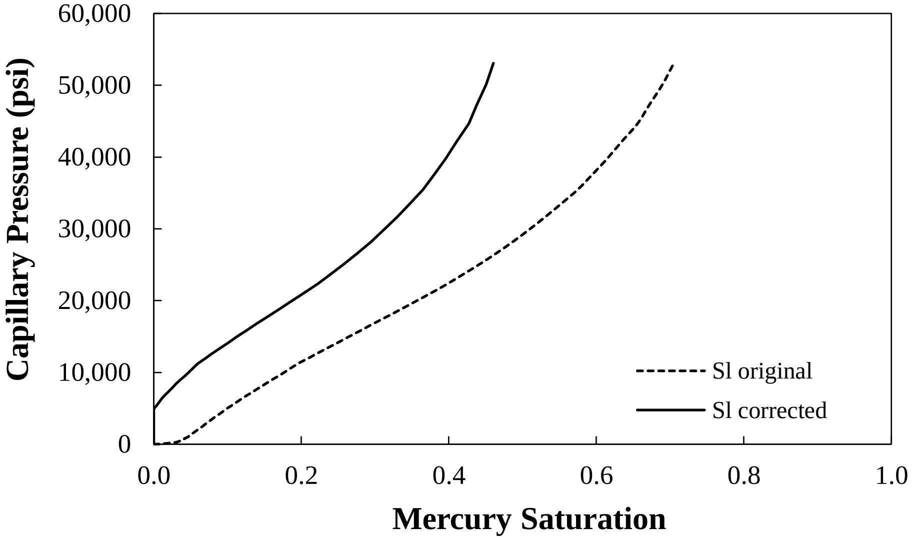

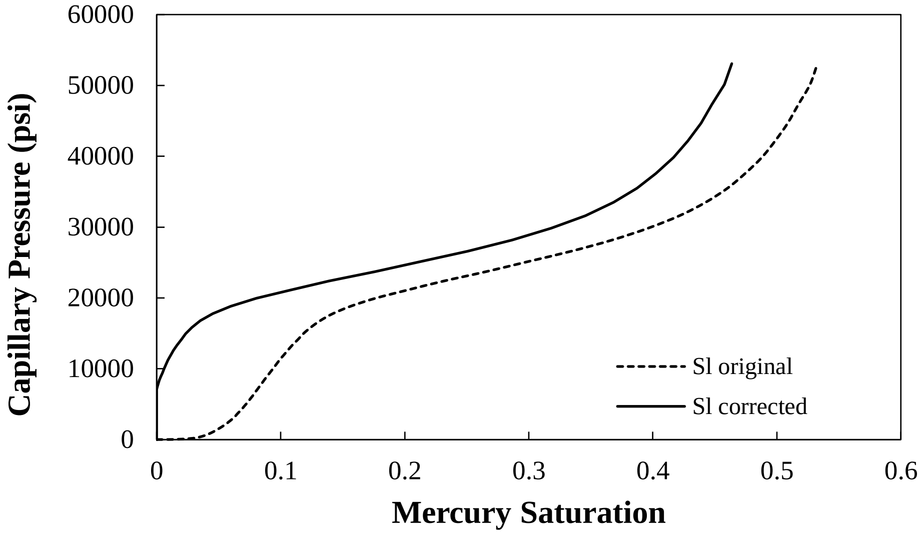

Figure 3.16 Original and corrected curves of mercury-intrusion capillary pressure vs. mercury saturation for Marcellus (top) and Wolfcamp (bottom) shale samples.

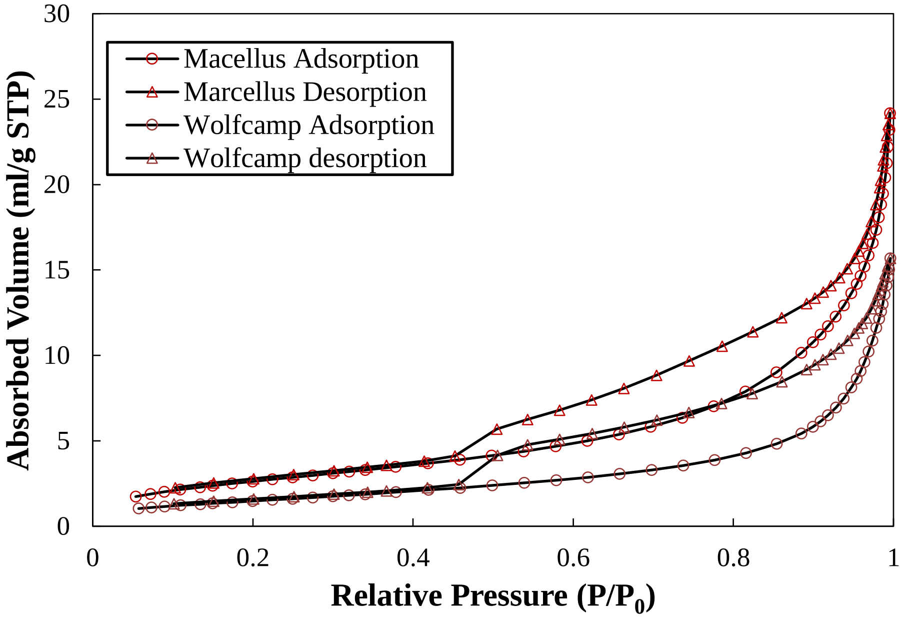

Figure 3.17 Nitrogen adsorption/desorption isotherm for shale samples from Marcellus and Wolfcamp formations.

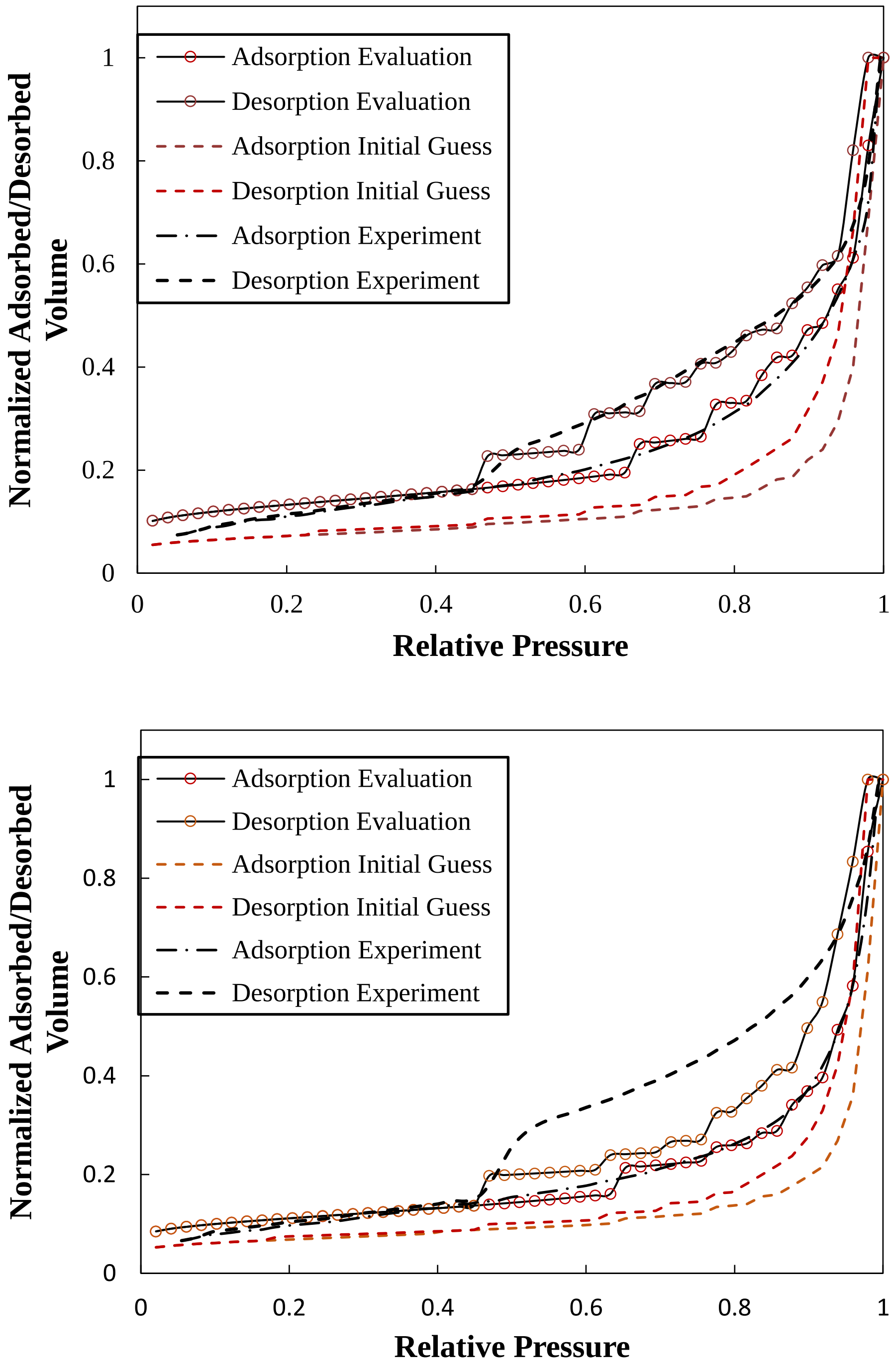

Figure 3.18 Simulated and measured adsorption/desorption isotherm for Marcellus (top) and Wolfcamp shales (bottom).

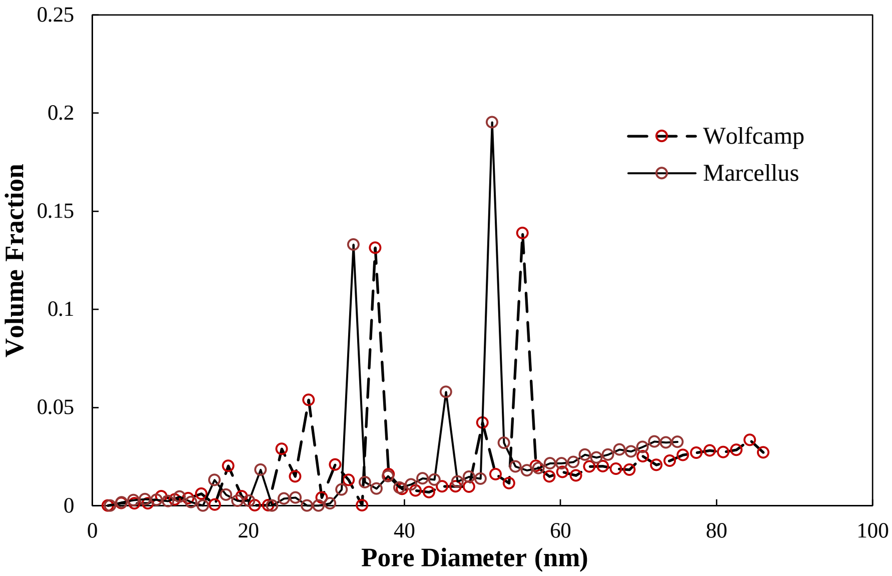

Figure 3.19 Pore-body size distributions of the shale samples from Marcellus and Wolfcamp formations characterized by isothermal adsorption/desorption measurement.

The dendroidal model is constructed at a scale factor of 10^{-9}, where the modeled sample is 10^{-9} times of the measured sample (2 cm^3). The static properties of a constructed dendroidal model are listed in table 3.2. Since the radii and lengths of the pores are distributed stochastically and fitted by experimental profiles, the distribution of the parameters of a dendroidal model is not unique. Therefore, the intrinsic permeability could be different for multiple realizations. However, the permeability difference of different dendroidal model realizations with respect to the same rock core sample is minute. The intrinsic permeabilities predicted from more than 600 realizations are shown in Figure 3.26.

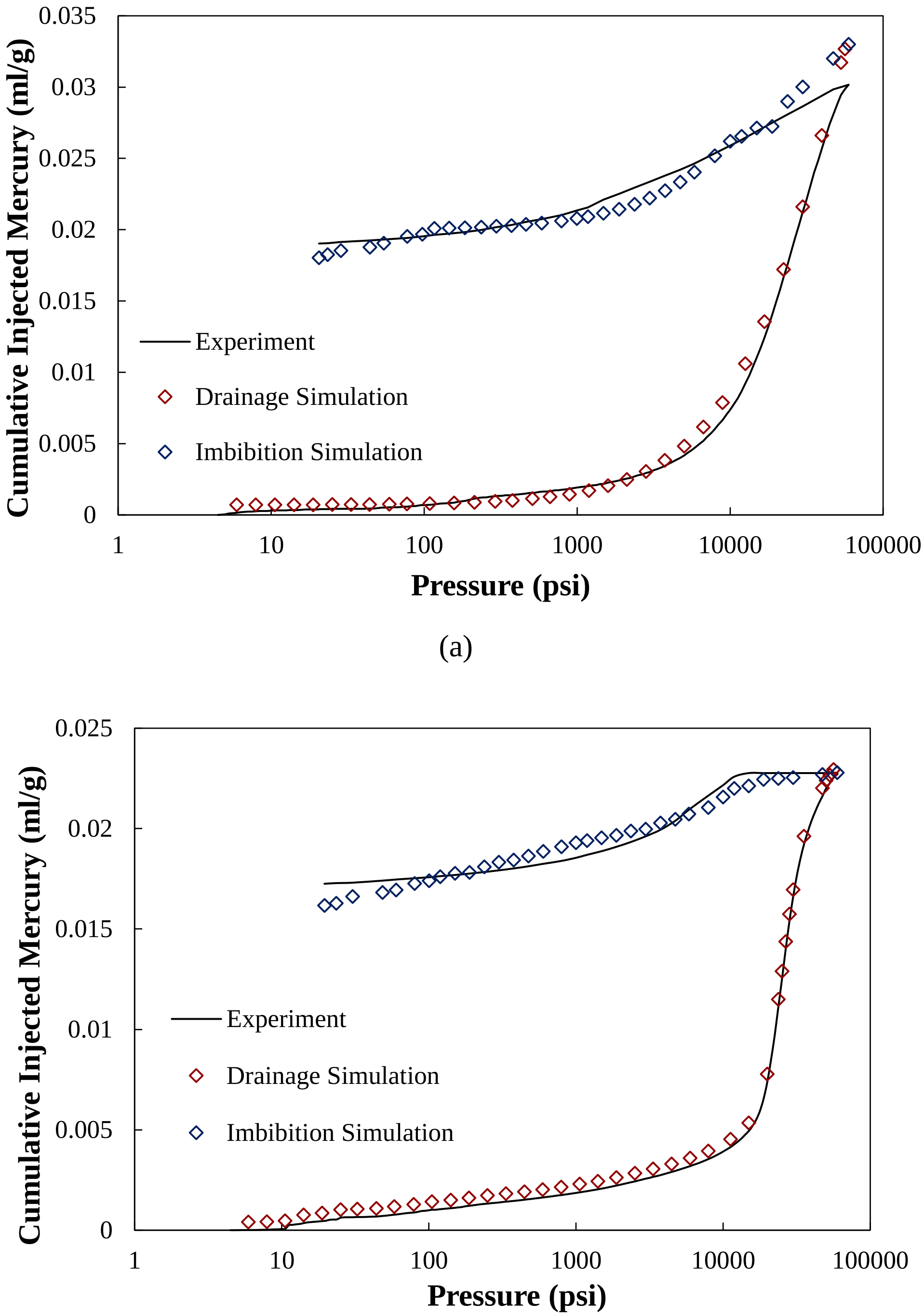

(a)

(b)

Figure 3.20 Measured and simulated mercury drainage and imbibition data for shale samples from (a) Marcellus and (b)Wolfcamp.

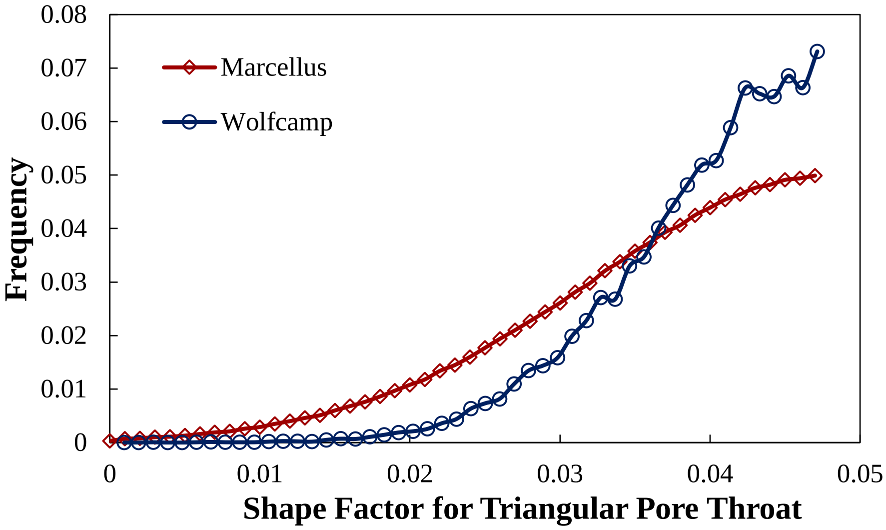

Figure 3.21 Frequency of the triangular pore-throat shape factor.

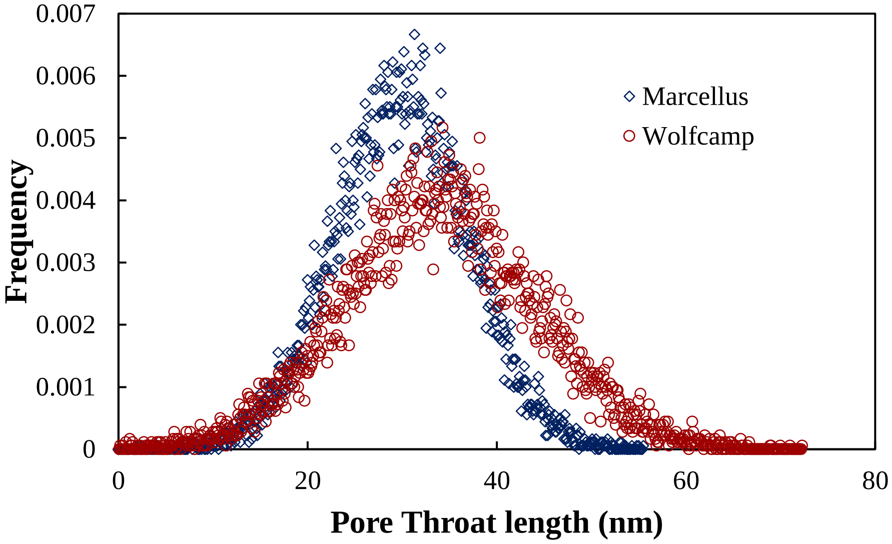

Figure 3.22 Frequency of the pore-throat lengths.

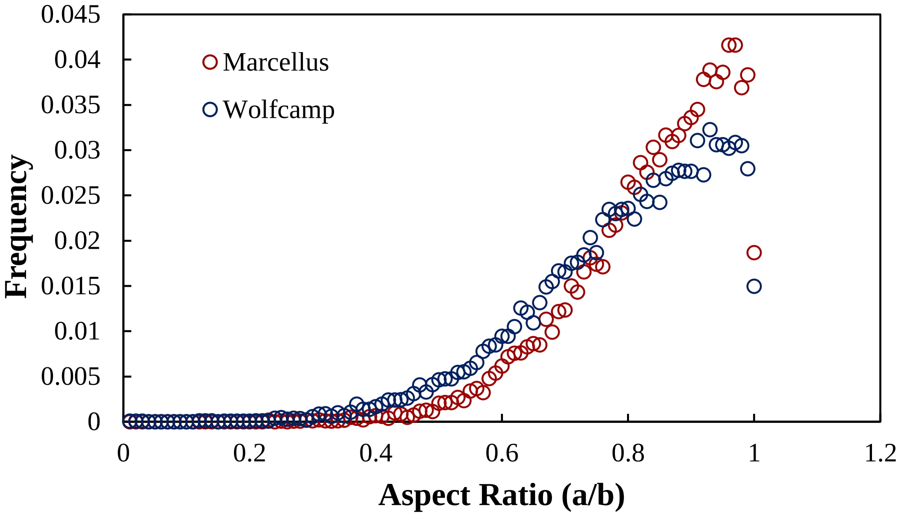

Figure 3.23 Frequency of the rectangular pore throat aspect ratio (a/b).

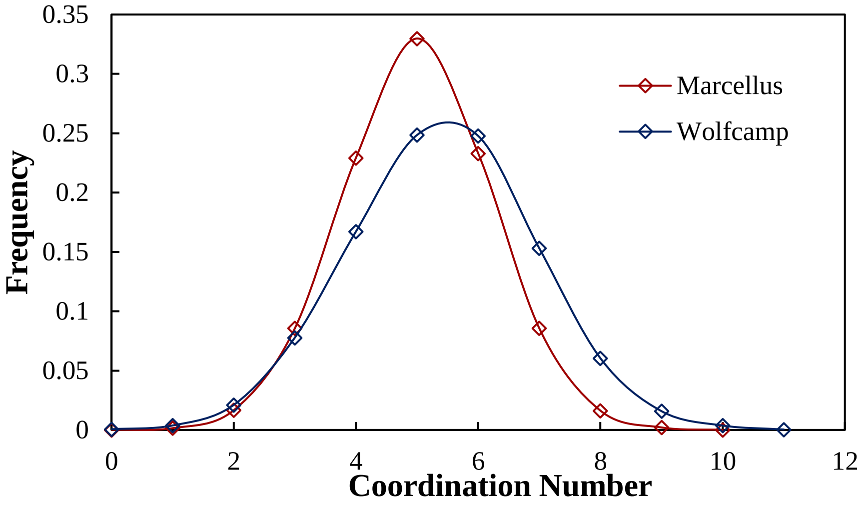

Figure 3.24 Frequency of the coordination number.

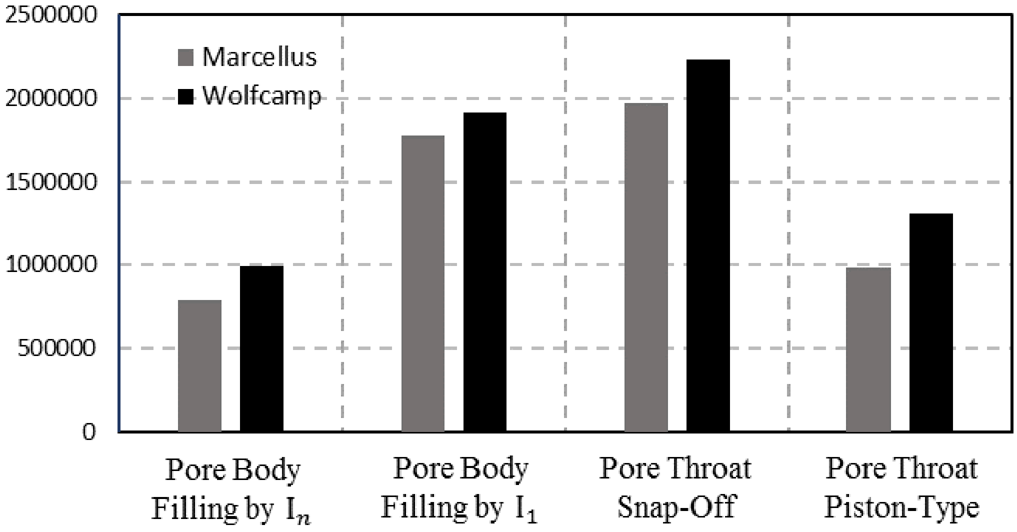

Figure 3.25 Frequency of the imbibition-events occurring during the simulation of mercury imbibition.

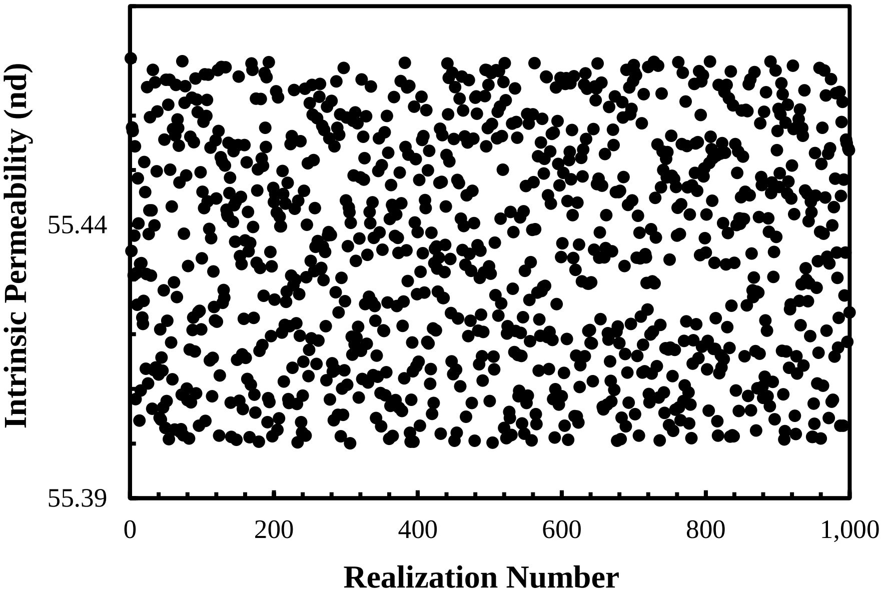

Figure 3.26 Intrinsic permeabilities of the Marcellus shale core sample calculated by the dendroidal model constructed with various spatial distribution of pores.

At first, the apparent permeability is calculated for the individual pores at a temperature of 343 K and pressure within the range of 200 psi to 5000 psi. Then, the apparent permeability of the entire system is calculated with various correlations, including Klinkenberg's slippage, Beskok-Karniadakis, Beskok-Karniadakis-Civan, Tang correlations, and Dusty Gas model (Figure 3.27). Because gas flow in this Marcellus sample falls into slip and transition flow regimes, which is identified by Knudsen number of each pore, the correction factor (f_c) predicted by the Klinkenberg's equation has a significant discrepancy with other correlations. It also indicates that Knudsen diffusion has a non-trivial effect on the total flux, since all the correction factors at various pressures are greater than 1. However, the Knudsen diffusion effect in not significant with pressure larger than 3000 psi, where the correction factor approaches 1.1.

In calculating the relative permeability, I assume the porous media is filled with oil (wetting phase) initially. With the capillary pressure increase, the relative permeability for each pressure incremental step is calculated. Figure 3.28 expresses the relative permeability changes with respect to different hydrocarbon saturation. In the waterflooding process, the network is assumed to be strongly oil-wet with a receding contact angle to be 0. Consequently, the relative permeability of both wetting phase and non-wetting phase are equal to 1 when the core sample is fully saturated by one fluid. The relative permeability of water starts to increase from zero at the water saturation equals to 0.3, because the porous media is filled with oil at first and the water initiate to flow across the entire dendroidal model at that specific saturation.

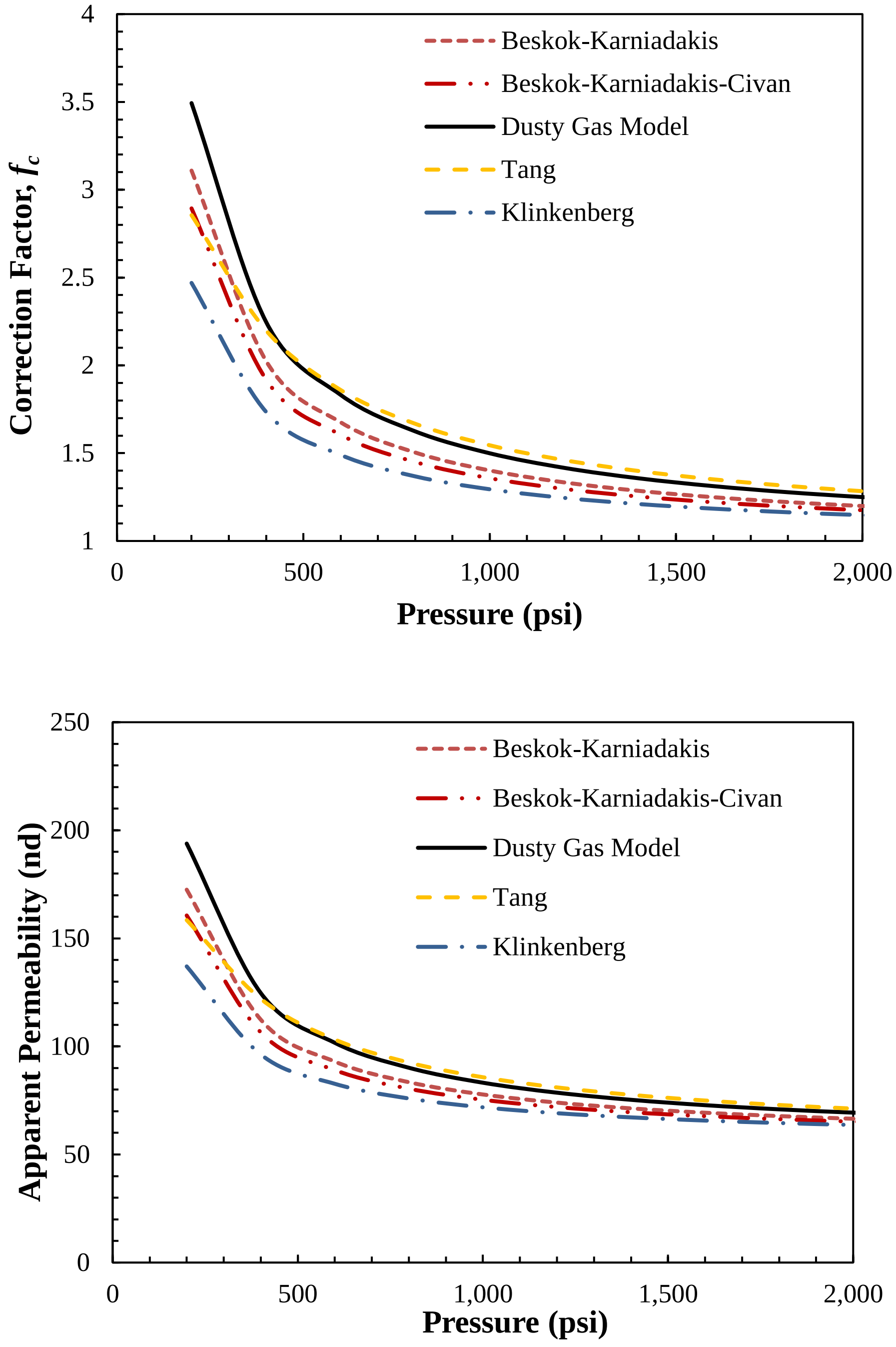

Figure 3.27 Correction factor and apparent permeability for Marcellus sample at various pressures predicted by the dendroidal model.

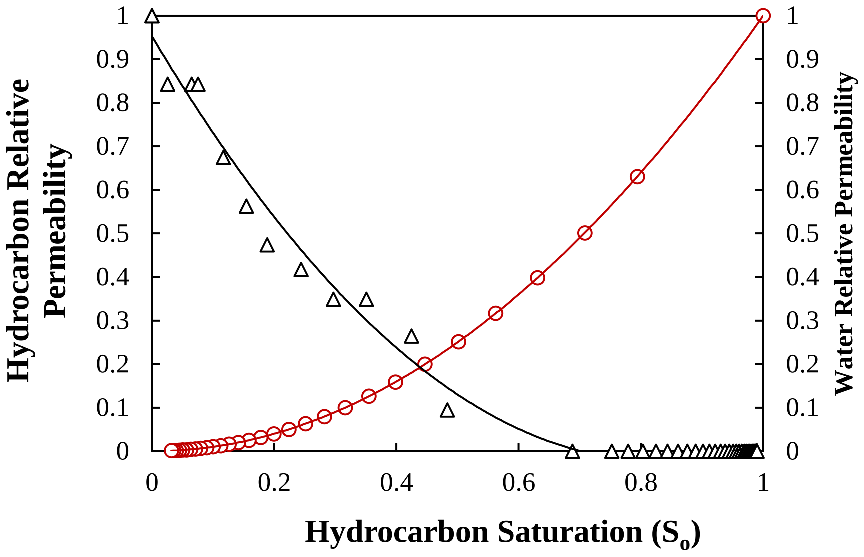

Figure 3.28 Relative permeability curve of the Marcellus shale sample predicted based on the dendroidal model.

3.8 Discussions

The traditional theoretical pore-network models developed for conventional reservoirs are not applicable for unconventional reservoirs, because they cannot capture the typical non-plateau shape of MICP curves. It indicates that they are not representative of the shale porous structure even though they can predict the intrinsic permeability. The semi-tree like model and tree-like model proposed by Sakhaee-pour (2012) for the first time successfully fit the non-plateau shape of shale MICP curves. However, the tree-like model and semi-tree like model deviate from the real void structure of shales for multiple reasons even though they can have a reasonable prediction of the intrinsic permeability. Thus, these models cannot represent the porous media and perform pore-scale simulations.

To implement the mercury drainage experiment to construct a theoretical pore-network model, the compressibility of shale core samples needs to be considered. However, the previous methods neglect the compressibility effect in the pore-network model construction. During the mercury drainage experiments, the intrusion capillary pressure can be as high as 60,000 psi, which causes the core sample to compress considerably. The core samples experience the phase of conformance, compression and intrusion. It has been shown that the invaded mercury volume can vary as much as 10% because of the compressibility effect. Unlike other theoretical pore-network models, the new proposed dendroidal model considers the compressibility effect using the dual-compressibility model, which makes the pore-network model more representative of the pore structure of shale core samples.

I interpret the topology of the SEM images extracted from shale core samples and develop the novel dendroidal model. In the SEM images and directly-extracted pore-network models, there are multiple main flow paths with large pore-throat radii and dead-end branching pores with smaller radii. The acyclic model is too simplified to reflect the pore spatial distribution. Maintaining the interaction among different main flow paths without sacrificing the limited connectivity of pores, I propose the dendroidal model.

In the tree-like model and semi-tree like model, all the pores are represented by straight tubes without distinguishing the pore bodies and pore throats. In the dendroidal model, I use the isothermal adsorption/desorption measurement (IADM) to characterize the pore-body size distribution. The differentiation of pore bodies and pore throats is important in simulating both mercury drainage and imbibition process. During mercury drainage experiments, pore throats restrict the mercury from injected into the porous media; while the pore bodies contribute most to the storing capacity of the void space. Therefore, the mercury saturation change with respect to each incremental step of capillary pressure is influenced by both pore bodies and pore throats. In the mercury imbibition process, the pore bodies are the restriction of mercury from being extracted from the void space. The pore throats and pore bodies perform different functions in the mercury drainage and imbibition experiments, so a theoretical pore-network model cannot be used to simulate these experiments without distinguishing the pore bodies and pore throats.

The cross-sectional geometry of pore throats is also important in constructing a pore-network model. In simulating the mercury drainage/imbibition process based on theoretical pore-network models, the trapping effect and snap-off mechanism cannot be captured without angular pore throats. Some of the previous models (lattice model, tree-like model and bundle-of-tube mode) use circular tube to represent the pore, therefore, these models cannot capture the trapping effect. From another perspective, it indicates that these previous models do not have good representative of the real porous media of rock core samples.

In the dendroidal model, the TOC is implemented to classify the organic and inorganic pores. I also use the FTIR measurement to determine the minerology of core samples and then classify the inorganic pores into different compositions. The previous theoretical pore-network models neglect the composition of pores. It will render different results of transport-properties prediction, because the fluid in organic and inorganic pores will have different chemical and physical effects. Even for the inorganic pores with different compositions, the gas-adsorption capacities are different. The dendroidal model can provide a more accurate prediction of apparent permeability with classifying the void space into different compositions.

Chapter 4 Extracted Pore-Network Model for Shales Characterizing Geometry of Void Space

In this chapter, I propose a new algorithm, based on the maximal-ball algorithm, to perform the extracted pore-network modeling for shale formations. The new algorithm can capture the unique features of shales, including nano-scaled pores and limited connectivity. Meanwhile, the novel algorithm can characterize the complex geometry of both pore bodies and throats. The connections between two adjacent pore bodies could be complex for some situations, but the extracted pore-network models implement simple straight tubes to represent the pore throats. To compensate the lack of representativeness of the simplified pore throats, this algorithm evaluates the size of pore throat to ensure an equivalent flow capacity.

4.1 Skeleton Characterization

The maximum inscribed sphere (MIS) is the core component in constructing the extracted pore-network model in this novel algorithm, and it is used to classify the pore bodies and throats and characterize the pore geometry. Since shale formations have limited connectivity and extremely small pores, a different algorithm is developed to determine the radius of MIS.

A Scanning Electron Microscope (SEM) image is composed of discrete 2D pixels which have a high resolution to capture the microstructure of hydrocarbon-bearing rocks. Then I use a statistical model to generate the synthetic 3D structures that capture the properties of 2D thin sections. The first step of the algorithm is to determine the MIS centered at each individual voxel. For each voxel, the seeking procedure starts from the voxel itself and add one unit-voxel-layer in each incremental step (Figure 4.1), and it stops once touching any matrix voxels. The MIS defined in this algorithm is the sphere that does not contain any matrix voxels.

The radius defined for a single voxel is indicated in Figure 4.2, which is different from the previous algorithms (Silin et al. 2006; Dong et al. 2009). The radius definition in the novel algorithm is designed to capture the unique characteristic of shales. The radii of the MIS with different sizes are defined in the same manner, which is from the center to the corner of the outermost voxel; the justification for this radius definition will be explained in the ensuing construction procedures. Additionally, the MIS-radius-determination algorithm based on the definition of "radius range" proposed by Dong (2009) is simplified in this method without losing any accuracy. All the voxel objects containing coordinates and the radius of MIS are stored in a list sorted by their coordinates, because it will be time-saving for the following procedures, like the procedure of redundant-MIS deletion.

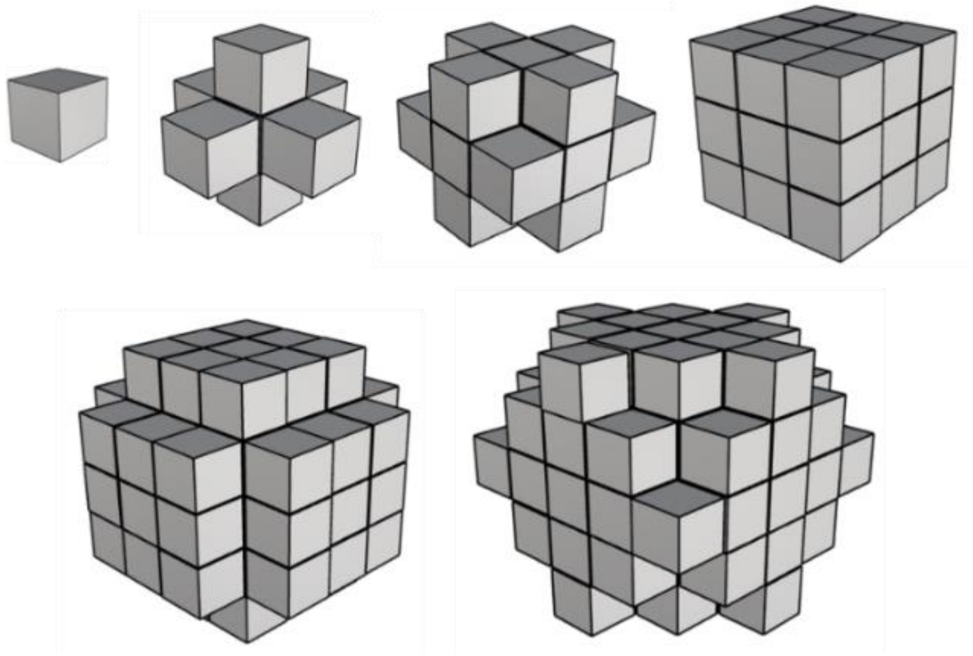

Figure 4.1 Schematic of the MIS seeking procedure which starts from a voxel itself.

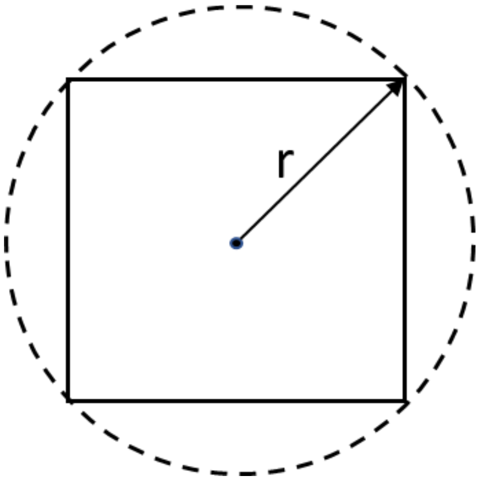

Figure 4.2 Radius definition of an MIS composed of a single voxel.

After the MIS seeking procedures are executed for all the voxels, the radius of each MIS is assigned to the corresponding center voxel. Some of the MIS could be fully nested within others, where all the voxels are repetitive. This type of nested MIS without carrying any additional information about the skeleton of the porous media is redundant. The removal of the redundant MIS with repetitive voxels is the second procedure. As a convention, $C_1(x_1, y_1, z_1)$ and $C_2(x_2, y_2, z_2)$ represent the coordinates of the center of MIS. The redundant MIS is identified by

$$(x_1 - x_2)^2 + (y_1 - y_2)^2 + (z_1 - z_2)^2 \leq max[R_1, R_2]. \tag{4.1}$$

It removes the MIS with smaller radius and the corresponding voxel object as well. Since the remaining voxel objects are still sorted by their coordinates, a large three-dimensional reconstructed model can be subdivided into smaller parts, in which the pore-network model extraction can be performed separately and then merged together. For the three-dimensional reconstructed model of shales containing the information of thousands of SEM images without pre-possessing, it will be intensely time-consuming to extract pore-network models. Thus, subdividing the reconstructed model and removing redundant MIS using parallel computing platform can mitigate the computational burden.

4.2 Classification of Pore Bodies and Pore Throats

Because the microstructure of void space within porous media is complex, it is difficult to propose a standard criterion of pore-type classification for different types of rock and different purposes. Many researchers have investigated this issue and explained their understanding of pore-classification (Dong et al. 2009; Silin et al. 2006). Different purposes require different definitions of pore bodies and throats. In this study, the algorithm constructs a pore-network model highly representative of shale core samples, with which mathematical simulations can be performed without prohibitively intense computation. This model can predict the key parameters like permeabilities and residual hydrocarbon saturation. In this extracted pore-network modeling, the main function of pore body is to provide the storage volume for hydrocarbon and water, while the pore throats are regarded as the determinant of flow capacities. Because of the size-difference of pore bodies and pore throats, the exclusion of pore bodies has negligible influence in the flow capacity. However, the trapping capacity of both pore body and throat is important to consider, because the volume of trapping fluid will significantly influence the relative permeability and ultimate residual saturation. With the definitive functions of pore body and throat, the classification algorithm can be adjusted to fulfill these requirements.

The algorithm developed in this work is to extract the pore-network model for shale core samples. The algorithm may not be suitable for other formation types as the corresponding verifications have not been performed. Some of the ideas implemented in the novel pore-network extraction algorithm are enlightened by Dong's method (2009), but the novel algorithm is designed to exclusively characterize the features of tight formations, including the extremely small pores and limited connectivity. With the voxel objects sorted by their coordinates, I construct another list of voxel object sorted by the size of MIS from large to small. The voxel objects with the largest MIS are regarded as the ancestors and denominated with different numbers, like "Ancestor 1" (Figure 4.3(a)). The MIS overlapping the ancestors are denominated with the same number and are regarded as the first generation. The two ancestors of the same size overlapping each other are both regarded as the same ancestor (Figure 4.3(b)).

Subsequently, I locate the MIS with the second largest radius in the entire system. If they do not overlap any MIS having or being ancestors, they will be defined as the ancestor themselves with different names from the ancestors assigned before ("Ancestor 23" for instance) (Figure 4.4(a)). If they have already been assigned as an offspring of some ancestor, no additional process needs to be performed (Figure 4.3(a)). If they are connected to some MIS with the same size or a bigger size which has already been assigned an ancestor, the specific MIS will be assigned as one more generation of that ancestor (Figure 4.4(b)). The similar algorithm of assigning ancestors and generations is implemented until the smallest MIS is reached. If one MIS overlaps two other MIS from different ancestors, that MIS will be regarded as the common offspring of the two ancestors. The pore throat is defined based on the common offspring (Figure 4.5). The detailed procedures of identifying pore throats and pore bodies will be explained subsequently.

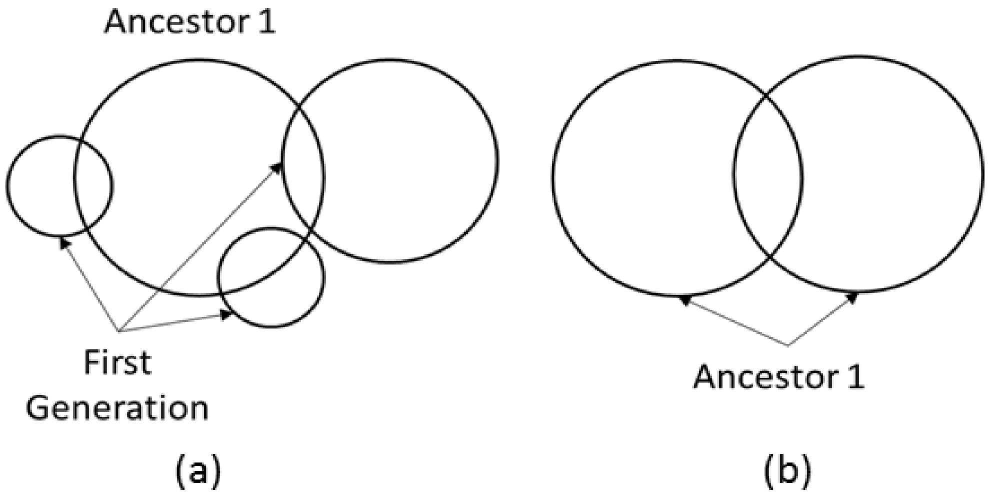

Figure 4.3 The largest MIS is located and assigned an as an ancestor. (a) Ancestor 1 has overlapping MIS with smaller radius, including the MIS with second-largest radius. (b) Ancestor 1 has an overlapping MIS with the same radius.

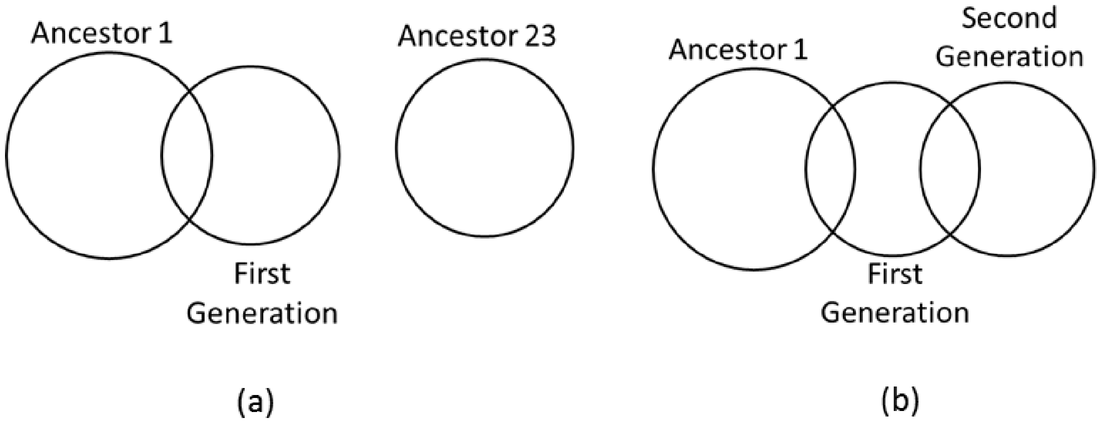

Figure 4.4 Schematic of locating the second-largest MIS. (a) The second-largest MIS without overlapping any ancestors is assigned as a new ancestor ("Ancestor 23"). (b) the second-largest MIS overlaps an ancestor ("Ancestor 1"), and it is regarded as the first generation of the ancestor. Another second-largest MIS overlapping the first generation is regarded as the second generation.

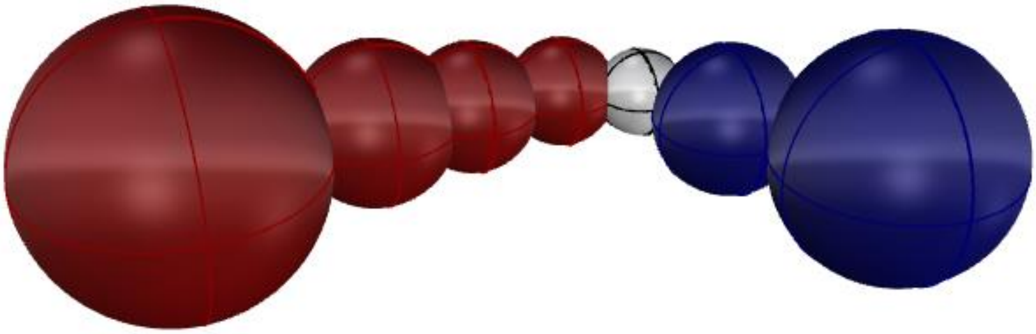

Figure 4.5 Schematic of two series of MIS belonging to two different ancestors, where red and blue balls represent ancestor or generations inheriting two different ancestors. The gray ball represents the common offspring.

Now, all the MIS are clustered into different groups with different ancestors, with which pore bodies and pore throats are classified. The general connection scenario of two series of MIS is shown in Figure 4.6, where all the MIS shown in this figure belong to two groups of different ancestors. The one-MIS-path will be used to identify the pore throat, while the ancestor and the corresponding overlapping MIS will be used to define the pore body. The pore throat in this connection is tortuous and complex, but it is represented by a straight tube with a constant cross section in the extracted pore-network model. This new algorithm calculates an equivalent radius of the pore throat to mitigate the discrepancy, which will be explained in the ensuing section.

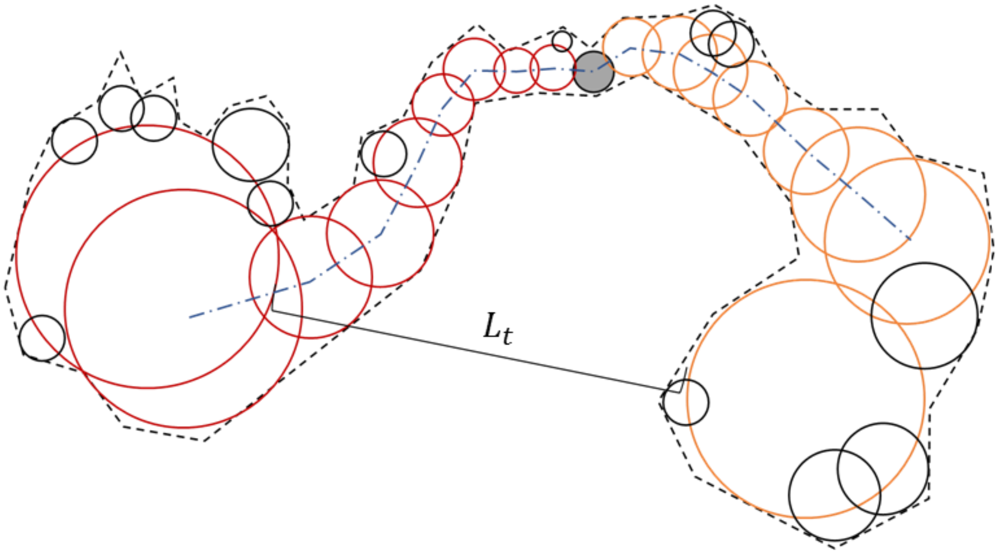

Figure 4.6 Schematic of two groups of MIS with different ancestor, where black dashed lines of the contour represent the real void space in porous media. The gray circle is the common offspring of the two MIS groups. The red and yellow circles represent the one-MIS-path between the common offspring and each ancestor. The black circles are the overlapping MIS of each group, and they also carry information about morphology of void space. The blue dashed line connecting one-MIS-path represent the true throat length, and L_t represents the Euclidean distant between the two ancestors.

Since the overlapping MIS can capture the geometry and volume of void space, they will be used to define the pore body as well. Consequently, the volume of the pore body is the summation of the volume of the ancestor and the extra volume of the overlapping MIS (Figure 4.7). The center of the pore body is the geometric center of the voxel assemblage. With defining the MIS radius (Euclidean distance from center to the corner of the outermost voxel (Figure 4.2)) and pore body (Figure 4.7) by the novel algorithm, the extremely small pores can be captured. The pore size can be extremely small in shale porous media (nanometer scale), where some pore only composed by several voxels (Figure 4.8). Sometimes the voxels composing a pore cannot construct a complete maximum inscribed sphere. However, the information of void space can be captured by considering the volume of the voxels themselves in this new algorithm (Figure 4.9).

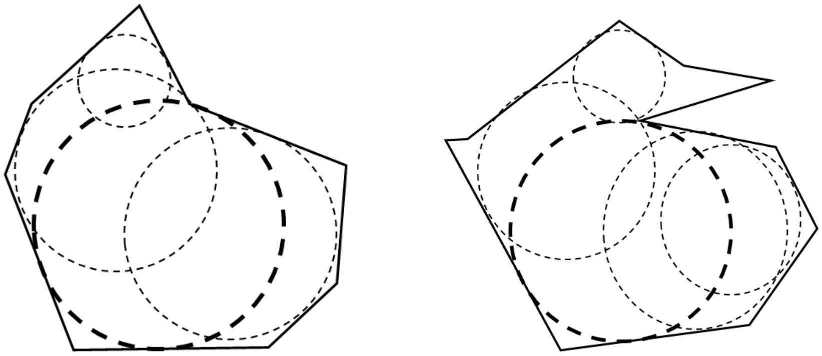

Figure 4.7 The schematic of pore body size definition, where the solid line represents the geometry of real void space. The thick-dashed-line circles represent the ancestor MIS, and the narrow-dashed-line circles represent the overlapping MIS containing morphological information about void space.

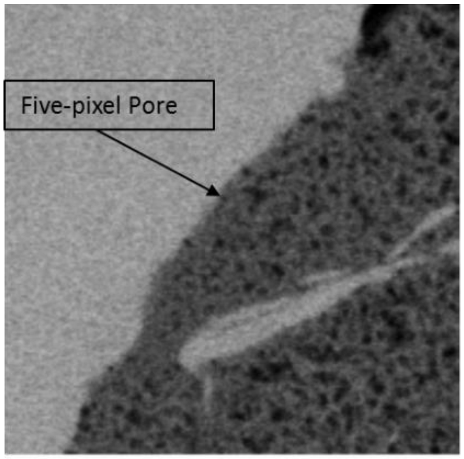

Figure 4.8 A Scanning Electron Microscope image with the resolution of 4 nm. A pore composed by 5 pixels is indicated in the image.

Pore throats are classified by the one-MIS-path connecting the common offspring and its ancestors, starting from the first generation. Even though the first-generation MIS sometimes could be large compared with other MIS in the entire system, it has the function of limiting fluid flow between this pair of pore bodies due to its size difference compared with its own ancestor.

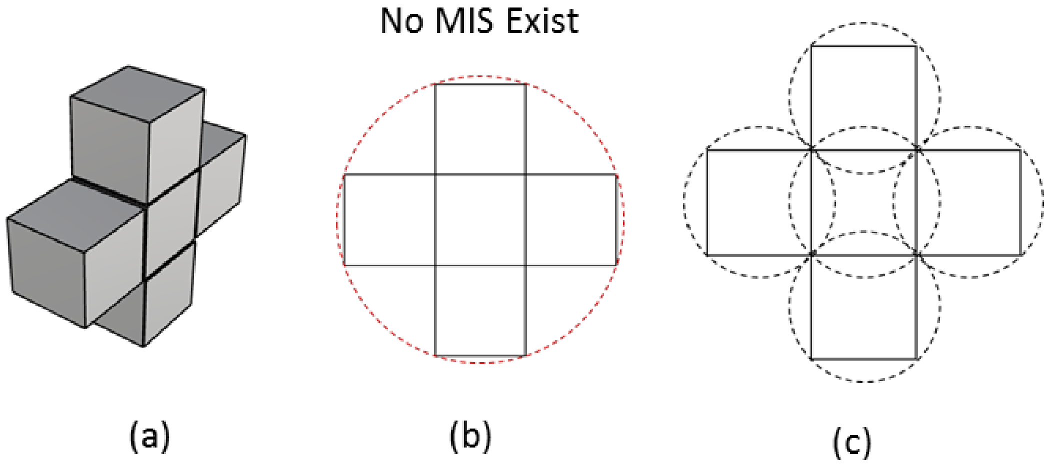

Figure 4.9 (a) A pore body represented by 5 voxels in the 3D reconstructed model. (b) The MIS cannot be determined in this manner because the voxels cannot form a full sphere. (c) The pore body can be captured with this new algorithm in this manner.

4.3 Pore Shape Characterization

The geometry of the pore throat and body is essential to be considered to characterize the flow capacity and trapping capacity of fluid in the porous media. The pore-throat geometry is determined by the matrix voxels surrounding the one-MIS-path, because MIS itself may lose some morphological information, especially for the angular pore throats.

Perpendicular to the direction of the straight line connecting adjacent centers of the first-generation MIS and the second-generation MIS, two cross sections are made at the center voxels of the first generations of each ancestor (Figure 4.10). The one-layer matrix voxels surrounding the void space between every two cross sections are captured to characterize the pore-throat geometry. The pore bodies, represented by the ancestor and the associated overlapping MIS, cannot be characterized by cross sections, because the uncertainty in determining the cross-section direction cannot be eliminated.

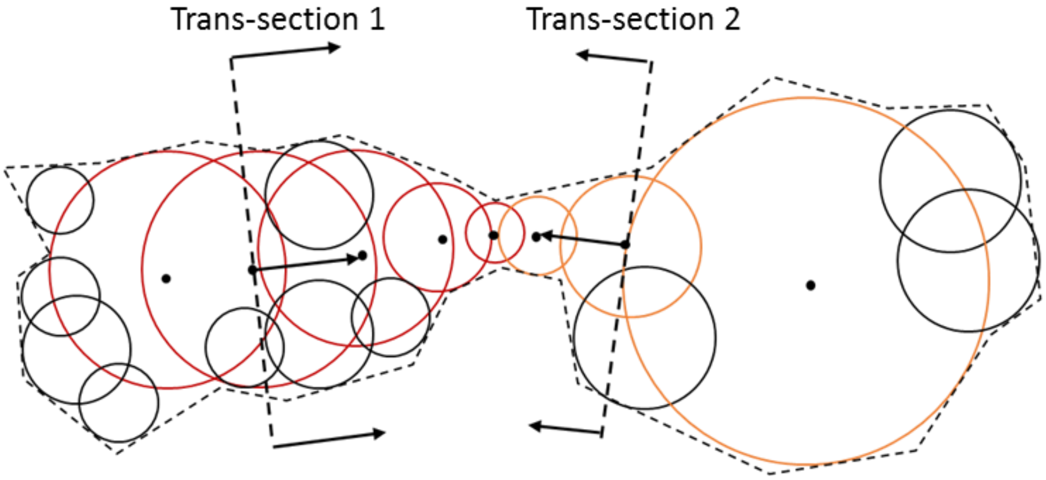

Figure 4.10 Schematic of pore-throat morphology characterization. Trans-section 1 and trans-section 2 are two cross sections of the pore throat, and their directions are indicated by the black arrows.

The pore-throat geometry is captured by analyzing the one-MIS-path and the surrounding matrix voxels, but the area and volume may be overestimated or underestimated because of their discrete and irregular shapes. There are several schemes to estimate the area and volume of the voxels (Figure 4.11), where I use 2D to represent 3D as the mechanisms are same. As described by Jiang (2007), the scheme in Figure 4.11(a) and Figure 4.11(d) underestimates the volume, and the schematic in Figure 4.11(b) overestimates the volume. The schematic in Figure 4.11(c), which is estimated by a second-order polynomial, preserves the volume well and smoothens the boundary, and it can provide a reasonable estimation of the volume and area. For the pore bodies, the area and volume can be estimated in an equivalent manner as shown in Figure 4.12.

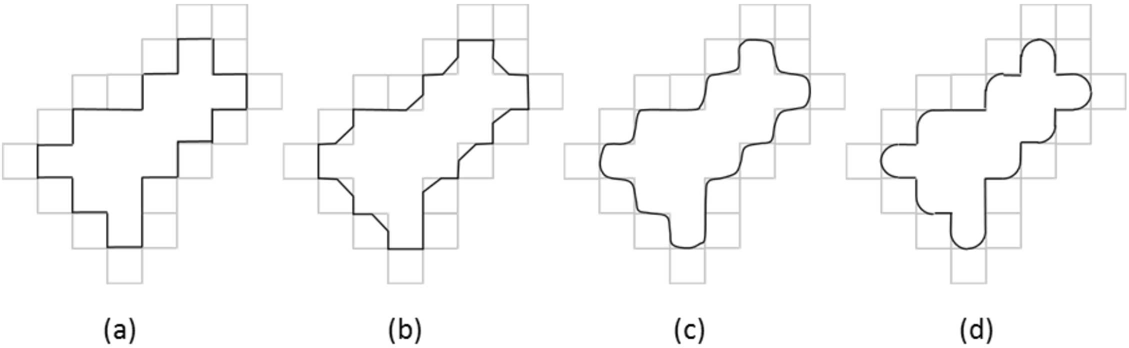

Figure 4.11 Comparison of the possible schemes of pore-throat volume and area estimation with its surrounded matrix voxels. These schemes are described in 2D, since their mechanism is same as 3D.

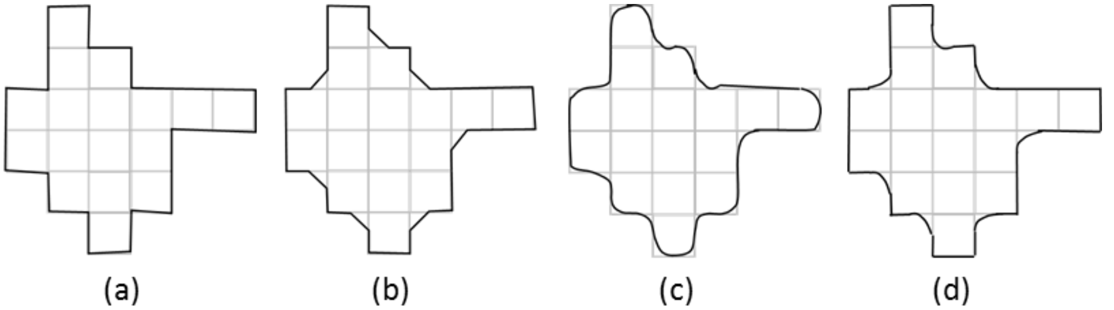

Figure 4.12 Comparison of the possible schemes of pore-body volume and area estimation with its surrounded matrix voxels. These schemes are described in 2D, since their mechanism is same as 3D.

The shape of pore body and throat is characterized by the dimensionless shape factor ($\boldsymbol{G}$),

$$G = \frac{VL}{A^2} \tag{4.2}$$

where V is the volume and A is the surface area. For the pore throats, L is the Euclidean distance between the center voxels of the first-generation MIS of the two ancestors (Figure 4.6); while for the pore bodies, L is longitudinal side of the pore-body voxel assemblage.

4.4 Pore Size Determination

The extracted pore-network model uses balls to represent pore bodies and tubes to represent pore throats. Since there is no angular pore in the extracted pore-network model, the trapping effect happening within the crannies and nooks cannot be captured. However, the trapping influence can be evaluated by using the dimensionless shape factor in mathematical simulations. Therefore, the emphasis is to preserve transport properties in determining the pore-throat size; while the hydrocarbon storing capacity needs to be preserved in determining the pore-body size.

In the extracted pore-network model, the pore-body position is determined by the geometric center of the voxel assemblage, which is composed by the ancestor MIS and the associated overlapping MIS exclusive of the first-generation offspring (Figure 4.7). The pore-body size is determined by the summation of all these voxel volumes. The pore throat length is calculated by

$$L_t = \sqrt{(x_1 - x_2)^2 + (y_1 - y_2)^2 + (z_1 - z_2)^2} - R_1 - R_2 \tag{4.3}$$

where $C_1(x_1, y_1, z_1)$ and $C_2(x_2, y_2, z_2)$ are the center of the two ancestor MIS, and R_1 and R_2 are the radius of two ancestor MIS. But the real length of pore-throat channel in porous media is the length of one-MIS-path (L_r) which is shown in dashed blue line in Figure 4.6.

Here, the tortuosity (L_r/L_t) of each pore throat needs to be considered to adjust the cross-sectional area of the pore throat to maintain the same flow capacity.

To determine the pore-throat radius, I first calculate the cross-sectional area across the center of each MIS within the one-MIS-path in the direction tangent to the connected straight line of adjacent MIS centers (Figure 4.13). The fluid flow rate at each cross section is expressed as

$$q = \frac{k_1 A_1}{\mu}\frac{\Delta p_1}{L_1} = \frac{k_2 A_2}{\mu}\frac{\Delta p_2}{L_2} = \cdots\cdots = \frac{k_n A_n}{\mu}\frac{\Delta p_n}{L_n} \tag{4.4}$$

where k and A are the permeability and area of each cross section, L is the length corresponding to half of the distance between the adjacent MIS centers, and n represents the total number of cross sections. Since the pore throats in the extracted pore-network model are represented by circular tubes, the permeability of each section is calculated by

$$k = \frac{r^2}{8} = \frac{A}{8\pi} \tag{4.5}$$

For the entire pore throat,

$$\frac{L_t}{A_t^2} = \frac{L_1}{A_1^2} + \frac{L_2}{A_2^2} + \cdots + \frac{L_n}{A_n^2} \tag{4.6}$$

where L_t is the pore-throat length and A_t is the pore-throat area. With the area formula of a circle, the pore-throat radius can be calculated.

In the pore-network reconstructions, some of the adjacent two pore bodies are connected by two flow paths, which in the MIS skeleton are characterized by two common offspring of the two ancestors (Figure 4.14). Thus, the algorithm of pore-throat size determination needs to be adjusted. The radius of pore throat (R) can be calculated by

$$R^4 = \frac{L_t}{\pi^2}\left(\frac{L_{11}}{A_{11}^2} + \frac{L_{12}}{A_{12}^2} + \cdots + \frac{L_{1n}}{A_{1n}^2} + \frac{L_{21}}{A_{21}^2} + \frac{L_{22}}{A_{22}^2} + \cdots + \frac{L_{2n}}{A_{2n}^2}\right)^{-1} \tag{4.7}$$

where A_{ij} and L_{ij} are the area and length of the ith flow path and jth segment.

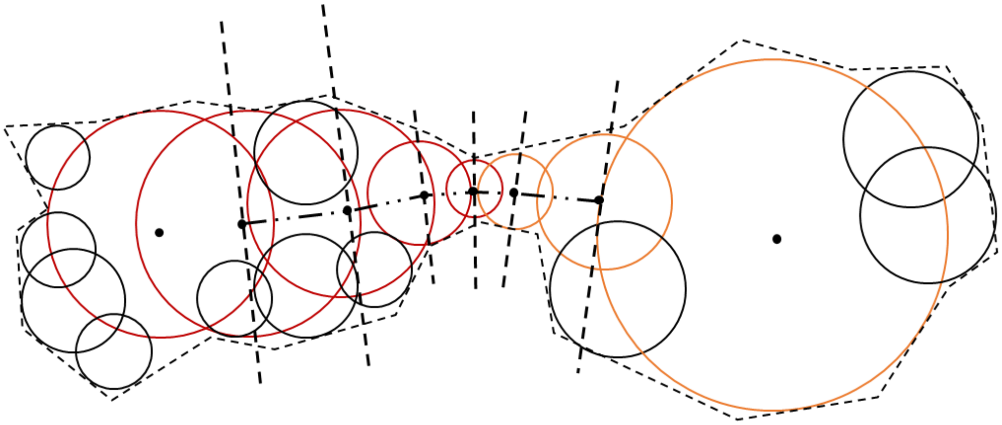

Figure 4.13 Schematic of the cross sections across each MIS center within one-MIS-path. The cross sections are used for pore-throat size determination.

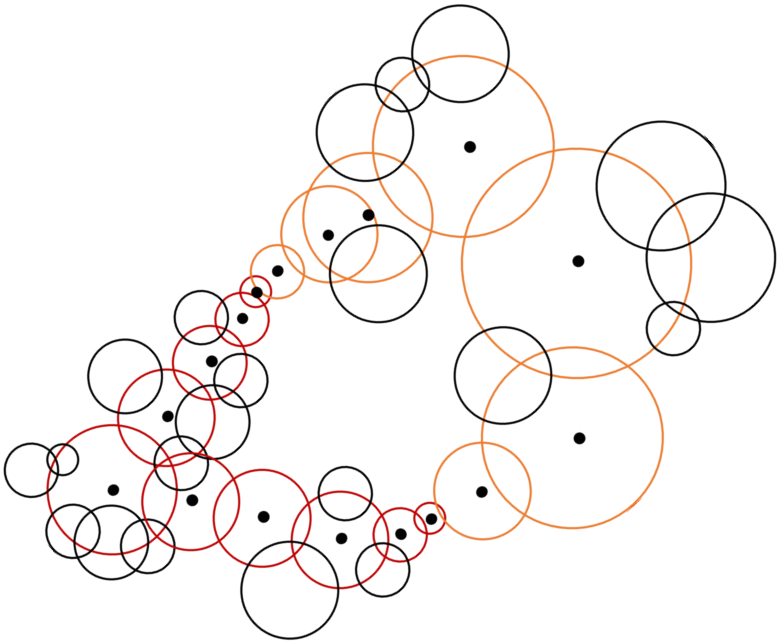

Figure 4.14 Schematic of two ancestors connected by two common offspring, where the red and yellow circles represent the one-MIS-path and the black circles are the overlapping MIS belongs to these two ancestors.

For another special situation shown in Figure 4.15, there is only one common offspring of the two ancestors, but there are two flow paths connecting one ancestor and its offspring. To ensure the equivalent flow capacity of this simplified pore throat in the extracted pore-network model, the radius of the pore throat can be calculated by combining Eq. 4.6 and Eq. 4.5. For all the other types of complex connections between adjacent pore bodies, the similar method can be implemented to determine the pore-throat radius to maintain the flow capacity.

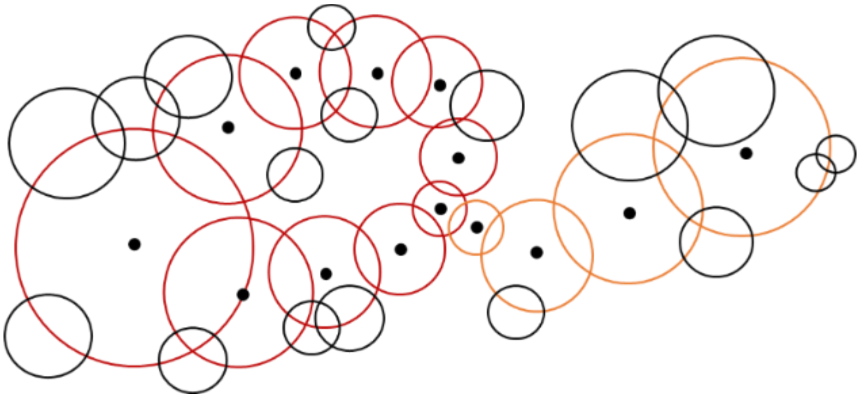

Figure 4.15 Schematic of two ancestors connected by one common offspring, but there are two paths connecting to this offspring from one ancestor. The red and yellow circles represent the one-MIS-path and the black circles are the overlapping MIS.

4.5 Case Study

The SEM images of Marcellus shale core samples are used to build the reconstructed 3D pore-scale model (Figure 4.17). The dimension of the Marcellus shale core sample is 15000 × 6144 × 5304 (nm), and the resolution of the scanning images is 4 nm. For this 3D reconstruction of the Marcellus core sample, I pick four subsections to extract the pore-network model using this novel algorithm. Based on the extracted pore-network model, I analyze the properties, including pore-size distribution, coordination-number distribution, and pore-throat length distribution. Figure 4.16 shows the SEM images of the top surface of those four investigated subsections with a dimension of

$900 \times 600 \times 300$ (nm). In this study, the compositions (organic or inorganic matter) of pores are not distinguished, where the voxels are binarized by only distinguishing the void space and matrix.

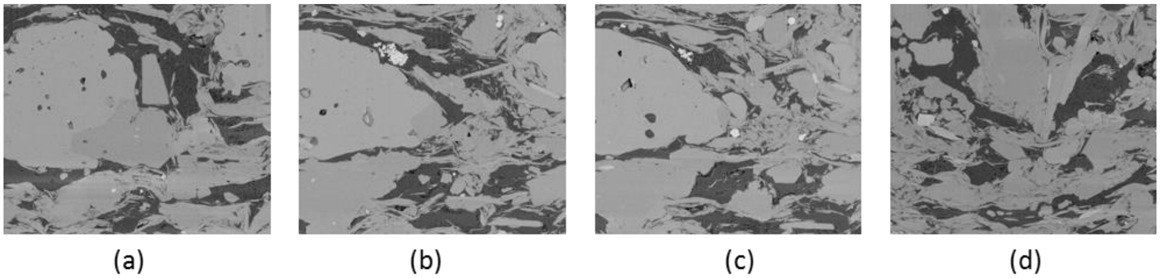

Figure 4.16 Top-surface SEM images of the four subsections of reconstructed pore-scale model.

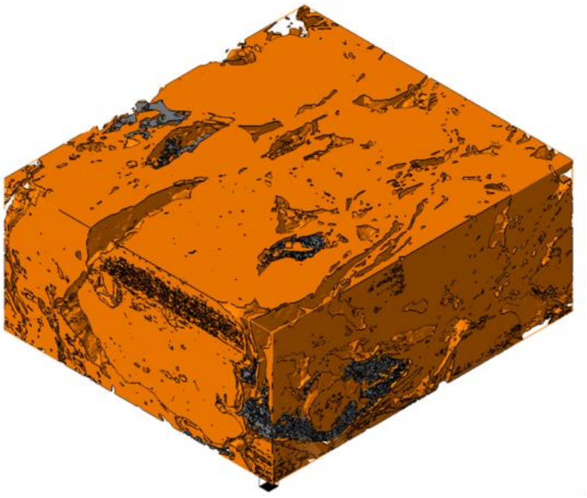

Figure 4.17 The three-dimensional pore-scale model reconstructed using SEM images with the resolution of 4 nm, where gray part represents organic matter and yellow part represents inorganic matter.

4.6 Results and Analysis

Following the algorithm developed in this work, the 3D pore-network models for the four subsections of the Marcellus shale core sample are shown in Figure 4.18. Figure 4.19 is the amplified view of a part of the subsection in Figure 4.16(a). The spatial distribution of pore bodies and pore throats are summarized, and the corresponding statistical properties are compared and analyzed.

Table 4.1 Statistics of pore body and pore throat of the four subsections from the Marcellus shale core sample.

	Marcellus 01	**Marcellus 02**	**Marcellus 03**	**Marcellus 04**
Number of Pore Bodies	23,141	33,180	22,161	27,124
Number of Pore Throats	2,741	6,520	30,738	7,138
Number of Isolated Pore	21,794	30,639	14,900	24,241
Number of Connected Pore	1,347	2,541	7,261	2,883

The number of pore bodies and pore throats in the extracted pore-network model is expressed in Table 4.1, where the isolated pores and connected pores are tabulated. From statistics, it can tell that most of the pores in Marcellus shale core sample are isolated, which is satisfied with the visual identification.

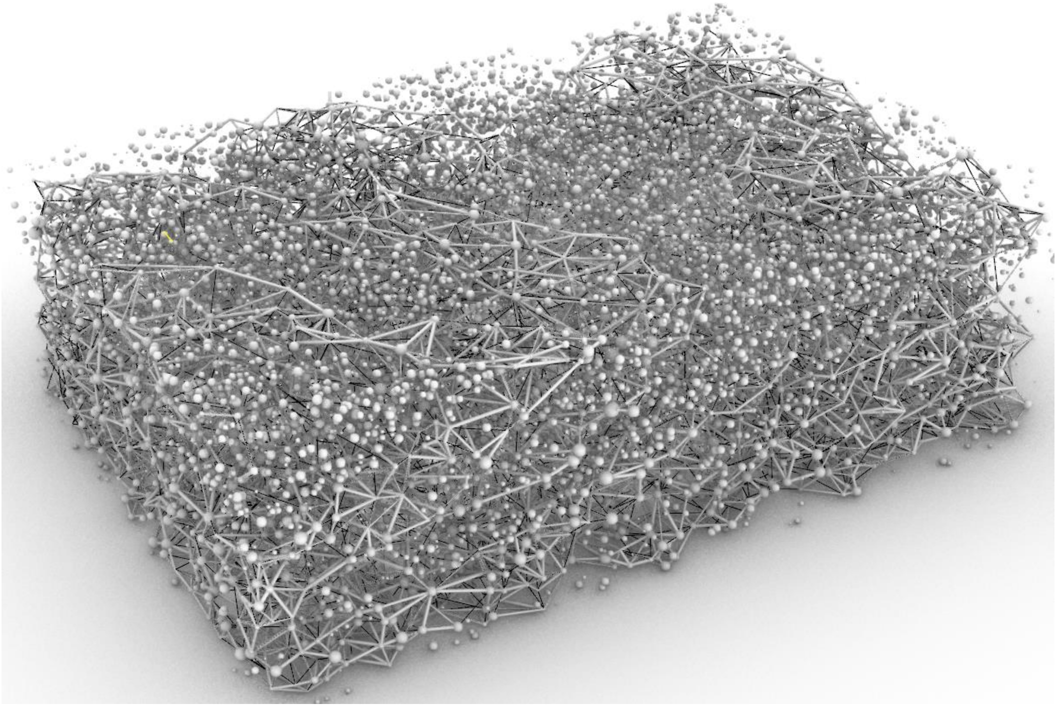

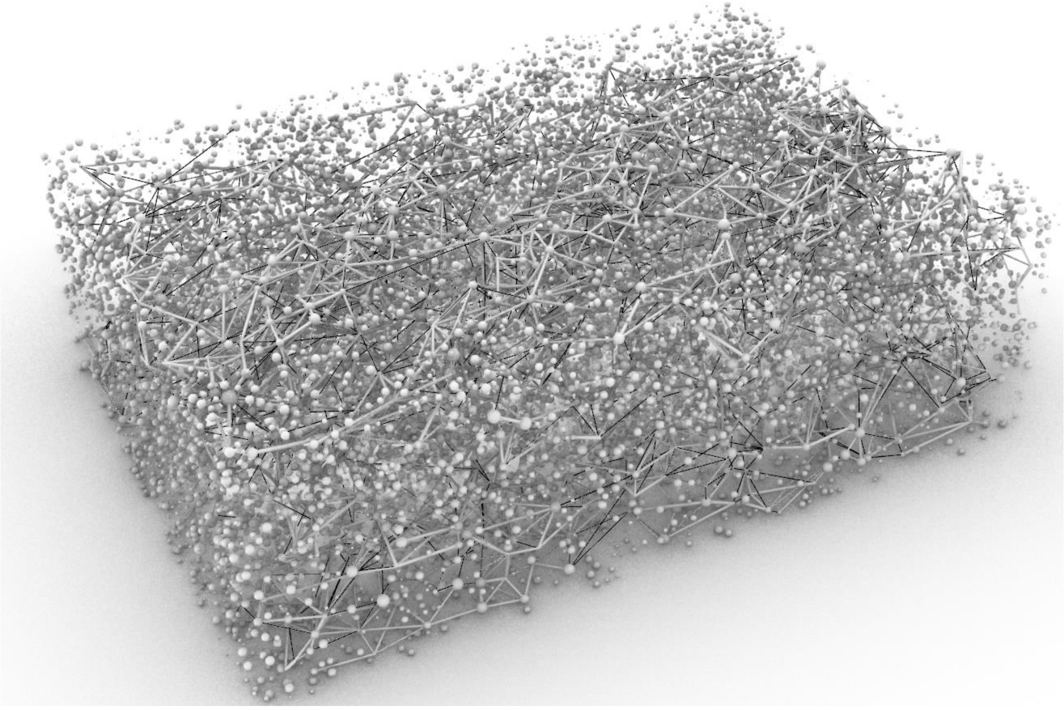

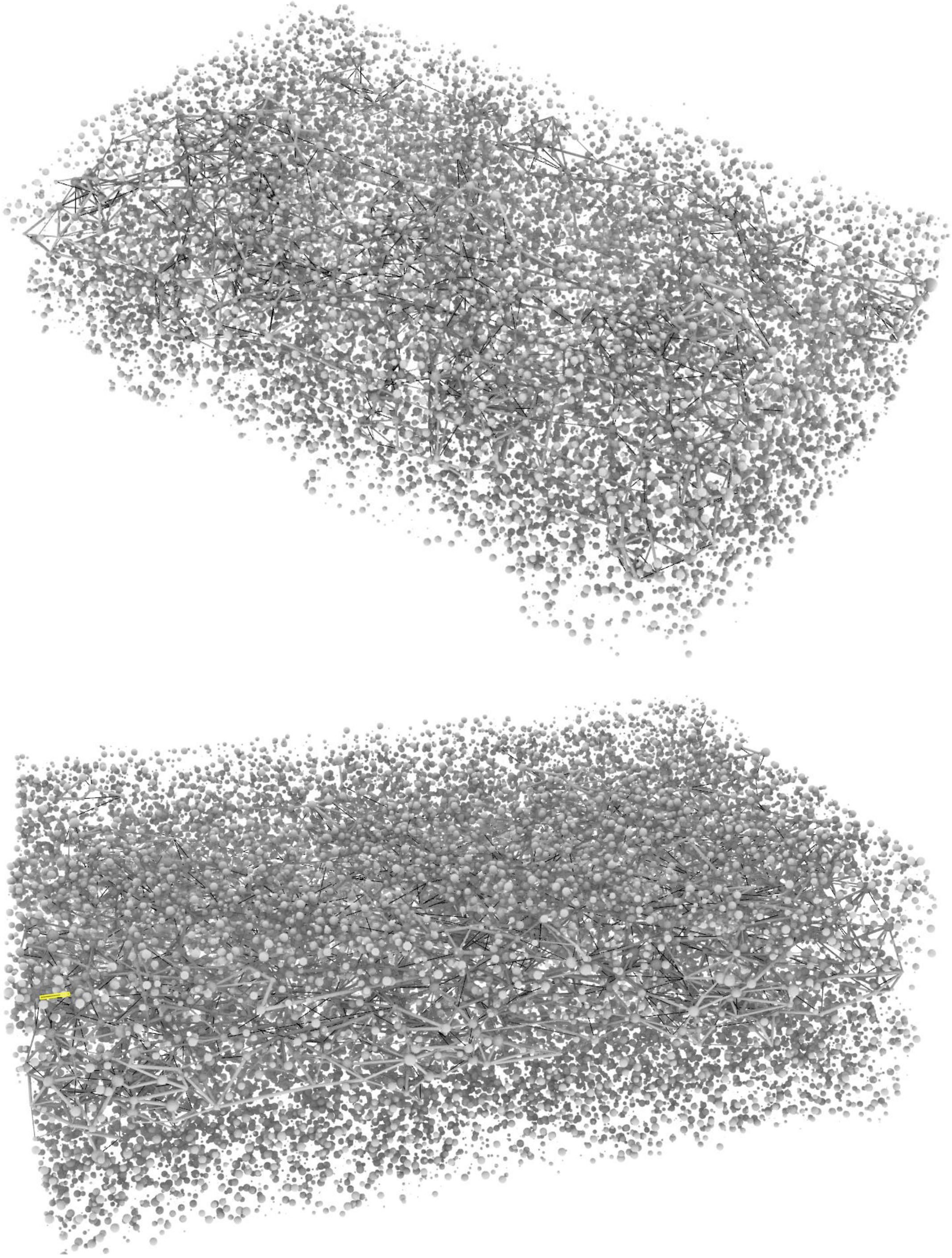

Figure 4.18 The pore-network models extracted by the novel algorithm from the four subsections $(\mathbf{900 \times 600 \times 300})$ $(\boldsymbol{nm})$ of the Marcellus shale core sample.

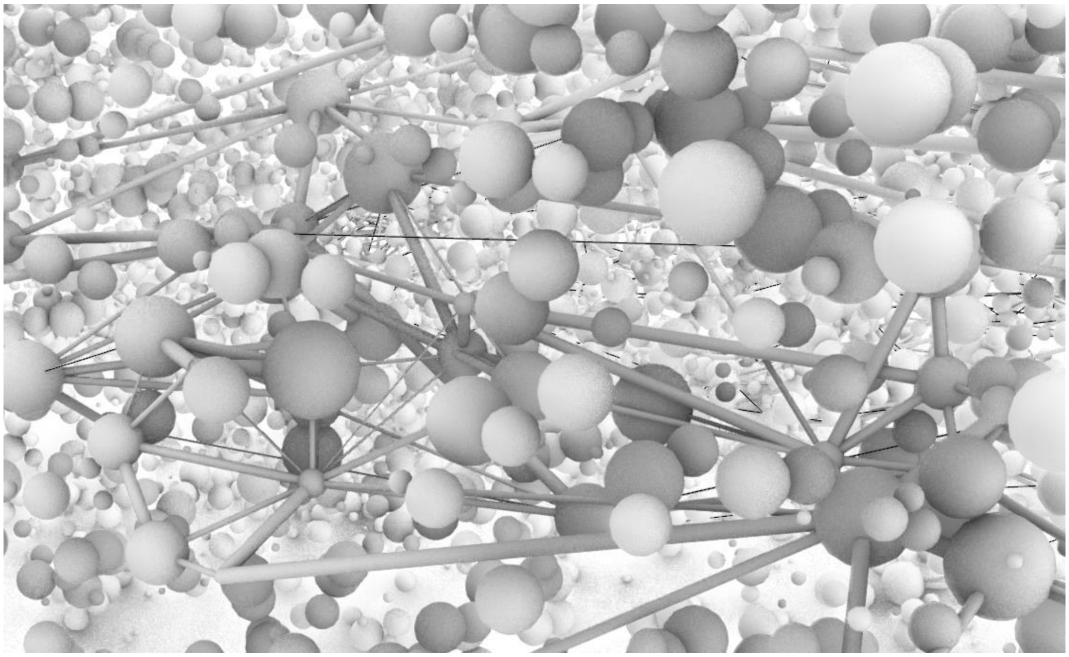

Figure 4.19 The extracted pore-network model of a part of the subsection in an amplified view.

The spatial distributions of pore bodies and pore throats are characterized by coordination numbers. The coordination-number distribution of the four subsections are shown in Figure 4.20. The average coordination numbers for the four subsections are respectively 3.49, 4.65, 8.27 and 4.53. The isolated pores are not counted in calculating the average coordination number. The resulting average number correspond well with the value reported by other investigators (Zhang et al. 2015; Soeder et al. 2010).

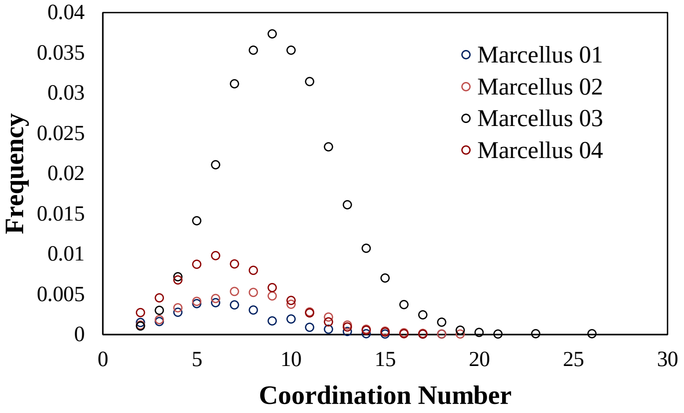

Figure 4.20 Coordination-number distributions of the four subsections of the Marcellus shale core sample.

The radius distributions of the pore bodies and throats are shown in Figure 4.21. The pore-throat size distributions are different from those characterized by the mercury drainage experiment or nuclear magnetic resonance spectroscopy. In a conventional sense, the pore-size distribution can be expressed by normal distribution or Weibull distribution. However, in this extracted pore-network model, the pore-throat size within the range of 3nm to 30nm have an approximately constant frequency. The pore-throat size in this extracted pore-network model is not the size of real pore throats, instead, they are the pore-throat size calculated to ensure an equivalent flow capacity. The shape factors of pore bodies and throats are shown in Figure 4.22. The distributions of pore-throat length are shown in Figure 4.23, where the average length is 103.3 nm.

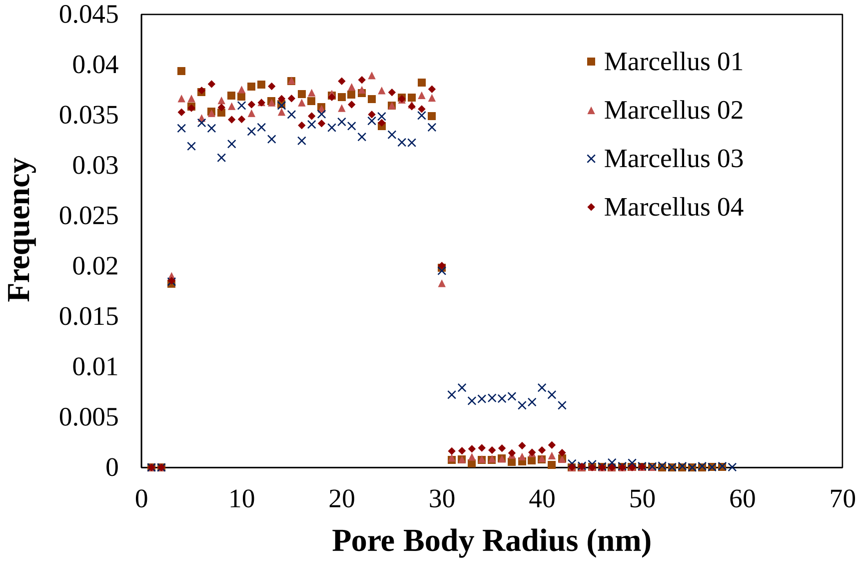

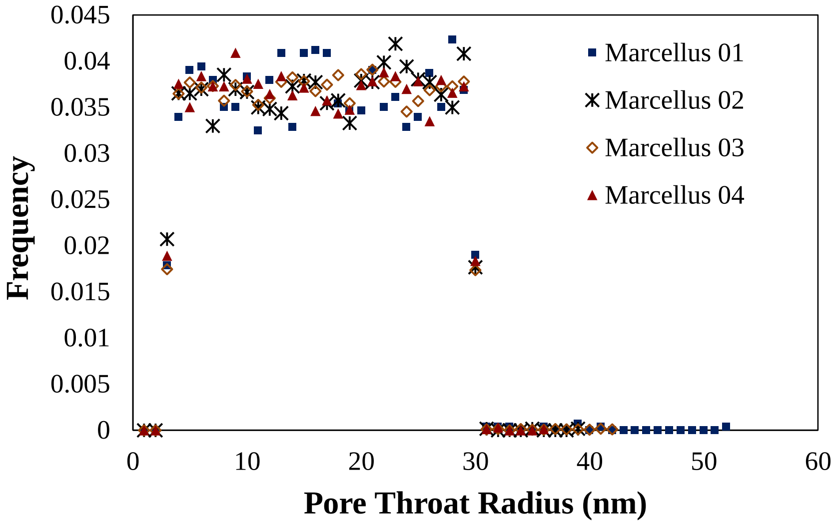

Figure 4.21 Size distributions of pore bodies and throats for the four subsections of the Marcellus shale core sample.

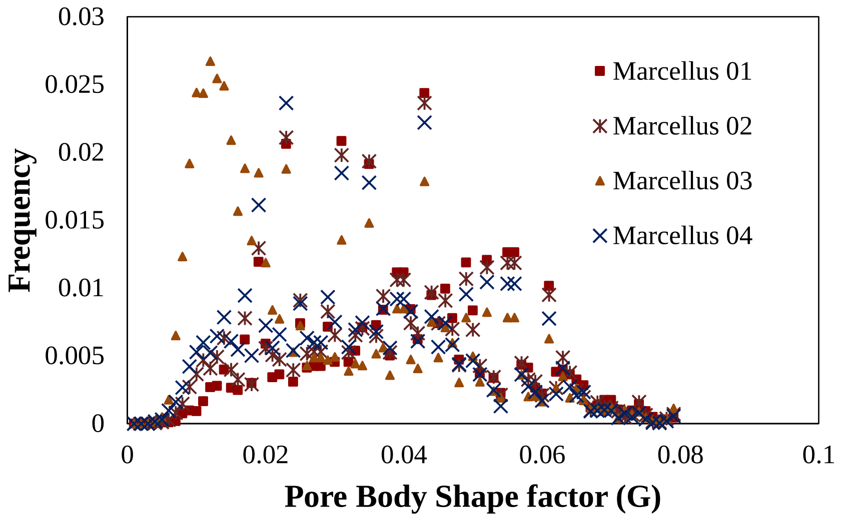

Figure 4.22 The shape-factor distribution of the pore bodies in the extracted pore-network model of the Marcellus shale core sample.

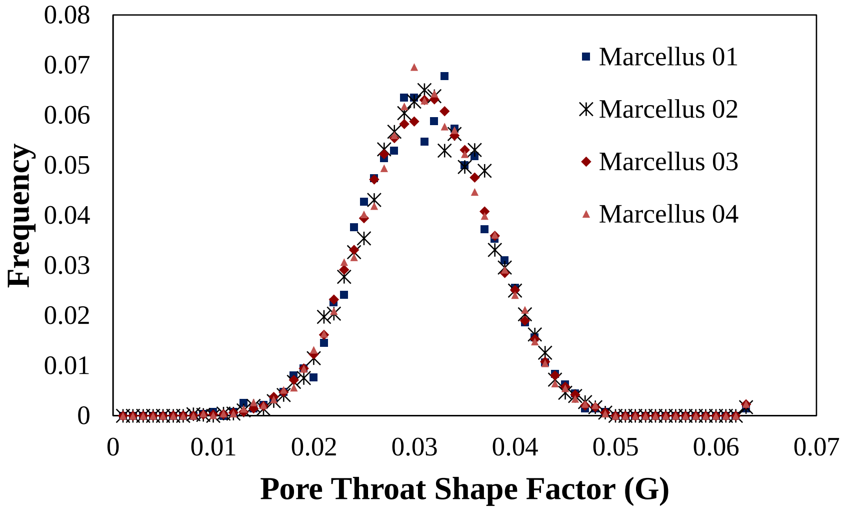

Figure 4.23 The shape-factor distribution of the pore throats in the extracted pore-network model of the Marcellus shale core sample.

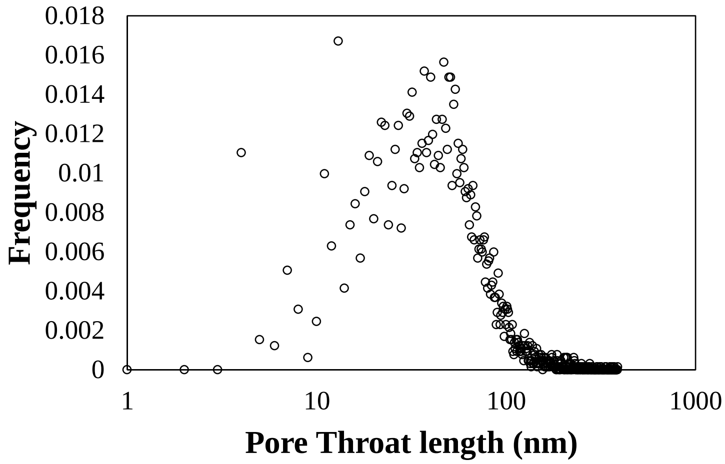
0.018
0.016
0.014
0.012
0.01
0.008
0.006
0.004
0.002
0
Frequency
1
10
100
1000
Pore Throat length (nm)

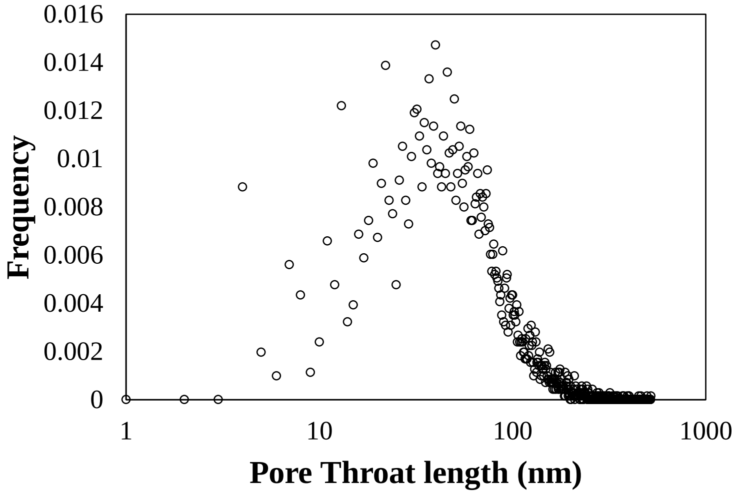
0.016
0.014
0.012
0.01
0.008
0.006
0.004
0.002
0
Frequency
1
10
100
1000
Pore Throat length (nm)

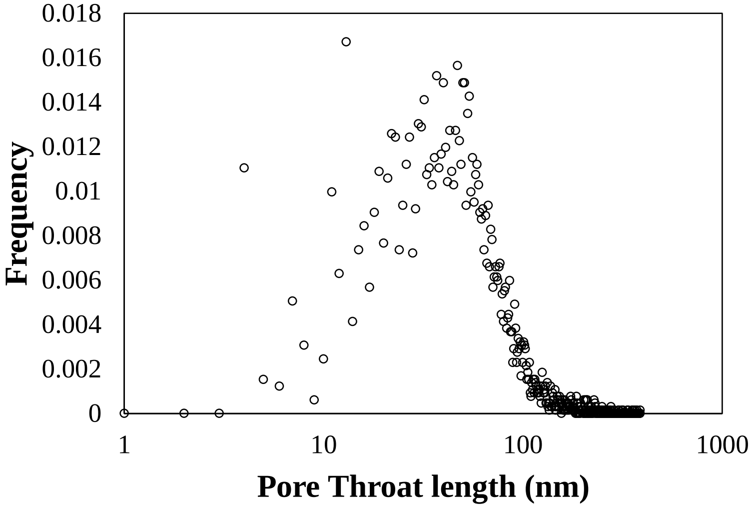

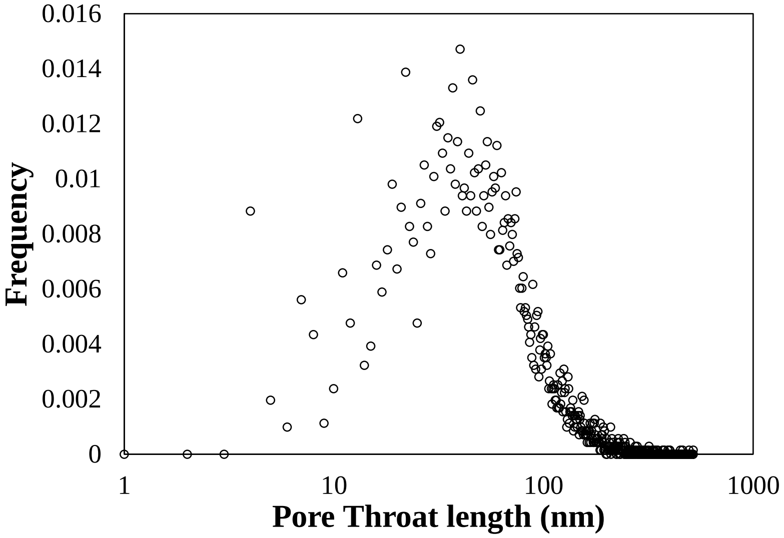

Figure 4.24 Pore-throat length distributions of the extracted pore-network model of the four subsections of the Marcellus shale core sample.

Chapter 5 Multi-scale Characterization of Liquid Flow in Shale Porous Media

5.1 Integrated Procedures of Multi-Scale Modeling of Liquid flow

In shale formations, understanding liquid flow behavior in nano-confined pores is central to solve the challenging problems in a larger scale. To accurately predict the apparent permeability of a core sample in centimeter-scale, I couple the molecular dynamics (MD) simulation and the dendroidal theoretical pore-network model to construct a multi-scale model for fluid flow in shale porous media. I use MD simulation to study the physics of liquid flow within a single nanopore. Then I derived the modified Navier-Stokes equation to characterize the apparent permeability of each single pore in the dendroidal model considering the boundary-slippage effect and nano-confinement effect.

Since the pore throats in the dendroidal model have various cross-sectional geometries representing the complex shape of pores in real porous media, the boundary conditions of the modified Navier-Stokes equation are complicated. Therefore, it is difficult to solve for the analytical solution. I implement finite element method to solve for the velocity distribution of fluid within the nanopores with various cross-sectional geometries.

Afterwards, I propose a correlation between the liquid flow capacity within a single pore and different properties, including temperature, pressure, and the hydraulic diameter of cross section. Implementing the fitted correlations into the dendroidal model, the multi-scale liquid flow model is constructed (Figure 5.1), with which the apparent permeability and relative permeability of rock core samples can be predicted by mathematical simulations.

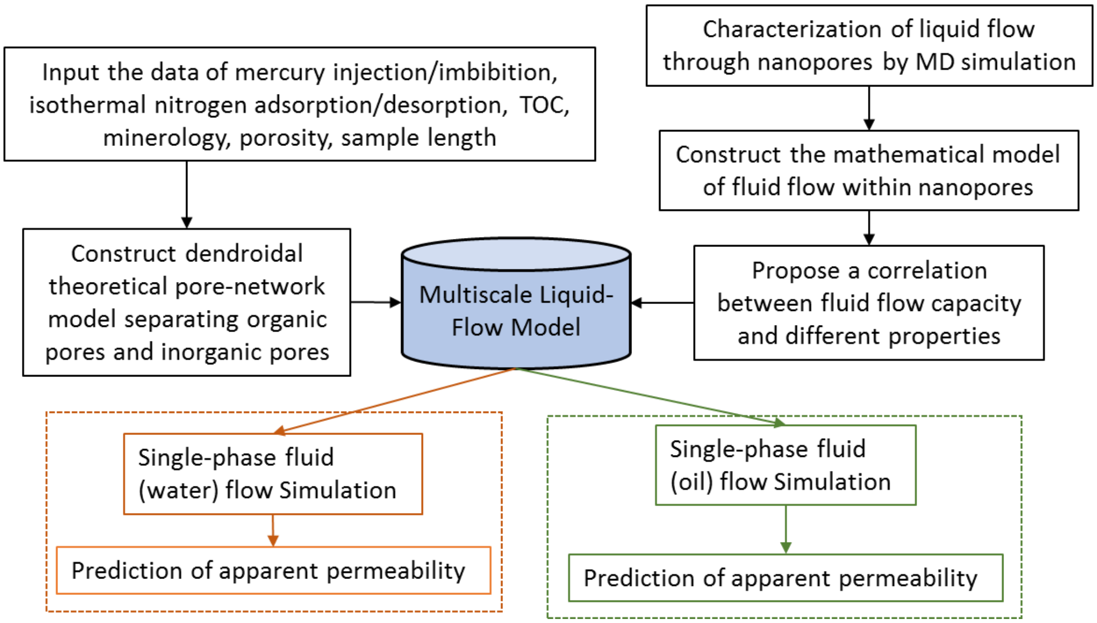

Figure 5.1 The flowchart of the construction of multi-scale liquid flow model and its applications.

5.2 Physical Mechanisms of Nanoconfined Fluid

The investigations indicate that the flow capacities differ dramatically from nano-confined fluid to bulk fluid (Heuberger et al. 2001; Werder et al. 2001; Rivera et al. 2002; Ye et al. 2017), because the molecules of the nano-confined fluid have strong interactions with the pore wall (Mashi et al. 2003; Krott et al. 2015). Some novel phenomenon have been investigated to advance the understanding of the dynamics of nanoconfined liquid flowing in tubes. Holt et al. (2001) implement experiments to measure the flow rate of water through a carbon nanotube membrane with the diameter of 1.5-7.2 nm, and they found that the measured flow rate is 2 to 5 orders faster than that calculated by the Navier-

Stokes equation with no-slip boundary condition; for the carbon tubes with 45 nm diameter, the flow rate is only one order faster (Whitby et al. 2008). However, some fluid flow capacity in nanopores could decrease caused by multi-layer sticking (Heinbuch et al. 1989). The interaction between the liquid molecules and wall varies significantly for different types of liquid and solid because of different interaction strength. Shannon et al. (2008) argued that the interaction between water and wall is strongly affected by the contact angle; while for oil, the interaction depends more on the composition of liquid and pore wall (Wang et al. 2016), instead of the contact angle.

Although the fluid flow capacity within nanotubes varies dramatically from that in the pores with larger diameters, the continuum flow description is still valid for liquid flowing in the nanopores with a diameter larger than 1.66 nm (Sparreboom et al. 2009). The main liquid-flow mechanisms in nanopores and micropores are similar, but the emerging physical mechanisms of nanoconfined fluid need to be considered, including slip-boundary condition, fluid-viscosity change (Klein et al. 1995) and fluid-density change (Monteiro et al. 2012).

The results of experiments and MD simulations in the literature are collected to investigate the liquid slippage on the wall. It has been proved that the density and viscosity of liquid adjacent to the wall have a dramatic change (Campbell et al. 1996) and the no-slip boundary condition is not applicable under some conditions (Cottin-Bizonne et al. 2003). The viscosity, density and boundary-slippage depend on the relative strength of the internal interaction among liquid molecules and the interaction between liquid molecules and the solid wall.

5.3 Modified Navier-Stokes Equation for Single-phase Nanoconfined Liquid Flow

Considering the boundary-slippage effect and nanoconfinement effect, I derive a new mathematical model for liquid flow within a nanopore. The new mathematical model is developed based on the Navier-Stokes equation of steady state and laminar flow. Thomas et al. (2009) proved that the continuum-flow regime is still applicable to characterize fluid flow within the channels with a diameter larger than 1.66 nm. Through the visualization of real pore structure by the technology of scanning electron microscope (SEM) and CT-scan, it indicates that the size of the micropores in shales are mostly within the range between 2 nm to 50 nm and the mesopores have even larger characteristic size (Josh et al. 2012). Therefore, the continuum-flow regime is still adopted in this model.

Different from the bulk-liquid flow, the mathematical model of nanoconfined liquid flow needs to couple the emerging phenomenon, including viscosity variation, density variation and boundary-slippage effect. Meanwhile, by analyzing the SEM images of porous media, Loucks et al. (2009) categorized the pores into different types, which are intrapartical and interpartical pores. The study indicates that most pores have irregular shapes, like circle, elliptical, polygon and slit. To implement the dendroidal theoretical pore-network model as a representative porous media in predicting the apparent permeability in centimeter-scale, I derive the modified Naiver-Stokes equations of liquid flowing in the pore throats with different cross-sectional shapes.

Myers (2011) proposed a two-fluid system in an annular tube to account for the viscosity change of the film liquid, which is the portion of liquid adsorbed on the solid wall (Pascal et al. 2011). In this work, the fluid flowing across the channel is divided into two regions, where one is the film liquid and the other is bulk liquid (Figure 5.2). The properties of the adsorbed liquid film vary significantly from those of the bulk liquid due to the vitiation of interaction strength between the liquid molecules and wall. Figure 5.3 shows the density distribution with respect to the distance from the solid wall. Both the density and viscosity distribution of liquid molecules oscillate dramatically within film-liquid region. In this modified Navier-Stokes equation, I use an average value to represent the density and viscosity of the film liquid. Therefore, the properties of film liquid, including viscosity and density, are regarded as constant values in the modified Navier-Stokes model.

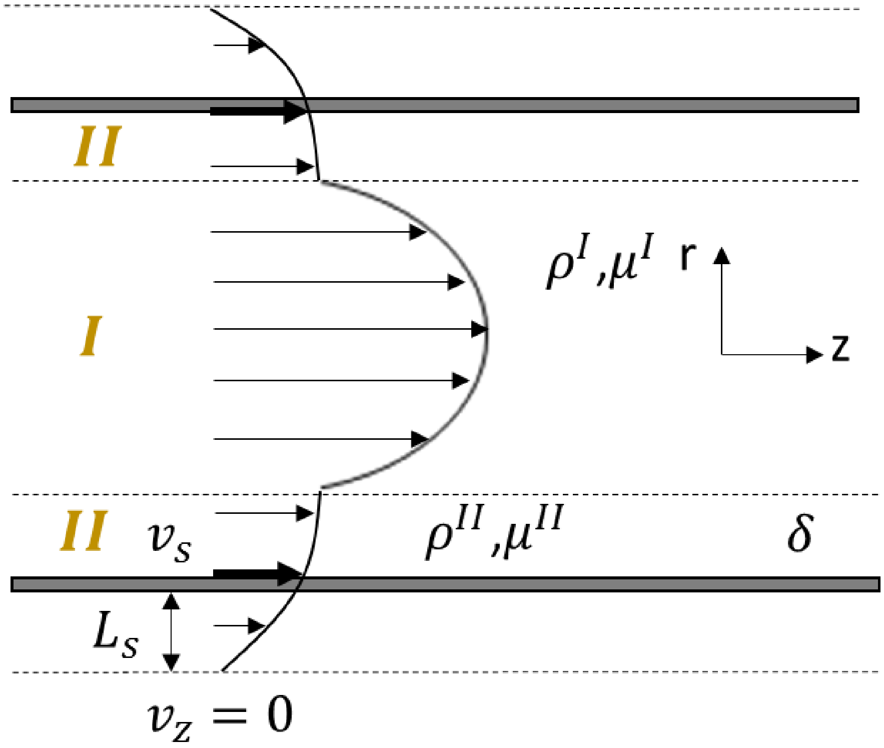

Figure 5.2 Schematic of modified Navier-Stokes model of single-phase fluid flow in a circular tube. *I* represents the central region (bulk fluid) and *II* represents the liquid film. L_s is the slip length and v_s is the slip velocity on wall. The velocity distribution outside the walls are fictious to represent the trend of velocity to $v_z = 0$.

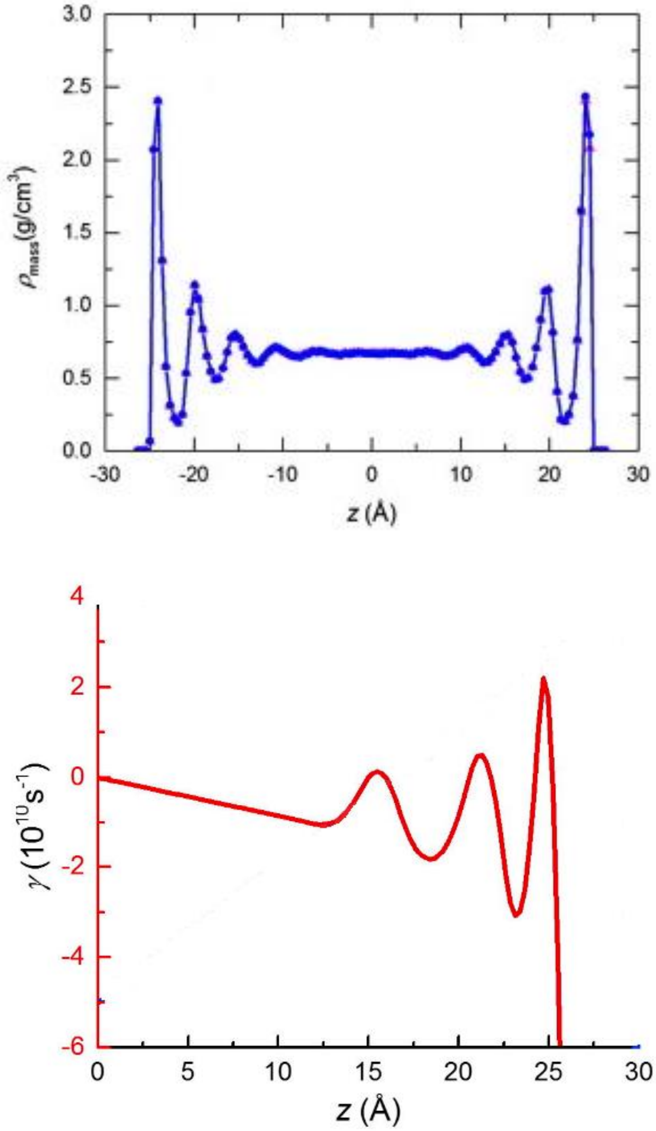

Figure 5.3 (a) Density distribution and (b) viscosity distribution of liquid computed by non-equilibrium molecular dynamics simulation in a 5.24 nm organic slit channel, where the temperature is 353K and the pressure is 30 MPa. (Wang et al. 2016a)

5.3.1 Nanotube with Circular Cross-section

For nano-scaled pore throats with circular cross-section (Figure 5.2), the equation describing the conservation of momentum is:

$$\frac{d}{dr}(r\tau_{rz}) = \frac{\Delta p}{L} r \tag{5.1}$$

where r is the distance in radial direction of the cross-section, τ_{rz} is the shear stress exerting on the plane perpendicular to radius in the axial direction. $\frac{\Delta p}{L}$ is the pressure gradient. For different flow region, Eq. 5.1 becomes

$$\tau_{rz}^{\mathrm{I}} = \frac{\Delta p}{2L} r + \frac{C_1^{\mathrm{I}}}{r}, for\ 0 < r < R - h \tag{5.2}$$

$$\tau_{rz}^{\mathrm{II}} = \frac{\Delta p}{2L} r + \frac{C_1^{\mathrm{II}}}{r}, for\ (R - h) < r < R \tag{5.3}$$

The boundary conditions are

B.C. 1: at $r = 0, \tau_{rz}^{\mathrm{II}} = finite$ (5.4)

B.C. 2: $at\ r = R - \delta, \tau_{rz}^{\mathrm{I}} = \tau_{rz}^{\mathrm{II}}$ (5.5)

B.C. 3: $at\ r = R - \delta, v_z^{\mathrm{I}} = v_z^{\mathrm{II}}$ (5.6)

B.C. 4: $at\ r = R, v_z^{\mathrm{II}} = \frac{\mu^{II}}{\varepsilon}\frac{\partial v_z^{\mathrm{II}}}{\partial r}$ (5.7)

where μ^{II} is the shear viscosity of fluid in region II, δ is the thickness of the liquid film adsorbed on the wall, ε is the surface friction factor and $\partial v_z^{\mathrm{II}}/\partial r$ is the strain rate. To easily capture the slippage effect,

$$\frac{\mu^{II}}{\varepsilon} = L_s \tag{5.8}$$

is implemented into Eq. 5.7, where L_s is the slip length on the wall. Calculated by the boundary condition 3, Eq 5.2 and Eq 5.2 become

$$v_z^I = -\left(\frac{\Delta p}{4\mu^I L}\right) r^2 + \frac{C_1^I}{2\mu_b r^2} + C_2^I \tag{5.9}$$

$$v_z^{II} = -\left(\frac{\Delta p}{4\mu^{II} L}\right) r^2 + \frac{C_1^{II}}{2\mu_f r^2} + C_2^{II} \tag{5.10}$$

where μ^I is the viscosity of fluid in region I, C_1 and C_2 are unknown parameters to be solved to get the fluid velocity distribution in the cross section. Since the velocities of bulk liquid and film liquid on the interface are same, Eq. 5.9 and Eq. 5.10 become

$$-\left(\frac{\Delta p}{4\mu^I L}\right) r^2 + \frac{C_1^I}{2\mu_b r^2} + C_2^I == -\left(\frac{\Delta p}{4\mu^{II} L}\right) r^2 + \frac{C_1^{II}}{2\mu_f r^2} + C_2^{II} \tag{5.11}$$

Implementing the boundary condition 1 and 2 into Eq. 5.11, because the velocity at any position are finite, I get

$$C_1^{\mathrm{I}} = C_1^{\mathrm{II}} = 0 \tag{5.12}$$

Plug in the Eq. 5.11 the boundary condition 4, and unknown parameters C_2^I and C_2^{II} can be calculated,

$$C_2^I = \frac{\Delta p}{L}\frac{RL_s}{2\mu^{II}} + \left(\frac{\Delta p}{4\mu^I L}\right)[R^2 - (R-\delta)^2] + \left(\frac{\Delta p}{4\mu^{II} L}\right)[(R-\delta)^2 - R^2] \tag{5.13}$$

$$C_2^{II} = \frac{\Delta p}{L}\frac{RL_s}{2\mu^{II}} \tag{5.14}$$

Solving the Eq. 5.2 and Eq. 5.3, velocity distribution of bulk liquid and film liquid can be expressed as follows,

$$v^I(r) = \left[\frac{RL_s}{2\mu^{II}} + \frac{1}{4\mu^{II}}\left(R^2 - \frac{\mu^{II}}{\mu^I} r^2\right) + \frac{(\mu^{II}-\mu^I)(R-\delta)^2}{4\mu^I \mu^{II}}\right]\frac{\Delta p}{L} \tag{5.15}$$

$$v^{II}(r) = \left(\frac{L_s R}{2\mu^{II}} + \frac{R^2 - r^2}{4\mu^{II}}\right)\frac{\Delta p}{L} \tag{5.16}$$

Because the densities of liquid in bulk region and film region are different, the flow capacity of each pore throat needs to be represented by mass flux, instead of volume flux,

$$\dot{m} = q^I \rho^I + q^{II} \rho^{II} \tag{5.17}$$

The flow rate can be predicted by calculating the volume flux of bulk-fluid and film-fluid separately,

$$q^I = \int_0^{R-\delta} v_z^I A dr = \int_0^{R-\delta} v_z^I 2\pi r dr = \int_0^{R-h} \left\{\frac{RL_s}{2\mu^{II}} + \frac{1}{4\mu^{II}}\left(R^2 - \frac{\mu^{II}}{\mu^I} r^2\right) + \frac{(\mu^{II}-\mu^I)(R-\delta)^2}{4\mu^I\mu^{II}}\right\}\frac{\Delta p}{L} 2\pi r dr \tag{5.18}$$

So, $q^I = \frac{\pi\Delta p}{8L\mu^I}(R-\delta)^2\left[\frac{\mu^I}{\mu^{II}}(4R\delta - 2\delta^2) + (R-\delta)^2 + \frac{8\mu^I R L_s}{2\mu^{II}}\right]$ (5.19)

The volume flux of film-liquid can be calculated by integrating it between $r = R$ and $r = R - \delta$, which is

$$q^{II} = \int_{R-\delta}^{R} v_z^{II} A dr = \int_{R-\delta}^{R} v_z^{II} 2\pi r dr = \int_{R-\delta}^{R} \left(\frac{L_s R}{2\mu^{II}} + \frac{R^2 - r^2}{4\mu^{II}}\right)\frac{\Delta p}{L} 2\pi r dr \tag{5.20}$$

Therefore, Eq. 5.20 becomes

$$q^{II} = \frac{\pi\Delta p}{8L\mu^I}(2R\delta - \delta^2)(2R\delta - \delta^2) \tag{5.21}$$

Substituting Eq 5.19 and Eq 5.21 into Eq. 5.17, it becomes

$$\dot{m} = \rho^I \frac{\pi\Delta p}{8L\mu^I}(R-\delta)^2\left[\frac{\mu^I}{\mu^{II}}(4R\delta - 2\delta^2) + (R-\delta)^2 + \frac{8\mu^I R L_s}{2\mu^{II}}\right] + \rho^{II}\frac{\pi\Delta p}{8L\mu^I}(2R\delta - \delta^2)(2R\delta - \delta^2) \tag{5.22}$$

Equation 5.22 is the expression of total mass flux of liquid flowing through a circular nanotube with the diameter larger than 1.66nm.

5.3.2 Nanotube with Rectangular and Triangular Cross-section

The dendroidal model use rectangular and triangular tubes to represent the pore throats, which have complex geometry in the real pore structure. Therefore, I derive the modified Navier-Stokes equation in rectangular and triangular tubes to predict the apparent permeability of a single pore.

As the length of each side of rectangular cross sections in constructing dendroidal model are stochastically assigned, I calculate the apparent permeability of rectangles with various aspect ratio. Since rectangle is symmetrical, computing the velocity distribution in only ¼ of the cross-sectional area is enough to characterize the apparent permeability in the entire cross section (Figure 5.4). For the pore throats with triangular cross section, the velocity distribution needs to be calculated within the entire area (Figure 5.5), since the triangular cross section of pore throats can be unsymmetrical in the dendroidal model. The corner angles determining the shape of a triangle are stochastically assigned, so the triangles are irregular.

For rectangular nanotube, the modified Navier-Stokes equation can be written as,

$$\frac{\partial^2 u_x^{\mathrm{I}}}{\partial y^2} + \frac{\partial^2 u_x^{\mathrm{I}}}{\partial z^2} = \frac{1}{\mu^{\mathrm{I}}}\frac{\partial p}{\partial x}, for\ 0 < y \leq b - \delta, 0 < z \leq c - \delta \tag{5.23}$$

$$\frac{\partial^2 u_x^{\mathrm{II}}}{\partial y^2} + \frac{\partial^2 u_x^{\mathrm{II}}}{\partial z^2} = \frac{1}{\mu^{\mathrm{II}}}\frac{\partial p}{\partial x}, \begin{cases} for\ b - \delta < y < b, 0 < z < c - \delta \\ for\ \ c - \delta < z < c, 0 < y < b - \delta \\ for\ b - \delta < y < b, c - \delta < z < b \end{cases} \tag{5.24}$$

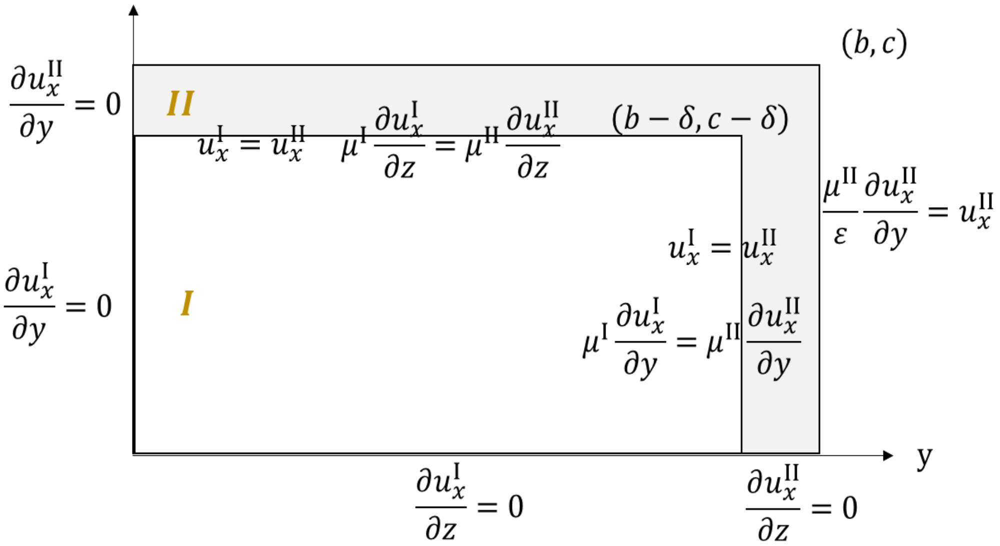

Figure 5.4 The schematic of 1/4 of a pore throat with rectangular cross section. The corresponding boundary condition is shown on each side. Region *I* is the bulk fluid and region *II* is the film fluid. The thickness of adsorbed liquid film is represented by *δ*, in the unit of nm.

And the boundary conditions are

B.C. 1: at $y = b - \delta, u_x^{\mathrm{I}} = u_x^{\mathrm{II}}$

B.C. 2: at $z = c - \delta, u_x^{\mathrm{I}} = u_x^{\mathrm{II}}$

B.C. 3: at $y = b - \delta, 0 < z < c - \delta, \tau_{zx}^{\mathrm{I}} = \tau_{zx}^{\mathrm{II}}$, which is $\mu^{\mathrm{I}} \frac{\partial u_x^{\mathrm{I}}}{\partial y} = \mu^{\mathrm{II}} \frac{\partial u_x^{\mathrm{II}}}{\partial y}$

B.C. 4: at $z = c - \delta, 0 < y < b - \delta, \tau_{yx}^{\mathrm{I}} = \tau_{yx}^{\mathrm{II}}$, which is $\mu^{\mathrm{I}} \frac{\partial u_x^{\mathrm{I}}}{\partial z} = \mu^{\mathrm{II}} \frac{\partial u_x^{\mathrm{II}}}{\partial z}$

B.C. 5: at $z = c, \frac{\mu^{\mathrm{II}}}{\varepsilon} \frac{\partial u_x^{\mathrm{II}}}{\partial z} = u_x^{\mathrm{II}}$

B.C. 6: at $y = \mathrm{b}, \frac{\mu^{\mathrm{II}}}{\varepsilon} \frac{\partial u_x^{\mathrm{II}}}{\partial y} = u_x^{\mathrm{II}}$

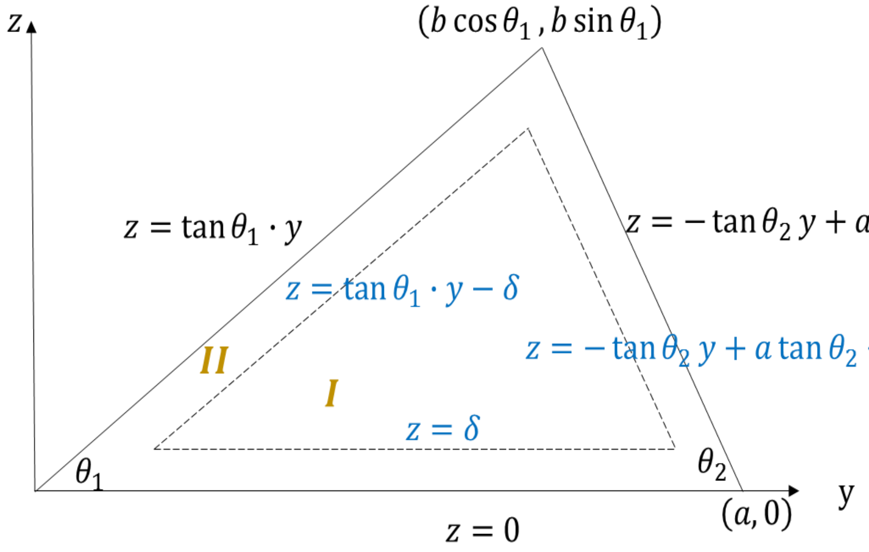

Figure 5.5 The schematic of the pore throat with triangular cross section. The corresponding equation of each side in the Cartesian coordination system are shown. Region *I* is the bulk fluid and region *II* is the film fluid. The thickness of adsorbed liquid film is represented by *δ*, in the unit of nm.

B.C. 7: at z= $0,0 < \mathrm{y} < \mathrm{b} - \delta, \frac{\partial u_x^{\mathrm{I}}}{\partial z} = 0$

B.C. 8: at z= $0, \mathrm{b} - \delta < \mathrm{y} < \mathrm{b}, \frac{\partial u_x^{\mathrm{II}}}{\partial z} = 0$

B.C. 9: at $y = 0,0 < \mathrm{z} < \mathrm{c} - \delta,\ \frac{\partial u_x^{\mathrm{I}}}{\partial y} = 0$

B.C. 10: at $y = 0, \mathrm{c} - \delta < \mathrm{z} < \mathrm{c},\ \frac{\partial u_x^{\mathrm{II}}}{\partial y} = 0$

Because the domain of this partial differential equation is complex, it is difficult to solve for the analytical solution. I implement the numerical method, finite element method, to solve for the velocity distribution. In nanometer scale, the value of different parameters can be orders different, which will make significant errors in calculating the velocity distribution using numerical methods. Consequently, the nondimensionalization of the equations is essential. First, the variables are transformed into corresponding non-dimensional parameters,

$$u_x^{\mathrm{I}} = u_{x0} s^{\mathrm{I}} \tag{5.25}$$

$$u_x^{\mathrm{II}} = u_{x0} s^{\mathrm{II}} \tag{5.26}$$

$$y = l_0 m \tag{5.27}$$

$$z = l_0 n \tag{5.28}$$

$$\delta = l_0 b \tag{5.29}$$

Then I implement the dimensionless groups to generalize the equation to be applicable into different scale,

$$\Pi_1 = \frac{{l_0}^2}{u_{x0}\mu^{\mathrm{I}}} \frac{\Delta p}{L} \tag{5.30}$$

$$\Pi_2 = \frac{{l_0}^2}{u_{x0}\mu^{\mathrm{II}}} \frac{\Delta p}{L} \tag{5.31}$$

$$\Pi_3 = \frac{L_s}{l_0} \tag{5.32}$$

$$\Pi_4 = \frac{\mu^{\mathrm{I}}}{\mu^{\mathrm{II}}} \tag{5.33}$$

where u_{x0} and l_0 are unit constants and they are the characteristic values of the variables. The characteristic values are determined using the physical parameters in this problem to make the dimensionless groups (Π_1, Π_2, Π_3 and Π_4) in a same scale. s^{I} and s^{II} are the dimensionless variables representing the fluid velocities within different regions. m and n are the dimensionless variables representing the distance in y and z direction, b is introduced to describe the dimensionless thickness of the liquid film (region II). With nondimonalization, the Eq 5.23 and Eq. 5.24 become

$$\frac{\partial^2 s^I}{\partial m^2} + \frac{\partial^2 s^I}{\partial n^2} = \Pi_I, in\ \Omega_I \tag{5.34}$$

$$\frac{\partial^2 s^{II}}{\partial m^2} + \frac{\partial^2 s^{II}}{\partial n^2} = \Pi_2, in\ \Omega_{II} \tag{5.35}$$

In this equation, Ω_{I} is the domain of region *I* representing the bulk liquid and Ω_{II} is the domain of region II representing the film liquid. Then, the boundary conditions become,

B.C. 1: on $\Gamma_I, s^I = s^{II}$

B.C. 2: on Γ_I, $\left(\frac{\partial s^{II}}{\partial m}\vec{\imath} + \frac{\partial s^{II}}{\partial n}\vec{\jmath}\right)\overrightarrow{nn_1} = \Pi_4\left(\frac{\partial s^I}{\partial m}\vec{\imath} + \frac{\partial s^I}{\partial n}\vec{\jmath}\right)\overrightarrow{nn_1}$

B.C. 3: on Γ_{II}, $\Pi_3\left(\frac{\partial s^{II}}{\partial m}\vec{\imath} + \frac{\partial s^{II}}{\partial n}\vec{\jmath}\right)\overrightarrow{nn_2} = s^{II}$

where $\overrightarrow{nn_1}$ and $\overrightarrow{nn_2}$ are the vectors in the direction perpendicular to the surface they exert on. The nondimensionalized equations can characterize liquid flow in nano-scaled pore throats with complex geometry (fig. 5.6) considering the boundary-slippage effect and nanoconfinement effect.

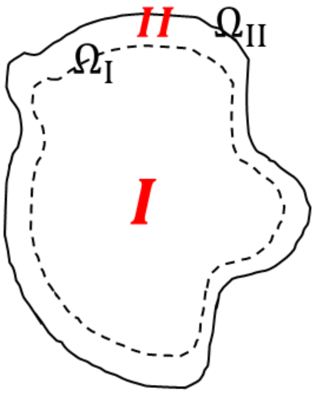

Figure 5.6 Schematic of a pore throat with complicated and irregular shape. Region I and II represent the bulk fluid and film liquid separately. Ω_I and Ω_{II} are the boundaries of different regions.

5.4 Modified Navier-Stokes Equation for Liquid Flow in Nanoconfined Pores with Adsorption Film

It is well-established that the void space in shale formations can be categorized in organic pores and inorganic pores (Josh et al. 2012; Zheng et al. 2018c). The inorganic pores are generally composed by clay minerals, most of which are water wet (Wu et al. 2017). Consequently, the characterization of oil flow in nanoconfined pores without considering the water-film effect can have significant discrepancies, and the prediction of apparent permeability of oil can be inaccurate. Here, I propose a modified Navier-Stokes equation to describe the liquid flow within the nanotubes with an adsorbed film composed by different liquid. Because of the confinement effect in nanopores, I propose the dual slippage effect, where the slippage happens between the film liquid and solid wall and it also happens on the interface between two types of fluid (Figure 5.7). The velocity “jump” on the two interfaces is calculated by the finite element method, the embedded discontinuous Galerkin method.

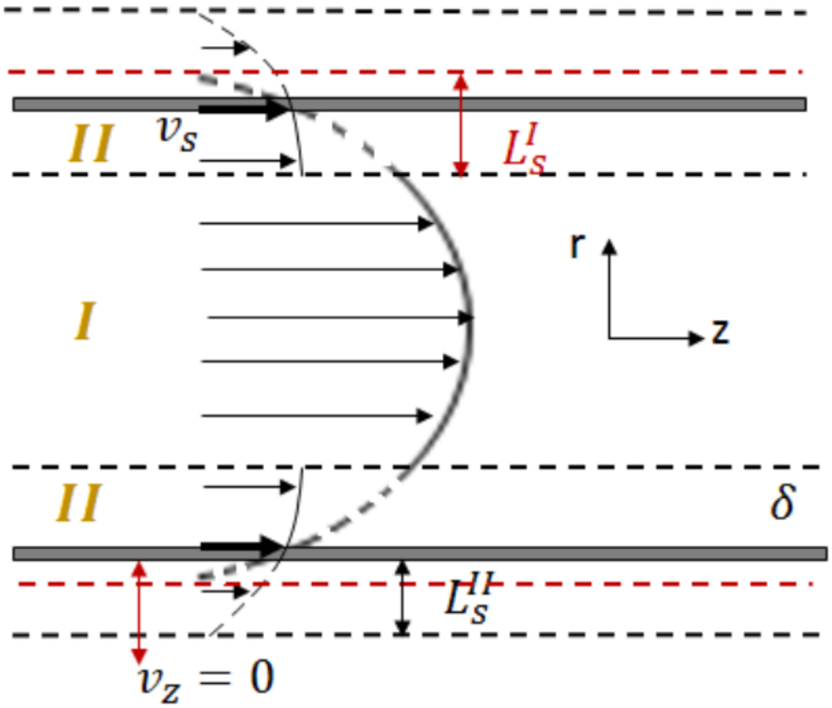

Figure 5.7 The schematic of two-fluid flow system. Region I and II represent the bulk and film liquid separately. The discontinuity of velocity distribution in different regions is caused by the slippage effect between different types of fluid. L_s^I and L_s^{II} are the slip lengths of two contact surfaces separately.

5.4.1 Nanotubes with Circular Cross-section

Since the pore-throat diameters visualized in the SEM images of shale porous media are larger than 2 nm, the continuum flow regime is still applicable in characterizing the two-phase fluid flow in nanopores. For the pore throats with circular cross section, the modified Navier-Stokes equation is implemented,

$$\tau_{rz}^{\mathrm{I}} = \frac{\Delta p}{2L} r + \frac{C_1^{\mathrm{I}}}{r}, for\ 0 < r < R - h \tag{5.36}$$

$$\tau_{rz}^{\mathrm{II}} = \frac{\Delta p}{2L} r + \frac{C_1^{\mathrm{II}}}{r}, for\ (R - h) < r < R \tag{5.37}$$

where C_1^{I} and C_1^{II} are unknown parameters. The boundary conditions are

B.C. 1: at $r = 0, \tau_{rz}^{\mathrm{II}} = finite$

B.C. 2: $at\ r = R - \delta, \tau_{rz}^{\mathrm{I}} = \tau_{rz}^{\mathrm{II}}$

B.C. 3: $at\ r = R - \delta, u_z^I = u_z^{II} + L_s^I \frac{\partial u_z^I}{\partial r}$

B.C. 4: $at\ r = R, v_z^{II} = L_s^{II} \frac{\partial v_z^{II}}{\partial r}$

where L_s^I is the slip length of bulk liquid on the contact interface with the film liquid; L_s^{II} is the slip length of film liquid with respect to solid wall. δ is the thickness of the liquid film adsorbed on the wall, $\partial v_z^{\mathrm{I}}/\partial r$ and $\partial v_z^{\mathrm{II}}/\partial r$ are the strain rates.

From boundary condition 1, C_1^{I} is calculated to be 0. With boundary condition 2, C_1^{II} is calculated to be 0 as well. The shear-stress definition is

$$\tau_{rz}^{\mathrm{I}} = -\mu^{\mathrm{I}} \frac{du_z^{\mathrm{I}}}{dr} \tag{5.38}$$

$$\tau_{rz}^{\mathrm{II}} = -\mu^{\mathrm{II}} \frac{du_z^{\mathrm{II}}}{dr} \tag{5.39}$$

Substituting Eq. 5.38 and Eq. 5.39 into Eq. 5.36 and Eq. 5.37, it becomes,

$$u_z^I = -\left(\frac{\Delta p}{4\mu^I L}\right) r^2 + C_2^I \tag{5.40}$$

$$u_z^{II} = -\left(\frac{\Delta p}{4\mu^{II} L}\right) r^2 + C_2^{II} \tag{5.41}$$

where C_2^I and C_2^{II} are unknown parameters to solve. Appling boundary condition 3, it is

$$-\left(\frac{\Delta p}{4\mu^I L}\right)(R-\delta)^2 + C_2^I = -\left(\frac{\Delta p}{4\mu^{II} L}\right)(R-\delta)^2 + C_2^{II} + L_s^I \frac{\Delta p}{2\mu^I L}(R-\delta) \tag{5.42}$$

Apply boundary condition 4 into Eq. 5.42, and it becomes

$$-\left(\frac{\Delta p}{4\mu^{II} L}\right) R^2 + C_2^{II} = -L_s^{II}\left(\frac{R\Delta p}{2\mu^{II} L}\right) \tag{5.43}$$

Solve C_2^I and C_2^{II} with Eq. 5.42 and 5.43,

$$C_2^I = -\left(\frac{\Delta p}{4\mu^{II}L}\right)(R-\delta)^2 - L_s^{II}\left(\frac{\Delta p}{2\mu^{II}L}\right)R + \left(\frac{\Delta p}{4\mu^{II}L}\right)R^2 + L_s^I\frac{\Delta p}{2\mu^I L}(R-\delta) + \left(\frac{\Delta p}{4\mu^I L}\right)(R-\delta)^2 \tag{5.44}$$

$$C_2^{II} = -L_s^{II}\left(\frac{\Delta p}{2\mu^{II}L}\right)R + \left(\frac{\Delta p}{4\mu^{II}L}\right)R^2 \tag{5.45}$$

Thus, Eq. 5.40 and Eq. 5.41 can be written as

$$u_z^I(r) = -\left(\frac{\Delta p}{4\mu^I L}\right)r^2 - \left(\frac{\Delta p}{4\mu^{II}L}\right)(R-\delta)^2 - L_s^{II}\left(\frac{\Delta p}{2\mu^{II}L}\right)R + \left(\frac{\Delta p}{4\mu^{II}L}\right)R^2 + L_s^I\frac{\Delta p}{2\mu^I L}(R-\delta) + \left(\frac{\Delta p}{4\mu^I L}\right)(R-\delta)^2 \tag{5.46}$$

$$u_z^{II} = -\left(\frac{\Delta p}{4\mu^{II}L}\right)r^2 - L_s^{II}\left(\frac{\Delta p}{2\mu^{II}L}\right)R + \left(\frac{\Delta p}{4\mu^{II}L}\right)R^2 \tag{5.47}$$

Integrating Eq. 5.46 from $r = 0$ to $r = R - \delta$, the volume flux of bulk liquid (q^I) can be calculated by

$$q^I = \int_0^{R-\delta} u_z^I A dr = \int_0^{R-\delta} u_z^I 2\pi r dr = \int_0^{R-h}\left\{-\left(\frac{\Delta p}{4\mu^I L}\right)r^2 - \left(\frac{\Delta p}{4\mu^{II}L}\right)(R-\delta)^2 - L_s^{II}\left(\frac{\Delta p}{2\mu^{II}L}\right)R + \left(\frac{\Delta p}{4\mu^{II}L}\right)R^2 + L_s^I\frac{\Delta p}{2\mu^I L}(R-\delta) + \left(\frac{\Delta p}{4\mu^I L}\right)(R-\delta)^2\right\}2\pi r dr \tag{5.48}$$

So,

$$q^I = -\left(\frac{\pi\Delta p}{8\mu^I L}\right)(R-\delta)^4 - \left(\frac{\pi\Delta p}{4\mu^{II}L}\right)(R-\delta)^4 - L_s^{II}\left(\frac{\pi\Delta p}{2\mu^{II}L}\right)R(R-\delta)^2 + \left(\frac{\pi\Delta p}{4\mu^{II}L}\right)R^2(R-\delta)^2 + L_s^I\frac{\pi\Delta p}{2\mu^I L}(R-\delta)^3 + \left(\frac{\pi\Delta p}{4\mu^I L}\right)(R-\delta)^4 \tag{5.49}$$

The volume flux of film liquid can be integrated between $r = R$ to $r = R - \delta$, which is calculated to be

$$q^{II} = \int_{R-\delta}^{R} v_z^{II} A dr = \int_{R-\delta}^{R} v_z^{II} 2\pi r dr = \int_{R-\delta}^{R}\left[\left(\frac{\Delta p}{4\mu^{II}L}\right)R^2 - \left(\frac{\Delta p}{4\mu^{II}L}\right)r^2 - L_s^{II}\left(\frac{\Delta p}{2\mu^{II}L}\right)R\right]2\pi r dr \tag{5.50}$$

So,

$$q^{II} = \frac{\pi \Delta p}{4L\mu^{I}} \left[R^2 - (R-\delta)^2\right] \left(\frac{\delta^2}{2} - 2L_s^{II} R - \delta R\right) \tag{5.51}$$

5.4.2 Nanotubes with Triangular and Rectangular Cross-section

Considering the pore throats with various cross sections, I derive the modified Navier-Stokes equation to characterize the liquid flow in rectangular and triangular tubes. The boundary conditions of 1/4 rectangular cross-section is shown in Figure 5.8.

For rectangular nanotubes, the modified Navier-Stokes equation can be written in the same from of Eq. 5.23 and 5.24, since both scenarios are 'two-regions' system. The difference is the boundary condition on the interface between two adjacent fluid regions. For completeness, the boundary condition for two-phase liquid case are expressed,

B.C. 1: at $y = b - \delta, u_x^{\mathrm{I}} = u_x^{\mathrm{II}} + L_s^I \frac{\partial u_x^{\mathrm{I}}}{\partial y}$

B.C. 2: at $z = c - \delta, u_x^{\mathrm{I}} = u_x^{\mathrm{II}} + L_s^I \frac{\partial u_x^{\mathrm{I}}}{\partial z}$

B.C. 3: at $y = b - \delta, 0 < z < c - \delta, \tau_{zx}^{\mathrm{I}} = \tau_{zx}^{\mathrm{II}}$, which is $\mu^{\mathrm{I}} \frac{\partial u_x^{\mathrm{I}}}{\partial y} = \mu^{\mathrm{II}} \frac{\partial u_x^{\mathrm{II}}}{\partial y}$

B.C. 4: at $z = c - \delta, 0 < y < b - \delta, \tau_{yx}^{\mathrm{I}} = \tau_{yx}^{\mathrm{II}}$, which is $\mu^{\mathrm{I}} \frac{\partial u_x^{\mathrm{I}}}{\partial z} = \mu^{\mathrm{II}} \frac{\partial u_x^{\mathrm{II}}}{\partial z}$

B.C. 5: at $z = c, \frac{\mu^{\mathrm{II}}}{\varepsilon} \frac{\partial u_x^{\mathrm{II}}}{\partial z} = u_x^{\mathrm{II}}$

B.C. 6: at $y = \mathrm{b}, \frac{\mu^{\mathrm{II}}}{\varepsilon} \frac{\partial u_x^{\mathrm{II}}}{\partial y} = u_x^{\mathrm{II}}$

B.C. 7: at $\mathrm{z} = 0, 0 < \mathrm{y} < \mathrm{b} - \delta, \frac{\partial u_x^{\mathrm{I}}}{\partial z} = 0$

B.C. 8: at $\mathrm{z} = 0, \mathrm{b} - \delta < \mathrm{y} < \mathrm{b}, \frac{\partial u_x^{\mathrm{II}}}{\partial z} = 0$

B.C. 9: at $y = 0, 0 < \mathrm{z} < \mathrm{c} - \delta$, $\frac{\partial u_x^{\mathrm{I}}}{\partial y} = 0$

B.C. 10: at $y = 0, \mathrm{c} - \delta < \mathrm{z} < \mathrm{c}$, $\frac{\partial u_x^{\mathrm{II}}}{\partial y} = 0$

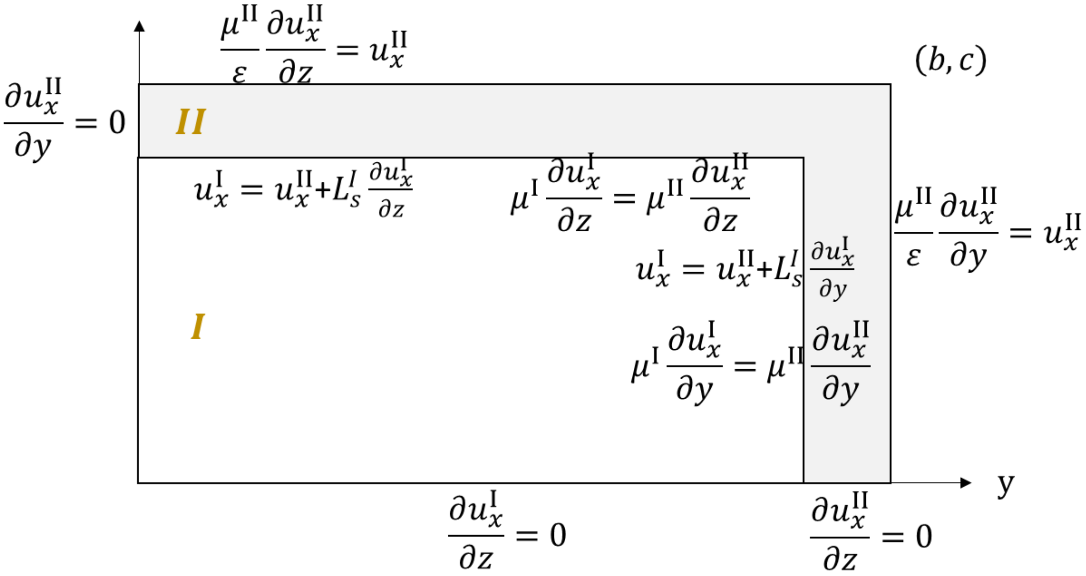

Figure 5.8 Schematic of modified Navier-Stokes equation within a rectangular nanotube. The boundary conditions are shown on each corresponding side. Region *I* is the bulk fluid and region *II* is the film fluid. The thickness of the adsorbed liquid film is represented by δ, in the unit of nm.

The nondimensionalization process for two-phase scenario is similar to the one-phase case. The nondimensional parameters are defined using equations from Eq. 5.25 to Eq. 5.29. However, since the boundary conditions are different, the dimensionless group extracted from the modified Navier-Stokes equations are different correspondingly, which are

$$\Pi_1 = \frac{{l_0}^2}{u_{x0}\mu^{\mathrm{I}}}\frac{\Delta p}{L} \tag{5.52}$$

$$\Pi_2 = \frac{{l_0}^2}{u_{x0}\mu^{\mathrm{II}}}\frac{\Delta p}{L} \tag{5.53}$$

$$\Pi_3 = \frac{L_s^{II}}{l_0} \tag{5.54}$$

$$\Pi_4 = \frac{\mu^{\mathrm{I}}}{\mu^{\mathrm{II}}} \tag{5.55}$$

$$\Pi_5 = \frac{L_s^{I}}{l_0} \tag{5.56}$$

where u_{x0} and l_0 are the unit constant and they are the characteristic value of the variables. The values are determined based on physical parameters in the problem to make the dimensionless group (Π_1, Π_2, Π_3, Π_4 and Π_5) in the same scale. L_s^I is the slip length of bulk fluid with respect to the film fluid, while L_s^{II} is the slip length of film fluid with respect to the solid wall. s^{I} and s^{II} are the dimensionless variables representing the velocity of fluid within different flow regions. m and n are the dimensionless variables representing the distance in y and z direction. b is introduced to describe the dimensionless thickness of the film liquid (region II). After the nondimensionalization of the variables, the Eq 5.23 and Eq. 5.24 become,

$$\frac{\partial^2 s^I}{\partial m^2} + \frac{\partial^2 s^I}{\partial n^2} = \Pi_I, in\ \Omega_I \tag{5.57}$$

$$\frac{\partial^2 s^{II}}{\partial m^2} + \frac{\partial^2 s^{II}}{\partial n^2} = \Pi_2, in\ \Omega_{II} \tag{5.58}$$

where Ω_{I} is the region I representing bulk liquid and Ω_{II} is the region II representing film liquid. The boundary conditions become,

B.C. 1: on $\Gamma_I, s^I = s^{II}$

B.C. 2: on Γ_I, $\left(\frac{\partial s^{II}}{\partial m}\vec{\imath} + \frac{\partial s^{II}}{\partial n}\vec{\jmath}\right)\overrightarrow{nn_1} = \Pi_4\left(\frac{\partial s^{I}}{\partial m}\vec{\imath} + \frac{\partial s^{I}}{\partial n}\vec{\jmath}\right)\overrightarrow{nn_1}$

B.C. 3: on Γ_{II}, $\Pi_3\left(\frac{\partial s^{II}}{\partial m}\vec{\imath} + \frac{\partial s^{II}}{\partial n}\vec{\jmath}\right)\overrightarrow{nn_2} = s^{II}$

B.C. 3: on Γ_I, $\Pi_5\left(\frac{\partial s^{II}}{\partial m}\vec{\imath}+\frac{\partial s^{II}}{\partial n}\vec{\jmath}\right)\overrightarrow{nn_1}+s^{II}=s^I$

where $\overrightarrow{nn_1}$ and $\overrightarrow{nn_2}$ are vectors in the direction perpendicular to the surface they exert on. This nondimensionalized equation is a general equation for different shapes, even for the irregular shapes.

5.5 Characterization of Alkane Flow in Nanotube

Recent investigations indicate that the shale rocks have stronger affinity to alkane than to water using (Ghanbari et al. 2015). Meanwhile, Xu et al. (2014) implement experiments to prove that the real driving force for oleic phase is higher than the capillary pressure estimated by Young-Laplace equation, which also proves the strong adsorption of alkane on pore wall. Wang et al. (2016a) implement MD simulation to study the density distribution of alkane in the cross sections of a flow channel composed by two parallel plates made of graphene or silica. Wang et al. (2016a) analyzed the structure of liquid phase and adsorption behavior based on MD simulations. Balasundaram et al. (1999) argued that the structure of molecules is shown by the density distribution achieved from the center-of-mass of alkane subunits instead of each hydrocarbon chain. Thus, the local density distribution of each section of oil implemented in this model is calculated by the subunits of alkane.

5.5.1 Density Distribution

As shown in Figure 5.3 (the density distribution of alkane within two parallel plates composed of graphene), the alkane density close to the solid surface oscillates intensely and the density distribution is symmetric with respect to the central plane. The pseudoatoms of octane stay at the positions with smaller potential energy caused by the uneven distribution between two slits, which has been proven by experiments (Christenson et al. 1987; Markesteijn et al. 2012). The positions with low potential are the peaks shown in the density profile of octane molecules within the cross section. The density troughs, at which region seldom molecules exist, are caused by the strong repulsion force of the dense layers of octane.

Wang et al. (2015) expressed that the octane molecules primarily stay in the parallel orientation to the surface due of the strong interactions between the solid wall and octane molecules. The decaying of density oscillation extends to four layers of alkane molecules from the silica substrate, where the thickness of each layer is measured to be approximate 4.5Å (Jin et al. 2000). Jin et al. (2000) measured the distance of density fluctuation using solvation force measurement, and the distance reveals to be 18-20 Å. The density of octane in the central part of the two slits is measured to be 0.686 g/cm^3 at temperature 353K and pressure 30Mpa. The density profile of alkanes was measured by experiments and MD simulations with respect to different types of solid materials, like silica, graphite and aluminum oxide (Ledyastuti et al. 2012; Le et al. 2015; Balasundaram et al. 1999). The trends of density oscillation near the solid are universal, and the spacing of layers is approximately the same as their molecular width instead of the chain length. However, the peak density of octane adjacent to the inorganic material is smaller than that near the organic matter, which indicates the strong adsorption force between liquid molecules and solid walls in organic pores.

The effect of the thickness of slit aperture on density distributions has been investigated by Wang et al. (2015). If the distance between two solid surfaces is smaller than 3.6 nm, the interaction potential of the two solid surfaces will strongly superimpose on each other and the bulk liquid is difficult to be distinguished from the film liquid. If the distance between the two parallel plates is larger than 3.6 nm, the confinement effect on the bulk liquid is small enough to be neglected. Then the bulk fluid and film fluid can be distinguished.

5.5.2 Viscosity Distribution and Slip Length

Recent literatures study the change of local alkane viscosity with respect to the distance from the solid surface while flowing across a nanopore. Different from the constant viscosity of bulk fluid in the central part of channel, the viscosity has been observed oscillating significantly in the interfacial region. I implement an average value to represent the oscillating viscosity of film liquid in characterizing alkane flow in nanoconfined tubes.

For octane flowing within a tube composed of graphene or silica, the slip velocity on the solid wall will increase with the pressure gradient increase (Wang et al. 2016a). However, in the low-pressure range, the slip length does not vary much with changing the pressure gradient. Botan et al. (2011) indicated that the slip length will be sensitive to driving force change if the pressure is larger than the critical value. It has been proved that the viscosity of the octane within liquid-film region has a negligible change with driving force variation. Wang et al. (2016a) and Wang et al. (2016b) proposed an experimental correlation between slip length and pressure gradient for both octane-silica and octane-graphene system by fitting the result of MD simulations. The fitting equation is:

$$L_s = C_1 exp\left(\frac{1}{C_2}\frac{dp}{dx}\right) + C_3 \tag{5.59}$$

In this equation, $\frac{dp}{dx}$ is the pressure gradient ($kcal/(mol$ Å)), L_s is the slip length (nm) and C_1, C_2 and C_3 are the fitting parameters. For the octane-graphene system, C_1 is 6.900, C_2 is 1.536×10^{-6} and C_3 is 87.901; for the octane-silica system, C_1 is 0.830, C_2 is 0.00495 and C_3 is -0.090.

Temperature is another factor affecting the properties of nanoconfined octane within both organic and inorganic tubes. The fluctuations in the density distribution of the octane adjacent to the solid surface are similar under different temperature. Fewer molecules can be adsorbed on the surface under higher temperature due to the increase of kinetic energy. Zhang et al. (2012) validated this theory using the experiment of methane adsorption in shale cores. Voronov et al. (2006) indicated that the alkane flow capacity in graphene tubes becomes higher with temperature increasing by implementing non-equilibrium molecular dynamics simulation of LJ particles. Voronov et al. (2006) argued that the temperature has complex influences on the slippage effect through affecting the molecular interactions. Wang et al. (2016a) provided an empirical equation describing the change of slip length with respect to the different temperature in both graphene and silica channels:

$$L_s = C_1 exp\left(\frac{1}{C_2}T\right) + C_3 \tag{5.60}$$

where T is the temperature in the unit of K. For octane-graphene system, C_1 is -1.260×10^{-6}, C_2 is 41.689 and C_3 is 138.946; for octane-silica system, C_1 is 4.47×10^{-5}, C_2 is 47.130 and C_3 is 0.714.

As the MD simulation indicated, the slippage effect is also affected by the thickness of slit aperture (Chen et al. 2008). With the pore size decreasing, the interaction of each solid surface on alkane molecules increase, which will cause the slip length increase correspondingly. In relatively large pores, the slip length varies slightly with diameter change; while within the pores whose size is smaller than the critical value, the slip length increases dramatically with the pore size decrease (Chen et al. 2008). The empirical relationship between the thickness of slit aperture with the slip length was proposed by Wang et al. (2016a):

$$L_s = C_1 exp\left(\frac{1}{C_2} w\right) + C_3 \tag{5.61}$$

where w is the thickness of slit aperture in the unit of nanometer. For the octane-graphene system, C_1 is 311.367, C_2 is -1.0236 and C_3 is 129.135; for the octane-silica system, C_1 is 0.387, C_2 is -32.470 and C_3 is 0.826.

5.6 Characterization of Water Flow in Nanotube

5.6.1 Slip Length

The water flow rate in graphene nanotubes is significantly affected by the slip length. Numerous molecular dynamics (MD) simulation studies and experiments are carried out, and they prove that the flow enhancement caused by the boundary-slippage effect differs by one to five orders of magnitude from the traditional Navier-Stokes equation with no-slip boundary condition (Kannam et al. 2013).

Recent studies have shown that water molecules can form a thermodynamically driven depletion layer on contacting a hydrophobic surface resulting in a low surface friction factor, which will cause a velocity ‘jump’ on interface (Joseph et al. 2007). Huang et al. (2008) argued that the thickness of depletion layer would decrease with the contact angle increase, and the slip length would decrease correspondingly. The relationship between slip length and the thickness of depletion layer ($b \propto \delta^4$), was proposed by Huang et al. (2008). So, the slippage effect will be mitigated in hydrophilic nanotubes because of the decrease of depletion-layer thickness. Wu et al. (2017) proposed the empirical relationship between true slip length of water flow with respect to contact angle is

$$L_s = \frac{0.41}{(\cos\theta + 1)^2} \tag{5.62}$$

where L_s is the slip length of water flowing at the solid wall and θ is the contact angle between water and the solid wall. The prerequisite of implementing Eq. 5.50 is that the viscosity needs to be constant of film-liquid region; so, the fitting equation is appropriate to be employed in the mathematical model proposed in this work since I use an average value to represent the equivalent viscosity of film region. Here 0.41 (Wu et al. 2017) is a fitting parameter from molecular dynamic simulation rather than by experiments, because the effective slip length estimated by experiments is a combination of many factors, including wall roughness, wall wettability and experiment environment (Granick et al. 2003; Schmatko et al. 2005; Doshi et al. 2005). Joly et al. (2006) argued that it needs to pay attention while using Eq. 5.50 with contact angle larger than 145°, because chances are high to make a significant discrepancy from the real slip length with even a small error.

It is essential to be noted that the slip length of water on the wall is also influenced by other factors besides contact angle. Even though slippage effect is more apparent contacting hydrophobic surface caused by the strong repulsion force, Ho et al. (2011) indicated that water also slip on hydrophilic interface by analyzing the result of MD simulation. Ho et al. (2011) argued that the reason of slippage phenomenon of water on hydrophilic surface is that water molecules migrating from one position to another can occur if the preferential adsorption sites are very close to each other. As reported by Li et al. (2012), the contact angles of water on graphene and boron nitride are similar and the structure of water molecules in contact with solid surface are also very similar, but the slip length varies significantly. This phenomenon has been investigated and attributed to the corrugation of energy landscape on boron nitride increasing because of electronic structure effects, so the slip length is not only related to contact angle (Tocci et al. 2014). It has been studied by MD simulations that the slip length depends on the electronic structure and on the composition of solid wall, which has been validated by experiments also (Suk et al. 2014; Hilder et al. 2009; Joly et al. 2006; Secchi et al. 2016). Although slippage effect is not exclusively determined by contact angle, many investigations express the influence of wetting behavior is significant (Cottin-Bizonne et al. 2002; Byun et al. 2008; Zhu et al. 2012). So, it is still reasonable to implement Eq. 5.62 to estimate the slip length using contact angle in characterizing flow capacity in nanoconfined tubes.

5.6.2 Viscosity Distribution

The viscosity of water near surface region increases with the decreasing of contact angle, because strong interaction caused by dense hydrocarbon bonding network will make the structure of water-film more stable (Qin et al. 2015). To characterize the relationship between viscosity and contact angle, I implement the empirical equation fitted with MD simulations (Wu et al. 2017),

$$\mu_i = \mu_\infty(-0.018\theta + 3.25) \tag{5.63}$$

where μ_i is the average viscosity of film-water, and μ_∞ is the viscosity of bulk-liquid. It needs to be noted that the water viscosity of film-liquid varies with confinement size as investigated through MD simulations implemented by Qin et al. (2015). Quantitively speaking, the viscosity of water-film on a hydrophilic surface decreases with confinement size increasing (Goertz et al. 2007); while for hydrophobic solid surface, the viscosity increases with tube-size increasing (Chen et al. 2008). Ortiz-Young et al. (2013) and Raviv et al. (2001) implement experiments of water flowing through nanoconfined channels and revealed that the viscosity of confined water varies spatially, which is attributed to the difference of dynamic properties and structures of nano-confined water adjacent to solid wall. However, the influence of size-confinement of nanopores with diameter larger than 1.4 nm is not dramatic compared to the influence of contact angle as proved by experiments performed by Raviv et al. (2001). The effect of other factors could be neglected on the change of viscosity, and I assume that the viscosity of water film is a constant value with fixed wettability.

5.7 Characterization of Water Film

Within inorganic pores, water molecules are adsorbed on the pore wall and clay particles by hydrogen bond, Van der Waals force and electrostatic force. Based on the theory of thermodynamic equilibrium between water and vapor, Li's model can be used to estimate the properties of water film. Li et al. (2016) proposed the formula:

$$\Pi(h)V_w = -RTln\left(\frac{p_v}{p_o}\right) \tag{5.64}$$

where h is the water-film thickness; $\Pi(h)$ is the disjoining pressure between water film and solid surface, which is a function of the thickness of water film; V_w is the water molar volume (m^3/mol); p_v is the partial pressure of vapor (MPa) and p_o is the saturated vapor pressure (MPa).

As described above, disjoining pressure is the summation of three molecular forces, including structure force, electrical force and London-Van der Waals force. Here the disjoining pressure for slit is expressed as (Li et al. 2016)

$$\Pi_w(h) = \Pi_1(h) + \Pi_2(h) + \Pi_3(h) \tag{5.65}$$

$$\Pi_1(h) = \frac{A_H}{h_w^3} + \frac{\varepsilon\varepsilon_o(\xi_1-\xi_2)^2}{8\pi h_w^2} + \kappa e^{-\frac{h_w}{\Gamma}} \tag{5.66}$$

$$\Pi_2(h) = \frac{A_H}{(h_{int}-h_w)^3} + \frac{\varepsilon\varepsilon_o(\xi_1-\xi_2)^2}{8\pi(h_{int}-h_w)^2} \tag{5.67}$$

$$\Pi_3(h) = \frac{A_{H^*}}{(h_{int}-2h_w)^3} \tag{5.68}$$

where $\Pi_1(h)$ (MPa) is the disjoining pressure between the solid surface and water film by considering the long-range molecular force and short-range structural force. $\Pi_2(h)$ (MPa) represents the disjoining force between the solid surface and water film at the opposite side of the silt. $\Pi_3(h)$ (MPa) represents the disjoining pressure between water films on the opposite side of the solid surface. A_{H^*} is the Hamaker constant for solid-liquid-vapor interactions and A_H is the Hamaker constant of solid-liquid interactions, both of which are in the unit of J. ξ_1 (mV) is the electrical potential of the water-solid interfaces and ξ_2 (mV) is the electrical potential of the water-octane interfaces. Γ (nm) is the characteristic length of water molecules. κ (N/m^2) represents the coefficient of the structural-force strength. ε (dimensionless) is the relative dielectric permittivity of water and ε_o (F/m) is the electric constant within vacuum condition. The thickness of water film can be predicted by substituting Eq. 5.65 into Eq. 64.

5.8 Construction of Multi-scale Liquid Flow Model

I implement MD simulation to evaluate the slip length of liquid on the solid boundary under different conditions, including driving force, temperature, hydraulic diameter and the composition of the solid wall. Then, the calculated slip length is implemented into the modified Navier-Stokes equation to characterize the flow capacity of liquid in nanotubes with different cross-sectional geometry and different composition. Since the pore throats in the dendroidal model are represented by nanotubes, the apparent permeability of each single nanotube characterized by the mathematical model can be implemented into the dendroidal model to predict the apparent permeability in core-scale.

The dendroidal model integrates the experimental data of mercury injection/imbibition, nitrogen isothermal adsorption/desorption, Fourier Transform Infrared (FTIR), Low Pressure Helium Pycnometry and Total organic carbon (TOC). Coupling the information from different aspects, dendroidal model have high representativeness of the real porous media of shale core samples.

The pores in shale porous media are categorized in the organic pore and inorganic pore generally, within which the liquid flow capacities are different. Moreover, the minerology of inorganic pores will influence the flow capacity as well, especially for water.

Most of the clay minerals in shale are hydrophilic (Sun et al. 2017), while organic matters are hydrophobic. In inorganic pores, the influence of minerology will be more significant on water than that on alkane, since the interaction force between a solid wall and fluid is strong for wetting phase. Consequently, this multi-scale model does not distinguish the inorganic pores with different compositions when simulating alkane flow through porous media. For water flow in the porous media, the multi-scale model distinguishes the inorganic pores with different composition.

Relative permeability is calculated by simulating the process of injecting water into the dendroidal model originally filled with oil. Initially, water is injected from left surface with an increasing pressure into a core sample. The capillary pressure required for water to invade into each pore throat is calculated by Eq. 5.2. For each pressure incremental step, water phase could invade into more pore throats, and the corresponding water saturation is recorded. The relative permeability is calculated by,

$$k_{rw} = \frac{q_{mw}}{q_{sw}} \tag{5.69}$$

$$k_{rnw} = \frac{q_{mnw}}{q_{snw}} \tag{5.70}$$

where q_{mw} is the flow rate of the wetting phase in multi-phase flow condition, and q_{sw} is the flow rate of wetting phase in single phase flow condition. q_{mnw} is the flow rate of non-wetting phase in multi-phase flow condition, and q_{snw} is the flow rate of non-wetting phase in single-phase flow condition. The total flow rate in multi-phase flow is calculated by mass conservation at the pore i,

$$\sum_j q_{i,j} = 0 \tag{5.71}$$

where j represents the pore-throats connected to specific pore i. I assume that the pressure drops caused by the viscose effect can be neglected compared with capillary pressure. The other assumption is that the fluid is incompressible. Then, the liquid flow rate in the pore throat between every two adjacent pores can be expressed as,

$$q_{w,ij} = \frac{k_{rw,ij} A_{ij}}{\mu L_{ij}} \left(p_i - p_j\right) \tag{5.72}$$

where $k_{rw,ij}$ is the relative permeability of wetting phase within pore throat j; A_{ij} and L_{ij} are the cross-sectional area and length of this pore throat j connected to pore i. Since there is no fluid trapping in circular pore throats, the pressure of pore i and j are represented by the single-phase pressure p_i and p_j. A linear equation set can be defined by implementing Eq. 5.71 and Eq. 5.72 in every pore throat, and then it can be solved in terms of pore pressure. With the pressure of each pore body calculated, relative permeability for each phase can be characterized correspondingly by Eq. 5.72.

5.9 Case Study

In this section, I implement the modified Navier-Stokes equation to characterize the apparent permeability of octane within a single pore with various cross-sectional geometry under different conditions, including temperature, driving force and hydraulic diameter. Then, I analyze the influence of different parameters on the apparent permeability of octane within the nanoconfined tubes. The apparent permeability of the whole core sample in centimeter scale can be predicted using dendroidal theoretical pore-network model, consequently.

5.9.1 Apparent Permeability of Single Tube

Wang et al. (2016a) and Wang et al. (2016b) published the results of 56 sets of MD simulations of octane flow simulation within graphene nanotubes and silica nanotubes, which will be used in this multi-scale liquid flow model to perform the characterization of octane flow in single nanopore. For convenience, I list the results of MD simulation of octane-graphene system in table 5.1 and those of octane-silica system in table 5.2. The effects of nanoconfinement and boundary slippage have been tested under different operational systems by MD simulations, with which I can implement the modified Navier-Stokes equation to characterize the influence of each single parameter on the flow capacity of octane in a single nanopore.

The slip length provided by the published works is measured by the MD simulation of fluid flow in slit-shape channels instead of closed-shape ones (circle, rectangle and triangle). Falk et al. (2011) implement MD simulations to investigate the flow capacity of different liquids (water, ethanol, decane and octamethylcyclotetrasiloxane) in carbon nanotubes, and the results indicate that both surface roughness and surface curvature will affect the surface friction factor. However, the effect of surface curvature on flow capacity will be negligible if the diameter of tube is larger than 2.8 nm. The effect of surface curvature is negligible in this model, because the sizes of most of the pores in shales are larger than 2.8 nm, which is characterized by the visualization of SEM images. Moreover, in the dendroidal model, the pore throats with extremely small diameters are in the branching paths, which have negligible effects on the predicted flow capacity of a core sample. Consequently, implementing the slip length measured by MD simulations in silt-shape pores into the pore throats with different cross sections (circular, rectangular and triangular) can still provide a reasonable prediction. However, a correction factor is required to implement the slip length measured in slit-shape channels. For octane flowing in nanotubes, the proposed method (Falk et al. 2011) can be implemented to correlate the slip length in the closed-shape tubes with the slip length in slit-shape tubes. At first, the hydraulic diameter is defined as:

$$R_h = \frac{4A}{P} \tag{5.73}$$

where R_h is the hydraulic diameter (nm); A is the area of pore-throat cross section (nm^2); P is the perimeter (nm). The slip length can be evaluated by Eq. 5.61, where the value of w should be the hydraulic diameter with correction. The correction is performed by $L_{s,e} = L_{s,r} - \varepsilon$, where $L_{s,r}$ is the real slip length measured by MD simulations, $L_{s,e}$ is the corrected slip length implemented into Eq. 5.61 and ε is the correction factor (nm). Figure 5.9 shows the change of correction factor with respect to the dimensionless geometry factor, which is the plot of 600 cases of pore throats with different cross sections. It indicates that the correction factor would be small at large geometry factors. The slip length changes dramatically with slit aperture thickness varies. If the thickness is smaller than the critical value, the cross sections with small dimensionless geometry factor will have large slip length. The correlation between the dimensionless geometry factor and the correction factor is as follows,

$$\varepsilon = -81.76 ln(G) - 229.11 \tag{5.74}$$

which will be used to estimate the real slip length of various cross sections.

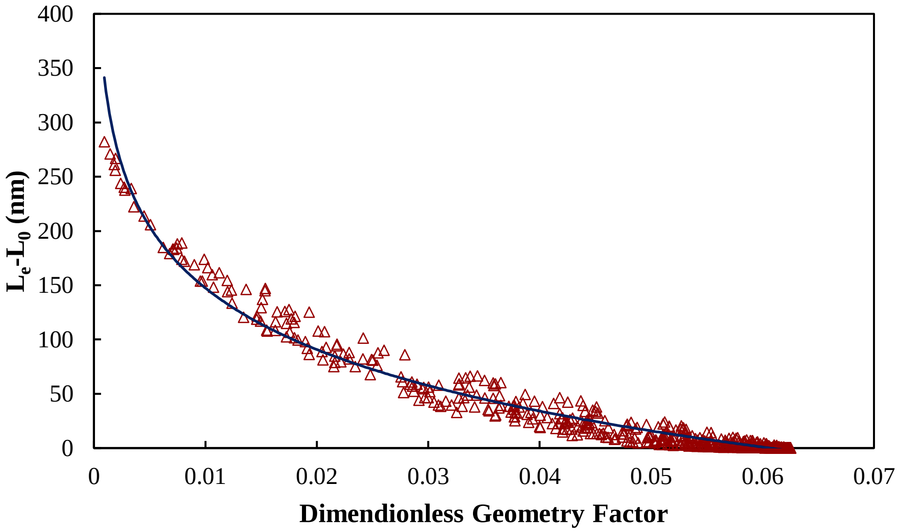

Figure 5.9 The difference of real slip length measured by MD simulation and estimated by hydraulic diameter with respect to difference geometry factor.

Figure 5.10, Figure 5.11 and Figure 5.12 show the velocity distribution of liquid flowing in the nanotubes with different cross-sectional geometry, which is characterized by the modified Navier-Stokes equation coupling nanoconfinement effect and boundary-slippage effect. Figure 5.10 shows the velocity distribution of octane flowing through an organic triangular tube. Figure 5.11 shows the velocity distribution of octane flowing through inorganic rectangular tubes. Figure 5.12 shows the velocity distribution of octane flowing across an organic rectangular tube. The other parameters (hydraulic diameter, temperature and driving force) of the simulations in Figure 5.10, Figure 5.11 and Figure 5.12 are same, where the only differences are the cross-sectional geometry and the solid wall composition. It can be identified that there are stagnant liquid films in the corner of the angular cross section, while there is no stagnant liquid film in the circular tubes. Thus, the flow capacity of liquid in the pore throats with circular cross section is larger than that in polygonal tubes, because the stagnant fluid causes an increase of resistance in fluid transport.

Table 5.1 Slip length estimated by non-equilibrium molecular dynamic simulation within octane-graphene system. (Wang et al. 2016a)

temperature (K)	**Width** (nm)	**nF** $(kcal/(mol\,\text{Å}))$	**Slip Length** (nm)	**Viscosity of Bulk-Octane** (μcp)
353	5.24	5.10E-07	97.95	354
353	5.24	1.02E-06	100.65	354
353	5.24	2.15E-06	116.18	354
353	5.24	2.87E-06	132.48	354
353	1.74	2.87E-06	184.97	354
353	3.46	2.87E-06	138.21	354
353	5.24	2.87E-06	132.48	354
353	7.61	2.87E-06	129.16	354
353	11.17	2.87E-06	128.41	354
353	5.24	2.87E-06	132.48	354
373	5.24	2.87E-06	130.40	308.80
393	5.24	2.87E-06	122.55	234.59
413	5.24	2.87E-06	113.94	171.85

Then I calculate the flow capacity of octane in the organic pores and inorganic pores with different cross sections and analyze the effect of each parameter on flow capacity within a single nanopore. For each case of the numerical calculation of the octane flow in a single nanopore, I randomly assign the side length of each side of a rectangle or a triangle, but the hydraulic diameter is maintained consistent. The cross-sectional shapes of all the cases are listed in table 5.3. I calculate the velocity profiles of bulk-octane in the central region and film-octane near the wall (table 5.4). The flux of bulk-octane in case 5, 6, 20, 21 is zero, because the pore size is too small to have a bulk region.

Table 5.2 Slip length estimated by non-equilibrium molecular dynamic simulation within octane-silica system. (Wang et al. 2016b)

temperature (K)	**Width** (nm)	**nF** $(kcal/(mol\,\text{Å}))$	**Slip Length** (nm)	**Viscosity of Bulk-Octane** (μcp)
353	5.40	1.00E-04	0.77	354
353	5.40	2.50E-04	0.78	354
353	5.40	5.00E-04	0.81	354
353	5.40	7.50E-04	0.87	354
353	5.40	1.00E-03	0.94	354
353	5.40	2.00E-03	1.15	354
353	1.74	7.50E-04	0.24	354
353	3.46	7.50E-04	0.26	354
353	5.24	7.50E-04	0.30	354
353	7.61	7.50E-04	0.30	354
353	11.17	7.50E-04	0.31	354
353	5.40	7.50E-04	0.28	354
373	5.40	7.50E-04	0.27	308.80
393	5.40	7.50E-04	0.24	234.59
413	5.40	7.50E-04	0.21	171.85

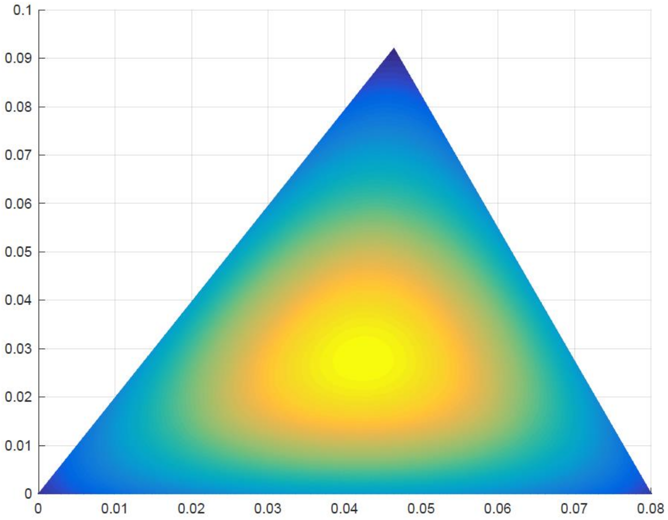

Figure 5.10 Schematic of the velocity profile in inorganic pore throats with a triangular cross section. x axis and y axis represent the dimensionless length, which are defined as $x = l_0\tilde{x}$ and $y = l_0\tilde{y}$, where l_0 is 100 nm.

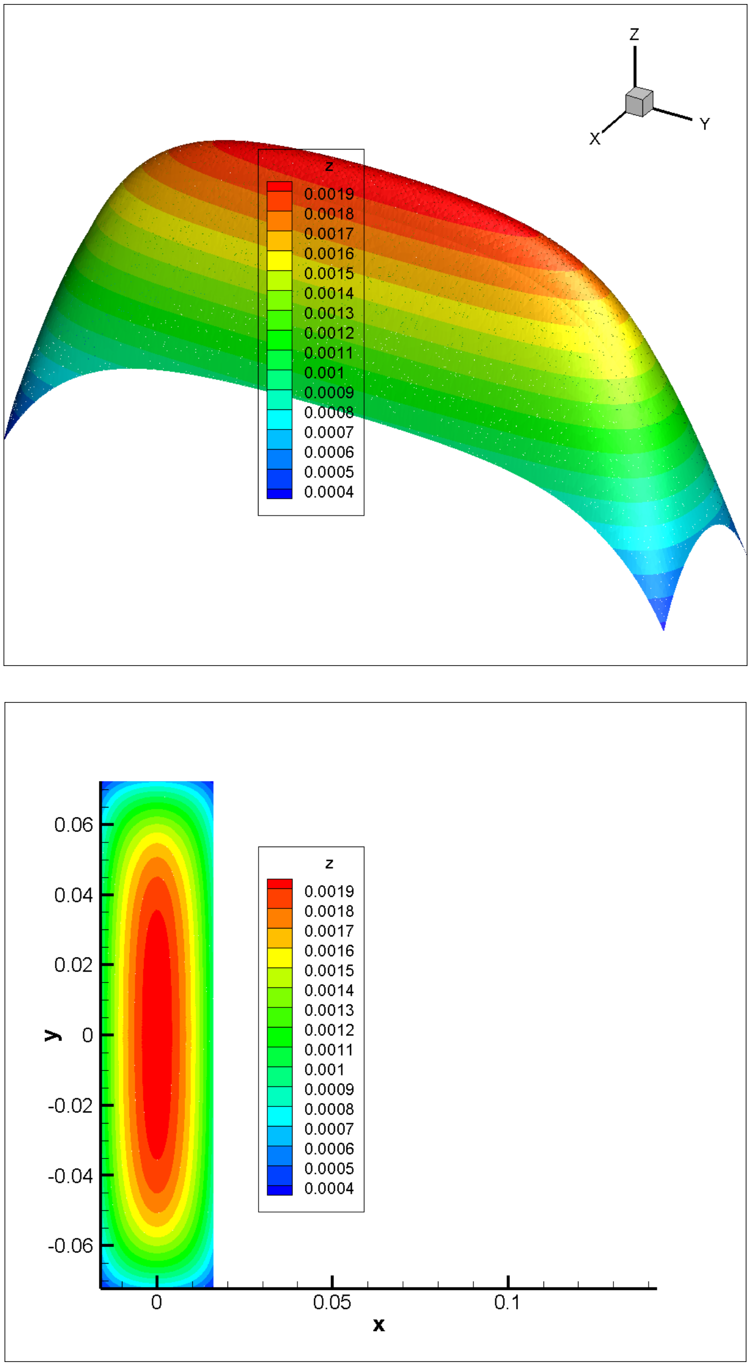

Figure 5.11 Schematic of the velocity profiles in organic pore throats with a rectangular cross-section. x axis and y axis represent dimensionless length, which are defined as $x = l_0\tilde{x}$ and $y = l_0\tilde{y}$, where l_0 is 100 nm.

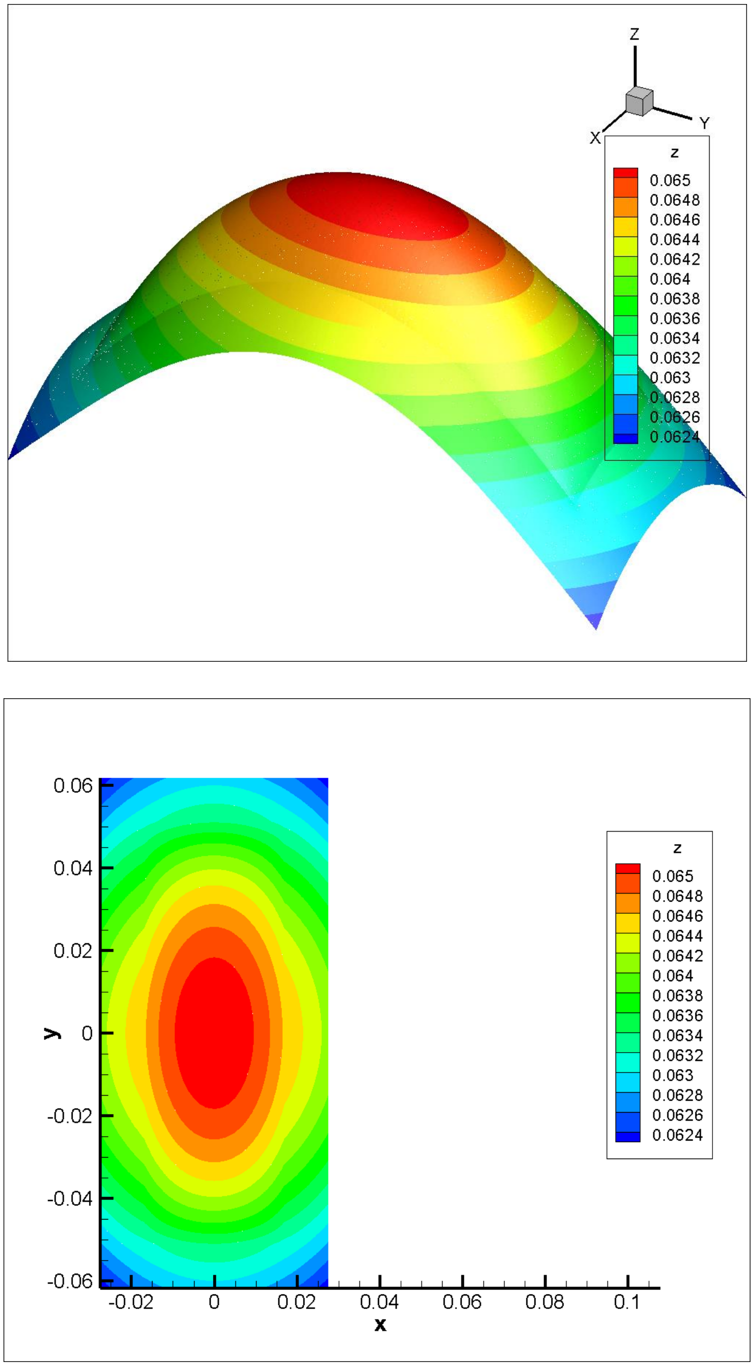

Figure 5.12 Schematic of the velocity profile in a inorganic pore throat with rectangular cross section. x axis and y axis represent dimensionless length, which are defined as $x = l_0\tilde{x}$ and $y = l_0\tilde{y}$, where l_0 is 100 nm.

Table 5.3 Geometry of the pore-throat cross section of each case.

Case Number	Composition	Rectangle Side-A (nm)	Rectangle Side-B (nm)	Triangle Side-A (nm)	Triangle Side-B (nm)	Triangle Side-C (nm)
1	Organic	4	7.59	8	9.8	10.31
2	Organic	4.5	6.27	7	12.98	14.7
3	Organic	3.2	14.46	7.2	12.8	15.1
4	Organic	2.9	27.14	8.33	9.2	10.5
5	Organic	1.2	3.16	2.5	3.54	4.02
6	Organic	2.1	9.82	5.31	10	13
7	Organic	3.5	10.42	6.54	15	15
8	Organic	5.5	12.35	11.27	15	18
9	Organic	7.2	24.9	13.86	59	65
10	Organic	5.24	5.24	6.68	14	14
11	Organic	3.5	10.42	7.2	12.74	15
12	Organic	3.8	8.44	7.9	12.15	15.8
13	Organic	4.2	6.96	5.9	32.31	31
14	Inorganic	4	7.59	8	9.8	10.31
15	Inorganic	4.5	6.27	7	12.98	14.7
16	Inorganic	3.2	14.46	7.2	12.8	15.1
17	Inorganic	2.9	27.14	8.33	9.2	10.5
18	Inorganic	3.2	14.46	7.2	12.8	15.1
19	Inorganic	2.9	27.14	8.33	9.2	10.5
20	Inorganic	1.2	3.16	2.5	3.54	4.02
21	Inorganic	2.1	9.82	5.31	10	13
22	Inorganic	3.5	10.42	6.54	15	15
23	Inorganic	5.5	12.35	11.27	15	18
24	Inorganic	7.2	24.9	13.86	59	65
25	Inorganic	5.24	5.24	6.68	14	14
26	Inorganic	3.5	10.42	7.2	12.74	15
27	Inorganic	3.8	8.44	7.9	12.15	15.8
28	Inorganic	4.2	6.96	5.9	32.31	31

Table 5.4 Flux in rectangular pore-throat calculated by the modified Navier-Stokes equation, where total octane flux is the flux of octane in the whole cross section.

Case Number	Composition	Bulk-Octane Flux (m/s)	Film-Octane Flux (m/s)	Total Octane Flux (m/s)
1	Organic	5.97	5.90	5.93
2	Organic	12.27	12.13	12.18
3	Organic	29.74	29.51	29.57
4	Organic	45.16	44.89	44.96
5	Organic	0.00	20.74	20.74
6	Organic	0.00	30.89	30.89
7	Organic	45.22	44.87	44.98
8	Organic	64.46	63.56	64.01
9	Organic	94.88	92.81	94.15
10	Organic	45.25	44.85	44.99
11	Organic	51.03	50.64	50.76
12	Organic	63.20	62.65	62.83
13	Organic	80.32	79.52	79.80
14	Inorganic	4.30	2.65	3.21
15	Inorganic	7.25	4.34	5.36
16	Inorganic	15.81	11.22	12.54
17	Inorganic	23.68	18.23	19.58
18	Inorganic	38.80	28.20	31.25
19	Inorganic	80.84	64.63	68.65
20	Inorganic	0.00	8.56	8.56
21	Inorganic	0.00	15.69	15.69
22	Inorganic	30.56	16.99	21.25
23	Inorganic	54.17	23.17	38.95
24	Inorganic	84.60	30.95	65.58
25	Inorganic	32.41	15.12	21.25
26	Inorganic	33.66	18.48	23.25
27	Inorganic	43.32	21.84	28.95
28	Inorganic	48.16	22.41	31.28

Table 5.5 Flux in triangular pore throats calculated by the modified Navier-Stokes equation, where total octane flux is the flux of octane in the whole cross section.

Case Number	Composition	Bulk-Octane Flux (m/s)	Film-Octane Flux (m/s)	Total Octane Flux (m/s)
1	Organic	7.00	5.89	5.96
2	Organic	13.10	11.70	12.40
3	Organic	30.63	29.53	30.13
4	Organic	45.79	44.59	45.19
5	Organic	0.00	20.77	20.77
6	Organic	31.49	31.49	31.49
7	Organic	45.85	45.85	45.85
8	Organic	64.78	64.78	64.78
9	Organic	108.47	100.47	105.47
10	Organic	47.68	45.68	45.68
11	Organic	52.00	51.60	51.60
12	Organic	64.48	63.88	63.88
13	Organic	89.23	88.63	88.63
14	Inorganic	4.64	2.56	3.30
15	Inorganic	7.64	4.13	5.37
16	Inorganic	16.48	12.02	12.60
17	Inorganic	27.11	15.46	19.59
18	Inorganic	41.44	26.49	31.33
19	Inorganic	91.80	55.98	68.68
20	Inorganic	0.00	8.65	8.65
21	Inorganic	23.15	14.40	15.72
22	Inorganic	33.73	14.49	21.31
23	Inorganic	56.28	20.14	38.95
24	Inorganic	75.41	44.64	65.64
25	Inorganic	10.79	34.15	21.32
26	Inorganic	10.67	30.41	23.28
27	Inorganic	14.59	38.50	29.03
28	Inorganic	16.50	39.44	31.31

5.9.2 Sensitivity Analysis of Octane Flow within Single Tube

In this section, I analyze the influence of each parameter, including pressure gradient, temperature and hydraulic diameter, on the flow capacity of octane within the pore throats composed of organic matter or inorganic matter.

Figure 5.13 (a)(b)(c)(d) compare the volume flux of octane subject to various driving force within the nanotubes with different cross section and different composition. The volume flux is characterized at the temperature of 373K. The hydraulic diameters of all the cases are 5.24 nm. With the pressure gradient increase, the flow capacity of octane within inorganic pore throats increases as well, which is a result of the increment of slip length. Figure 5.13 (a)(b) indicate that the flux of bulk-fluid is larger than that of film fluid, which is agreed with the results characterized either MD simulations or mathematical models (Zhang et al. 2017; Wu et al. 2017; Wang et al. 2016a). Figure 5.13 (a) indicates that the flux of film liquid is smaller than that of bulk liquid. While for Figure 5.13 (c), which represents the flux varies with the change of pressure gradient in rectangular organic tubes, shows that the bulk fluid has similar flux with film-liquid flux. The difference of the figures for organic and inorganic tubes is caused by the variance of slip length. Since the slip length is larger in organic tubes, the properties difference (density and viscosity) between film liquid and bulk liquid would not cause a significant difference on the film-liquid flux and bulk-liquid flux. Because the slip length is small for octane flowing in inorganic tubes, the flux difference of bulk fluid and film fluid caused by the different density and viscosity is more significant.

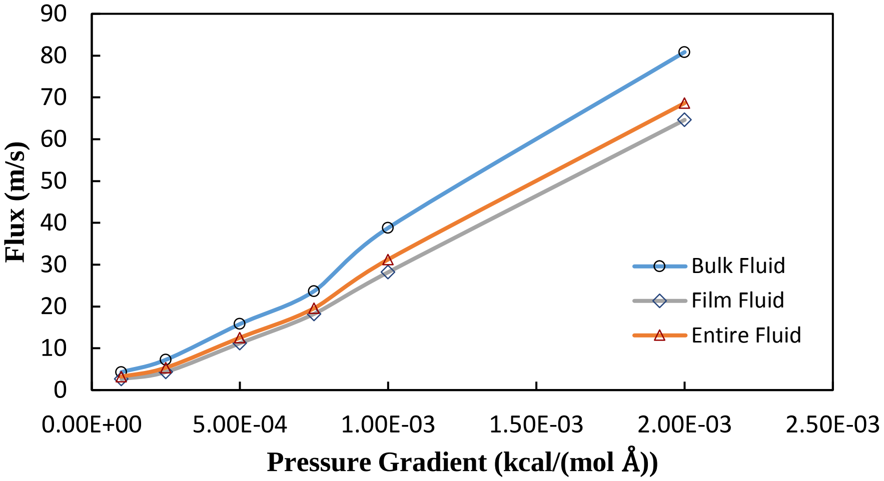
90
80
70
60
50
40
30
20
10
0
Flux (m/s)
0.00E+00
5.00E-04
1.00E-03
1.50E-03
2.00E-03
2.50E-03
Pressure Gradient (kcal/(mol Å))
Bulk Fluid
Film Fluid
Entire Fluid

(a)

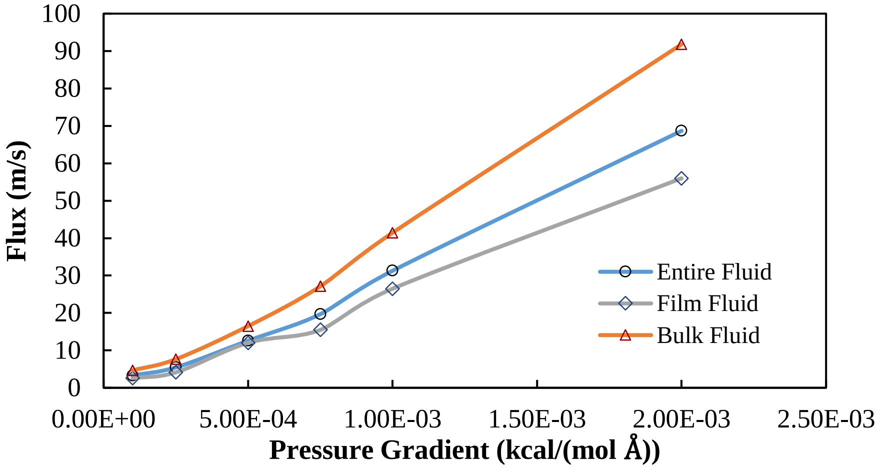
100
90
80
70
60
50
40
30
20
10
0
Flux (m/s)
0.00E+00
5.00E-04
1.00E-03
1.50E-03
2.00E-03
2.50E-03
Pressure Gradient (kcal/(mol Å))
Entire Fluid
Film Fluid
Bulk Fluid

(b)

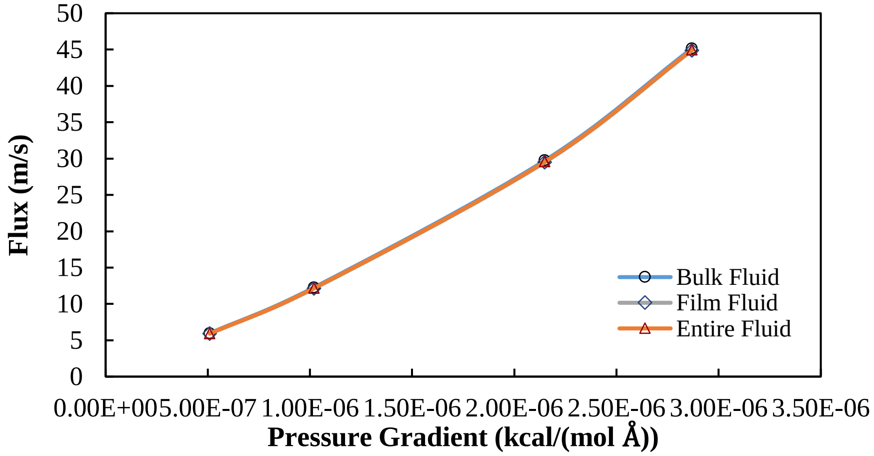
50
45
40
35
30
25
20
15
10
5
0
Flux (m/s)
0.00E+00
5.00E-07
1.00E-06
1.50E-06
2.00E-06
2.50E-06
3.00E-06
3.50E-06
Pressure Gradient (kcal/(mol Å))
Bulk Fluid
Film Fluid
Entire Fluid

(c)

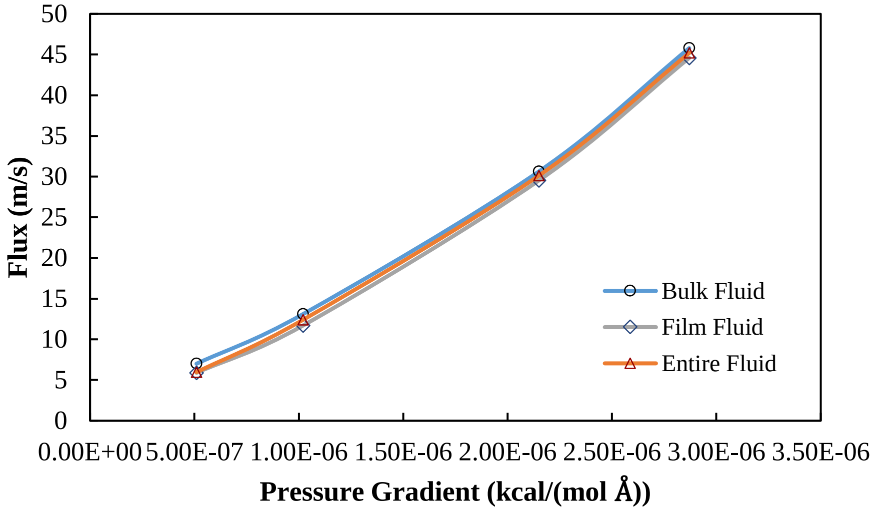

(d)

Figure 5.13 Change of flux of bulk liquid, film liquid and entire liquid with respect to the variation of pressure gradient in both inorganic pores and organic pores. The measurements are under the same operation conditions except for the pressure gradient. (a) Inorganic rectangle pore; (b) Inorganic triangle pore; (c) Organic rectangle pore; (d) Organic triangle pore.

Figure 5.14 (a)(b)(c)(d) indicate the volume flux change with respect to different hydraulic diameter for both organic tubes and inorganic tubes. The flux is measured at the temperature of 373K, and the pressure gradient of all cases are $7.5 \times 10^4\ kcal/(mol \cdot \text{Å})$. Figure 5.14 indicates that the flux would increase with the hydraulic diameter increase for both organic tubes and inorganic tubes regardless of the cross-sectional shape. However, Wang et al. (2016b) have proved that the slip length decreases with hydraulic diameter increase. In figure 5.14, the volume flux of bulk fluid in nanotubes with the hydraulic diameter of 1.74 nm is zero. Because the hydraulic diameter of the cross section of pore throat is extremely small, the bulk fluid does not exist, where all the fluid molecules are accounted as the film fluid due to the strong force of the solid wall. Since the slip length is large in organic pores, the difference of flux between bulk fluid and film fluid in the organic pore is not apparent.

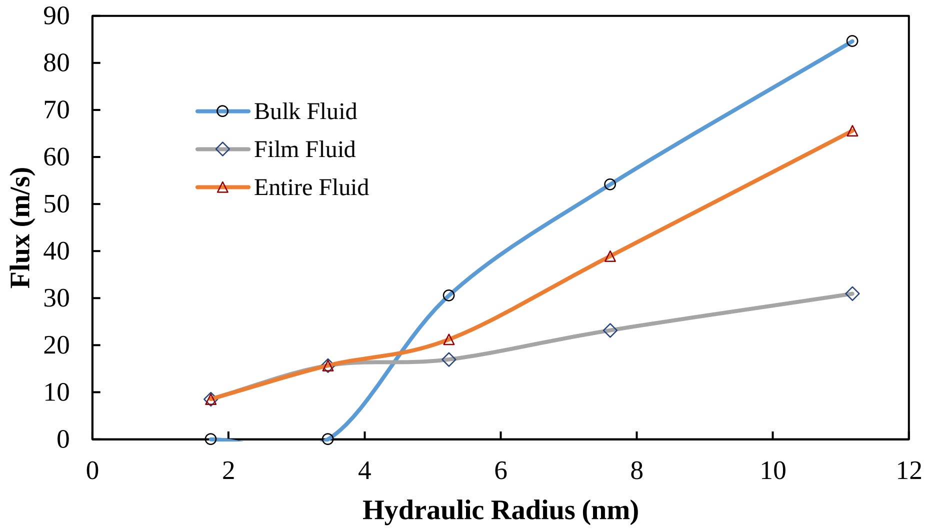

(a)

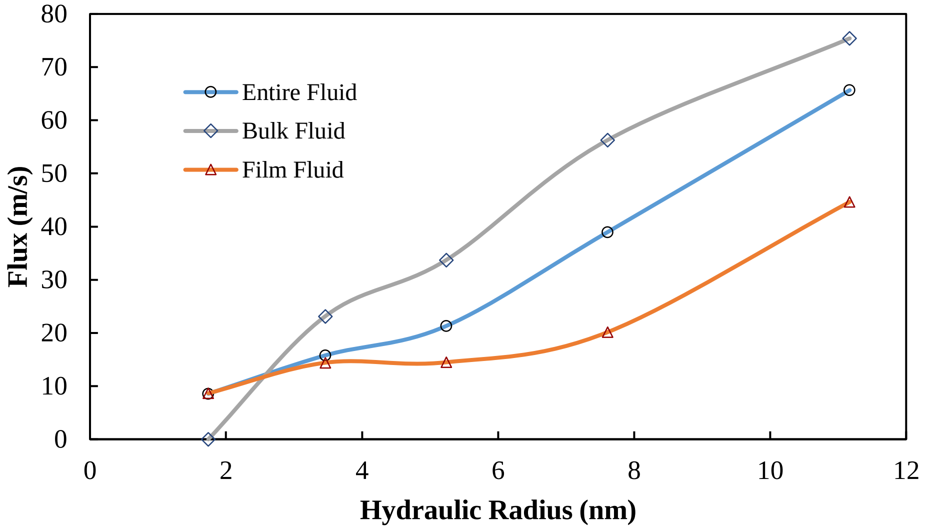

(b)

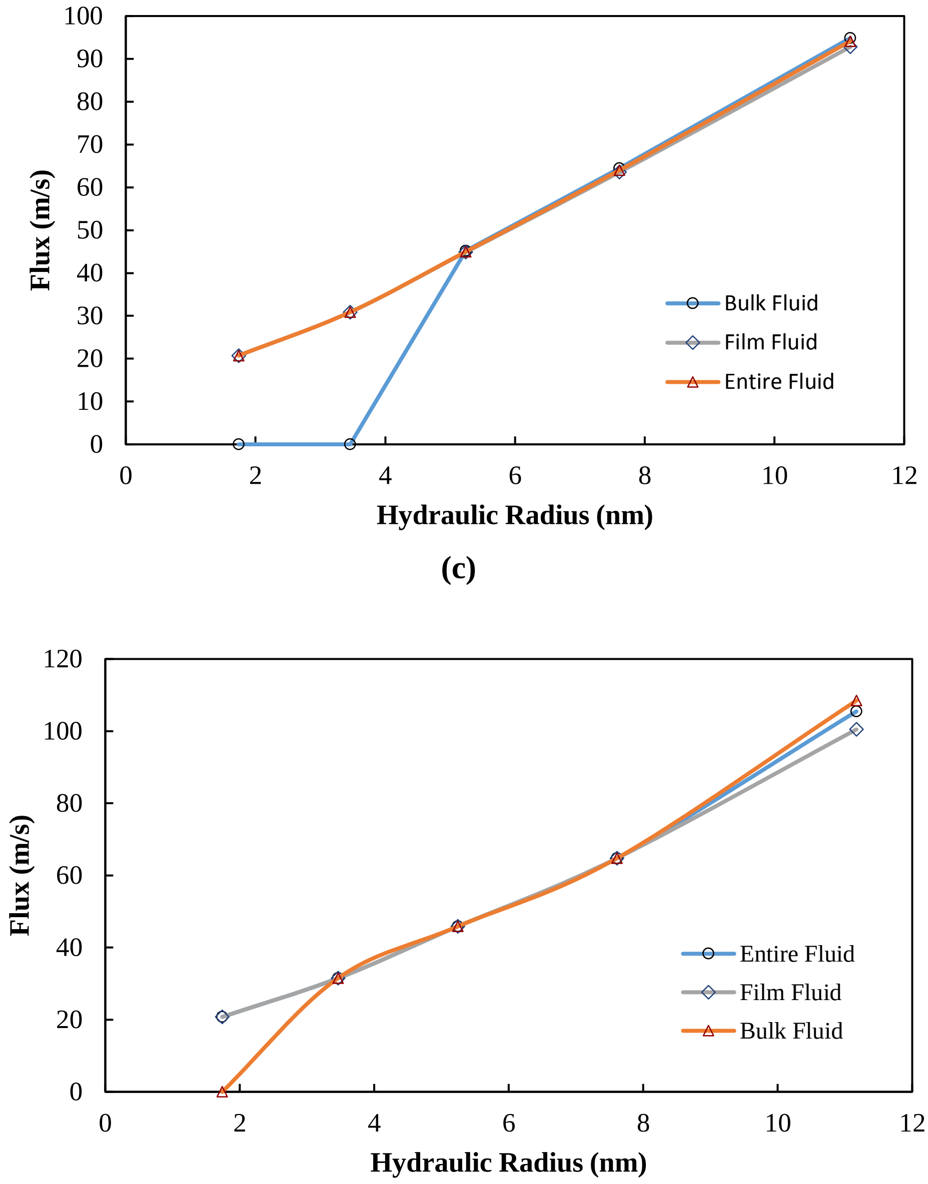

(c)

(d)

Figure 5.14 Change of flux of bulk fluid, film fluid and entire fluid with respect to the variation of the hydraulic radius in both inorganic pores and organic pores. The measurements are under the same operation conditions except for the hydraulic radius. (a) Inorganic rectangle pore; (b) Inorganic triangle pore; (c) Organic rectangle pore; (d) Organic triangle pore.

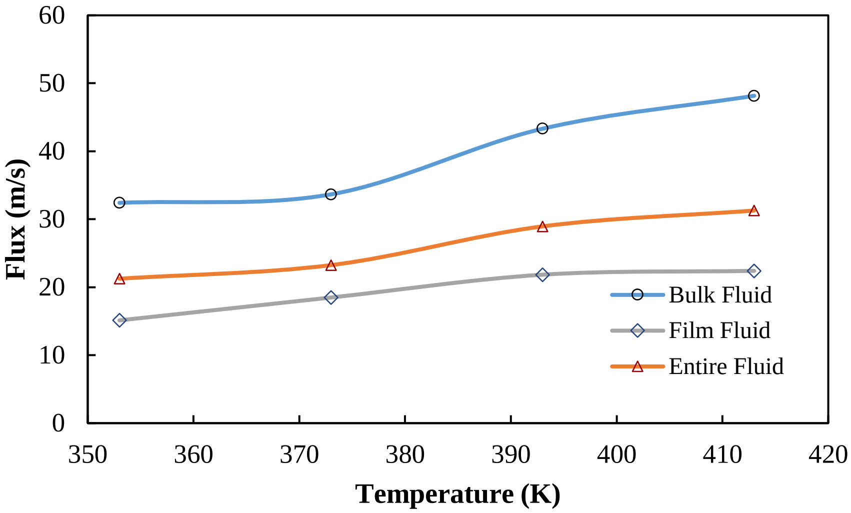

60
50
40
30
20
10
0
Flux (m/s)
350
360
370
380
390
400
410
420
Temperature (K)
Bulk Fluid
Film Fluid
Entire Fluid

(a)

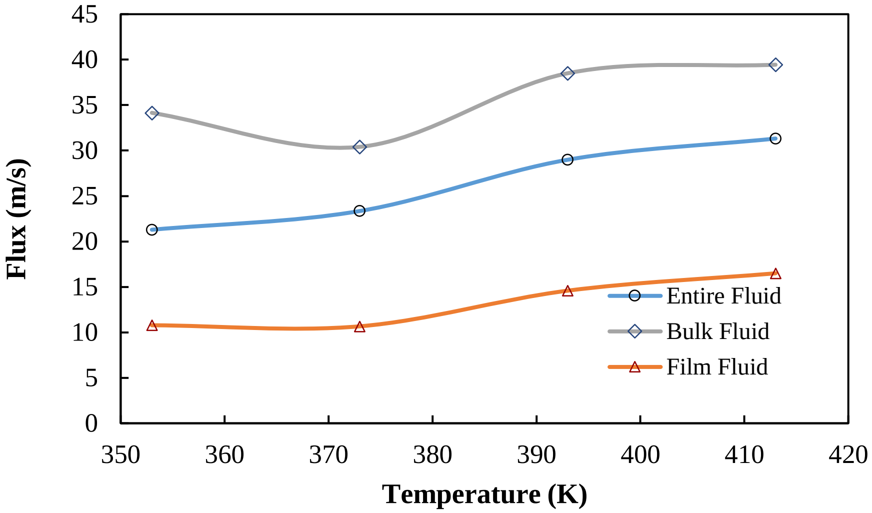

45
40
35
30
25
20
15
10
5
0
Flux (m/s)
350
360
370
380
390
400
410
420
Temperature (K)
Entire Fluid
Bulk Fluid
Film Fluid

(b)

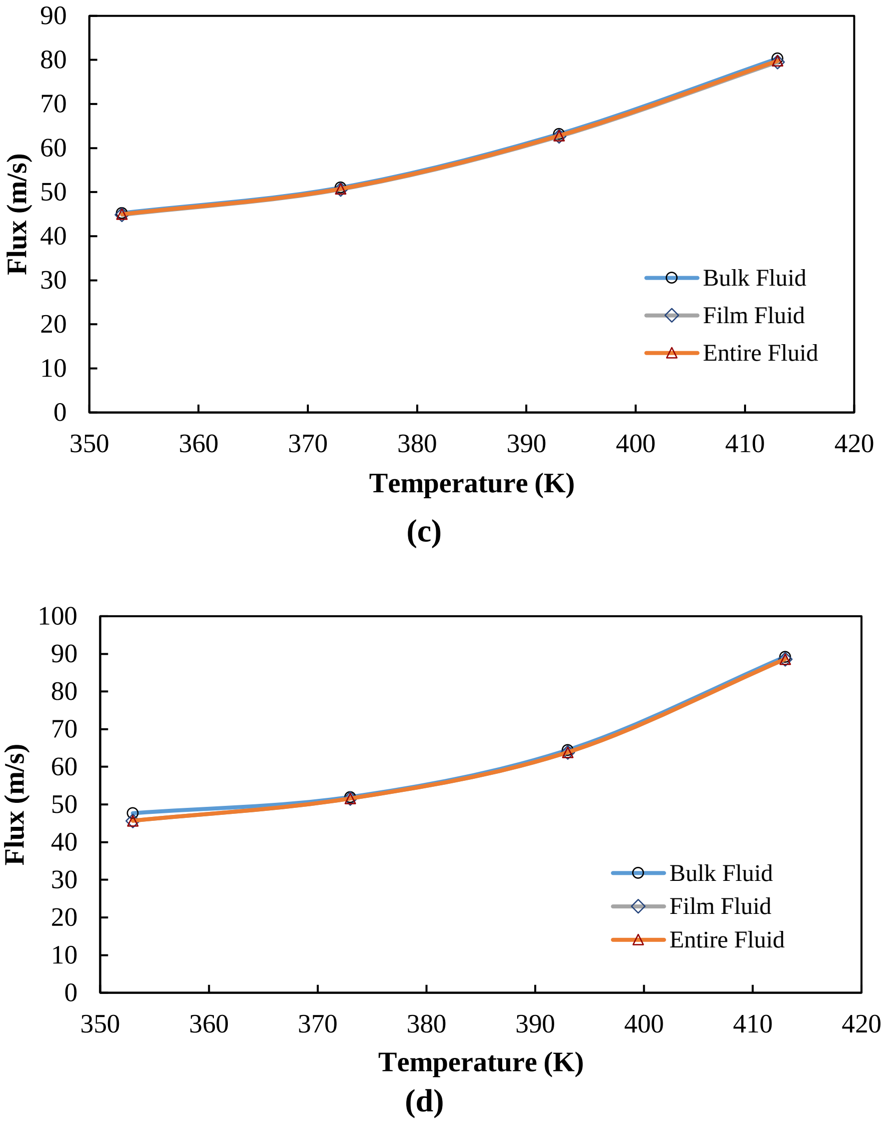

Figure 5.15 Change of flux of bulk liquid, film liquid and entire fluid with respect to the variation of temperature in both inorganic pores and organic pores. The measurements are under the same operation environments except for the temperature. (a) Inorganic rectangle pore; (b) Inorganic triangle pore; (c) Organic rectangle pore; (d) Organic triangle pore.

Figure 5.15 (a)(b)(c)(d) show the flux change with respect to different temperature. The flux is measured at the hydraulic diameter equals to 5.24 nm, and the pressure gradient of all cases are $7.5 \times 10^4\ kcal/(mol \cdot Å)$. In the MD simulation, it has been proved that the slip length would decrease with temperature increase, which is caused by the change of interaction intensity between the solid wall and fluid molecules. However, with temperature increase, the viscosity of fluid will decrease. The rate of viscosity decrease of the film fluid and the bulk fluid are different. Accounting for these two effects overall, the flux will increase with the temperature increase, even though the slip length decrease. The results of this new mathematical model are same as thoes of the MD simulations proposed by Wang et al. (2016a).

Here, I use the parameter, the enhancement factor, to account for the enhancement of apparent permeability with both boundary-slippage effect and nanoconfinement effect with respect to the intrinsic permeability without these effects considered,

$\varepsilon = k_{app}/k_{abs}$,

where k_{app} is the apparent permeability considering boundary-slippage effect and k_{abs} is the absolute permeability. Figure 5.16 (organic tubes) and Figure 5.17 (inorganic tubes) indicate the change of enhancement factor with respect to different parameters, including driving force, hydraulic diameter and temperature. The magnitude of enhancement factor of octane within organic nanotubes is larger than that in inorganic nanotubes, which is caused by the difference of slip length. In the MD simulation, it has been investigated that the slip length of octane in organic pores is approximately ten time larger than that in inorganic pores.

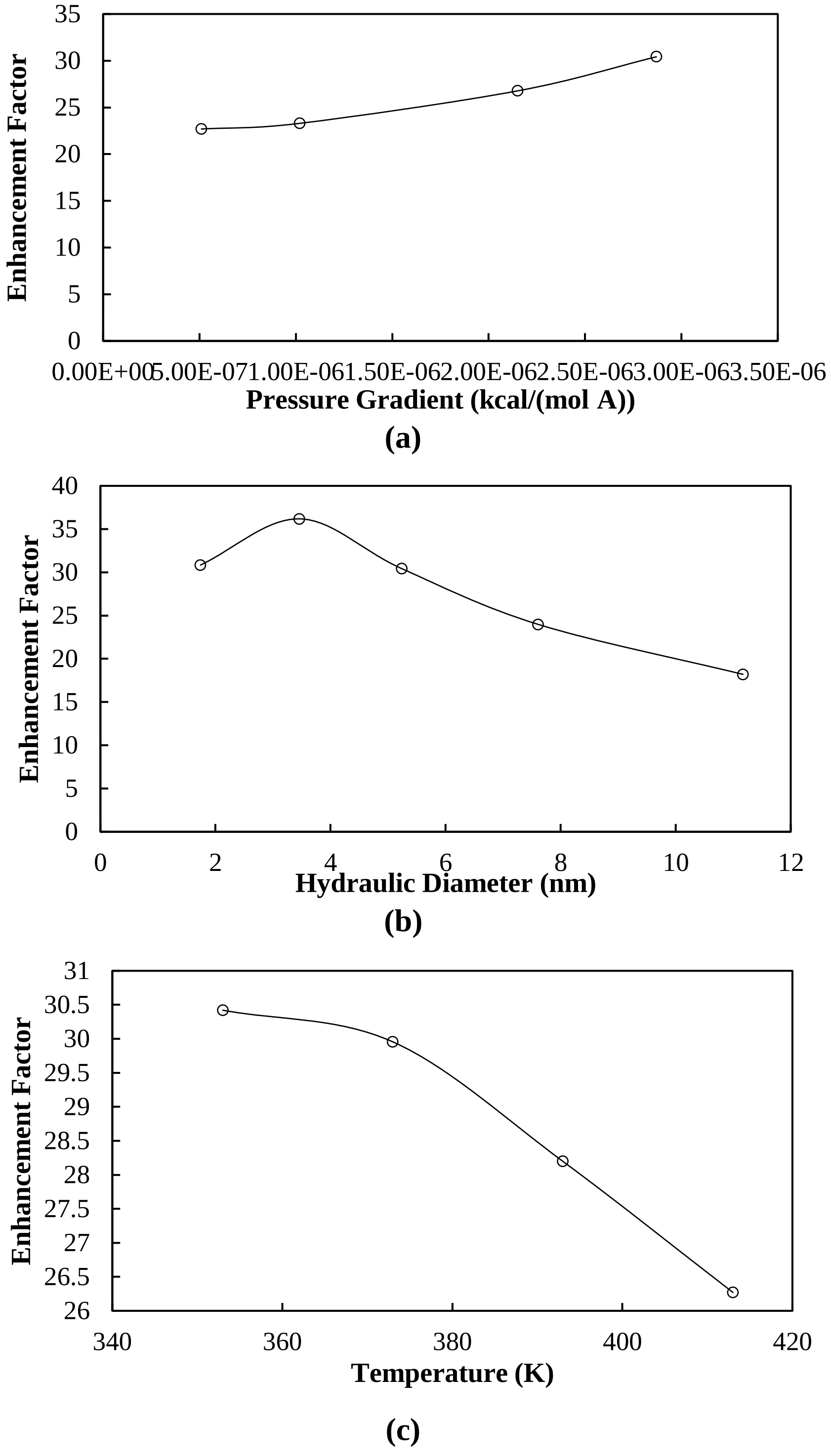

Figure 5.16 In organic pores, the change of enhancement factor with respect to different parameters, including (a) driving force, (b) hydraulic diameter, and (c) temperature.

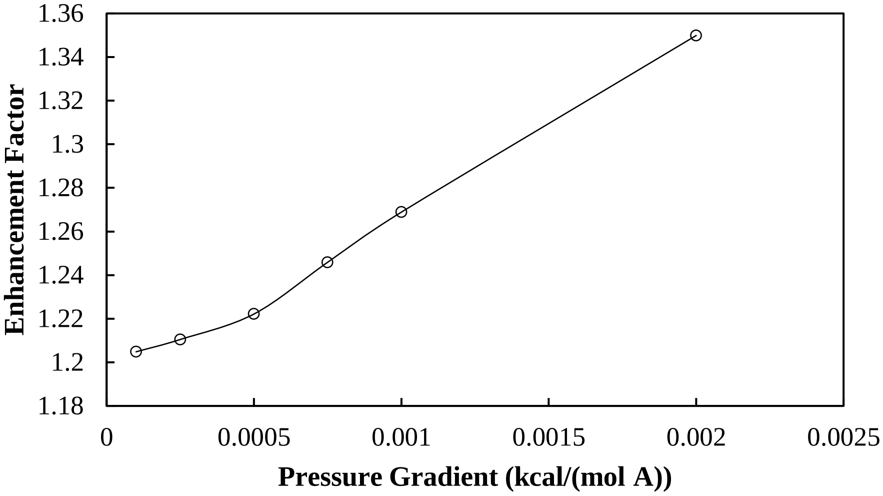
1.36
1.34
1.32
1.3
1.28
1.26
1.24
1.22
1.2
1.18
Enhancement Factor
0
0.0005
0.001
0.0015
0.002
0.0025
Pressure Gradient (kcal/(mol A))

(a)

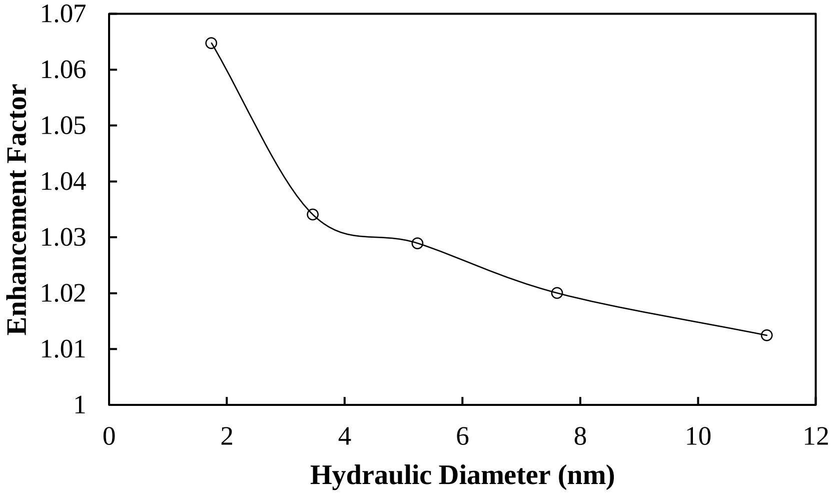
1.07
1.06
1.05
1.04
1.03
1.02
1.01
1
Enhancement Factor
0
2
4
6
8
10
12
Hydraulic Diameter (nm)

(b)

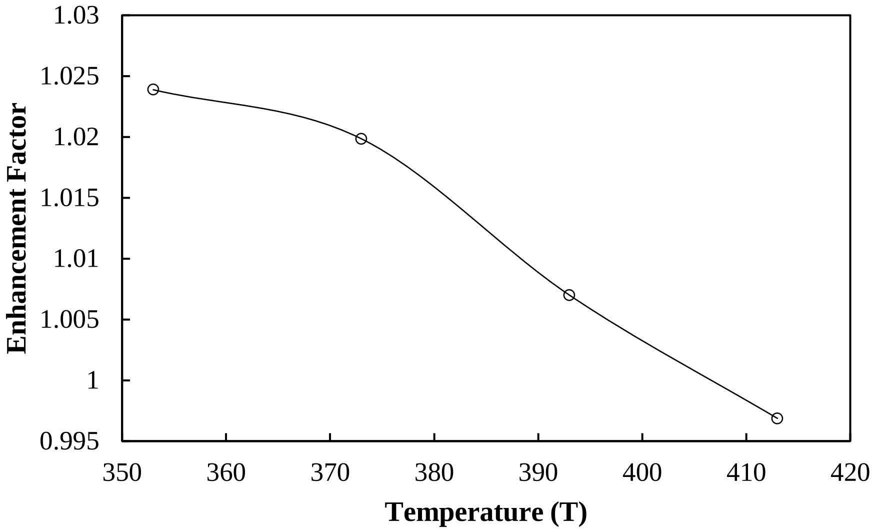

(c)

Figure 5.17 In inorganic tubes, the enhancement factor change with respect to different parameters, including (a) driving force, (b) hydraulic diameter, and (c) temperature.

5.9.2 Prediction of Apparent Permeability of Core Sample

In this section, I construct a dendroidal theoretical pore-network model to perform the prediction of apparent permeability of octane in a shale core sample. As mentioned above, the effect of minerology of inorganic pores on octane flow capacity within a single pore is negligible, so the dendroidal model in this case does not distinguish the minerology of inorganic pores. Only the organic pores and the inorganic pores are classified, and the inorganic pores are not sub-classified further.

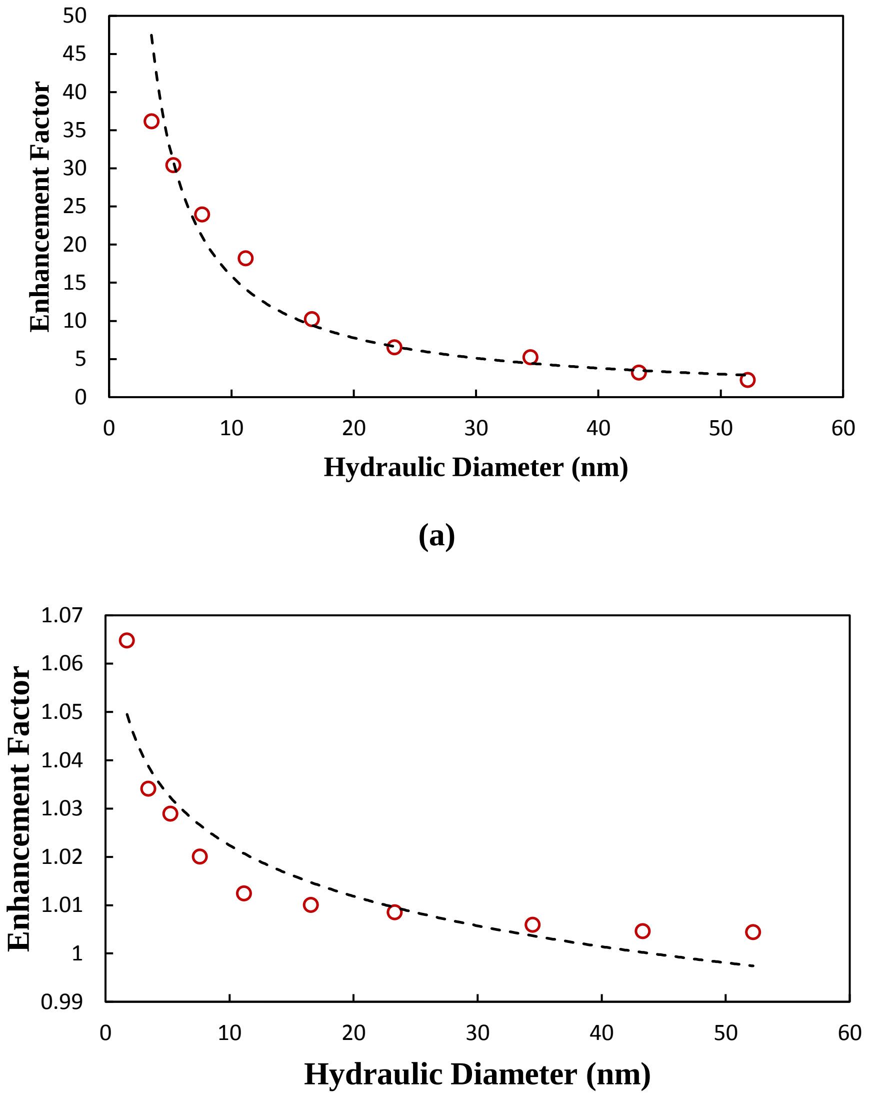

(a)

(b)

Figure 5.18 Enhancement factor with respect to different hydraulic diameter in (a) organic pores and (b) inorganic pores.

I use the core samples from Marcellus shale and Wolfcamp shale to perform the prediction of apparent permeability of octane. The detailed procedure of constructing the dendroidal model is explained in chapter 3. In the dendroidal model, the pore throats are in the geometry of triangle, rectangle and circle. The apparent permeability of each single pore considering boundary-slippage effect and nanoconfinement effect has been systematically characterized before. The effect of geometry on flow capacity is accounted for by implementing the hydraulic diameter and the dimensionless geometry factor.

The procedure of evaluating apparent permeability by the dendroidal model has been explained. Here, I calculate the apparent permeability of octane in shale core samples considering boundary-slippage effect and nanoconfinement effect. With the temperature equals to 374K and the driving force equals to $5 \times 10^4 kcal/(mol \cdot \text{Å})$, Figure 5.18 shows the enhancement factor with respect to different hydraulic diameters calculated by the modified Navier-Stokes equation, which will be implemented in the dendroidal model subsequently. It expresses that the enhancement factor of the pore throats with large hydraulic diameter is small. moreover, the enhancement factor is even negligible for the inorganic tubes with large hydraulic diameter. The intrinsic permeability of Marcellus shale and Wolfcamp shale without considering boundary-slippage effect and nanoconfinement are predicted to be 55 nd and 72 nd respectively, while the apparent permeabilities are 69 nd and 95 nd. Therefore, the enhancement factor for the core sample of Marcellus shale and Wolfcamp shale are 1.18 and 1.31 respectively. The results indicate that the enhancement factor for both two core samples are small, which is caused by the spatial distribution of the pores in shale porous media. The main flow paths contribute to most of the flow capacity of shale porous media. In these main flow paths, which have relatively large hydraulic diameter, the boundary-slippage effect is not significant. While the branching paths, which have relatively large enhancement factor, do not contribute much to the flow capacity of the core sample. Meanwhile, the enhancement factor of a core sample is significantly affected by the distribution of organic pores and inorganic pores, where the slippage effect is more significant in organic pores than inorganic pores.

Chapter 6 Limitations and Future Recommendations

6.1 Limitations

In this work, I developed the dendroidal theoretical pore-network model and improved the algorithm of extracted pore-scale modeling. Meanwhile, I predict the apparent permeability of shale core samples. However, there are some limitations in these two pore-network models and the multi-scale permeability characterization model.

In the dendroidal theoretical pore-network model, the interaction between natural fractures and the pores in matrix is considered. Therefore, the scale of this model is limited to the range of several centimeter. The model needs to be improved to consider facture distribution and its connection with pores, then it can be implemented to characterize the porous media in a larger scale.

The pores in a core sample are composed by different types of minerals, which have been characterized in the dendroidal model by implementing the Fourier Transform Infrared Spectroscopy (FTIR) experiment and the total organic carbon measurement. With the fraction of each mineral, I randomly distributed the minerals in the dendroidal model to assign the pore wall with different compositions. However, the randomly distribution of minerology cannot be accurately validated by experiments, which will cause discrepancies from the real minerology distribution in core samples.

The extracted pore-network model has limitations in accurately estimating ultimate recovery factor of rock core samples, because it stores the geometry information by dimensionless geometry factor, which cannot accurately capture the trapping effect of pore throats and pore bodies. Meanwhile, implementing the dimensionless geometry factor to characterize the geometry of the pores is too simplified to accurately estimate the relative permeability, since the trapping mechanisms of the pores with various geometry would have different influences on the relative permeability.

For the model of multi-scale characterization of apparent permeability of rock core samples, it uses three shapes (triangle, rectangle and circle) to represent the cross sections of the pore throats. Even though the geometry of cross section is random by stochastically assigned the lengths and angles, it cannot represent the complex geometry of pores in the real core samples accurately.

6.2 Future Recommendation

In constructing a theoretical pore-network model, the minerology distribution should be validated by experiments or scanning image analysis. With a reasonable minerology distribution, the influence of minerology on the apparent permeability and relative permeability can be characterized more accurately. Meanwhile, the fracture distribution and the interactions between fractures and the pores in matrix should be characterized in the pore-network model as well. Nuclear Magnetic Resonance (NMR) can characterize the pore-size distribution, which is the combination of the distribution of pore bodies and pore throats (Li et al. 2017a; Li et al. 2017b). After construction of the dendroidal model, NMR measurement can be implemented to validate the pore-size distribution to make it more representative of the real pore structure.

In the extracted pore-network model, the geometry of each pore body and pore throat should be stored in detail, instead of using the dimensionless geometry factor. Correspondingly, the ultimate recovery factor and relative permeability can be estimated to a more accurate extent. The information of minerology should be characterized as well in the extracted pore network model, since the influence of minerology on the flow capacity and the trapping capacity of different fluid could be significant. Therefore, to accurately predict the ultimate recovery factor and transport properties, including apparent permeability and relative permeability, the information of minerology and geometry of both pore bodies and pore throats should be characterized in the extracted pore-network model.

In the multi-scale characterization of liquid flow in shale porous media, instead of using simple geometries (rectangle, triangle and circle) to derive the relationship between apparent permeability of a single nanotube with different geometries, a more representative relationship should be proposed. Therefore, the relationship can be implemented into the extracted pore network model to predict the apparent permeability of a rock core sample in micrometer scale with higher accuracy than the theoretical pore-network model. The apparent permeability characterized by multi-scale model can be implemented into reservoir simulation and production data analysis (Zheng et al. 2016a; Zheng et al. 2016b; Yuan et al. 2016).

Chapter 7 Conclusion

Integrating seven distinct types of experimental data, the dendroidal pore-network model is constructed, which can capture the unique characteristics of shale core samples. Pore bodies and pore throats with various cross-sectional shapes are implemented to improve the representativeness of the pore-network model. The stochastically distributed pore-throat lengths, coordination numbers and spatial distributions render a more realistic analog of the shale porous media. The parameters in these distributions are adjusted based on the analysis of the mercury imbibition experiments considering contact-angle hysteresis and trapping hysteresis. The dual-compressibility model is introduced into constructing a pore-network model for the first time to eliminate the compressibility effects during mercury-drainage experiments. The measurements of total organic carbon and minerology are implemented to characterize the composition of pores. Pore composition can have a significant influence in predicting permeabilities.

Following the complete procedures of constructing a dendroidal model, I build theoretical pore-network models for shale core samples of Marcellus and Wolfcamp formations. The parameters and spatial distributions are evaluated, and the frequency of imbibition events are summarized. Absolute permeability without slippage effect is calculated and proved to be in a reasonable range.

A novel algorithm based on the maximal-ball method has been developed to extract pore-network models for shale core samples from scanning-electron microscopy images. Our novel approach considers extremely small pores and the limited connectivity in shales. The size of the pore bodies and pore throats can be identified more precisely using this method than available approaches in the literature. This significantly reduces the pore-volume estimation error. Different configurations of pore connectivity have been investigated using this pore-network modeling framework. The shape factors of each pore throat and pore body can also be characterized precisely. Thus, the extracted pore-network models can be used to determine transport properties and oil-recovery factor to yield more realistic values as this model accounts for complex geometry and extremely small size of the pore bodies and pore throats. I verified this novel pore-network modeling method using the samples from Marcellus shale. I analyzed in details the pore characteristics of four subsections from the Marcellus shale sample using this approach.

Because of the significantly large number of pores in shales compared to that in conventional reservoirs, simulating large volume of shales porous media can be time-consuming using extracted pore-network models. However, this model can leverage on high-performance parallel computational techniques by dividing the sample into subsections.

Molecular dynamics (MD) simulation of steady-state liquid flow in nano-confined tubes captures the complex physics caused by the strong interaction between the solid wall and fluid molecules. The properties, including viscosity, density and surface friction factor, vary in the cross section of nanotubes. I developed a modified Navier-Stokes equation to characterize the velocity distribution of liquid in nanotubes with different cross-sectional geometries and compositions. Correspondingly, it calculates the apparent permeability of single nanotubes coupling the boundary-slippage and nanoconfinement effects. Afterwards, I implement the dendroidal model to predict the apparent permeability of shale core samples in centimeter scale. The dendroidal model, integrating the information of pore structure from different experiments, yields high representativeness of the shale porous media. The apparent permeability of a single pore is highly sensitive to the composition of pores. The dendroidal model, which distinguishes the organic and inorganic pores, provides a relatively accurate prediction of apparent permeability.

The results from MD simulation indicate that the flow capacity of nano-confined liquid can be 1 to 3 orders of magnitude different from that calculated by Navier-Stokes equation without considering the boundary-slippage effect. The geometry and composition also have considerable effect on the surface friction factor and viscosity in the near-wall liquid film, which in turn influence the flow capacity in nano pores significantly. I quantify the apparent permeability in core-scale under different pressures and temperatures. The apparent permeability in core-scale appears to be sensitive of the spatial distribution of pore throats with different sizes, geometries and compositions. Whereas, the distribution of pore bodies does not have considerable influence of apparent permeability in core-scale. Without coupling the effect of boundary-slippage effect in predicting the apparent permeability in core-scale, the discrepancy could be significant.

Reference

Adesida, A.G., Akkutlu, I., Resasco, D.E. and Rai, C.S., 2011, January. Characterization of barnett shale kerogen pore size distribution using DFT analysis and grand canonical monte carlo simulations. In SPE Annual Technical Conference and Exhibition. Society of Petroleum Engineers.

Al-Kharusi, A.S. and Blunt, M.J., 2007. Network extraction from sandstone and carbonate pore space images. Journal of Petroleum Science and Engineering 56: 219-231.

Balasundaram, R., Jiang, S. and Belak, J., 1999. Structural and rheological properties of n-decane confined between graphite surfaces. Chemical Engineering Journal, 74(1-2), pp.117-127.

Barrett, E.P., Joyner, L.G. and Halenda, P.P., 1951. The determination of pore volume and area distributions in porous substances. I. Computations from nitrogen isotherms. Journal of the American Chemical society, 73(1), pp.373-380.

Barrat, J.L. and Bocquet, L., 1999. Large slip effect at a nonwetting fluid-solid interface. Physical review letters, 82(23), p.4671.

Bertrand, G., 1994. Simple points, topological numbers and geodesic neighborhoods in cubic grids. Pattern recognition letters, 15(10), pp.1003-1011.

Bertrand, G., 1996. A Boolean characterization of three-dimensional simple points. Pattern recognition letters, 17(2), pp.115-124.

Blunt, M.J., 1997. Pore level modeling of the effects of wettability. SPE Journal, 2(04), pp.494-510.

Blunt, M.J., Jackson, M.D., Piri, M. and Valvatne, P.H., 2002. Detailed physics, predictive capabilities and macroscopic consequences for pore-network models of multiphase flow. Advances in Water Resources, 25(8-12), pp.1069-1089.

Blunt, M.J., Bijeljic, B., Dong, H., Gharbi, O., Iglauer, S., Mostaghimi, P., Paluszny, A. and Pentland, C., 2013. Pore-scale imaging and modelling. Advances in Water Resources, 51, pp.197-216.

Botan, A., Rotenberg, B., Marry, V., Turq, P. and Noetinger, B., 2011. Hydrodynamics in clay nanopores. The Journal of Physical Chemistry C, 115(32), pp.16109-16115.

Broadbent, S.R. and Hammersley, J.M., 1957, July. Percolation processes: I. Crystals and mazes. In Mathematical Proceedings of the Cambridge Philosophical Society (Vol. 53, No. 3, pp. 629-641). Cambridge University Press.

Bryant, S.L., Mellor, D.W. and Cade, C.A., 1993. Physically representative network models of transport in porous media. AIChE Journal, 39(3), pp.387-396.

Byun, D., Kim, J., Ko, H.S. and Park, H.C., 2008. Direct measurement of slip flows in superhydrophobic microchannels with transverse grooves. Physics of Fluids, 20(11), p.113601.

Campbell, S.E., Luengo, G., Srdanov, V.I., Wudl, F. and Israelachvili, J.N., 1996. Very low viscosity at the solid–liquid interface induced by adsorbed C60 monolayers. Nature, 382(6591), p.520.

Calabi, L. and Hartnett, W.E., 1968. A Motzkin-type theorem for closed nonconvex sets. Proceedings of the American Mathematical Society, 19(6), pp.1495-1498.

Cargill III, G.S., 1984, February. Radial distribution functions and microgeometry of dense random packings of hard spheres. In AIP Conference Proceedings (Vol. 107, No. 1, pp. 20-36). AIP.

Chen, L., Zhang, L., Kang, Q., Viswanathan, H.S., Yao, J. and Tao, W., 2015. Nanoscale simulation of shale transport properties using the lattice Boltzmann method: permeability and diffusivity. Scientific reports, 5.

Chen, S. and Doolen, G.D., 1998. Lattice Boltzmann method for fluid flows. Annual review of fluid mechanics, 30(1), pp.329-364.

Chen, X., Cao, G., Han, A., Punyamurtula, V.K., Liu, L., Culligan, P.J., Kim, T. and Qiao, Y., 2008. Nanoscale fluid transport: size and rate effects. Nano letters, 8(9), pp.2988-2992.

Christenson, H.K., Gruen, D.W.R., Horn, R.G. and Israelachvili, J.N., 1987. Structuring in liquid alkanes between solid surfaces: Force measurements and mean-field theory. The Journal of chemical physics, 87(3), pp.1834-1841.

Comisky, J.T., Newsham, K., Rushing, J.A. and Blasingame, T.A., 2007, January. A comparative study of capillary-pressure-based empirical models for estimating absolute permeability in tight gas sands. In SPE Annual Technical Conference and Exhibition. Society of Petroleum Engineers.

Cottin-Bizonne, C., Barrat, J.L., Bocquet, L. and Charlaix, E., 2003. Low-friction flows of liquid at nanopatterned interfaces. Nature materials, 2(4), p.237.

Cottin-Bizonne, C., Jurine, S., Baudry, J., Crassous, J., Restagno, F. and Charlaix, E., 2002. Nanorheology: an investigation of the boundary condition at hydrophobic and hydrophilic interfaces. The European Physical Journal E, 9(1), pp.47-53.

Curtis, M.E., Ambrose, R.J., Sondergeld, C.H. and Rai, C.S., 2011, January. Investigation of the relationship between organic porosity and thermal maturity in the Marcellus Shale. In North American unconventional gas conference and exhibition. Society of Petroleum Engineers.

Curtis, M. E., Goergen, E. T., Jernigen, J. D., Sondergeld, C. H., & Rai, C. S. (2014, August 25). Mapping of Organic Matter Distribution on the Centimeter Scale with Nanometer Resolution. Unconventional Resources Technology Conference. doi:10.15530/URTEC-2014-1922757

Delerue, J.F., Perrier, E., Yu, Z.Y. and Velde, B., 1999. New algorithms in 3D image analysis and their application to the measurement of a spatialized pore size distribution in soils. PHYSICS AND CHEMISTRY OF THE EARTH PART A SOLID EARTH AND GEODESY, 24, pp.639-644.

Doyen, P.M., 1988. Permeability, conductivity, and pore geometry of sandstone. Journal of Geophysical Research: Solid Earth, 93(B7), pp.7729-7740.

Dong, H. and Blunt, M.J., 2009. Pore-network extraction from micro-computerized-tomography images. Physical review E, 80(3), p.036307.

Doshi, D.A., Watkins, E.B., Israelachvili, J.N. and Majewski, J., 2005. Reduced water density at hydrophobic surfaces: effect of dissolved gases. Proceedings of the National Academy of Sciences of the United States of America, 102(27), pp.9458-9462.

Fatt I. The network model of porous media. I. Capillary pressure characteristics. AIME Petrol Trans 1956; 207:144–59.

Falk, K., 2011. The molecular origin of fast fluid transport in carbon nanotubes: theoretical and molecular dynamics study of liqui/solid friction in graphitic nanopores (Doctoral dissertation, Université Claude Bernard-Lyon I).

Finney, J.L., 1970. Random packings and the structure of simple liquids. I. The geometry of random close packing. Proc. R. Soc. Lond. A, 319(1539), pp.479-493.

Flory, P.J., 1941. Molecular size distribution in three dimensional polymers. I. Gelation1. Journal of the American Chemical Society, 63(11), pp.3083-3090.

Ghanbari, E. and Dehghanpour, H., 2015. Impact of rock fabric on water imbibition and salt diffusion in gas shales. International Journal of Coal Geology, 138, pp.55-67.

Gladkikh, M. and Bryant, S., 2005. Prediction of imbibition in unconsolidated granular materials. Journal of colloid and interface science, 288(2), pp.526-539.

Goertz, M.P., Houston, J.E. and Zhu, X.Y., 2007. Hydrophilicity and the viscosity of interfacial water. Langmuir, 23(10), pp.5491-5497.

Granick, S., Zhu, Y. and Lee, H., 2003. Slippery questions about complex fluids flowing past solids. Nature materials, 2(4), p.221.

Heath, J.E., Dewers, T.A., McPherson, B.J., Petrusak, R., Chidsey Jr, T.C., Rinehart, A.J. and Mozley, P.S., 2011. Pore networks in continental and marine mudstones: Characteristics and controls on sealing behavior. Geosphere, 7(2), pp.429-454.

Heinbuch, U. and Fischer, J., 1989. Liquid flow in pores: Slip, no-slip, or multilayer sticking. Physical Review A, 40(2), p.1144.

Heuberger, M., Zäch, M. and Spencer, N.D., 2001. Density fluctuations under confinement: when is a fluid not a fluid?. Science, 292(5518), pp.905-908.

Hilder, T.A., Gordon, D. and Chung, S.H., 2009. Salt rejection and water transport through boron nitride nanotubes. Small, 5(19), pp.2183-2190.

Ho, T.A., Papavassiliou, D.V., Lee, L.L. and Striolo, A., 2011. Liquid water can slip on a hydrophilic surface. Proceedings of the National Academy of Sciences, 108(39), pp.16170-16175.

Holt, J.K., Park, H.G., Wang, Y., Stadermann, M., Artyukhin, A.B., Grigoropoulos, C.P., Noy, A. and Bakajin, O., 2006. Fast mass transport through sub-2-nanometer carbon nanotubes. Science, 312(5776), pp.1034-1037.

Huang, D.M., Sendner, C., Horinek, D., Netz, R.R. and Bocquet, L., 2008. Water slippage versus contact angle: A quasiuniversal relationship. Physical review letters, 101(22), p.226101.

Hughes, R.G. and Blunt, M.J., 2000. Pore scale modeling of rate effects in imbibition. Transport in Porous Media, 40(3), pp.295-322.

Jiang, Z., Wu, K., Couples, G., Van Dijke, M.I.J., Sorbie, K.S. and Ma, J., 2007. Efficient extraction of networks from three-dimensional porous media. Water Resources Research, 43(12).

Jin, R.Y., Song, K. and Hase, W.L., 2000. Molecular dynamics simulations of the structures of alkane/hydroxylated α-Al2O3 (0001) interfaces. The Journal of Physical Chemistry B, 104(12), pp.2692-2701.

Joly, L., Ybert, C., Trizac, E. and Bocquet, L., 2006. Liquid friction on charged surfaces: From hydrodynamic slippage to electrokinetics. The Journal of chemical physics, 125(20), p.204716.

Josh, M., Esteban, L., Delle Piane, C., Sarout, J., Dewhurst, D.N. and Clennell, M.B., 2012. Laboratory characterisation of shale properties. Journal of Petroleum Science and Engineering, 88, pp.107-124.

Joseph, S. and Aluru, N.R., 2008. Why are carbon nanotubes fast transporters of water?. Nano letters, 8(2), pp.452-458.

Kannam, S.K., Todd, B.D., Hansen, J.S. and Daivis, P.J., 2013. How fast does water flow in carbon nanotubes?. The Journal of chemical physics, 138(9), p.094701.

Kirkpatrick, S., 1973. Percolation and conduction. Reviews of modern physics, 45(4), p.574.

Klein, J. and Kumacheva, E., 1995. Confinement-induced phase transitions in simple liquids. Science, 269(5225), pp.816-819.

Kwiecien, M.J., Macdonald, I.F. and Dullien, F.A.L., 1990. Three-dimensional reconstruction of porous media from serial section data. Journal of Microscopy, 159(3), pp.343-359.

Kong, T.Y. and Rosenfeld, A., 1989. Digital topology: Introduction and survey. Computer Vision, Graphics, and Image Processing, 48(3), pp.357-393.

Krott, L.B., Bordin, J.R. and Barbosa, M.C., 2014. New structural anomaly induced by nanoconfinement. The Journal of Physical Chemistry B, 119(1), pp.291-300.

Lan, Y., Ghanbarnezhad Moghanloo, R. and Davudov, D., 2017. Pore compressibility of shale formations. SPE Journal.

Laurent, J., Bouteca, M.J., Sarda, J.P. and Bary, D., 1993. Pore-pressure influence in the poroelastic behavior of rocks: Experimental studies and results. SPE Formation Evaluation, 8(02), pp.117-122.

Le, T., Striolo, A. and Cole, D.R., 2015. Propane simulated in silica pores: Adsorption isotherms, molecular structure, and mobility. Chemical Engineering Science, 121, pp.292-299.

Ledyastuti, M., Liang, Y., Kunieda, M. and Matsuoka, T., 2012. Asymmetric orientation of toluene molecules at oil-silica interfaces. The Journal of Chemical Physics, 137(6), p.064703.

Levinger, N.E., 2002. Water in confinement. Science, 298(5599), pp.1722-1723.

Li, H. and Zeng, X.C., 2012. Wetting and interfacial properties of water nanodroplets in contact with graphene and monolayer boron–nitride sheets. ACS nano, 6(3), pp.2401-2409.

Li, H. and Misra, S., 2017a. Prediction of subsurface NMR T2 distribution from formation-mineral composition using variational autoencoder. In SEG Technical Program Expanded Abstracts 2017 (pp. 3350-3354). Society of Exploration Geophysicists.

Li, H. and Misra, S., 2017b. Prediction of subsurface NMR T2 distributions in a shale petroleum system using variational autoencoder-based neural networks. IEEE Geoscience and Remote Sensing Letters, 14(12), pp.2395-2397.

Li, J., Li, X., Wu, K., Wang, X., Shi, J., Yang, L., Zhang, H., Sun, Z., Wang, R. and Feng, D., 2016. Water sorption and distribution characteristics in clay and shale: effect of surface force. Energy & Fuels, 30(11), pp.8863-8874.

Lindquist, W.B., Lee, S.M., Coker, D.A., Jones, K.W. and Spanne, P., 1996. Medial axis analysis of void structure in three-dimensional tomographic images of porous media. Journal of Geophysical Research: Solid Earth, 101(B4), pp.8297-8310.

Lohou, C., and G. Bertrand (2005), A 3D 6-subiteration curve thinning algorithm based on P-simple points, Discrete Appl. Math., 151(3), 198–228.

Loucks, R.G., Reed, R.M., Ruppel, S.C. and Hammes, U., 2012. Spectrum of pore types and networks in mudrocks and a descriptive classification for matrix-related mudrock pores. AAPG bulletin, 96(6), pp.1071-1098.

Malandain, G. and Fernández-Vidal, S., 1998. Euclidean skeletons. Image and vision computing, 16(5), pp.317-328.

Markesteijn, A.P., Hartkamp, R., Luding, S. and Westerweel, J., 2012. A comparison of the value of viscosity for several water models using Poiseuille flow in a nano-channel. The Journal of chemical physics, 136(13), p.134104.

Mashl, R.J., Joseph, S., Aluru, N.R. and Jakobsson, E., 2003. Anomalously immobilized water: a new water phase induced by confinement in nanotubes. Nano Letters, 3(5), pp.589-592.

Mason, G. and Morrow, N.R., 1991. Capillary behavior of a perfectly wetting liquid in irregular triangular tubes. Journal of Colloid and Interface Science, 141(1), pp.262-274.

Milliken, K.L., Rudnicki, M., Awwiller, D.N. and Zhang, T., 2013. Organic matter–hosted pore system, Marcellus formation (Devonian), Pennsylvania. AAPG bulletin, 97(2), pp.177-200.

Monteiro, P.J., Rycroft, C.H. and Barenblatt, G.I., 2012. A mathematical model of fluid and gas flow in nanoporous media. Proceedings of the National Academy of Sciences, 109(50), pp.20309-20313.

Morgenthaler, D.G., 1981. Three-dimensional simple points: sereial erosion, parallel thinning and skeletonization. TR-1005.

Mousavi, M.A. and Bryant, S.L., 2007, January. Geometric models of porosity reduction mechanisms in tight gas sands. In Rocky Mountain Oil & Gas Technology Symposium. Society of Petroleum Engineers.

Mousavi, M.A., 2010. Pore-scale characterization and modeling of two-phase flow in tight gas sandstones (Doctoral dissertation).

Myers, T.G., 2011. Why are slip lengths so large in carbon nanotubes?. Microfluidics and nanofluidics, 10(5), pp.1141-1145.

Oren, P.-E., Bakke, S., and Arntzen, O. J. 1998. Extending Predictive Capabilities to Network Models. Society of Petroleum Engineers.

Ortiz-Young, D., Chiu, H.C., Kim, S., Voïtchovsky, K. and Riedo, E., 2013. The interplay between apparent viscosity and wettability in nanoconfined water. Nature communications, 4, p.2482.

Pascal, T.A., Goddard, W.A. and Jung, Y., 2011. Entropy and the driving force for the filling of carbon nanotubes with water. Proceedings of the National Academy of Sciences, 108(29), pp.11794-11798.

Patzek, T. W. (2001, June 1). Verification of a Complete Pore Network Simulator of Drainage and Imbibition. Society of Petroleum Engineers. doi:10.2118/71310-PA

Porter, M.L., Schaap, M.G. and Wildenschild, D., 2009. Lattice-Boltzmann simulations of the capillary pressure–saturation–interfacial area relationship for porous media. Advances in Water Resources, 32(11), pp.1632-1640.

Pudney, C., 1996, Distance-based skeletonization of 3D image, in Proceedings 1996 IEEE TENCON: Digital Signal Processing Applications, pp. 209–214, Inst. of Electr. and Electron. Eng., New York.

Pudney, C., 1998, Distance-ordered homotopic thinning: A skeletonization algorithm for 3D digital images, Comput. Vision Image Understanding, 72(3), 404–413.

Purcell WR. Capillary pressure – their measurements using mercury and the calculation of permeability therefrom. AIME Petrol Trans 1949; 186:39–48.

Qin, Z. and Buehler, M.J., 2015. Nonlinear viscous water at nanoporous two-dimensional interfaces resists high-speed flow through cooperativity. Nano letters, 15(6), pp.3939-3944.

Raviv, U., Laurat, P. and Klein, J., 2001. Fluidity of water confined to subnanometre films. Nature, 413(6851), p.51.

Rivera, J.L., McCabe, C. and Cummings, P.T., 2002. Layering behavior and axial phase equilibria of pure water and water+ carbon dioxide inside single wall carbon nanotubes. Nano Letters, 2(12), pp.1427-1431.

Saito, T., and J. I. Toriwaki (1995), A sequential thinning algorithm for three dimensional digital pictures using the Euclidean distance transformation, paper presented at 9th Scandinavian Conference on Image Analysis (SCIA'95), Int. Assoc. for Pattern Recognition, Uppsala, Sweden.

Sakhaee-Pour, A. and Bryant, S.L., 2015. Pore structure of shale. Fuel, 143, pp.467-475.

Schmatko, T., Hervet, H. and Leger, L., 2005. Friction and slip at simple fluid-solid interfaces: the roles of the molecular shape and the solid-liquid interaction. Physical review letters, 94(24), p.244501.

Schmidt, V. and McDonald, D.A., 1979. The role of secondary porosity in the course of sandstone diagenesis.

Seaton, N.A., 1991. Determination of the connectivity of porous solids from nitrogen sorption measurements. Chemical Engineering Science, 46(8), pp.1895-1909.

Secchi, E., Marbach, S., Niguès, A., Stein, D., Siria, A. and Bocquet, L., 2016. Massive radius-dependent flow slippage in carbon nanotubes. Nature, 537(7619), p.210.

Shannon, M.A., Bohn, P.W., Elimelech, M., Georgiadis, J.G., Marinas, B.J. and Mayes, A.M., 2008. Science and technology for water purification in the coming decades. Nature, 452(7185), pp.301-310.

Sheppard, A.P., Sok, R.M. and Averdunk, H., 2005. Improved pore network extraction methods. Proceedings of International Symposium of the Society of

Shin, H., Lindquist, W.B., Sahagian, D.L. and Song, S.R., 2005. Analysis of the vesicular structure of basalts. Computers and Geosciences, 31: 473-487.

Silin, D.B., Jin, G. and Patzek, T.W., 2003, January. Robust determination of the pore space morphology in sedimentary rocks. In SPE Annual Technical Conference and Exhibition. Society of Petroleum Engineers.

Silin, D. and Patzek, T., 2006. Pore space morphology analysis using maximal inscribed spheres. Physica A: Statistical mechanics and its applications, 371(2), pp.336-360.

Siria, A., Poncharal, P., Biance, A.L., Fulcrand, R., Blase, X., Purcell, S.T. and Bocquet, L., 2013. Giant osmotic energy conversion measured in a single transmembrane boron nitride nanotube. Nature, 494(7438), p.455.

Soeder, D.J., 2010. The Marcellus shale: Resources and reservations. Eos, Transactions American Geophysical Union, 91(32), pp.277-278.

Sparreboom, W., van den Berg, A. and Eijkel, J.C., 2009. Principles and applications of nanofluidic transport. Nature nanotechnology, 4(11), p.713.

Stockmayer, W.H., 1943. Theory of molecular size distribution and gel formation in branched‐chain polymers. The Journal of chemical physics, 11(2), pp.45-55.

Suk, M.E., Raghunathan, A.V. and Aluru, N.R., 2008. Fast reverse osmosis using boron nitride and carbon nanotubes. Applied Physics Letters, 92(13), p.133120.

Sun, Z., Li, X., Shi, J., Zhang, T. and Sun, F., 2017. Apparent permeability model for real gas transport through shale gas reservoirs considering water distribution characteristic. International Journal of Heat and Mass Transfer, 115, pp.1008-1019.

Tang, G.H., Tao, W.Q. and He, Y.L., 2005. Gas slippage effect on microscale porous flow using the lattice Boltzmann method. Physical Review E, 72(5), p.056301.

Thane, C.G., 2006. Geometry and topology of model sediments and their influence on sediment properties (Doctoral dissertation).

Thomas, J.A. and McGaughey, A.J., 2009. Water flow in carbon nanotubes: transition to subcontinuum transport. Physical Review Letters, 102(18), p.184502.

Tocci, G., Joly, L. and Michaelides, A., 2014. Friction of water on graphene and hexagonal boron nitride from ab initio methods: very different slippage despite very similar interface structures. Nano letters, 14(12), pp.6872-6877.

Veldsink, J.W., van Damme, R.M., Versteeg, G.F. and van Swaaij, W.P.M., 1995. The use of the dusty-gas model for the description of mass transport with chemical reaction in porous media. The Chemical Engineering Journal and the Biochemical Engineering Journal, 57(2), pp.115-125.

Venkatarangan, A.B., 2000. Geometric and statistical analysis of porous media.

Voronov, R.S., Papavassiliou, D.V. and Lee, L.L., 2006. Boundary slip and wetting properties of interfaces: Correlation of the contact angle with the slip length. The Journal of chemical physics, 124(20), p.204701.

Wang, S., Feng, Q., Javadpour, F., Xia, T. and Li, Z., 2015. Oil adsorption in shale nanopores and its effect on recoverable oil-in-place. International Journal of Coal Geology, 147, pp.9-24.

Wang, S., Javadpour, F. and Feng, Q., 2016. Molecular dynamics simulations of oil transport through inorganic nanopores in shale. Fuel, 171, pp.74-86.

Wang, S., Javadpour, F. and Feng, Q., 2016. Fast mass transport of oil and supercritical carbon dioxide through organic nanopores in shale. Fuel, 181, pp.741-758.

Warner, N.R., Jackson, R.B., Darrah, T.H., Osborn, S.G., Down, A., Zhao, K., White, A. and Vengosh, A., 2012. Geochemical evidence for possible natural migration of Marcellus Formation brine to shallow aquifers in Pennsylvania. Proceedings of the National Academy of Sciences, 109(30), pp.11961-11966.

Werder, T., Walther, J.H., Jaffe, R.L., Halicioglu, T., Noca, F. and Koumoutsakos, P., 2001. Molecular dynamics simulation of contact angles of water droplets in carbon nanotubes. Nano Letters, 1(12), pp.697-702.

Whitby, M., Cagnon, L., Thanou, M. and Quirke, N., 2008. Enhanced fluid flow through nanoscale carbon pipes. Nano letters, 8(9), pp.2632-2637.

Wu, K., Chen, Z., Li, J., Li, X., Xu, J. and Dong, X., 2017. Wettability effect on nanoconfined water flow. Proceedings of the National Academy of Sciences, p.201612608.

Xu, M. and Dehghanpour, H., 2014. Advances in understanding wettability of gas shales. Energy & Fuels, 28(7), pp.4362-4375.

Ye, Zhi, and Ghassemi, A. 2016a. "Deformation Properties of Saw-Cut Fractures in Barnett, Mancos and Pierre Shales." Proceeeding: 50th US Rock Mechanics/Geomechanics Symposium, Houston, Texas, (2016).

Ye, Zhi, Ghassemi, A., and Riley, 2016b S. "Fracture Properties Characterization of Shale Rocks." Proceeeding: Unconventional Resources Technology Conference, San Antonio, Texas.

Ye, Zhi, and Ghassemi, A., 2017, "Experimental Investigation of Injection-driven Shear Slip and Permeability Evolution in Granite for EGS Stimulation." Proceeeding: 42nd Stanford Geothermal Workshop, Stanford, California.

Ye, Zhi, and Ghassemi, A., 2018a, " Injection-induced Fracture Propagation and Coalescence Under Triaxial Loading." 52nd US Rock Mechanics / Geomechanics Symposium held in Seattle, Washington, USA.

Ye, Zhi, and Ghassemi, A., 2018b, "Experimental study on injection-induced fracture propagation and coalescence for EGS stimulation." 43rd Workshop on Geothermal Reservoir Engineering. Stanford, CA, USA.

Yuan, B., Zheng, D. and Ghanbarnezhad Moghanloo, R., 2016, August. Integrated Production Analysis Using the Concept of Dynamic Drainage Volume: Modelling, Simulation and Field Applications. In SPE Asia Pacific Hydraulic Fracturing Conference. Society of Petroleum Engineers.

Yuan, B., Zheng, D., Moghanloo, R.G. and Wang, K., 2017. A novel integrated workflow for evaluation, optimization, and production predication in shale plays. International Journal of Coal Geology, 180, pp.18-28.

Zapata, Y. and Sakhaee-Pour, A., 2016. Modeling adsorption–desorption hysteresis in shales: Acyclic pore model. Fuel, 181, pp.557-565.

Zhang, P., Hu, L., Meegoda, J.N. and Gao, S., 2015. Micro/nano-pore network analysis of gas flow in shale matrix. Scientific reports, 5, p.13501.

Zhang, T., Ellis, G.S., Ruppel, S.C., Milliken, K. and Yang, R., 2012. Effect of organic-matter type and thermal maturity on methane adsorption in shale-gas systems. Organic geochemistry, 47, pp.120-131.

Zhao, H.Q., Macdonald, I.F. and Kwiecien, M.J., 1994. Multi-orientation scanning: a necessity in the identification of pore necks in porous media by 3-D computer reconstruction from serial section data. Journal of colloid and interface science, 162(2), pp.390-401.

Zheng, D., 2016. Integrated production data analysis of horizontal fractured well in unconventional reservoir.

Zheng, D., Moghanloo, R.G., Yuan, B. and Dong, X., 2016, August. Modeling dynamic drainage volume for multi-stage fractured wells in composite shale systems: new analytical solution for transient linear flow. In SPE Asia Pacific Hydraulic Fracturing Conference. Society of Petroleum Engineers.

Zheng, D., Yuan, B. and Moghanloo, R.G., 2017. Analytical modeling dynamic drainage volume for transient flow towards multi-stage fractured wells in composite shale reservoirs. Journal of Petroleum Science and Engineering, 149, pp.756-764.

Zheng, D. and Reza, Z., 2018a. Prediction of pore-scale transport properties in unconventional reservoirs using novel theoretical dendroidal pore-network model. Journal of Petroleum Science and Engineering, 170, pp.712-720.

Zheng, D., Zapata, Y. and Reza, Z.A., 2018b, July. Characterization of Transport Properties of Shale Using Novel Theoretical Pore-scale Dendroidal Model. In SPE/AAPG/SEG Unconventional Resources Technology Conference. Unconventional Resources Technology Conference.

Zheng, D., and Reza, Z.A., 2018c. Extracted Pore-Network Model for Shales Characterizing Geometry of Void Space. Unconventional Resources Technology Conference (URTEC).

Zhu, W.C., Liu, J., Sheng, J.C. and Elsworth, D., 2007. Analysis of coupled gas flow and deformation process with desorption and Klinkenberg effects in coal seams. International Journal of Rock Mechanics and Mining Sciences, 44(7), pp.971-980.

Zhu, L., Attard, P. and Neto, C., 2012. Reconciling slip measurements in symmetric and asymmetric systems. Langmuir, 28(20), pp.7768-7774.

Zimmerman, R.W., Somerton, W.H. and King, M.S., 1986. Compressibility of porous rocks. Journal of Geophysical Research: Solid Earth, 91(B12), pp.12765-12777.